THEORY OF SYMMETRY AND ASYMMETRY IN TWO-DIMENSIONAL MAGNETIC RECORDING HEADS

Submitted by

Ammar Isam Edress Mohamed

to the University of Exeter as a thesis for the degree of

Doctor of Philosophy (Ph.D.) in Mathematics, May 2016

I certify that all material in this thesis which is not my own work has been identified and that no material has previously been submitted and approved for the award of a degree by this or any other university.

Signature: ……..

Abstract

As part of the natural evolution and continued optimisation of their designs, current and future magnetic recording heads, used and proposed in technologies such as perpendicular recording, shingled magnetic recording and two-dimensional magnetic recording, often exhibit asymmetry in their structure. They consist of two semi-infinite poles separated by a gap (where the recording field is produced), with an inner gap faces inclined at an angle. Modelling of the fields from asymmetrical structures is complex, and no explicit solutions are currently available (only implicit conformal mapping solutions are available for rational inclination angles). Moreover, there is limited understanding on the correlation between the gap corner angle and the magnitude, distribution and wavelength response of these head structures. This research was therefore set out to investigate approximate analytical and semi-analytical methods for modelling the magnetic potentials and fields of two-dimensional symmetrical and asymmetrical magnetic recording heads, and deliver a quantitative understanding of the behaviour of the potentials and fields as functions of gap corner angles. The accuracy of the derived expressions (written in terms of the normalised root-mean-square deviation) was assessed by comparison to exact available solutions for limited cases, and to finite-element calculations on Comsol Multiphysics.

Two analytical methods were derived to approximately model the fields from two-dimensional heads with tilted gap corners in the presence and absence of a soft magnetic underlayer (SUL): in the first method, the potential near a single, two-dimensional corner

held at a constant potential is derived exactly through solution of Laplace's equation for the scalar potential in polar coordinates. Then through appropriate choice of enclosing boundary conditions, the potentials and fields of two corners at equal and opposite potentials and displaced from each other by a distance equal to the gap length were superposed to map the potential and field for asymmetrical and symmetrical heads. For asymmetrical heads, the superposition approximation provided good agreement to finite-element calculations for the limited range of exterior corner angles θ_0 from 0° (right-angled corner) to 45°, due to the mismatch of surface charge densities on both poles for this geometry. For symmetrical head structures, the superposition approximation was found to yield remarkable agreement to exact solutions for all gap corner orientations from 0° (right-angled head) to 90° ("thin" gap head).

In the second method derived in this research for modelling asymmetrical heads involved using a rational function approximation with free parameters to model the surface potential of asymmetrical heads. The free parameters and their functional dependence on corner angle were determined through fitting to finite-element calculations, enabling the derivation of analytical expressions for the magnetic fields that are in good agreement with exact solutions for all corner angels (0° to 90°).

To complement the two approximate methods for modelling the fields from asymmetrical and symmetrical heads, a new general approach based on the sine integral transform was

derived to model the reaction of soft underlayers on the surface potential or field of any two-dimensional head structure, for sufficiently close head-to-underlayer separations. This method produces an infinite series of correction terms whose coefficients are functions of the head-to-underlayer separation and gap corner angle, that are added to the surface potential or field in the absence of an underlayer. This new approach demonstrated good agreement with finite-element calculations for sufficiently close head-to-underlayer separations, and with the classical Green's functions solutions for increasing separations.

Using the derived analytical method and explicit expressions in this work, an understanding of the nature of the magnetic fields and their spectra as functions of the gap corner angles is gained. This understanding and analytical theory will benefit the modelling, design and optimisation of high performance magnetic recording heads.

Table of Contents

List of Figures

List of Tables

Declaration

No portion of the work referred to in the thesis has been submitted in support of an application for another degree or qualification of this or any other university or other institute of learning.

Acknowledgments

First and foremost, praises and thanks to Allah, the Almighty, for his showers of blessings throughout my research work.

Secondly, I would like to express my special appreciation and thanks to my supervisor **Dr. Mustafa Aziz**, you have been a tremendous mentor for me. I would like to thank you for encouraging my research and for allowing me to grow as a researcher. Your advice on research has been priceless. I could not have wished for a better advisor and mentor for my PhD.

A special thanks to my family. Words cannot express how grateful I am to my mother, father, brothers, sisters, my mother-in law, father-in-law, and friends for all of the sacrifices that you've made on my behalf. Your prayer for me was what sustained me thus far. I would also like to thank all of my friends who supported me to strive towards my goal. At the end, I would like express appreciation to my beloved wife **Shrmeen** for being so patient with me and for providing more support than she could ever imagine.

This thesis is dedicated to them and in particular, to my father who died with 64 years old in Feb 2016.

Chapter 1: Introduction to Magnetic Recording

1.1 Magnetic Recording

The hard disk drive (HDD) can be also called rigid disk files or direct access storage devices (DASD). HDD industry is slightly more than half a century old, the six decades of this industry have experienced many excellent and triumphant technological innovations. It took creativity and hard work of many scientists and engineers to transfer from the earliest HDD of 1956 to the current status. Therefore, a historical development of the HDD introduced for comparison to the disk drives we see these days. The introduction of recording densities on rigid disk media at these levels has of course, meant a dramatic reduction in the size of an actual bit and a dramatic increase in the track density on the surface of the disk, these changes are shown in Figure 1.1 where bit sizes extending out to 100 Gbits/in^2 are represented.

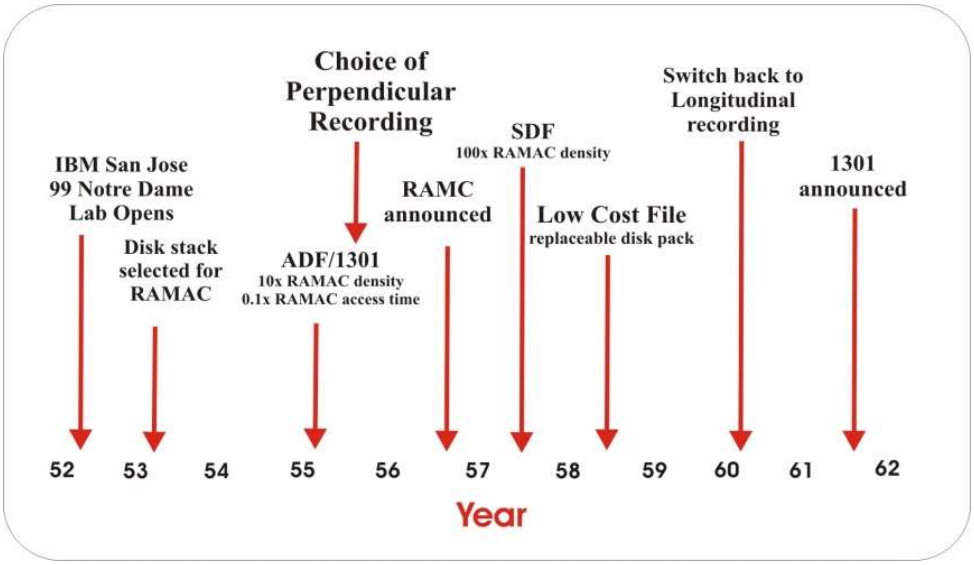

Figure 1.1 Time line, magnetic disk-drive projects at IBM San Jose in the 1950s [1].

The twenty first century is considered as the generation of HDD developments and aims to raise both linear density and track density to achieve the lowest cost per megabyte and faster access time.

The last four decades is considered as a revelation of the phenomenal increase in the storage capacity of HDDs [2]. All HDDs store the data as tiny areas of either positive or negative magnetisations in the magnetic storage disks to represent “bits” of information. The bits are written closely-spaced to form circular “tracks” on the rotating disk. Many such concentric tracks cover the surfaces of the disks. There are millions of bits on each track and many tens of thousands of tracks on each disk surface. The total storage capacity of a HDD depends directly on how small the recorded area can made, and the smaller the bits-the greater the storage capacity [3].

The term ‘Areal Density’ refers to the amount of data that can be stored on one-inch square of the magnetic storage material. It’s usually represented in billions of bits per square inch on a hard drive platter. Areal density growth-rate is a frequently quoted measure of the rate of advance of the technology. In recent years the growth-rate has slowed down (see Figure 1.2) because of fundamental limits in magnetic recording [4] which will be reviewed later in this chapter.

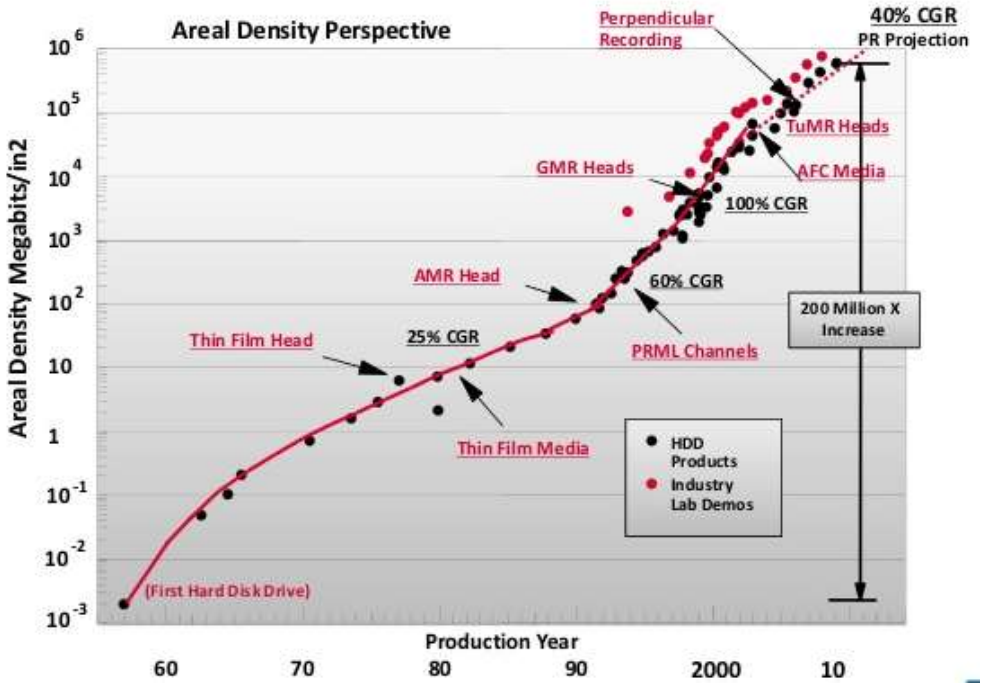

Figure 1.2 Bit areal density progress in magnetic hard disk drive [5].

The 1990s can be considered as the fastest period in bit areal density progress, mainly due to the introduction of thin-film head technology and magnetoresistive sensors for readouts. As indicated in Figure 1.2, the first hard disk drive (RAMAC) supported an areal density of 2000 bits/in^2 only. HDD areal densities are projected to climb to a maximum 1.8 T bit/in^2 platter by 2016, from 744 GB/in^2 in 2011 [6]. The current products of HDD reached more than 1Tb/in^2 areal densities, and likely to increase into 2Tb/in^2 within the next 3 years [6, 7]. This 60-100% growth rate in storage capacity was supported by development of thin-film high energy media and advancements in digital recording channels [9]. In order to support the increased demands in storage capacities, the current development of hard-disk drive technologies has been continuing to push the areal density by at least 30 - 40% annually, moreover, the transition to perpendicular magnetic recording (PMR) from longitudinal magnetic recording (LMR) made a significant

contribution to the hard-disk technology and continued increases in their storage capacity [10]. Nevertheless, there is a fundamental limit on the current technology such as thermal stability [11], which will be outlined later in this chapter.

1.2 LMR and PMR

Longitudinal magnetic recording used to be the main recording method in HDDs for over 50 years since the first released HDD by IBM [2]. The storage capacity of the first HDD was 5MB at a recording density of 2kBits/in^2 [12]. In longitudinal recording, the magnetisation is in the plane of the disk medium and lying parallel and anti-parallel to the direction of the moving disk (see Figure 1.3). The inductive write element records data in horizontal magnetisation patterns. The magnetoresistive (MR) readout element is used to sense the stray magnetic fields from the transition between regions of opposite magnetisation to produce the readout voltage [13].

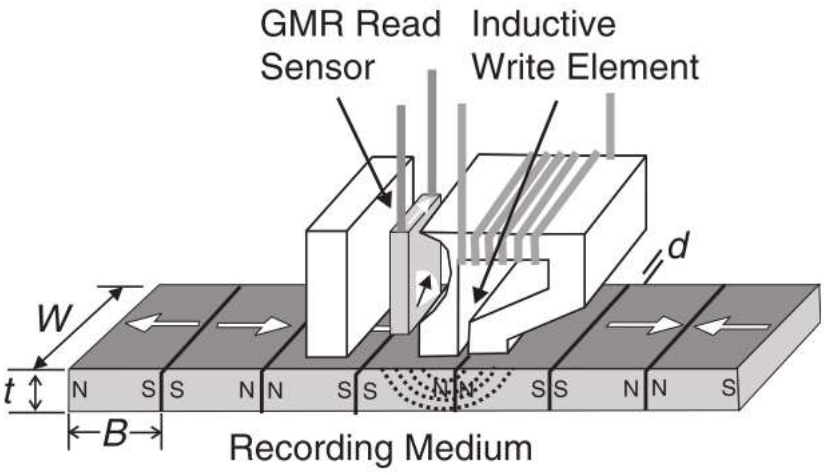

Figure 1.3 Schematic drawing of a longitudinal recording system. *B* is the bit length, *W* is the track width and *t* is the medium thickness. *d* is the flying height of the head above the medium [14].

Traditionally, the areal density can be increased by simply reducing the size of the data bit on the medium and scale down the recording heads. However, there are limits on how small the bit length can be made due to the thermal stabilities as will be discussed later. Thus, an improved medium with high coercivity is required. However, there is the problem of writing on such media with ring-type heads due to the fact that the maximum write field for longitudinal recording heads is limited to around $2\pi M_s$ Gauss (SI units), where M_s is the saturation magnetisation of the heads material. Hence, longitudinal recording recorded an approximately 100Gb/in^2 as the highest areal density achievable [15]. To overcome these problems, perpendicular magnetic recording has been introduced and implemented in HDDs.

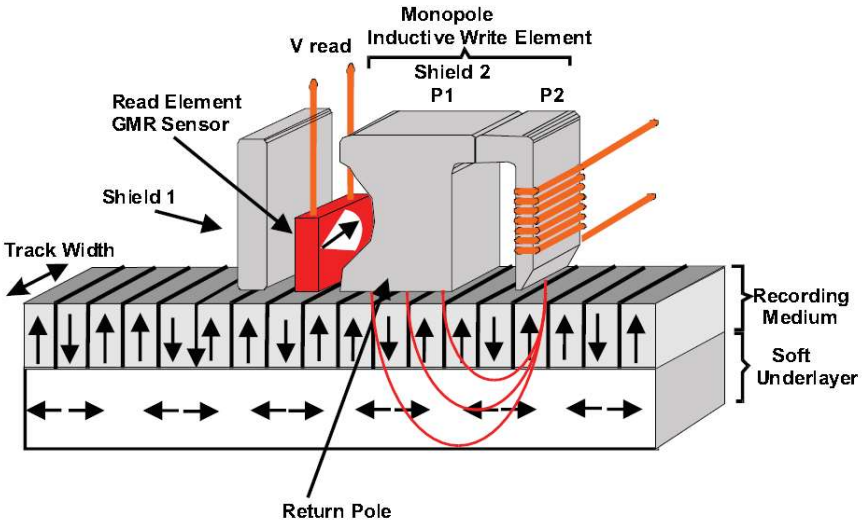

Figure 1.4 Perpendicular magnetic recording system with a SUL and single-pole head [16].

Perpendicular magnetic recording was proposed for the first time about three decades ago by Professor Shun-ichi Iwasaki [13]. However, another separate research effort on perpendicular recording development started much earlier by Rey Johnson in 1952 [1].

As illustrated in Figure 1.4, in perpendicular recording the easy axis of the recording medium is perpendicular to the disk surface; hence, the orientation of the magnetisation is pointing either "up" or "down" [17]. In the perpendicular recording mode, a single pole head (SPH) is used for writing along with a double-layer recording medium consisting of a "hard" perpendicular magnetic layer and a "soft" magnetic underlayer (SUL). The purpose of the soft underlayer is to "close" the path for the magnetic flux generated in the coil of the recording head and to increase the perpendicular magnetic recording field by approximately a factor of two i.e. to almost $4\pi M_s$ [13].

PMR offers the following advantages compared to LMR:

- The single-pole type write head is used in PMR which doubles the field produced by a ring-type head [14, 15], where a higher write field would increase the write efficiency [20] and increases the storage density.
- The thermal stability of the magnetised regions or bits in PMR is more than in LMR [21].
- The adjacent bits are placed side by side rather than end-to-end and therefore there is reduction in medium demagnetising fields and increase in linear density [22].
- The added Soft magnetic Underlayer (SUL) offers a larger effective write field and field gradient which can increase the data storage significantly [11, 18, 19].

1.3 Fundamental limits of magnetic recording

Data on a magnetic recording medium are stored as spatial variations of the magnetisation [16]. To achieve the highest areal densities, it is necessary to use a magnetic recording configuration capable of writing over a small number of grains and a signal processing

system capable of recovering the data reliably from each bit that is recorded on these small grains. Simple scaling argument shows that thermal stability of the medium will become the primary physical concern at very high areal densities. Thermal stability indicates the lower limit of the grain size in the recording system. Grains' sizes smaller than this limit are unstable and likely to switch the magnetisation within a shorter time than the desired time-scale for data storage [13].

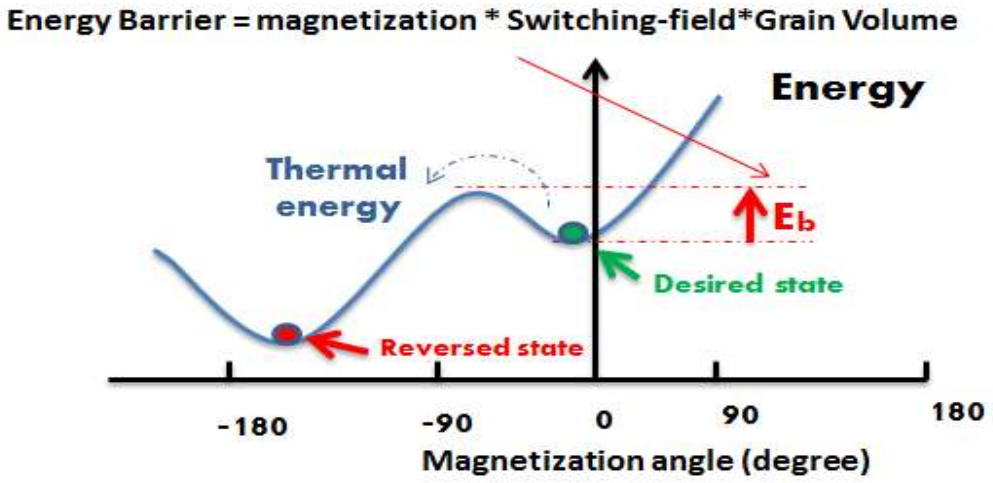

Figure 1.5 The concept of superparamagnetic limit due to random magnetic field fluctuation [25].

The concept of this superparamagnetic behaviour, as illustrated above in Figure 1.5 has been explained by Nèel, in 1949 [26]. The stable magnetisation direction of a uniaxial grain can be switched to other with the assistance of thermal energy to surmount an energy barrier E_b. The energy barrier is dependent on the quantity $K_U V$ for a single grain, where K_U is represented the magnetic anisotropy energy per unit volume and V is the grain volume [10, 23]. According to statistical physics, even for a relatively large value of K_U (compared to the characteristic thermal energy density) because of the thermal

fluctuations there is a finite probability for the grain to reverse its magnetic moment, as given by the following expression [24]:

$$f\pm = f_0 exp(-\frac{E_b \pm}{K_B T}) \quad (1.1)$$

where f_0 is a characteristic frequency in the range from 10^9 to 10^{12} Hz, K_B is Boltzmann's constant, T is the temperature, $E_b=K_uV$ is the energy barrier between the two energy states and the subscripts "+" and "-" represents the magnetisation directions. For a medium to be thermally stable the ratio of K_uV/K_BT should be substantially greater than 40, [24] i.e.:

$$\frac{K_U V}{K_B T} \gg 40 \quad (1.2)$$

This defines the minimum grain volume required to produce a stable bit:

$$V \gg \frac{40 K_B T}{K_U} \quad (1.3)$$

Thus when using small grains to achieve higher areal densities, the anisotropy energy density K_u should be increased in order to sustain thermal stability. However, the write head needs to be able to write onto the high anisotropy medium. Therefore, perpendicular recording is perfectly suited for writing on such high anisotropy media due to the strong write fields that can be generated (up to $4\pi M_s$) by the single-pole/soft underlayer arrangement. The use of higher anisotropy materials allows higher areal densities without

compromising thermal stability of the recording data [24], however at the expense of writability using existing recording head materials.

1.4 Current efforts to overcome the fundamental limits of magnetic recording

To overcome the thermal stability and writability challenges, a number of alternative storage techniques were investigated by researchers. Among key alternative technologies to conventional perpendicular magnetic recording are:

1.4.1 Heat-Assisted Magnetic Recording (HAMR)

This approach utilised laser annealing to reduce the magnetic anisotropy of the recording medium. Thus, the switching field, which is the value of the field required to switch the magnetic state of the medium, is significantly reduced and the write head field becomes sufficient to reverse the magnetisation as shown in Figure 1.6. After heating, the medium is quickly cooled back to ambient temperature to complete the write process [20, 21, 22].

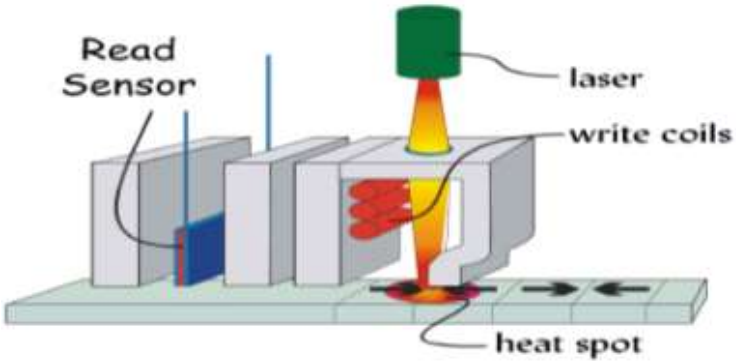

Figure 1.6 Heat-Assisted Magnetic Recording [23].

1.4.2 Bit Patterned Media (BPM)

This involves patterning the magnetic recording medium into islands of nanometer sized in order to store one bit of information for each island (See Figure 1.7) [30]. Due to shape anisotropy or interlayer exchange coupling, the thermal stability for individual island is reserved and reformed to close patterned which is achieve higher areal densities.

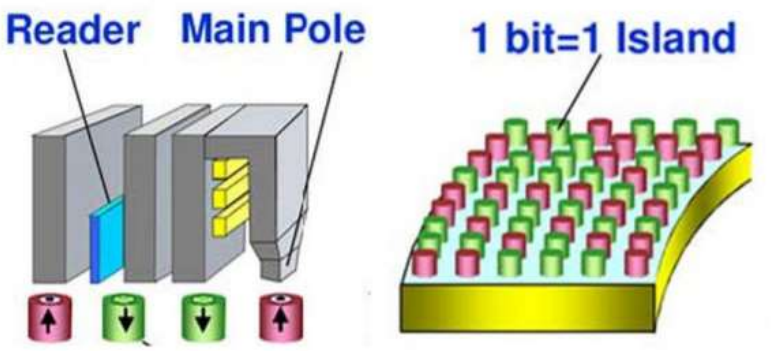

Figure 1.7 Patterned Media Magnetic Recording [12].

1.4.3 Microwave Assisted Magnetic Recording (MAMR)

Another possible technique is used fields significantly below the media coercivity during writing process to achieve a higher areal densities [31]. This is known as "microwave assisted magnetic recording" where the information can be recorded with a write field that normally would be too small to cause the reversal as illustrated in Figure 1.8.

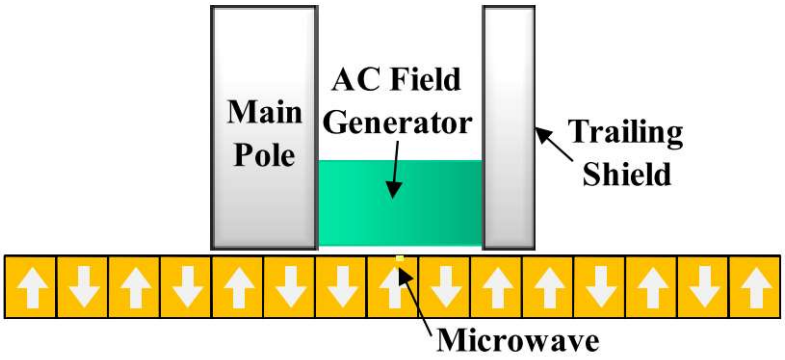

Figure 1.8 Schamatic of Microwave Assisted Magnetic Recording (MAMR) [32].

These alternative techniques require fundamental changes in the recording head and storage media configurations and are currently under intense investigation.

1.4.4 Shingled Magnetic Recording (SMR)

SMR is considered as a powerful technology that augments conventional magnetic recording by writing overlapping tracks without separating guard bands, just like shingling bricks on a house roof as illustrated in Figure 1.9. Placing tracks closer together increases the track density and therefore in general the areal density [33]. This approach is based on existing conventional recording technology, however changes to the write heads (tilted, corner heads with appropriate shielding [34] and [35] and coding schemes are needed to increase the field gradients and reduce corner fringing fields to write narrower tracks with less cross-track interference. Moreover, writing and erasure of individual tracks is no longer possible and block write/erase is instead used following the approach used in solid-state drives.

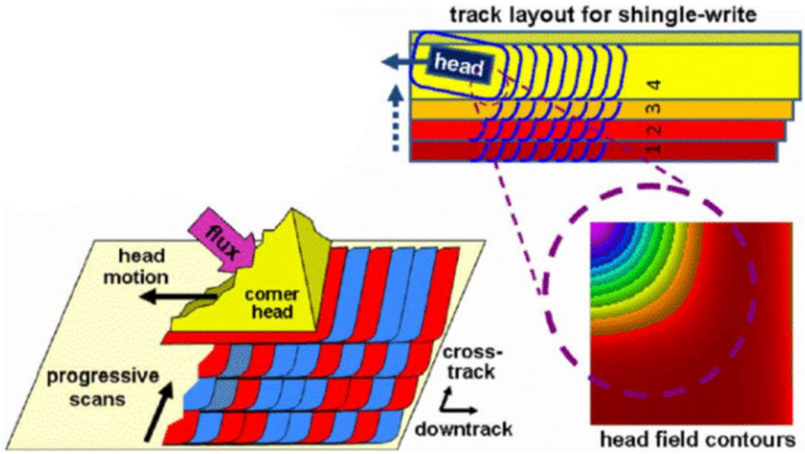

Figure 1.9 Shingled Magnetic Recording-Writing Process [36].

1.4.5 Two Dimensional Magnetic Recording (TDMR)

This approach has recently been proposed as promising technique for ultra-high densities towards 10 Tbits/in^2 [37]. The ultimate goal of TDMR is to record one bit of information per grain of a continuous recording medium and combines two important techniques: Shingled Magnetic Recording (SMR) and 2-D readback and signal-processing as shown in Figure 1.10 [23]. However, TDMR was predicted to yield recording densities of 10 Tb/in^2, a limit that can be reached provided that the writing and read-back processes have a high resolution and low noise [12]. TDMR uses conventional media to extend recording densities and thus avoids the challenges associated with Bit Patterned Media (BPM), or Heat/Microwave Assisted Magnetic Recording [30].

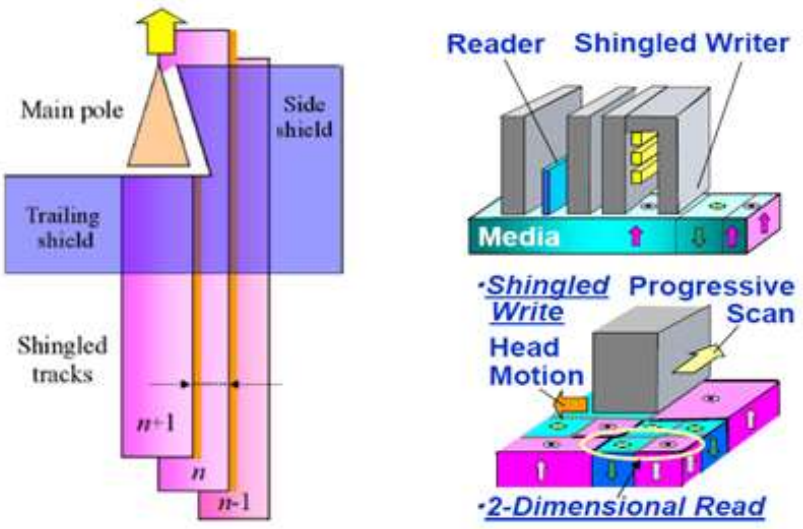

Figure 1.10 Schematic shows TDMR combining shingled write recording (SWR) and 2-D readback and signal-processing [23].

The ability to write or address individual grains or a small volume in the recording medium requires new recording head designs. Corner-type recording heads have been suggested for shingled and two-dimensional magnetic recording [31, 32, 33]. The design of the apex of these heads and associated shielding can be exploited to produce focused fields and high field gradients over small volumes of the recording medium to achieve higher areal densities.

1.5 Magnetic Recording Heads

The previous overview of magnetic recording technology makes clear the fundamental role of the recording head in defining the shape and extent of the recorded magnetic 'bits' in the storage medium, and therefore the attainable areal storage density in bits per square metre. There is a wide variety of magnetic recording head geometries, with specific configurations optimised for particular recording modes (for example with the use of

shields). Nevertheless all of these configurations are derived from three main geometries based on the magnetic fringing fields they produce, which include the ring head, single-pole head and finite-pole thin-film head [40]. It is vital to understand and analyse the effects of the head shape on the generated recording field distributions in order to study the performance of any combination of head and medium in magnetic recording. Thus, in order to gain a fundamental understanding of digital magnetic recording heads, a brief description for the common magnetic recording heads will be presented next.

1.5.1 The Ring head (RH)

The conventional longitudinal recording head is the ring head which consists of two relatively long poles of opposite polarity separated by a narrow gap of length g, where the fringing recording fields are produced. The magnitudes and distributions of the magnetic fields are functions of the gap length and separation from the head surface. The ring head is mainly used for longitudinal recording, and the magnetic transitions in the medium are normally written near the trailing edge (relative to the movement direction of the head/medium) of the gap corner where the field gradients are near their maximum. This head may also be used for PMR combined with a single layered media due to its easy implementation. However, this type of head has lower vertical head field strength and gradient at compared to the single pole type (SPT) head [41]. Numerous investigations for an improvement in perpendicular magnetic recording by using a ring-type head, Iwasaki, and Ouchi's study which is used CO double layer media to obtain higher recording resolution along with a very thin semi-hard back layer with high saturation moment. This study demonstrates a dramatic increase of reproducing output over a wide density region, while the recording sensitivity was also improved [42]. Wilton

derived an accurate Fourier coefficients, this mathematical study demonstrated the effect of the presence an underlayer on the magnetic field [43], Figure 1.11 illustrate the ring head geometries with underlayer.

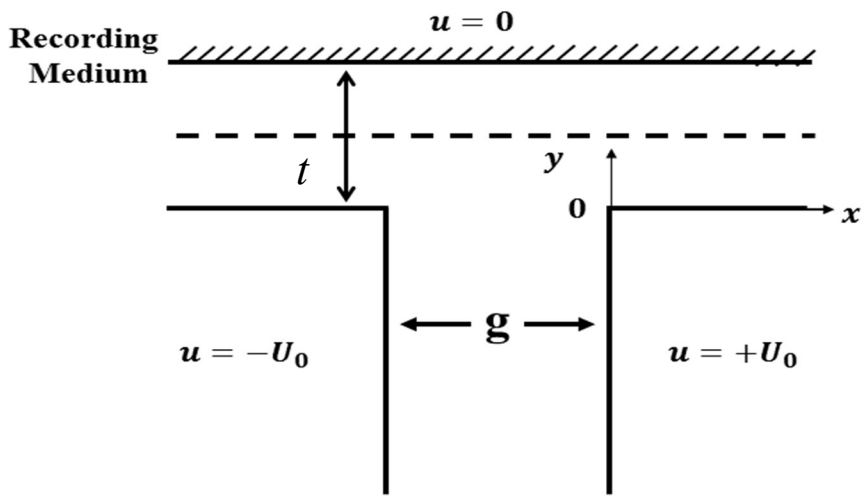

Figure 1.11 Perpendicular recording head geometries, the ring head with underlayer [43].

1.5.2 Single pole head (SPH)

In a conventional LMR head, the magnetic field is generated from a thin non-magnetic gap in the ring head, and it has a higher longitudinal component than a perpendicular component. In PMR, the medium has magnetisation oriented in the up-down direction. To achieve efficient writing, a PMR head needs to generate fields having the perpendicular component higher than the longitudinal component, which is normally achieved through the inclusion of a high permeability, soft magnetic underlayer (SUL) located beneath the recording medium and at a distance *t* from the head (See Figure 1.12). This SUL then forms part of the 'magnetic circuit' of the SPH and provides a normal (to the medium surface) flux path and therefore higher perpendicular fields and field

gradients in the PMR mode [44, 24]. The magnetic field strength and distribution in a single pole head (SPH) depend on at least two geometric factors: pole width 2L and the distance between pole head and underlayer *t*, due to the presence of a highly permeable underlayer [45]. A number of designs have been proposed to improve the performance of single pole heads, through using shield which include monopole type [46], trailing shielded type [12, 41] , and wraparound type heads [48] (See Figure 1.13).

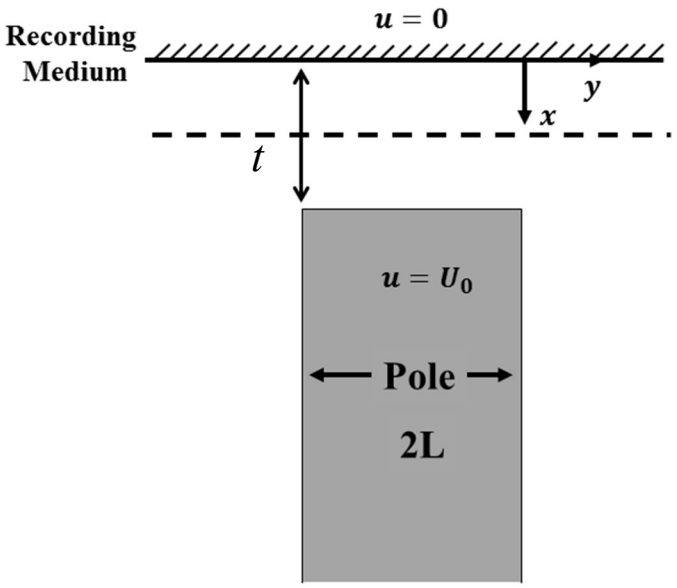

Figure 1.12 SPH system, with a semi-infinite pole of width 2L and at potential U_0 lies a distance *t* from an infinite plane at zero potential [49].

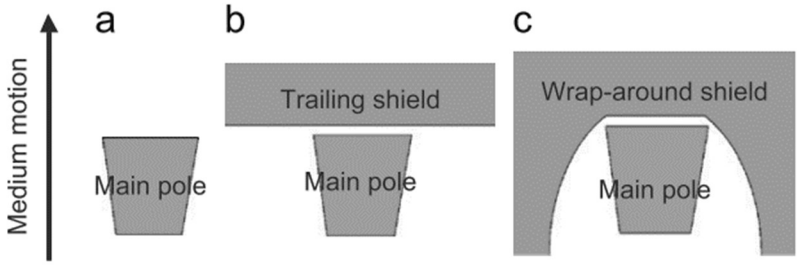

Figure 1.13 Single pole writing head type: (a) monopole structure, (b) trailing shield structure, and (c) wraparound structure [46].

1.5.3 Thin-film head (TFH)

Recording head manufacturers adopted the thin-film techniques used in the semiconductor and electronics industry due to its excellent control over critical head dimensions to produce magnetic heads with finer dimensions and realise higher storage capacities. Thin-film heads are normally characterised by finite pole and gap lengths; Figure 1.14 illustrates the general structure of a non-symmetrical thin-film head, where g is represents the gap length, and, L head length, L1 = 2P1 + g and L2 = 2P2 + g where P1 and P2 are the lengths of the left-hand and right-hand poles respectively. Thin-film heads commonly fabricated using SENDUST (*AlFeSi*) and Permalloy. The SENDUST offers a mechanical hardness, so that it's used as pole tips, while the Permalloy used due to their low coercivity and high permeability. All current (mechanical) hard disk drives employ thin-film heads.

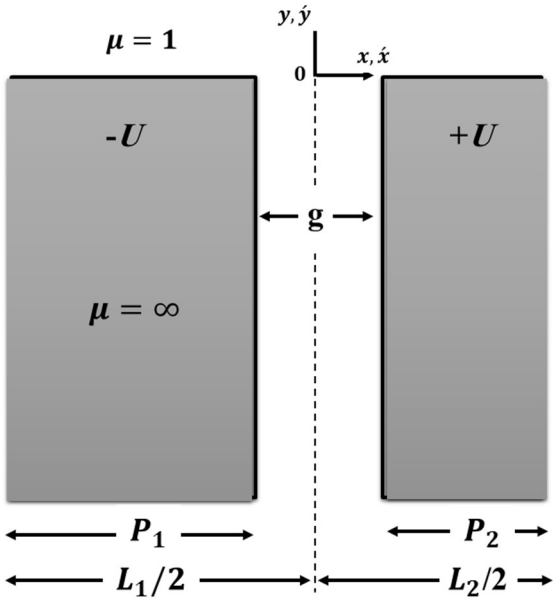

Figure 1.14 Schematic of Thin-film head (TFH), with gap length g, ±*U* are the potential, and *P*1 and *P*2 are the lengths of the left-hand and right-hand poles respectively [50].

1.6 Project aim and objectives

With the continued demand for increases in the storage capacity of hard disk drives and the research and development of the emerging new routes for overcoming the fundamental limitations of conventional magnetic recording (in heads and media), necessitated changes in the geometry of magnetic recordings from the right-angled structures (including shielded structures) shown in the previous section to tapered and inclined or 'tilted' symmetrical and asymmetrical structures. For example, asymmetric heads as illustrated in Figure 1.15 were proposed as means of increasing the recording resolution for the longitudinal and perpendicular recording modes due to the increased field gradients near the acute pole corner in the gap region of this geometry [39].

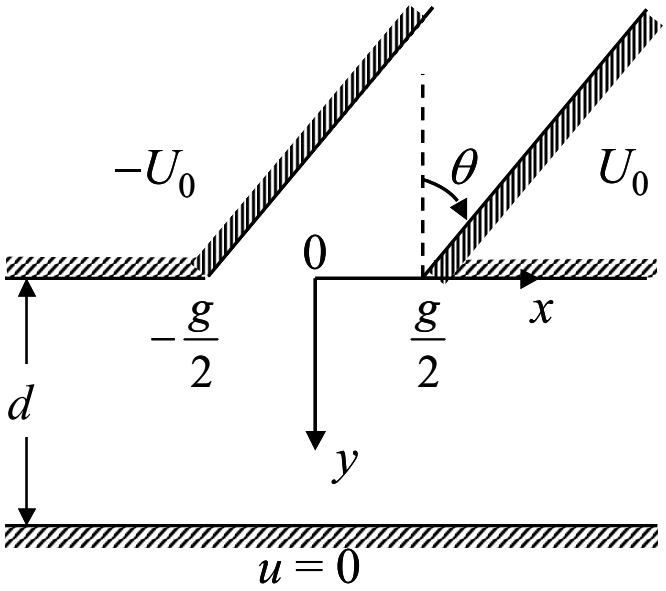

Figure 1.15 Two-dimensional geometry of the asymmetrical head, with gap length *g* and exterior corner inclination angle θ. The poles are assumed to have infinite permeability with potentials $\pm U_0$, at a distance *d* from a soft magnetic underlayer (SUL) held at zero potential. To model two-dimensional heads without an underlayer, the SUL is removed with $d \to \infty$.

Primarily as the asymmetry changes the pole corner charge redistributes towards one corner thus reducing the 'effective' gap length, g, of the head to resolve shorter recorded magnetic patterns on the recording medium. More recently, asymmetric ring-type head structures are emerging as part of corner-type head designs for shingled and two-dimensional magnetic recording [34] which is suggested the head design for shingled magnetic recording to reach the predicted areal density 2-3 Tbit/in^2. An investigation of asymmetric head design and corner shield design has been published which aims to obtain larger recording fields and higher field gradients using the FEM as shown in Figure 1.16 [38]. Victora et. al, concluded that using asymmetrical heads increases the potential to advance magnetic recording into the multiple Tbits/in^2 regime [37].

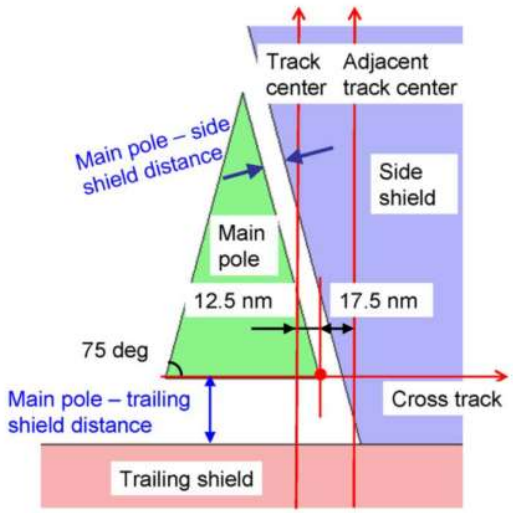

Figure 1.16 The main pole tip, trailing and side shields. Field data were taken along the track center, adjacent track center and cross track lines [34].

The previous studies on asymmetrical heads are numeric, except the conformal mapping studies which is provide an explicit solution for the fields of an infinitely permeable asymmetrical finite-pole-tip ring head geometry as illustrated in Figure 1.17 [51].

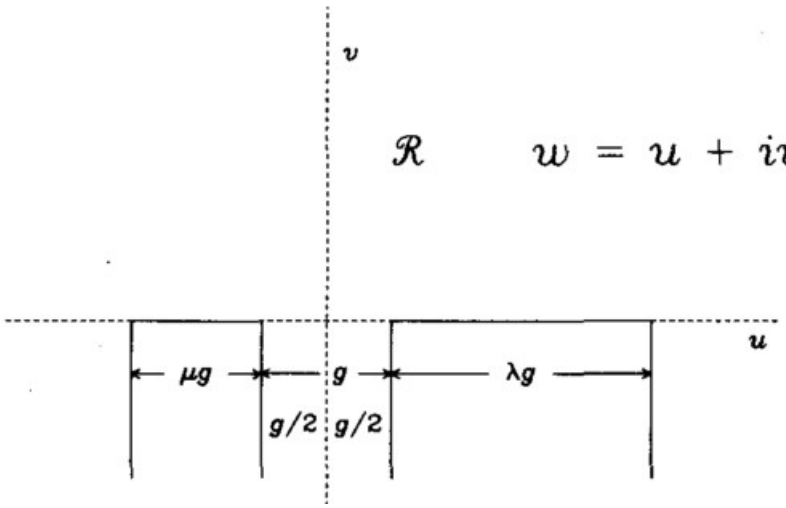

Figure 1.17 An infinitely permeable asymmetrical finite-pole-tip ring head geometry [51].

Another study discussed the effect of the saturation on head field distribution, writability and reading efficiency for large inclination angles of asymmetrical ring head geometry as shown in Figure 1.18 [52].

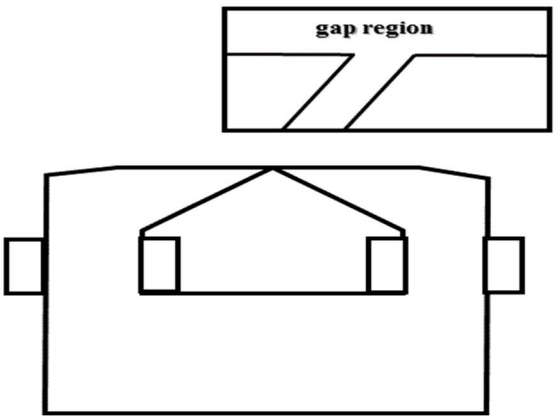

Figure 1.18 Two Dimensional model of an asymmetric ring head [52].

A third research is demonstrated that using asymmetric heads without an underlayer with large inclination (See Figure 1.19) which has a good effect which led to increase bit density recording [39].

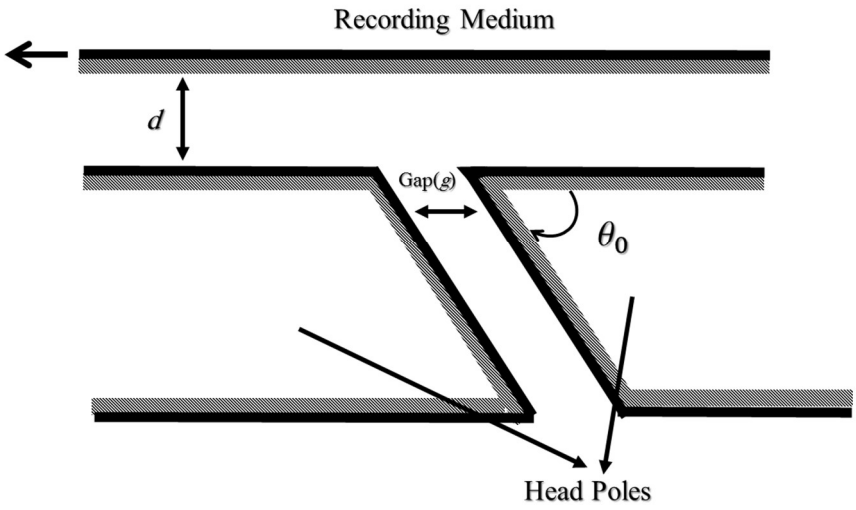

Figure 1.19 Asymmetric ring head without an underlayer [39].

However, the conventional ring head (symmetric) with a soft underlayer is efficient for perpendicular recording [42, 43], an inclined corner ring head with an underlayer is highly suitable candidate for extending density perpendicular recording head as presented previously in Figure 1.15 [55].

Mapping of the magnetic fields of conventional magnetic recording heads such as the ring head and single pole head, with right-angled corners, received considerable attention throughout the history of magnetic recording starting from the 1950s with the works of Westmijze [56] and Karlqvist [57] on the solution of Laplace's equation in two-dimensions for the ring head. This was followed by extensive theoretical developments

to model the fields from such head structures analytically with more accuracy that were instrumental to explicitly understand the dependence of the field magnitudes and distributions on the critical dimensions of the heads, and to enable the optimisation of head designs for high capacity and high data rate magnetic data storage. The newer recording head structures and those proposed for future recoding concepts such as corner-type heads, involve tapering of the poles and symmetrical and asymmetrical tilted gap corners. The magnetic fields from these structures were mainly modelled numerically or through conformal mapping which requires numerical inversion. There are currently neither explicit nor approximate expressions for the potential and fields for asymmetrical magnetic recording heads. Therefore the explicit functional dependence of the corresponding magnetic fields' magnitude, gradient, and wavelength response on the head parameters (such as θ, g and d) is not well understood. The difficulty in deriving explicit solutions for the potentials and fields of asymmetrical heads arises from the fact that this geometry does not conform to conventional coordinate systems, for which formal methods of solution can be applied. It is therefore the aim of this thesis to map the magnetic fields of two-dimensional symmetrical and asymmetrical magnetic heads with tilted corner angles analytically.

This project's objectives hence include:

- Carry out extensive literature search and review of analytical methods of field mapping of two-dimensional magnetic recording heads.
- Develop new theoretical approaches based on the above research to model the magnetic fields from two-dimensional heads with tilted gap corners.

- Evaluate the accuracy of these new theoretical approaches by comparison to exact analytical solutions for certain limits, and to finite-element simulations.
- Study the limitations of the newly developed models and their applicability.

Significant portions of this project were dedicated to producing mathematical models of corner-type heads, and deriving approximate analytical solutions for the fields from symmetrical and asymmetrical heads without a soft magnetic underlayer once, and when the underlayer is presents.

1.7 Outline of the thesis

In this thesis, chapter 2 will review the mathematical methods employed for mapping the potentials and fields of static, two-dimensional magnetic recording heads. The focus in this chapter is on the approaches that yield exact solutions for the potential and fields for two dimensional magnetic recording heads, where the thickness or depth of the head is assumed much larger than the other dimensions in the head. The finite-element method is also briefly described as an important numerical tool for assessing the accuracy of the derived expressions.

In chapter 3, the magnetic potential near a two-dimensional corner is derived exactly. The method of superposition of two corner potentials is then employed, as the first novel theoretical modelling approach, to derive approximate expressions for the magnetic potential and fields of asymmetrical heads in the absence of a soft magnetic underlayer (SUL). The approximate expressions for the fields are compared to finite-element calculations to assess the validity of the derived analytical expression and estimate their error.

The superposition-based theoretical approach for asymmetrical heads derived in chapter 3 is extended in chapter 4 to include the presence of a SUL. This is achieved through the use of the appropriate Green's function with the derived surface potential/field, the outcomes for modelling the inclusion of a SUL in the magnetic circuit are compared with finite-element calculations and the error is estimated.

The second developed theoretical approach for modelling asymmetrical magnetic heads is detailed in Chapter 5, and is based on fitting to numerical finite-element calculations. This chapter also details a generalised theoretical treatment for the reaction of the underlayer on the surface potential for any two-dimensional head structure using a translated Fourier series. The calculated potentials and fields are also compared to available exact solutions for limiting case and to finite-element simulations to estimate the accuracy of these developed theoretical approaches.

The superposition-based theoretical approach for asymmetrical heads derived in chapter 3 and 4 is extended to calculate the potential/fields for symmetrical head geometry in the case of the absence and presence of a SUL. Conclusions and the future works will be drawn in Chapter 7.

Chapter 2: Mathematical Methods and Review of Analytical Solutions of Magnetic Potentials and Fields from Magnetic Recording Heads

2.1 Introduction

This chapter will review the mathematical methods employed for mapping the potentials and fields of magnetic recording heads. The focus is on the approaches that yield exact solutions for the potentials and fields of two-dimensional magnetic recording heads, where the thickness or depth is assumed much larger than the other dimensions in the head (such as the gap length and head-to-underlayer separation). These methods will form the basis for the approaches adopted in this work to arrive at analytical expressions for the field and potentials from asymmetrical and symmetrical heads later in chapters 3, 4, 5, and 6. The Finite-element method will be utilised as a benchmark to validate the derived analytical expressions for the potentials and fields later in the thesis.

This chapter will start by describing the fundamental partial differential equations for modelling the static magnetic potentials and fields of magnetic heads. The mathematical methods which were used extensively for modelling the potentials and fields of magnetic recording heads are then described, including the Fourier transform, the Fourier series and method of superposition. Semi-analytical and numerical techniques were also used for modelling complex head structures, and these include conformal mapping and the finite-element method. These methods are reviewed and discussed with emphasis on the ring-type head for illustration and due to its relevance to the asymmetrical head (or generalised symmetrical head with tilted corner angles), which is the focus of this thesis.

2.2 Physical and mathematical background

The magnetic fields are generated by the movement of the charge either as an electric current flowing through a circuit or within the atoms of magnetic materials due to an unbalance in the spins of the electrons. Starting with Maxwell's equations, the static or magnetostatic field can be described by [58] :

$$\nabla \times \bar{H} = \bar{J} \tag{2.1}$$

$$\nabla \times \bar{B} = 0 \tag{2.2}$$

where $\bar{H}$ is the magnetic field, $\bar{J}$ is the current density and $\bar{B}$ is magnetic flux density. In the absence of current sources, (2.1) becomes $\nabla \times \bar{H} = 0$ which allows the introduction of the scalar magnetic potential φ

$$\bar{H} = -\nabla\varphi \tag{2.3}$$

Since $\bar{B} = \mu\bar{H}$ where μ is permeability then (2.2) may be written as:

$$\nabla \cdot \mu\bar{H} = \nabla \cdot (-\mu\nabla\varphi) = 0 \tag{2.4}$$

Assuming a linear magnetic medium (which is applicable to non-saturated magnetic heads) where μ is constant, then (2.4) reproduces Laplace's equation for the scalar magnetic potential:

$$\nabla^2 \varphi = 0 \tag{2.5}$$

Solution of Laplace's equation subject to the appropriate boundary conditions enable the determination of the magnetic fields from (2.3).

Magnetic recording head material normally exhibits very high permeability, thus producing equipotentials inside the head core, allowing the boundaries to be described using constant (surface) potentials. Deviation from this behaviour occurs when the permeability changes value inside the core, due to head saturation for example. In this case the vector magnetic potential approach must be utilised for modelling the potentials and fields of magnetic heads [59]. Nevertheless, when the permeability becomes constant, the vector potential formulation reduces to a Laplace's equation for the normal vector potential in two-dimensions. In this case, the magnetic fields are derived from the curl of the potential with the field source defined as a surface current density [54]. The fields derived in this manner are identical to those derived using the scalar potential, but are only convenient to use when a surface field distribution is known.

In this thesis, the focus is on the solution of Laplace's equation for the scalar magnetic potential where it is assumed that the head cores have infinite permeability with constant pole potentials. Laplace's equation in two-dimensions for the Cartesian, and Polar coordinate systems are given by:

$$\nabla^2 u \equiv \frac{\partial^2 u}{\partial x^2} + \frac{\partial^2 u}{\partial y^2} = 0 \tag{2.6}$$

$$\nabla^2 u \equiv \frac{1}{\rho}\frac{\partial}{\partial \rho}\left(\rho \frac{\partial u}{\partial \rho}\right) + \frac{1}{\rho^2}\frac{\partial^2 u}{\partial \emptyset^2} = 0 \qquad (2.7)$$

Equation (2.6) is used for modelling the fields from magnetic head structures with surfaces to conform to the Cartesian coordinate system, while (2.7) is used to model the potential of tilted head configurations.

2.3 Methods of solution of 2D Laplace's equation

As indicated in chapter 1, evaluating the performance of any magnetic recording head geometry requires knowledge of the field magnitudes and distributions. There are two main approaches for field mapping based on the methods of solution of the relevant partial differential equations: an analytical approach, and the semi-analytical and/or numerical approach. The analytical methods include the use of the Fourier series and Fourier integral/transform to arrive at exact and explicit solutions where possible [4, 5, 6]. The other semi-analytical and numerical approaches involve the use of Conformal mapping [7, 8, 9, 10], which yields implicit solutions and require numerical inversion, and the use of finite-elements. These methods will be reviewed in this chapter with focus on the two-dimensional ring head as an example and since exact solutions are possible for this geometry. Nevertheless, these methods are general and will be adapted in subsequent chapters of this thesis to model symmetrical and asymmetrical head structures.

2.3.1 The Fourier Transform Method

The Fourier transform is one of fundamental importance in a broad range of applications, including solution of the ordinary and partial differential equations, quantum mechanics, signal and image processing, control theory, and probability, to name but a few [64]. In modelling the potential and fields of semi-infinite magnetic recording heads, the Fourier transform is extensively used to reduce Laplace's equation in two-dimensions to a more manageable ordinary differential equation describing the variation of potential or field above the head surface [3].

The Fourier transform has different definitions, the most often used expression in field mapping is the spatial Fourier transform, which for the spatial function $g(x)$ is defined as:

$$G(k) = \int_{-\infty}^{\infty} g(x) e^{-ikx} dx \tag{2.8}$$

where k is the wavenumber which is defined as $k = \frac{2\pi}{\lambda}$, where λ is the wavelength.

The corresponding inverse Fourier transform is:

$$g(x) = \frac{1}{2\pi} \int_{-\infty}^{\infty} G(k) e^{ikx} dk \tag{2.9}$$

Some of the useful properties and relations of the Fourier transform that will be used in this thesis are listed in Table 2.1. In addition and of particular importance is the convolution property of two functions:

$$f(x) * g(x) \equiv \int_{-\infty}^{\infty} f(\acute{x})g(\acute{x} - x)d\acute{x} \overset{FT}{\Rightarrow} F(k).G(k) \tag{2.10}$$

which is the product of their Fourier transforms. Another useful relation called Parseval's theorem which indicates that the total energy of a function is the same whether it is expressed in the real space (x) or in the Fourier space (k) [64]:

$$\int_{-\infty}^{\infty} |g(x)|^2 dx = \frac{1}{2\pi} \int_{-\infty}^{\infty} |G(k)|^2 dk \tag{2.11}$$

Table 2.1 Some properties and relations of Fourier transform space [24]

	Function	**Fourier transform**
Differentiation	$\partial f(x)/\partial x$	$ikF(k)$
Translation	$f(x-a)$	$e^{-ika}\,F(k)$
Modulation	$e^{ik_0 x}\,f(x)$	$F(k-k_0)$
Convolution	$f(x) * g(x)$	$F(k)G(k)$
Multiplication	$f(x)g(x)$	$F(k) * G(k)$

In next section the Fourier transform is used to solve Laplace's equation for the scalar magnetic potential and derive the corresponding head fields.

2.3.1.1 Fourier Transform of Laplace's equation

The static distribution of magnetic fields from magnetic recording heads is determined from the solution of Laplace's equation for the scalar potential, which is then used to obtain the magnetic field by evaluating the gradient of the potential.

Starting with the two-dimensional (*x*-*y* plane) Laplace's equation defined as:

$$\frac{\partial^2 u(x,y)}{\partial x^2} + \frac{\partial^2 u(x,y)}{\partial y^2} = 0 \tag{2.12}$$

and applying the Fourier transform with respect to *x* and applying the differentiation property in Table 2.1, yields the ordinary differential equation:

$$k^2 u(k,y) + \frac{\partial^2 u(k,y)}{\partial y^2} = 0 \tag{2.13}$$

where $u(k,y) = \int_{-\infty}^{\infty} u(x,y)\, e^{-ik}\ dx$, denotes the Fourier transform of the potential with respect to x.

The general solution of the ordinary differential equation in (2.13) can be written as:

$$u(k,y) = A(k)e^{ky} + B(k)e^{-ky} \tag{2.14}$$

The coefficients *A* and *B* are determined according to the appropriate boundary conditions. The potential and fields are derived next for a ring head geometry without a soft magnetic underlayer (SUL), and then when an underlayer is present.

2.3.1.2 Fourier Transform for ring-type heads without underlayer

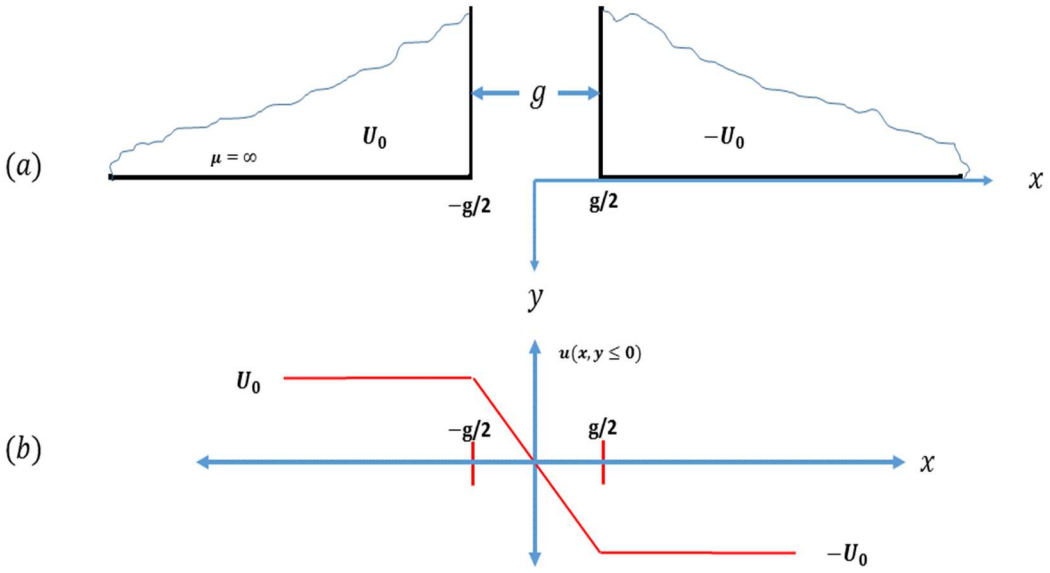

Figure 2.1 Schematic of (a) semi-infinite ring head and (b) the assumed (approximate) magnetic potential at surface of the head following Karlqvist [14].

The ring-type head illustrated in Figure 2.1 represents the earliest and most common recording head geometries in magnetic recording. This head model is based on the following assumptions [3]:

1. The head thickness (in the z direction) is much larger than the other critical head dimensions (such as the gap length g and head separation y).
2. The pole pieces are infinitely permeable and therefore each has a constant magnetic potential distribution $\pm U_0$ on the pole faces
3. The pole pieces have perfectly rectangular (90°) gap corners.

4. The pole pieces extend to infinity in the negative *y* direction.

Applying the boundary conditions indicated in Figure 2.1 to the general solution in (2.14) with an assumed surface potential distribution $u(k,0)$ at $y=0$, and vanishing potential as $y \to \infty$, yields:

$$u(k,y) = u(k,0)e^{-|k|y} \quad , y > 0 \tag{2.15}$$

The free space potential $u(x,y)$ beyond the head surface can be obtained by taking the inverse Fourier transform of $u(k,y)$ in (2.15):

$u(x,y) = FT^{-1}[u(k,y)\ ] = FT^{-1}[u(k,0)e^{-|k|y}\ ]$. Which, may be written as a convolution:

$$u(x,y) = \ u(x,0) * \ FT^{-1}[e^{-|k|y}] = u_s(x)\frac{y}{\pi(x^2+y^2)} \tag{2.16}$$

where $u_s(x) \equiv u(x,0)$ is surface magnetic potential at $y = 0$, and the second term on the right-hand of (2.16) represents the Green function for this semi-infinite geometry beyond the head surface. Writing the convolution integral yield the potential everywhere as function of the surface potential $u_s(\acute{x})$:

$$u(x,y) = \frac{y}{\pi}\int_{-\infty}^{\infty}\frac{u_s(\acute{x})}{(x-\acute{x})^2+y^2}d\acute{x} \tag{2.17}$$

This is a general description that applies to the magnetic potentials and fields beyond the surface of a semi-infinite two-dimensional structure [65]. The success and accuracy of

this approach depends on the accurate description of the surface potential $u_s(\acute{x})$, if known. The most commonly used surface potential approximation, known as Karlqvist head approximation, is described next.

I. Karlqvist Approximation

In the Karlqvist approximation the potential in the gap at $y = 0$ is assumed to follow the linear potential variation between the two parallel, inner faces of the poles deep in the gap as indicated in Figure 2.1(b) and described by:

$$u_s(x) = \begin{cases} -U_0 & for \quad x \geq g/2 \\ \dfrac{-2U_0 x}{g} & for \quad |x| \leq g/2 \\ U_0 & for \quad x \leq -g/2 \end{cases} \tag{2.18}$$

Substituting the surface potential in (2.17) and integrating provides the potential everywhere as:

$$u(x,y) = -\frac{2U_0}{\pi g}\left[\left(x+\frac{g}{2}\right)\tan^{-1}\left(\frac{x+\frac{g}{2}}{y}\right) - \left(x-\frac{g}{2}\right)\tan^{-1}\left(\frac{x-\frac{g}{2}}{y}\right) - \frac{y}{2}Ln\frac{(x+\frac{g}{2})^2+y^2}{(x-\frac{g}{2})^2+y^2}\right] \tag{2.19}$$

The field components H_x and H_y can now be determined from the gradient of the potential in (2.19) and are given by:

$$H_x(x,y) = -\frac{\partial u}{\partial x} = \frac{2U_0}{\pi g}\left[\tan^{-1}\left(\frac{x+\frac{g}{2}}{y}\right) - \tan^{-1}\left(\frac{x-\frac{g}{2}}{y}\right)\right] \tag{2.20}$$

$$H_y(x,y) = -\frac{\partial u}{\partial y} = -\frac{U_0}{\pi g}\ln\frac{(x+\frac{g}{2})^2 + y^2}{(x-\frac{g}{2})^2 + y^2} \tag{2.21}$$

These fields are plotted in Figure 2.2. The x field component is 'bell' shaped and has even symmetry with a maximum at the gap centre for $y/g > 0.2$ (See Figure 2.2 (a)), while the y component exhibits odd symmetry with maxima near the gap corners for $y/g > 0.2$ and vanishes at the gap centre (See Figure 2.2(b)).

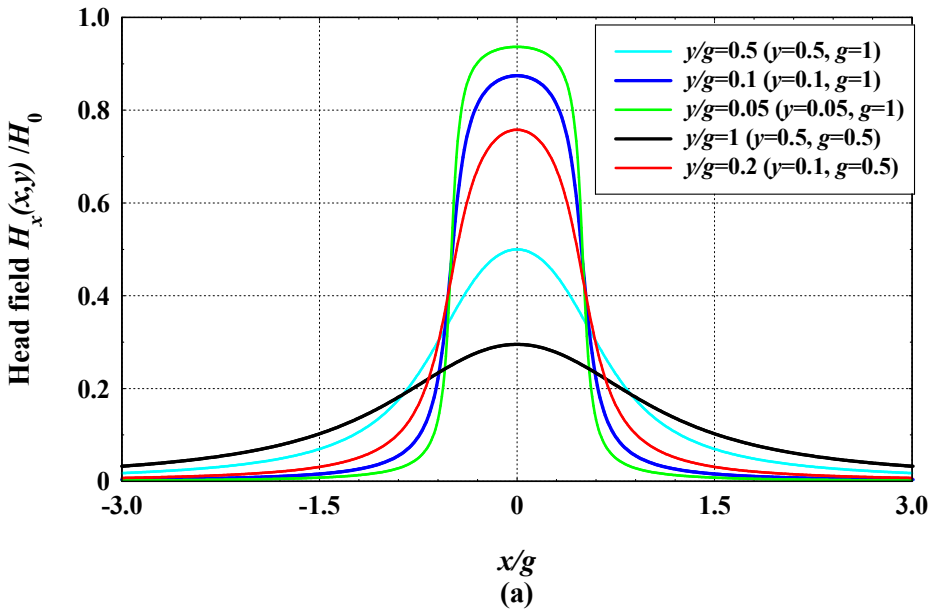

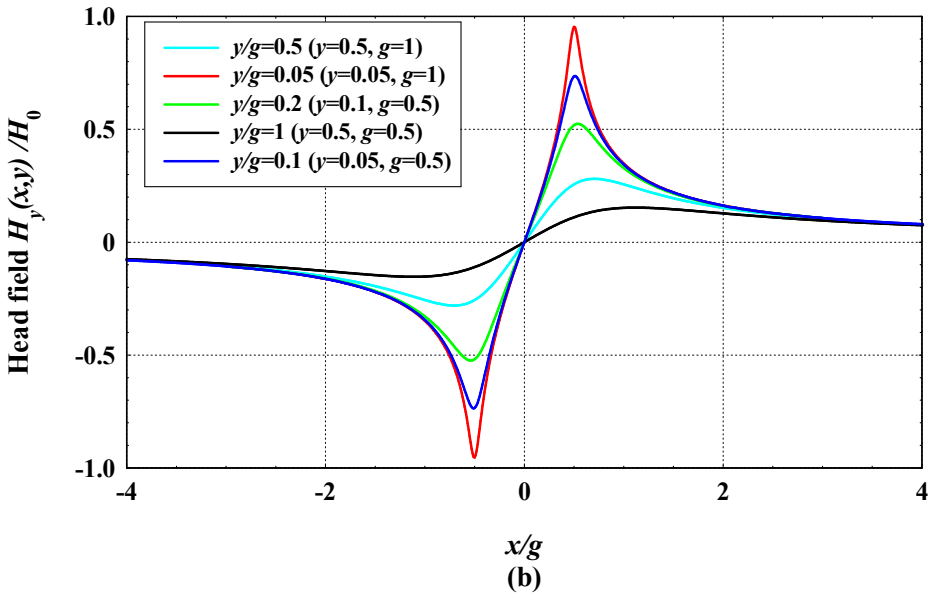

Figure 2.2 Plot of the (a) *x*-field components (b) *y*-field components for the Karlqvist approximation (2.20) and (2.21) normalised by deep gap field $H_0 = 2U_0/g$ for different flying height-to-gap length ratios.

Figure 2.2 demonstrates the effect of gap length on both *x*, and *y*-field components, where increasing gap length with small *y* (small flying height-to-gap length ratio) maximise the field magnitudes at the gap centre for the horizontal field components. On the other hand, it's maximise the vertical field components magnitudes near the gap corners.

Next, the narrow gap case for the ring head is discussed which represents the special case from the classical ring type head geometry (Karlqvist Head).

II. Narrow Gap Head

At large separations from the head surface or when the gap length is very small compared to other dimensions in the system (for example the head to medium separation), then the Karlqvist surface potential approximation reduces to the step function description:

$$u(x,0) = \begin{cases} -U_0 & for\ x \geq g/2 \\ U_0 & for\ x \leq -g/2 \end{cases} \tag{2.22}$$

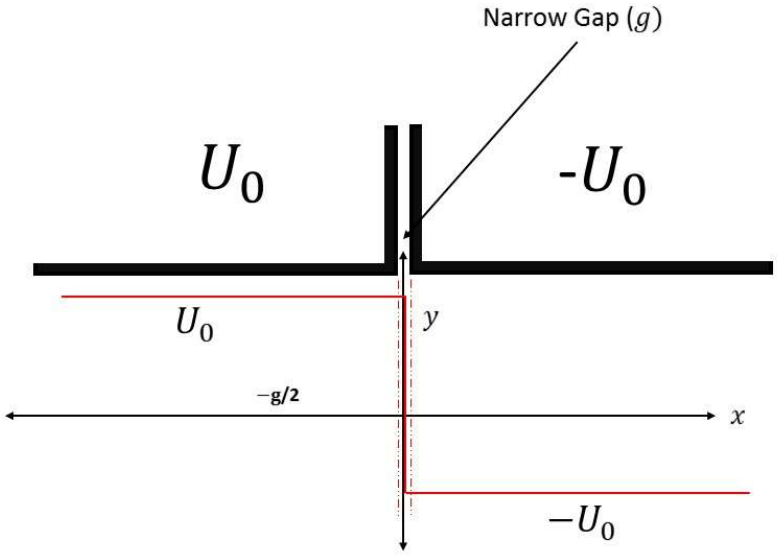

Figure 2.3 Schematic of Narrow gap head and magnetic potential

By substituting the surface potential from (2.22) in (2.17) and carrying out the integration over the head surface yields the potential:

$$u(x,y) = \frac{2U_o}{\pi}\tan^{-1}\left(\frac{x}{y}\right) \tag{2.23}$$

This can be also obtained by expanding (2.19) to a first order Taylor expansion for small gap length g. The field components H_x and H_y are easily derived from the gradient of (2.23) and are given by:

$$H_x = \frac{-2U_0 y}{\pi(x^2 + y^2)} \tag{2.24}$$

$$H_y = \frac{2U_0 x}{\pi(x^2 + y^2)} \tag{2.25}$$

These fields are plotted in Figure 2.4, and exhibit the same features as the Karlqvist, finite-gap approximation fields, but now the field distributions are narrower in the gap region due to the small gap, far field approximation.

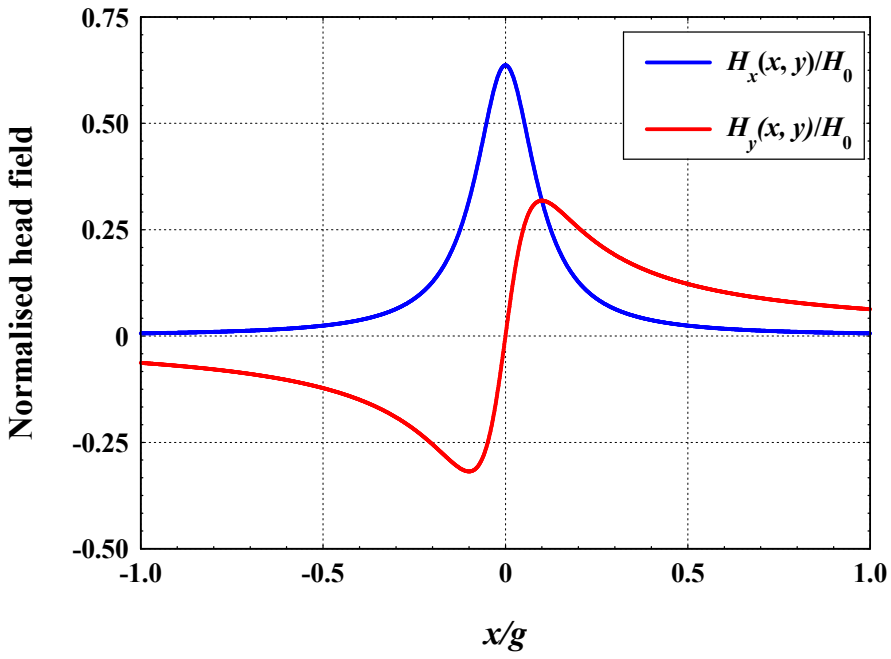

Figure 2.4 Schematic shows field components for the far-field approximation (2.24) and (2.25). The fields are plotted for fixed *y/g*, but the shapes shown are invariant with separation since the *x*-axis can be scaled by *x/g*.

Above section discussed the use of the Fourier transform for solving Laplace's equation for the Karlqvist head without an underlayer (keeper). In the next section the same problem is discussed but in the case when the underlayer is present.

2.3.1.3 The Fourier Transform of the ring heads with underlayer

Figure 2.5 represent an idealised model of a ring head with a soft underlayer. The head poles are assumed to have infinite width and extend to infinity in the negative y direction. The head poles' permeability is assumed to be infinite, with potentials $+U_0$ and $-U_0$ and separated by gap g. The underlayer is located at a distance $y = d$ from the head surface and held at zero potential. The magnetic potential U_0 satisfies Laplace's equation in the region below the underlayer and exterior to the two poles.

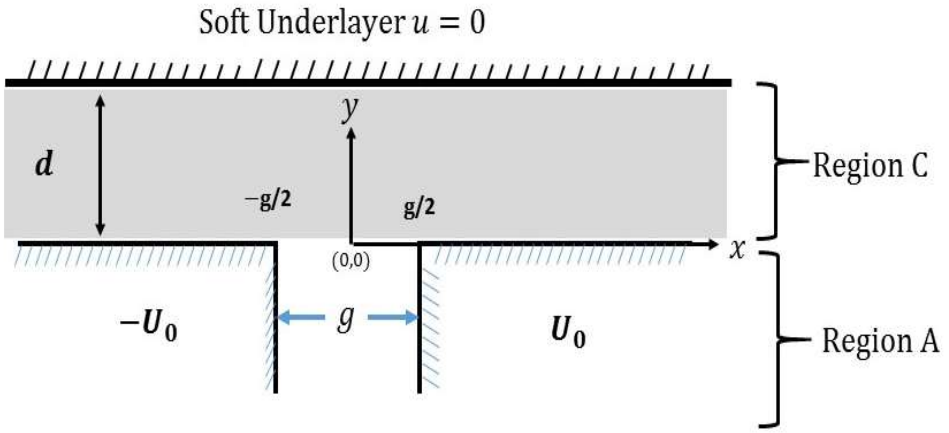

Figure 2.5 Two-dimensional geometry of the Ring head with underlayer, with gap length g, the poles are assumed to have infinite permeability and therefore with equipotential $\pm U_0$, at a distance d from a soft magnetic underlayer (SUL) held at zero potential.

In the case when the underlayer is present, the following boundary conditions must be considered to determine the coefficients of the general solution in (2.14):

(i) $u = u(x,0)$ at $y = 0$

(ii) $u = 0$ at $y = d$

Applying the above boundary conditions to equation (2.14) yields the particular transform solution:

$$u(k,y) = u(k,0)\frac{sinh(k(d-y))}{sinh(kd)} \tag{2.26}$$

where $y \leq d$. The x and y components of the magnetic field are then evaluated using the potential gradient:

$$\bar{H}(x,y) = -\left(\frac{\partial u}{\partial x}\bar{x} + \frac{\partial u}{\partial y}\bar{y}\right) \tag{2.27}$$

Using the surface fields rather than potentials to determine the magnetic fields directly is easier mathematically with the convolution integrals evaluated only over the gap region.

The Fourier transform of field can be written as [25]:

$$\bar{H}(x,y) = -\left(jku(k,y)\bar{x} + \frac{\partial u(k,\mathrm{y})}{\partial y}\bar{y}\right) \tag{2.28}$$

Taking the inverse Fourier transform and invoking the convolution theorem yields the x-component of the magnetic field as [66].

$$H_x(x,y) = \frac{-\partial u}{\partial x} = \tag{2.29}$$

$$= \frac{-\sin(\pi\, y/d)}{2d} \int_{x'=-\infty}^{\infty} \frac{H_x(x',0)}{\cos(\pi\, y/d) - \cosh(\pi(x'-x)/d)}\, dx'$$

While the *y*-component was found to be:

$$H_y(x,y) = \frac{-\partial u}{\partial y} = \tag{2.30}$$

$$= \frac{1}{2d} \int_{x'=-\infty}^{\infty} \frac{H_x(x',0)\sinh(\pi(x'-x)/d)}{\cos(\pi\, y/d) - \cosh(\pi(x'-x)/d)}\, dx'$$

where $H_x(\dot{x},0)$ is the horizontal surface field.

Equations (2.29) and (2.30) are general formulae that allow the determination of the magnetic fields in the presence of an underlayer when the surface potential or field is known. These equations will be used later in the thesis to determine the fields for asymmetrical heads.

In the case of the Karlqvist linear potential in (2.18), the surface field is simply the *x*-derivative of the potential and is given by:

$$H_x(\dot{x},0) = \frac{2U_0}{g} = H_0 \tag{2.31}$$

where H_0 is the x-component of the deep-gap which needs to be scaled to the appropriate surface field at y=0.

By substituting (2.31) in (2.29) and (2.30) and evaluating the integrals over the gap region (since the field is zero over the pole regions) provides the magnetic field components as:

$$H_x = \frac{H_0}{\pi}\left[tan^{-1}\left[cot\left(\frac{\pi y}{2d}\right)tanh\left(\frac{\pi(g-2x)}{4d}\right)\right] - tan^{-1}\left[cot\left(\frac{\pi y}{2d}\right)tanh\left(\frac{\pi(g+2x)}{4d}\right)\right]\right] \quad (2.32)$$

$$H_y = \frac{-d^2 H_0}{2\pi}\left[ln\left[cot\left(\frac{\pi y}{d}\right) - cosh\left(\frac{\pi(g-2x)}{2d}\right)\right] + ln\left[cot\left(\frac{\pi y}{d}\right) - cosh\left(\frac{\pi(g+2x)}{2d}\right)\right]\right] \quad (2.33)$$

The horizontal and vertical field components in (2.32) and (2.32) are plotted in Figure 2.6 for different head to underlayer spacings (d/g=1, 0.5, and 0.25), and at separations y/d=0.05 and 0.1 from the head surface. Figure 2.6 illustrates a decrease in the amplitude of H_x and increase in H_y with reduction in the head-to-underlayer separation d, thus demonstrating the effect of the underlayer in enhancing the y-component of the magnetic field and explaining its advantage in perpendicular recording. Beyond the head corners and over the pole regions, H_y tends to a constant magnitude that again depends only on the ratio of d/g as demonstrated in Figure 2.6(b). This dependence can be easily derived from (2.30) by evaluating the limit $x \to \pm\infty$, thus reducing the convolution integral to $1/2d\int_{x'=-g/2}^{g/2} H_x(x',0)dx'$. Substitution of H_x = H_0 and integration yields the constant normalised field $H_y/H_0 \approx \pm g/2d$.

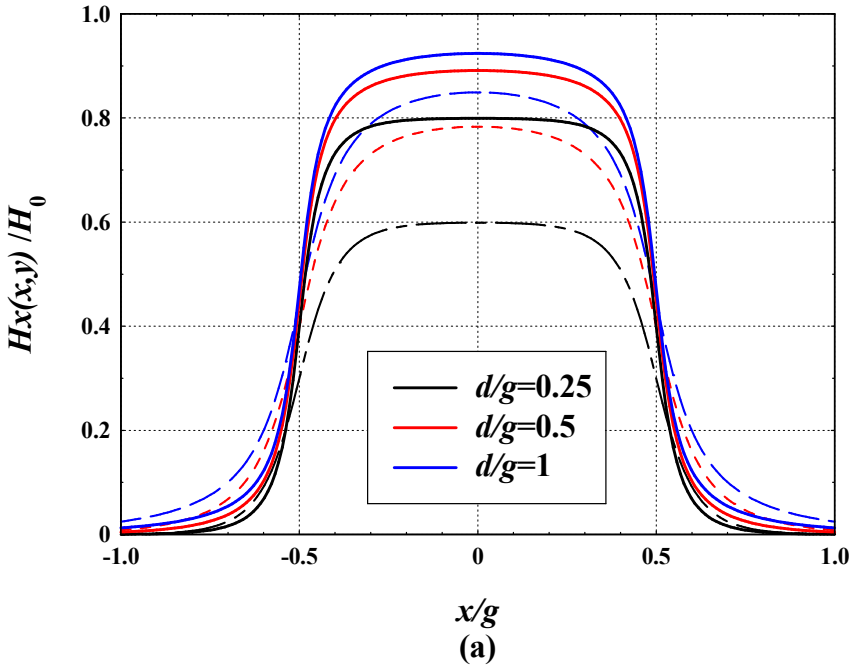

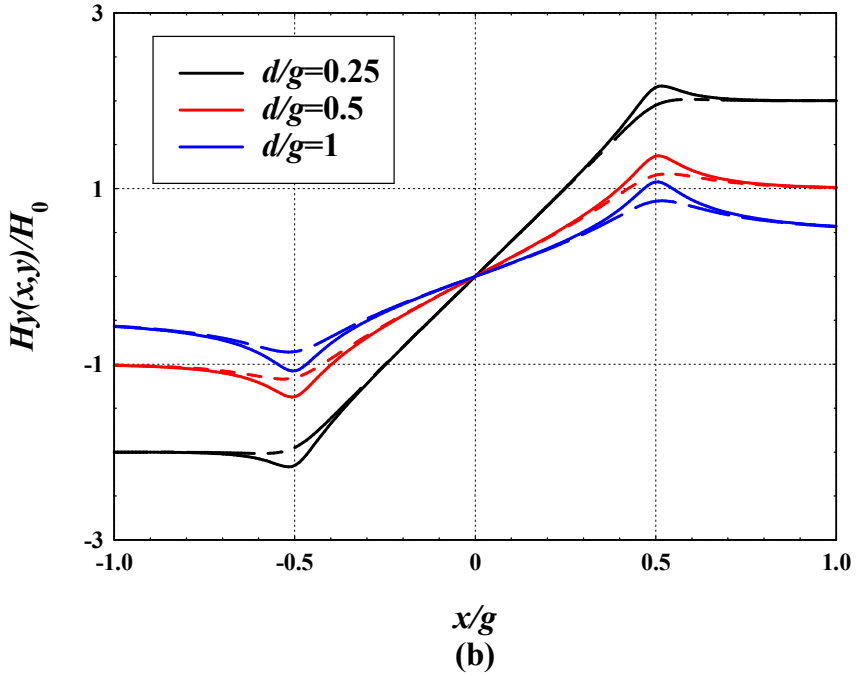

Figure 2.6 (a) *x*-component (b) *y*-component field distributions for the ring head in the presence of an underlayer at head separations *y/g*=0.05 (solid lines) and *y/g*=0.1 (dashed lines) using the equations (2.32) and (2.33).

It is important to emphasise that the Green's function formulation in (2.29) and (2.30) is based on the functional description of the head surface field or potential in the absence of the SUL. Thus this formulation does not take into account the role of the underlayer on modifying the surface potential or field, and is thus expected to become more accurate with increasing the head-to-underlayer separations in the range $d/g > 0.5$. This limitation will be addressed later in the Chapter 5 using a Fourier integral technique.

The Fourier transform technique has been discussed to solve the magnetic problem for ring-type head including the head without underlayer, and then when the underlayer is present. As previously indicated, the applicability and accuracy of this approach is dependent on the availability of an accurate description of the surface potential or field for the given head geometry. Thus in the case of the Karlqvist linear gap approximation, the calculated potential and fields using this technique are only accurate for sufficiently large separations from the head surface. This is because this approximation only accounts for the contribution of the magnetic charger on the inner (parallel) surfaces of the gap, and ignores the contribution of surface charges on the pole faces and near the corners at $y = 0$. Moreover, this method of mapping the head magnetic fields does not take into account the reaction of a SUL on the surface potential or field.

The next section will focus on the Fourier series method for evaluating the potential and fields for the ring head. This method does not require any functional description of the surface potential and field and is therefore more exact, but at the expense of mathematical complexity.

2.3.2 The Fourier series techniques

The methods of the Fourier series has been used for the first time in magnetic recording head problems by Fan in 1960 to calculate the head field distribution of a single pole head with an underlayer [60] and a ring head [67]. The Fourier method has been used since obtain exact analytical solutions for various head configurations. The infinite series solution to Laplace's equation permits each of the head's dimensions to be taken into account and provides an explicit expression which is relatively easy to apply to design work [68]. Fan's analyses [67] have been a subject of further investigations which are providing a closed-form expressions for the integrals contain in the Fan equations for the magnetic field near a recording head [69]. Fan's coefficients were evaluated by Huang and Deng for the ring head and single-pole-type (SPT) head of different gap widths/pole thicknesses [70]. Also, the magnetic fields that are generated by both the ring and single-pole recording heads are examined mathematically providing accurate Fourier coefficients by Wilton [49].

2.3.2.1 Fourier series analysis for ring head without soft Underlayer

It is necessary that the solution obtained for the potential obeys Laplace's equation for the two dimensional case as defined in equation (2.12), and also that it satisfies the boundary conditions that the pole faces are equipotential surfaces at $\pm U_0$. Starting with Laplace's equation in (2.12) and applying variable separation leads to the general solution:

$$u(x,y) = (Ae^{ky} + Be^{-ky})(C\,sin(kx) + Dcos(kx)) + Ex \qquad (2.34)$$

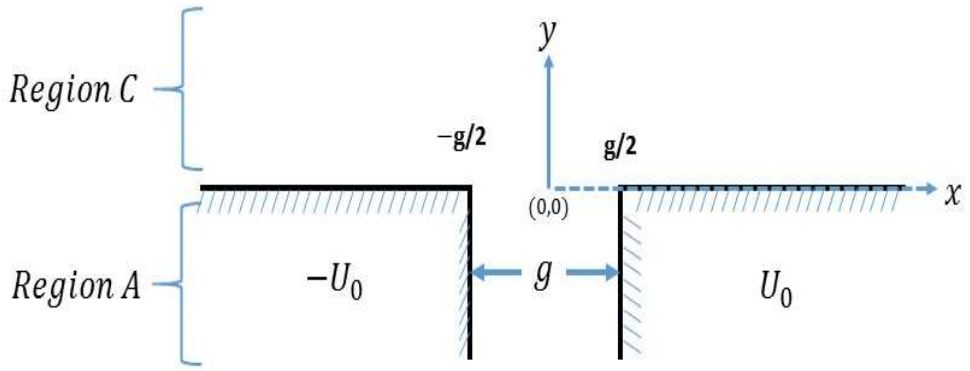

Figure 2.7 Ring head model, with gap length *g*, the poles are assumed to have infinite permeability and therefore with equipotential ±U_0 [1].

Now, according to Figure 2.7 the potential is solved in two regions:

I. Solution of potential in the gap region (region A):

The boundary conditions in this region are formulated as:

$$\begin{aligned} &\text{(i)} && \text{At } x = 0,\ u = 0 \\ &(ii) && y \to -\infty,\ u = \frac{xU_0}{g/2} \quad -g/2 < x < g/2 \\ &\text{(iii)} && \text{At } x = \pm\frac{g}{2},\ u = \pm U_0 \end{aligned} \tag{2.35}$$

Applying condition (i) on the general solution of (2.33) yields:

$$0 = D.(Ae^{ky} + Be^{-ky}) \tag{2.36}$$

This will leads to *D*=0. Thus (2.34) becomes:

$$u_{\mathrm{A}}(x,y) = sin(kx).(Fe^{ky} + Ge^{-ky}) + Ex \tag{2.37}$$

where $F=AC$ and $G=BC$

Applying the second condition gives:

$$Ex = \frac{xU_0}{g/2} - sin(kx).Ge^{-ky} \tag{2.38}$$

Substituting back into (2.37) and rearranging yields:

$$u_A(x,y) = \frac{xU_0}{g/2} + sin(kx).Fe^{ky} \tag{2.39}$$

Using (iii) in (2.35) leads to:

$$0 = sin(k.g/2).Fe^{ky} \tag{2.40}$$

Solving for k yields:

$$k = \frac{2n\pi}{g} \text{ where n= 1, 2, 3…}$$

Substituting for k in (2.39) and summing for all n and replacing $F=A_n$ gives an expression for the potential inside the gap in terms of A_n as:

$$u_A(x,y) = \frac{xU_0}{g/2} + \sum_{n=1}^{\infty} A_n \, sin\left(\frac{2n\pi}{g}x\right) e^{(\frac{2n\pi}{g})y} \qquad \begin{matrix} y<0 \\ -g/2 \le x \le g/2 \end{matrix} \tag{2.41}$$

II. Solution of potential beyond the pole faces (region C):

The boundary conditions in this region are formulated as:

$$\begin{aligned} &\text{(i)} \quad \text{At } x = 0,\ u = 0 \\ &\text{(ii)} \quad \text{As, } y \to +\infty, u \to 0 \end{aligned} \tag{2.42}$$

Applying the first condition in (2.42) yields:

$$0 = D.(Ae^{ky} + Be^{-ky}) \tag{2.43}$$

whose solution is D=0. Hence, (2.43) becomes

$$u_C(x,y) = sin(kx).\left(Fe^{ky} + Ge^{-ky}\right) + Ex \tag{2.44}$$

Applying (ii) in (2.42) gives:

$$Ex = -sin(kx).Fe^{ky} \tag{2.45}$$

for which E=0 is the solution. Then (2.44) becomes:

$$u_C(x,y) = sin(kx).Ge^{-ky} \tag{2.46}$$

Letting G=$C(k)$ and integrating over all k gives the potential beyond the pole pieces in terms of $C(k)$:

$$u_C(x,y) = \int_{k=0}^{\infty} C(k)\, sin(kx)\, e^{-ky}\, dk \qquad \begin{matrix} y > 0 \\ -g/2 \le x \le g/2 \end{matrix} \qquad (2.47)$$

The coefficients A_n and $C(k)$ are determined from the continuity of the potentials and normal fields in both regions at the interface *y*=0, and from application of the orthogonal property of the Fourier series.

By requiring that the potentials (2.41) and (2.47) are matching at $y = 0$, we obtain

$$\int_{k=0}^{\infty} C(k)\, sin(kx)\, dk = \begin{matrix} \dfrac{xU_0}{g/2} + \displaystyle\sum_{n=1}^{\infty} A_n \sin\left(\frac{2n\pi}{g}x\right) & 0 < x < g/2 \\ u_0 & g/2 < x < \infty \end{matrix} \qquad (2.48)$$

To find *C*(*k*), apply the Fourier sine transform, with *k* as a parameter, defined by:

$$\int_{x=0}^{\infty} sin(kx)\,.\,f(x)dx \qquad (2.49)$$

on both sides of (2.48) and employ the following identities:

$$\int_{x=0}^{\infty} sin(kx)\, sin(kx)\, dx = \frac{\pi}{2}\delta(k-\sigma) \qquad (2.50)$$

$$\int_{x=0}^{\infty} \delta(k-\sigma) f(k) dk = f(\sigma) \qquad (2.51)$$

$$\int_{x=0}^{\infty} sin(\sigma x)\, dx = \pi\delta(\sigma) + \frac{1}{\sigma} \tag{2.52}$$

where $\delta(\sigma)$ is the Dirac Delta function defined as [71]:

$$\delta(\sigma) = \begin{cases} 0 & \sigma \neq 0 \\ \infty & \sigma = 0 \end{cases}$$

$$\frac{\pi}{2} C(\sigma) = \frac{U_0}{(\frac{g}{2})} \frac{sin(\sigma \frac{g}{2})}{\sigma^2} + \frac{g}{2} \sum_{n=1}^{\infty} \frac{(-1)^n\, nA_n\, sin(\sigma \frac{g}{2})}{(\sigma \frac{g}{2})^2 - (n\pi)^2} \tag{2.53}$$

To evaluate A_n, differentiate the potential in regions *A* and *C* given by equations (2.41) and (2.47) with respect to *y* and force them to match at *y*=0, ie:

$$\sum_{n=1}^{\infty} \frac{n\pi}{(g/2)} A_n\, sin\left(\frac{2n\pi}{g} x\right) = -\int_{k=0}^{\infty} k\, C(k).\, sin(kx)\, dk \tag{2.54}$$

which is defined over $0 < x < g/2$. To reduce the left-hand side of equation (2.54), multiply both side by $sin(\frac{2m\pi x}{g})$, where *m* is an integer, and integrate over *x* from 0 to g/2:

$$\sum_{n=1}^{\infty} nA_n \left(\frac{\sin((m-n)\pi)}{(m-n)} - \frac{\sin((m+n)\pi)}{(m+n)} \right) = -\frac{\mathrm{g}}{2} m\pi(-1)^m \int_{k=0}^{\infty} \frac{kC(k).sin(k\frac{g}{2})}{(k\frac{g}{2})^2 - (m\pi)^2} dk \tag{2.55}$$

In the case $n \neq m$ the summation of n on the left-hand side vanishes and hence the summation with respect to n has no contribution. On the other hand, for the $n=m$ case, we obtain:

$$\frac{A_m}{2} = \frac{g}{2}(-1)^{m+1} \int_{k=0}^{\infty} \frac{kC(k).sin(\sigma\frac{g}{2})}{(\sigma\frac{g}{2})^2 - (m\pi)^2} dk \tag{2.56}$$

Apply the substitution $k = \acute{k}/\ (g/2)$ to simplify the analysis and eliminating $C(k)$ using (2.53) produces:

$$(-1)^{m+1} L_m = \frac{\pi}{4}\frac{A_m}{U0} + \pi \sum_{n=1}^{\infty} \frac{A_n}{Uo}\ n(-1)^{n+m}\ L_{mn} \tag{2.57}$$

where $L_m = \int_{k=0}^{\infty} \frac{\sin^2(k)}{\acute{k}[\acute{k}^2 - (m\pi)^2]} d\acute{k} = \frac{-1}{2(m\pi)^2}[\gamma + \ln(2m\pi) - Ci(2m\pi)]$

and $L_{mn} = \begin{cases} \frac{-1}{2m} Si(2m\pi) & m = n \\ \frac{1}{2\pi^2(n^2-m^2)}\left[\ln\left(\frac{m}{n}\right) - Ci(2m\pi) + Ci(2n\pi)\right] & m \neq n \end{cases}$

γ= Euler constant = 0.5772156649…, *Ci* and *Si* are cosine and sine integrals respectively. They are defined by [72]:

$$Ci(2m\pi) = -\int_{x=2m\pi}^{\infty} \frac{cos(x)}{x}\, dx \tag{2.58}$$

$$Si(2m\pi) = \int_{x=0}^{2m\pi} \frac{sin(x)}{x}\, dx \tag{2.59}$$

Equation (2.34) is effectively an infinite set of linear algebraic equations of the from Huang and Deng [70], and Wilton [49]:

$$\boldsymbol{Ax} = \boldsymbol{b} \tag{2.60}$$

where $x_m = A_m/U_0$ with

$$A_m = (-1)^{n+m}\, n\pi L_{mn} + \begin{cases} \frac{\pi}{4} & m = n \\ 0 & m \neq n \end{cases} \tag{2.61}$$

$$b_m = (-1)^{m+1} L_m \tag{2.62}$$

Equations (2.60)-(2.62) were solved approximately using LU decomposition [73] by truncating the series with N = 2000. The computed values agree with the coefficient published by Huang and Deng [70] and up to 6 decimal places with the more accurate computations of Wilton [49].

Wilton et al. (1990) derived an explicit method to determine the harmonic coefficients of Fan's Fourier solution, by matching Fan's solution in the gap region [67], with an expanded conformal mapping solution for the potential of a ring head from Westmijze [56]. Table 2.2 shows the first ten normalised coefficients $\acute{A}$, where $\acute{A}_n = A_n/U_0$.

Table 2.2 The first ten terms of the Fourier series coefficient $A'_n = A_n/ U_0$ [61].

n	A'_n	$\acute{A}_n$ (Correct to 8 d.p.)
1	$-2e^{-2}/\pi$	-0.08615712
2	$5e^{-4}/\pi$	0.02915024
3	$-58e^{-6}/3\pi$	-0.01525422
4	$539e^{-8}/6\pi$	0.00959250
5	$-6934e^{-10}/12\pi$	-0.00668033
6	$38081e^{-12}/15\pi$	0.00496516
7	$-918970e^{-14}/63\pi$	-0.00386090
8	$109167851e^{-16}/1260\pi$	0.00310358
9	$-166282598e^{-18}/315\pi$	-0.00255909
10	$9303339907e^{-20}/2835\pi$	0.00215301

Figure 2.8 shows the accurate surface potential using (2.37) and the coefficients $\acute{A}_n$ from Table 2.1 compared with the approximate surface potential provided by Karlqvist representing the zeroth order term in (2.37).

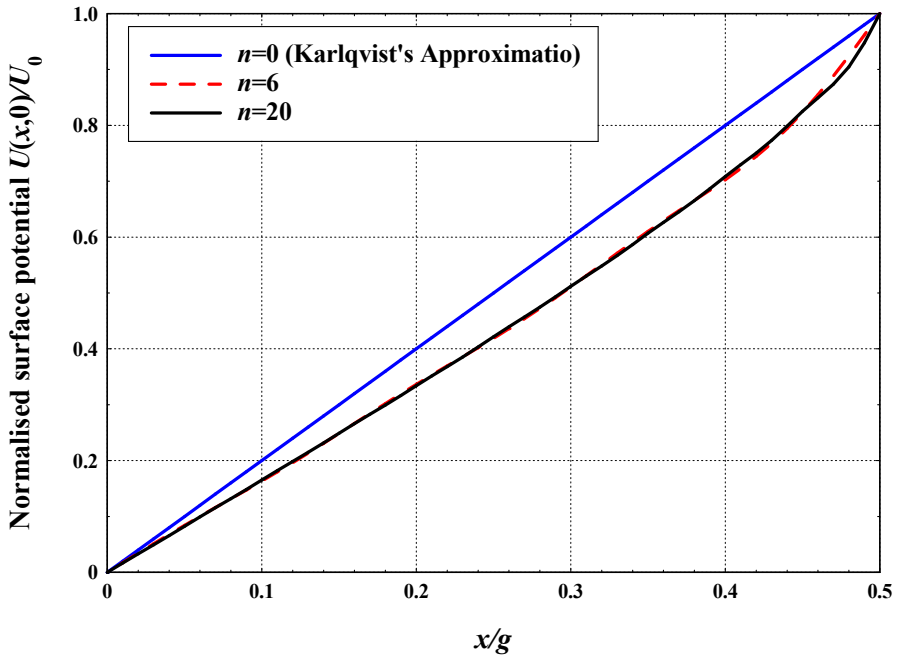

Figure 2.8 Schematic shows the accurate surface potential using the elements of A_n/U_0 those are provided by Table2.2 (dashed line), with linear Karlqvist surface (solid line).

Substituting of the surface potential (2.41) (or (2.47)) into the Green's function convolution in (2.17) and integrating yields

$$H_x(x,y) = \frac{-H_0}{\pi}\left[tan^{-1}\left(\frac{\frac{g}{2}+x}{y}\right) + tan^{-1}\left(\frac{\frac{g}{2}-x}{y}\right)\right] - \frac{1}{(\frac{g}{2})}\sum_{n=1}^{\infty} 2n(-1)^n A_n \int_{k=0}^{\infty} \frac{k\, sin(\frac{kg}{2})\ cos(kx)}{k^2-(2n\pi/g)^2} e^{-ky} dk \tag{2.63}$$

for the x-component of the magnetic field, and

$$H_y(x,y) = \frac{H_0}{2\pi} ln\left[\frac{y^2 + (\frac{g}{2} + x)^2}{y^2 + (\frac{g}{2} - x)^2}\right] + \frac{1}{(\frac{g}{2})} \sum_{n=1}^{\infty} 2n(-1)^n A_n \int_{k=0}^{\infty} \frac{k\ sin(\frac{kg}{2})\ sin(kx)}{k^2 - (2n\pi/g)^2} e^{-ky} dk \tag{2.64}$$

for the *y*-component of the magnetic field, where $H_0 = \frac{2U_0}{g}$.

It's clear that the first terms on the left hand side of both H_x and H_y in (2.63) and (2.64) are the Karlqvist field approximations which are defined in (2.20) and (2.21). The additional terms in (2.63) and (2.64) can be considered as correction terms to the Karlqvist approximation. The integrals in (2.63) and (2.64) were determined by Baird [69] in terms of the complex exponential integral. The *x* and *y* field components for Fan's equation have been computed and plotted in Figure 2.9 at different spacings from the head surface. This figure shows that the amplitude of the magnetic fields increases in the gap corner regions closer to the head surface (due to increased charge density near the corners).

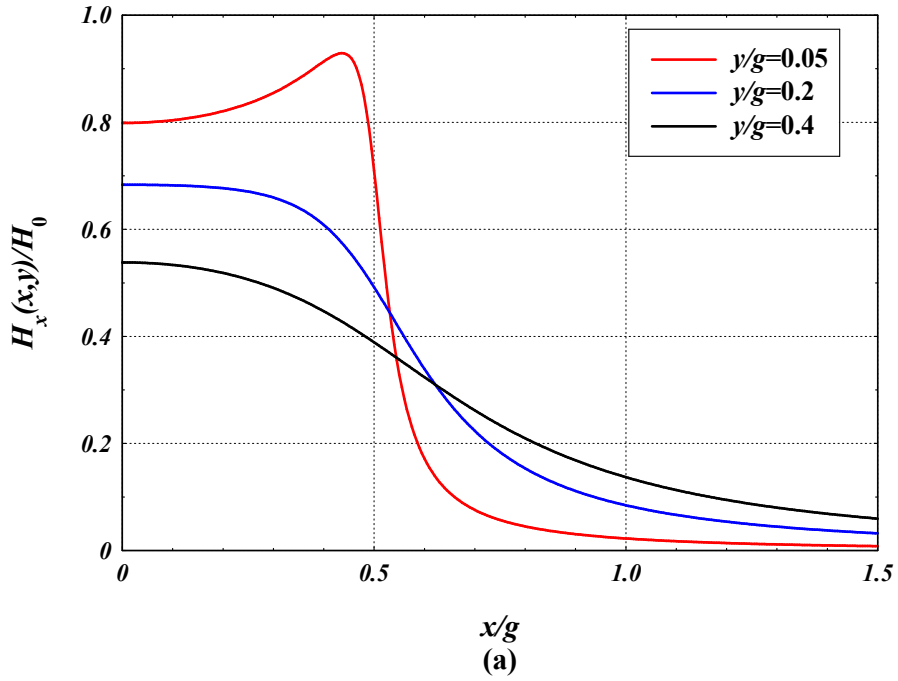

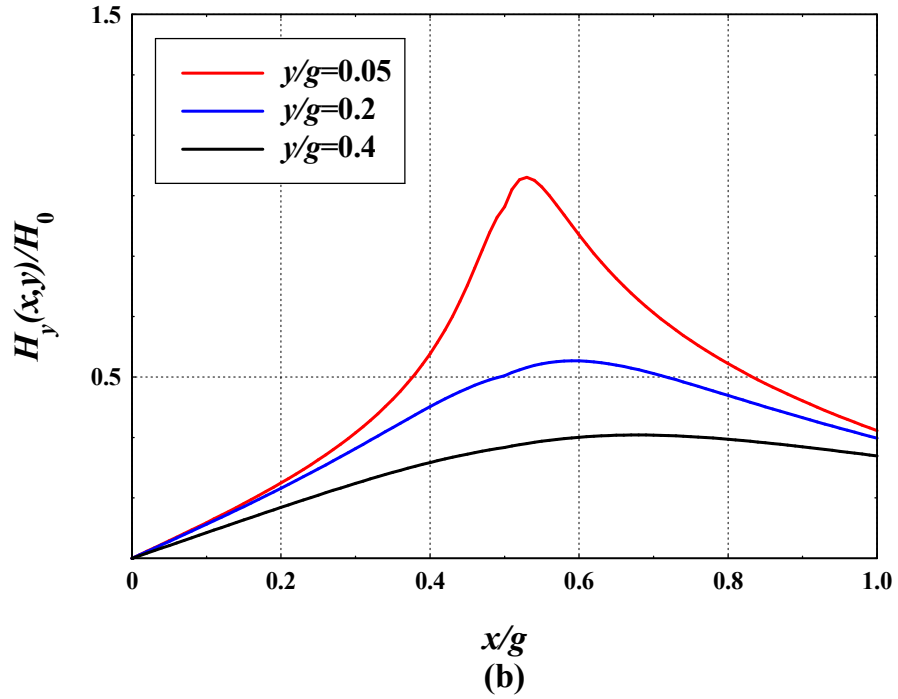

Figure 2.9 Plot of (a) longitudinal and (b) vertical field components as calculated using Fan's equations for different spacing-to-gap length ratios with *n*=20.

The estimated percentage error of the difference between results given by Fan in (2.63) and (2.64) and the Karlqvist approximations in (2.20) and (2.21) decreases with the subsequent increase in the ratio *y/g* as illustrated in Figure 2.10 for H_x, and H_y

components. This again illustrates that the Karlqvist approximation is only valid for sufficiently large distances from the head surface, since it does not include the contribution of surface charges (which are included in the Fourier series solution).

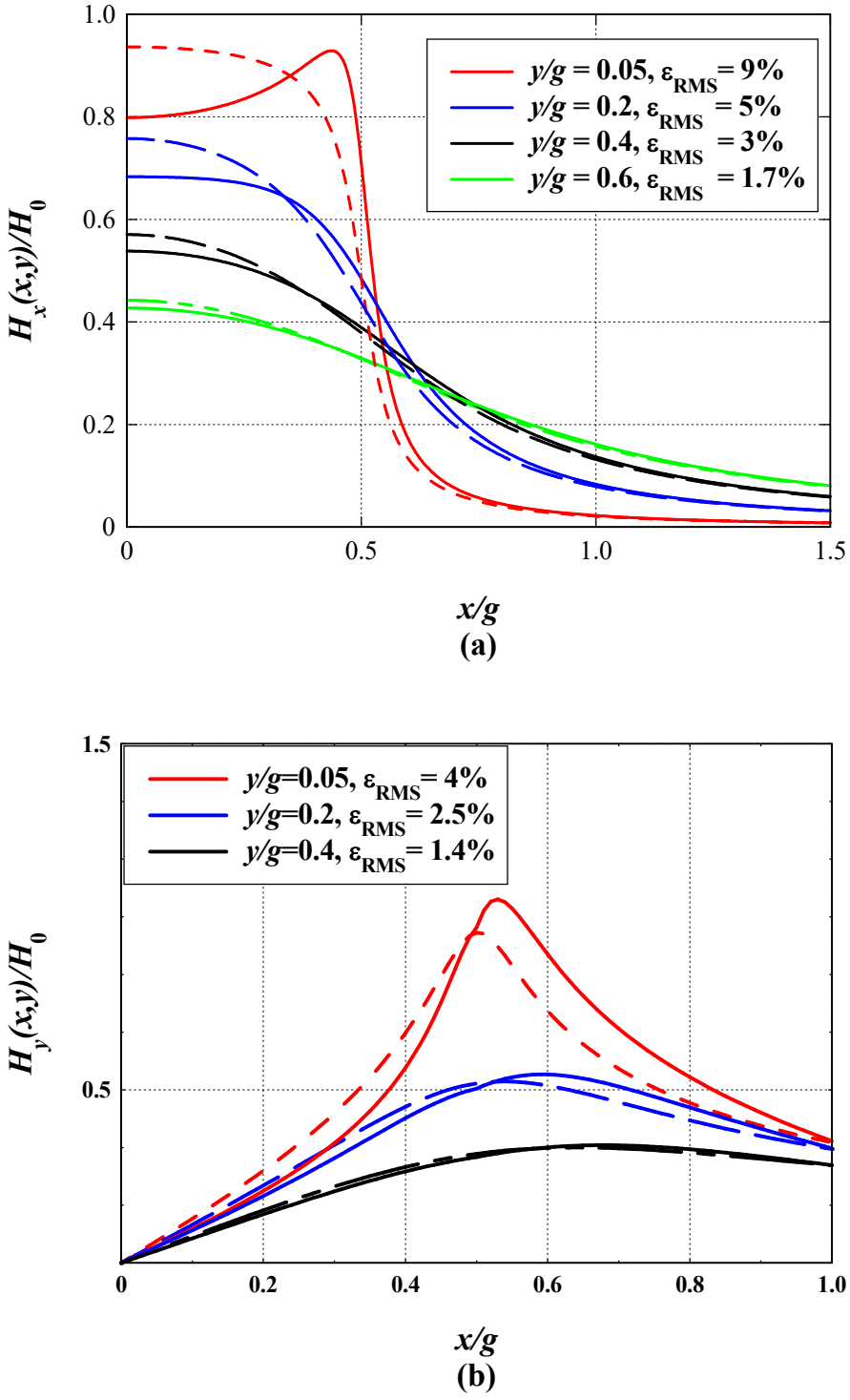

Figure 2.10 Comparison between Fan (solid line) and Karlqvist (dashed line) (a) longitudinal (b) vertical fields for different flying height-to-gap length ratios.

In order to bridge the gap between the simple and approximate field model of Karlqvist's linear gap potential and the Fourier based infinite series solution, Ruigrok presented an accurate approximation by superposing half the constant Karlqvist surface field and half the surface field of the thin-gap head [22, 23]:

$$H_x(x,0) \approx \frac{U_0}{g}\left(1 + \frac{2}{\pi\sqrt{1-(\frac{2x}{g})^2}}\right) \tag{2.65}$$

The surface potential $u(x,0)$ in this case is produced easily by integrating (2.65) with respect to x, which is given by:

$$\frac{u(x,0)}{U} = \frac{x}{g} + \frac{1}{\pi} sin^{-1}(\frac{2x}{g}) \tag{2.66}$$

The surface potential in (2.66) is plotted along with Fan's Fourier series solution and Karlqvist approximation for comparison. The error between Fan and Ruigrok's approximations for the surface potential was less than 2%, which demonstrates the validity of Ruigrok's superposition assumption as illustrated in Figure 2.11.

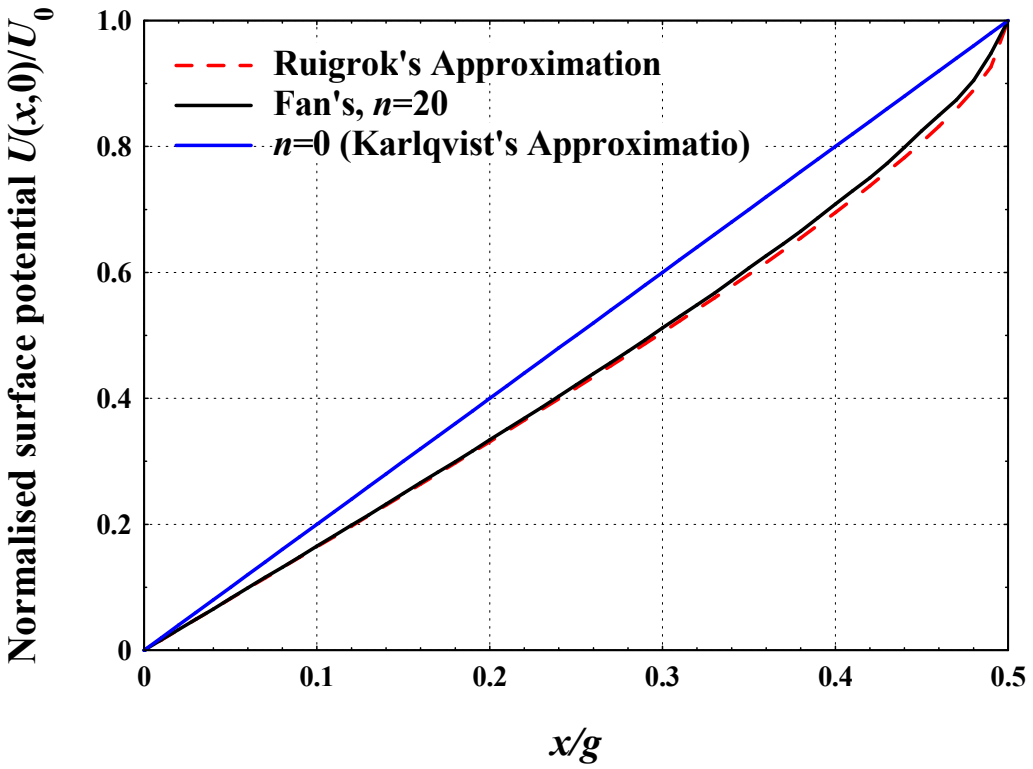

Figure 2.11: Surface potential evaluated using Ruigrok 'thin-pole' approximation compared with Fan and Karlqvist head surface potentials.

The horizontal and vertical field components can be evaluated by substituting (2.65) in (2.17) and integrating exactly to yield:

$$H_x(x,y) = \frac{-H_0}{2\pi}\left[\tan^{-1}\left(\frac{\frac{g}{2}+x}{y}\right) + \tan^{-1}\left(\frac{\frac{g}{2}-x}{y}\right)\right]$$

$$-\frac{gH_0}{2\sqrt{2\pi}}\left\{\frac{\left[\sqrt{[x^2-y^2-\left(\frac{g}{2}\right)^2]^2+4x^2y^2} - x^2+y^2+(g/2)^2\right]^{1/2}}{\sqrt{[x^2+y^2-\left(\frac{g}{2}\right)^2]^2+4y^2(g/2)^2}}\right\} \qquad (2.67)$$

$$H_y(x,y) = \frac{H_0}{4\pi} ln\left[\frac{y^2 + (\frac{g}{2}+x)^2}{y^2 + (\frac{g}{2}-x)^2}\right]$$

$$+ sgn(x)\frac{gH_0}{2\sqrt{2\pi}}\left\{\frac{\left[\sqrt{[x^2 - y^2 - \left(\frac{g}{2}\right)^2]^2 + 4x^2y^2} + x^2 - y^2 - (g/2)^2\right]^{1/2}}{\sqrt{[x^2 + y^2 - \left(\frac{g}{2}\right)^2]^2 + 4y^2(g/2)^2}}\right\} \quad (2.68)$$

Equations (2.67) and (2.68) are plotted along with Fan's exact Fourier series solution and Karlqvist's approximation for *y/g*=0.05 in Figure (2.12).

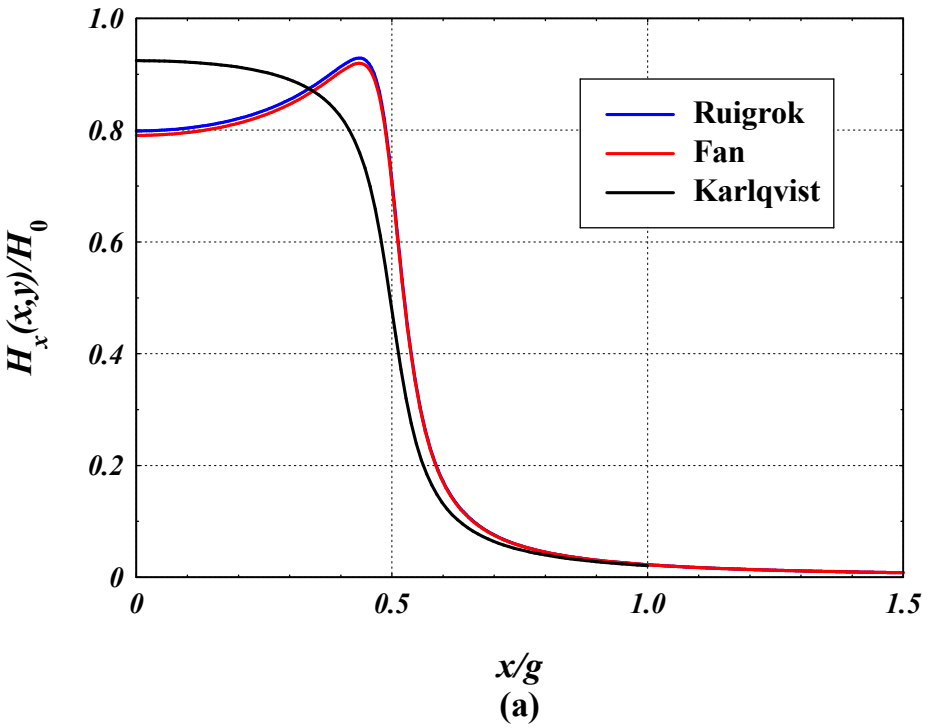

(a)

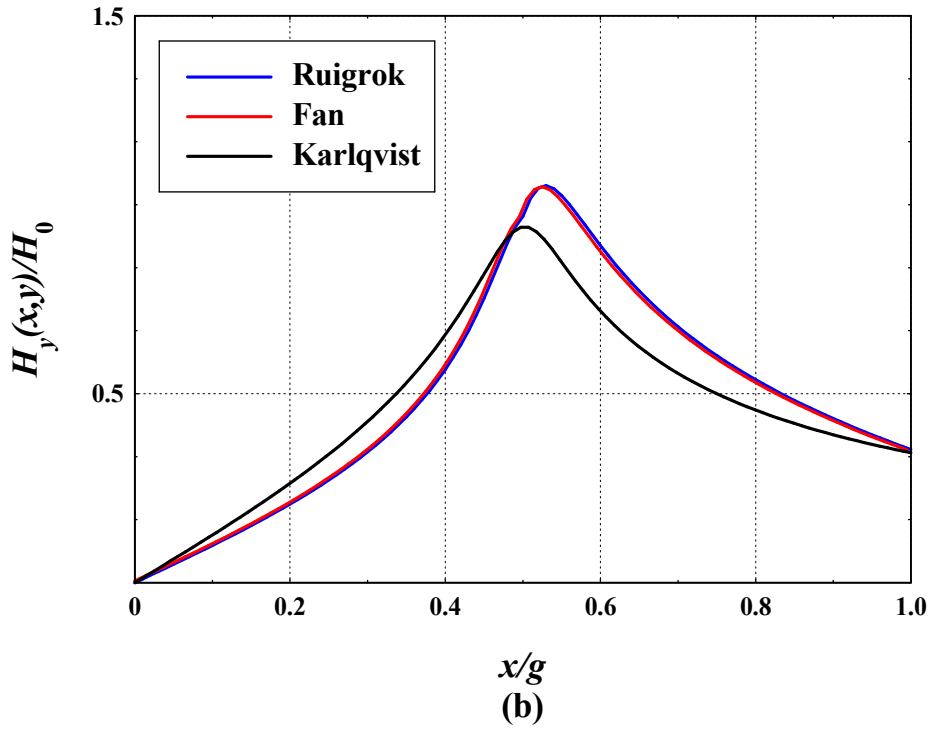

Figure 2.12 (a) H_x and (b) H_y from Ruigrok's 'thin-gap' approximation compared with corresponding Fan and Karlqvist fields for y/g=0.05.

Figure 2.12 shows a very good agreement between Ruigrok's approximation and Fan's analysis, where the percentage root mean square error is about 2% for both horizontal and vertical field components. The success of Ruigrok's approximation is in realising that the added fraction of the thin-gap surface field/potential is equivalent to adding, to the Karlqvist approximation, the contribution of the charge density due to the head pole surfaces at $y = 0$, which was missing in the Karlqvist approximation.

Next, the Fourier series method will be applied to formulate the potential and the field for the ring head in the presence of an underlayer (or keeper).

2.3.2.2 Fourier series analysis for ring head with soft underlayer

As discussed in the previous section, the magnetic fields for the ring type heads have been studied by several researchers, using different methods including the Fourier series analysis. In 1980, Iwasaki [45] proposed the idea of improving the single-pole head performance for perpendicular recording by adding a highly permeable, soft underlayer (SUL). It was shown that the existence of the SUL leads to doubling of the vertical field component [3, 7, 25]. Iwasaki's idea has been extended by many authors to include the ring-type head for perpendicular recording. Fields from ring-type heads with an underlayer were theoretically studied using conformal mapping [4, 5], the Fourier integral method [54], and finite-difference method [76]. The ring-type head has been analysed by Wilton in [43] under the same assumptions listed in section (2.3.1.2), where they considered the two-dimensional model in Figure 2.5. This section applies the Fourier series method for the solution for the symmetric ring-type head following Wilton [43].

The magnetic potential satisfies Laplace's equation in the "T-shaped" region exterior to the poles and the infinitely permeable underlayer shown in Figure 2.5. The area exterior to the pole pieces and the underlayer is divided into two regions A and C (See Figure 2.5). In a practical system, the recording medium would pass through region C only.

Using the method of separation of variables which are leads directly to general solution defined in (2.33) and according to Figure 2.5 the potential is solved in two regions as shown below:

I. Solution of potential in the gap region (region A):

$$\text{At } x = 0,\ u = 0$$

$$y \to -\infty,\ u = \frac{xu_0}{g/2} \qquad -g/2 < x < g/2 \tag{2.69}$$

$$\text{At } x = \pm\frac{g}{2},\ u = \pm u_0$$

Applying the boundary condition (2.45) in region A gives the potential as[43]:

$$u_A(x,y) = \frac{xu_0}{g/2} + \sum_{n=1}^{\infty} A_n \sin\left(\frac{2n\pi}{g}x\right) e^{(\frac{2n\pi}{g})y} \tag{2.70}$$

For n=1,2,3,…

Equation (2.70) is exactly the same as (2.41) which represents the potential in the gap region for a ring head without underlayer.

II. Solution of potential beyond the pole faces (region C):

$$\text{At } x = 0,\ u = 0$$
$$\text{As, } y \to d, u \to 0 \tag{2.71}$$

In region C the potential above the pole pieces and below the underlayer subject to the boundary conditions in (2.71) is given by [43]:

$$u_C(x,y) = \int_{k=0}^{\infty} C(k)\, sin\left(\frac{kx}{g}\right) sinh\left(\frac{k(d-y)}{g}\right) dk \qquad (2.72)$$

Finding the coefficients $C(k)$ and A_n in (2.70) and (2.72) is the next required step in order to evaluate the potential and then the fields. Wilton (1991) [43] solved the magnetic field for a ring head with an underlayer present using Fourier analysis and provided explicit Fourier coefficients for different values of *d*. The A_n coefficients have been determined by matching the derivatives of both $u_A(x,y)$, and $u_C(x,y)$ with respect to *y* along the interval (-*g*/2, *g*/2) at *y*=0. The orthogonality properties of the sine function is then used to determine the coefficients A_n which are computed from an $N = 40$ system and provided in Table 2.3 for a range of *g/d* [43].

Table 2.3 Coefficients A/U_0 computed from an $N = 40$ system [43].

g/d	**1**	**0.75**	**0.5**	**0.25**	**0.1**	**0.25**
A_1/U_0	-0.1322	-0.1144	-0.0996	-0.0896	-0.0866	-0.0861
A_2/U_0	0.0412	0.0366	0.0327	0.0300	0.0292	0.0291
A_3/U_0	-0.0209	-0.0187	-0.0169	-0.0156	-0.0153	-0.0125
A_4/U_0	0.0129	0.0116	0.0105	0.0098	0.0096	0.0095
A_5/U_0	-0.0089	-0.0080	-0.0073	-0.0068	-0.0067	-0.0066
A_6/U_0	066	0.0059	0.0054	0.0051	0.0049	0.0049

The horizontal and vertical components above the head surface (region C) were determined from the gradient of the potential as follows:

$$H_{Cx}(x,y) = -\frac{\partial u_C(x,y)}{\partial x} = -\frac{-2u_0}{\pi g} J_0 - \sum_{n=1}^{\infty} A_n \frac{2n}{g} (-1)^n J_n \qquad (2.73)$$

where

$$J_n = \int_{k=0}^{\infty} \frac{k \sin k \cos kx/g}{k^2 - (n\pi)^2} \frac{\sinh k(d-y)/g}{\sinh kd/g} dk \tag{2.74}$$

and

$$H_{Cy}(x,y) = -\frac{\partial u_C(x,y)}{\partial y} = -\frac{2u_0}{\pi g} K_0 - \sum_{n=1}^{\infty} A_n \frac{2n}{g} (-1)^n K_n \tag{2.75}$$

where

$$K_n = \int_{k=0}^{\infty} \frac{k \sin k \sin kx/g}{k^2 - (n\pi)^2} \frac{\cosh k(d-y)/g}{\sinh kd/g} dk \tag{2.76}$$

The magnetic fields in region C are of particular interest where the recording medium passes through the area exterior to the pole pieces for writing. J_n and K_n in (2.74) and (2.76) respectively cannot be integrated exactly and require numerical integration. When g/d increases towards infinity, the integrations for J_n and K_n will approach the corresponding integral for the ring head without underlayer [30, 6]. Figure (2.13) illustrates the both horizontal and vertical field components given by Wilton [43] for a range of a ratio g/d where the magnetic field has been normalised by the deep gap field $H_g = U_0/g$, while the distances have been normalised by the full gap width $G = 2g$.

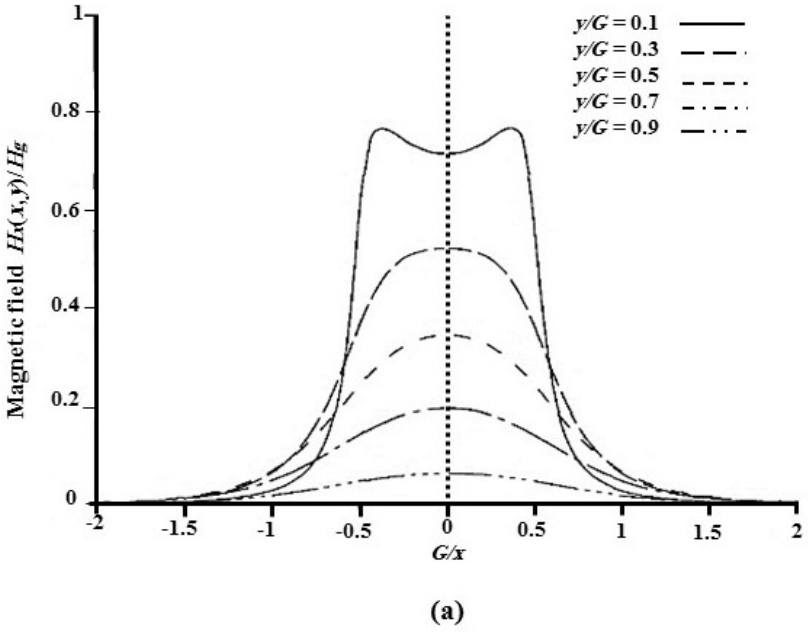

Figure 2.13 Horizontal and vertical magnetic field of a ring head with an underlayer, *y*/*d*=0.5 [43].

2.3.3 The Superposition Method

The familiar concept of superposition is an influential mathematical technique for analysing certain types of complex problems in many science and technology fields. The principle of superposition states that problem solutions can be added together to obtain composite solutions [32, 32]. This technique was applied for mapping 2D and 3D fields of magnetic recording heads. One of the particular advantages of this method is that it enables modelling of finite-pole width, finite-track width head structures in a simple manner. The reasons and characteristics of utilising the superposition technic in magnetic recording analysing has been discussed by Tjaden [80], in addition to presenting some experimental results using a large-scale simulation model. Lindholm in [79] determined the spatial frequency response of ring-type reproduce heads with finite depth and finite pole length assumptions. The same author is also demonstrated the spatial frequency response of reproducing of heads with infinite depth, but finite pole length [81]. Lindholm continue his research of superposition by giving a closed form of field solution for 3D finite gap, infinite length heads of either semi-infinite or zero track width [82]. Okuda et. al., 1988 [83] have been developed a simple analytical model for a 3D head field for a single-pole perpendicular recording head with a underlayer [83]. Due to the aim of this thesis, which is mapping the magnetic fields of two-dimensional symmetrical and asymmetrical magnetic heads, the scope will be on the 2D case only. The study of the 3D fields of magnetic recording heads case will be left for future studies.

2.3.3.1 Modelling 2-Dimensional fields

As indicated above, Lindholm in [81] utilised the superposition method on the general finite-pole width, finite-depth geometry as illustrated in Figures 2.14 and 2.15. In these

figures, the coordinate system is chosen in which the y axis is the vertical axis of symmetry and the x axis coincides with the top surface of the head. The track width, and permeability are considered to be infinite, while the gap length g and head depth b are finite. The pole length is $p = (b - g)/2$. Lindholm used the following three head types to utilise in the superposition of potentials for thin film head:

1. Gapped, Infinite Pole Head: $g \neq 0$,
2. Parallel plate head: for this case $p=0$, so that $g=b$.
3. Gapless, Finite Pole Head: $g=0$, p and d are finite, with $p=b$.

The gap potential evaluated from the gapped head (type 1) as shown in 2.14 and 2.15 (a) to be added to the potential of the parallel plate head (type 2) as illustrated in 2.13 and 2.14 (b). Next step is subtracting the resulting potentials above from the potential in the gapless head defined in type 3.

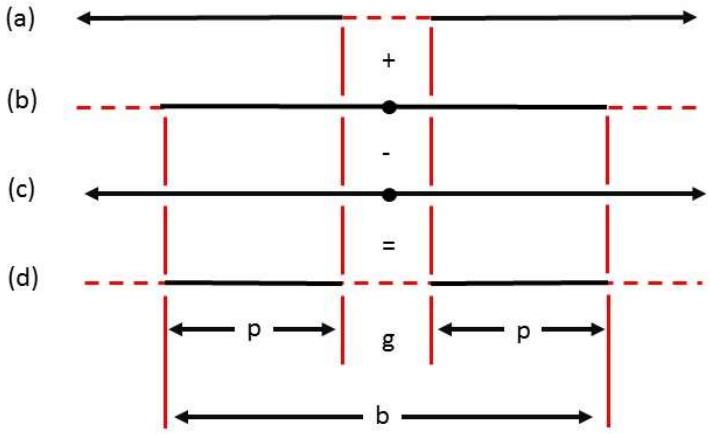

Figure 2.14 Superposition of zero depth heads to obtain 'patch' [81]

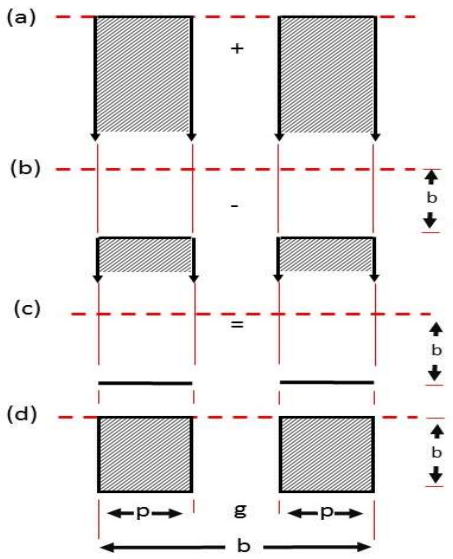

Figure 2.15 Superposition of infinite depth and patch heads to obtain finite depth head with rectangular pole pieces [81]

The previous superposition analysis yields computationally simple formulae which are compared with frequency response deduced by analogy from electrostatic experiments.

In chapter 3, for the first time, detailed and comprehensive derivations based on the principle of superposition for the magnetic scalar potentials and fields from two separated asymmetrical poles (asymmetrical head) without soft magnetic underlayer (SUL) are provided, while the case when the soft magnetic underlayer (SUL) is present covered in chapter 4.

2.3.4 Conformal mapping technique

Conformal mapping, also called conformal transformation, or angle-preserving transformation is a mathematical technique used to convert (or map) one mathematical problem and solution into another. This method has been a topic of theoretical interest and a useful implementation for solving boundary value problems of classical potential theory for more than 100 years. Introduction books to this field have been given by Gaier [84] and Henrici [85], and the book by Driscoll and Trefethen [86] on Schwarz-Christoffel mapping, in addition to a review paper by Wegmann [87] where review more recent work and applications of conformal mapping. Modern computers and advanced computer aided design software tools nowadays enable the solution of many fully three dimensional problems. Nevertheless, the interest in conformal mapping technique continues especially in two dimensional methods [88].

2.3.4.1 Conformal mapping method for magnetic recording heads

The methods of conformal mapping were employed by several researchers to calculate the exact head fields implicitly for two-dimensional idealised models of magnetic recording heads, including:

- Gapped heads [41, 20, 42]
- Symmetric ring heads, without underlayer [42, 20, 4, 43, 41], and with underlayer [4, 5].
- Symmetrical thin-film heads, without underlayer [91].
- Single pole heads [45, 46], and infinitely thin single pole heads [94].
- Asymmetric ring heads without underlayer [48, 49], and with underlayer [50 ,51].

- Asymmetric thin film heads [97], and symmetric and asymmetric polygonal thin film heads [98].

The conformal mapping method has the following limitations:

1. Conformal mapping method gives the solution in terms of x, and y as functions of the magnitude of potential or head fields, rather than provides an explicit expression for the potential and field. Therefore, it requires a numerical inversion to evaluate the potential or head field which is more complex [62].

2. This method is just valid for 2D head structures [89].

2.3.5 The Finite-elements method

The Finite-element method (FEM) can be considered as a general numerical solution tool for partial differential equations in science and engineering. Historically, the popularity of the FEM took place simultaneously with the development of digital computers in the early of 1950s. However, interest in approximate solutions of field equations dates as far back in time as the development of the classical field theories (e.g. elasticity, electro-magnetism) themselves. The work of Lord Rayleigh (1870) and W. Ritz (1909) on vibrational methods and the weighted-residual approach taken by B. G. Galerkin (1915) and others form the theoretical framework to the finite element method.

Basically, the FEM involves modelling of multiplication in a virtual environment, for the purpose of finding and solving for the dependent variable. The basic idea is that the modelled entity is broken down into domains and subdomains, and the occupying space is discretised using simple geometrical elements for each (e.g. triangles), commonly

referred to as finite elements. The unknown function, *u* say, is represented within each element by an interpolating polynomial which is continuous along with its derivatives to a specified order within the element [71]. For instance, Figure 2.16 illustrate the classical Karlqvist head design broken down into a triangular mesh. For each element, an approximated solution is produced by a linear interpolation of the values of potential at the three vertices of the triangle. The linear algebra problem is formed by minimizing a measure of the error between the exact differential equation and the approximate differential equation as written in terms of the linear trial functions [99]. Algorithms exist that allow the resulting linear algebra problem to be solved, usually in a short amount of time [71]. One of the biggest advantages of the FEM is transforming the problem from a complex but small, and difficult problem into a relatively easy but big to solve problem.

There are many available software packages that implement the finite element method for solving partial differential equation such as: Abaqus [100], COMSOL Multiphysics [57, 58], CST Studio Suite [103], Finite Element Method Magnetics [99]. The research in this thesis used COMSOL Multiphysics® that has a number of advantages including: ease of use in terms of defining the problems, boundary conditions, and postprocessing, and flexibility and robustness in meshing and solving complex geometries using a variety of numerical solvers [102]. Finally, it is capable of modelling coupled, multiphysics problems involving many partial differential equations simultaneously.

2.3.5.1 Modelling a ring head using a PDE Mode

This is a simple example that illustrates the steps that were used for modelling the potential and fields of magnetic recording heads used in this research and thesis. In order

to build a two-dimensional model of the most classical head (Karlqvist Head),–the following steps were followed:

Step 1: Choosing the suitable Partial Differential Equation (PDE) Mode, where many classical PDEs can be considered. In the case of the magnetic recording head, Laplace's equation in 2D is considered here.

Step 2: Drawing objects, draw the boundary $\partial\Omega$. The domain should be closed and simply connected, i.e., the boundary cannot intersect itself. The interest area is under the poles, and specifically contain the corners and the gap between the both poles. The pole length, and the distance between the poles and the bounded frame under have been set as 10 times larger than gap length to prevent any possible other corner fields interacting with the gap field.

Step 3: Identifying boundary conditions, the aim is to set constant potentials, $u=r$, at the boundary. This type of boundary condition is called a Dirichlet boundary condition. The potential for each poles as shown in Figure 2.16 was set as ±1, and 0 for the outer bounded area.

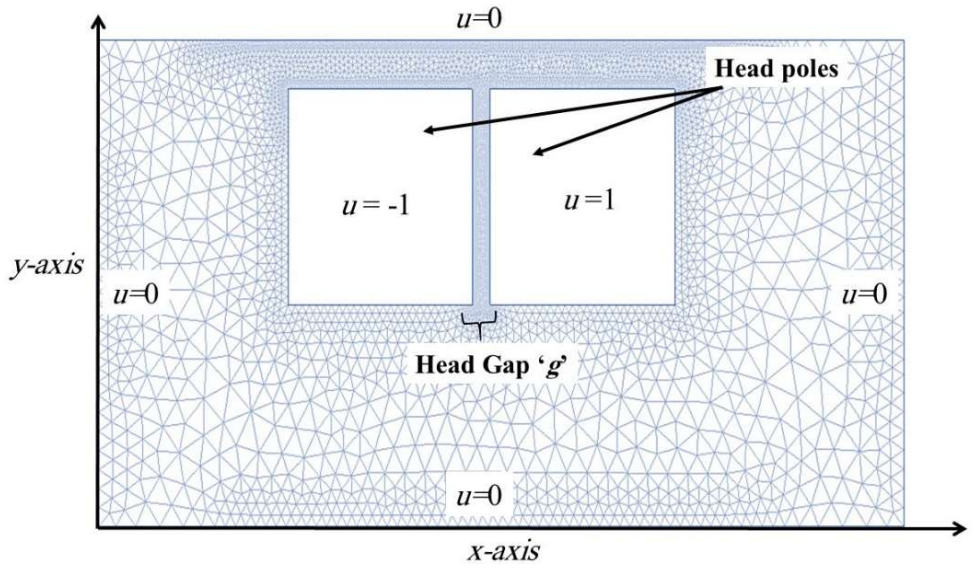

Figure 2.16 FEM for Karlqvist head design.

Step 4: Initializing mesh, the default mesh resolves the geometry by creating a denser mesh in areas with high curvature. This is clearly visible under and between the poles, where the mesh is denser than in the parts with a less pronounced curvature. There is an option to refine mesh for all meshed region, or for a specific region which is very useful to examine the solution in particular region.

Step 5: After doing steps 1- 4, the problem is ready to be solved and plotted easily by choosing a number of the available predefined quantities, such as: *u* for the potential, *ux* for the *x*-component of the magnetic field, *uy* for the *y*-component of the magnetic field, and other options. The solution data can be exported into text files, and then used as a bench mark for comparison with the result from the approximated method in this thesis.

2.4 Root Mean Square Deviation (RMSD)

In this thesis, the closeness of the approximate potential and field models to the more accurate finite-element calculations is estimated using the absolute root-mean-square deviation (RMSD), defined as:

$$\text{RMSD} = \sqrt{\frac{1}{\text{N}}\sum_{n=1}^{N}\left(\hat{f}_n - f_n\right)^2} \tag{2.77}$$

where $\hat{f}_n$ is the approximated model value, f_n is the finite-element data and the summation is taken over N data points. The RMSD is a global, absolute measure with the same units as the potential or fields used in the estimation, with lower values indicating less deviation from the accurate finite-element simulations. The RMSD will therefore be normalised by the extrema in the potential or field magnitudes to estimate the percentage deviation [59, 60].

2.5 Summary

This chapter reviewed the mathematical methods used for mapping the magnetic potentials and fields of two-dimensional magnetic recording heads. The analytical methods reviewed include: the Fourier transform and Fourier series methods. While the semi-analytically and numerical methods reviewed include: conformal mapping, and the finite-element method. However, the numerical methods may have presented a preference in terms of speed, and flexibility to work on more complex configurations, neither gives a convenient representation of the solution for further calculation or for parameter investigation. The analytical methods provide an explicit or at least closed-form

representation of the solution, even though in the form of an infinite series as in Fourier series method. In summary, this chapter has covered:

- Laplace's equation derivation for the magnetic potential.
- The Fourier transform technique for calculating fields from 2D structures using an assumed surface potential.
- The Fourier series method.
- Analytical solutions for the ring head without and with underlayer have been presented.
- The concepts of the Superposition technique for 2D, with a review of previous studies of this method, applied to recording heads.
- Conformal mapping technique for magnetic recording heads, with a review of the previously published work.
- The Finite-elements method and the using of COMSOL Multiphysics software package.
- The absolute root-mean-square deviation (RMSD) definition, and how it is used to examine the closeness of the approximate potential and field models to the more accurate finite-element calculations.

Chapter 3: Modelling Asymmetric Magnetic Recording Heads Without an Underlayer Using Superposition

3.1 Introduction

As discussed in chapter 1, the magnetic head is an integral part of a magnetic recording system. The head geometry and dimensions determine the magnitude and distribution of the fringing gap fields and their gradients, therefore affecting the size and shape of the recorded magnetisation pattern in the magnetic medium during recording, and the resolving performance of the head in readout [106]. The design of magnetic heads therefore has direct impact on the achievable storage density of magnetic recording systems.

Conventional two-dimensional magnetic heads, including the ring-type, finite-pole thin-film and single pole head structures have symmetrical pole geometry and produce mostly symmetrical fringing fields in the gap or pole corner regions as illustrated in chapter 2 for the ring head. Asymmetric heads differ by rotating, in parallel, the pole corners in the gap region through exterior angle θ_0 ($\theta_0 = \frac{\pi}{2} - \theta_1$) as indicated in two-dimensions in Figure 3.1, where the x-axis is the direction along the head/medium motion, and the y-axis is normal to the head surface. In this two-dimensional geometry, the head depth along the z direction is assumed larger in extent compared to the gap length g.

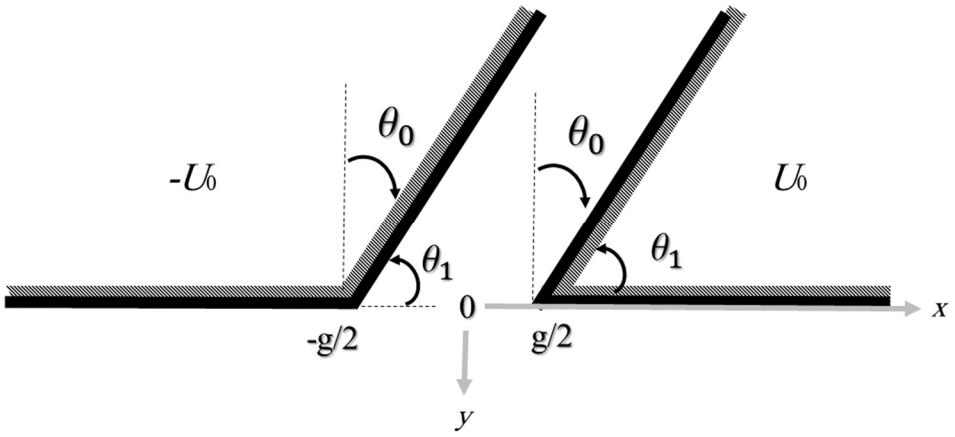

Figure 3.1 Two-dimensional geometry of the asymmetrical head, with gap length *g* and exterior corner inclination angle θ_0. The poles are assumed to have infinite permeability with potentials $\pm U_0$.

The significance of the asymmetrical head shown in Figure 3.1 arises from the increased magnetic charge density in the acute head corner [58]. This leads to an increase in the magnitude of the magnetic fields in this region and narrowing of their distributions as will be shown later in this chapter. Asymmetric heads were therefore proposed for increasing the recording resolution in longitudinal and perpendicular recording due to the increased field gradients near the acute pole corner in the gap region [39]. Asymmetrical heads were also suggested as a method of increasing the readout resolution of ring-type inductive heads and develop 'gap-null free' heads [95], primarily through the natural reduction in the 'effective' gap length of the head with the increase in θ_0 enabling shorter recorded magnetisation patterns in the recording medium to be resolved by the head. Asymmetric head designs were also incorporated in perpendicular heads with tapering in both the main pole and side shields to increase the recording fields and their gradients and to reduce side fringing [5, 6]. These tapered single-pole head structures with tapered

shields, incorporating the asymmetric gapped geometry, were also investigated as part of corner-type head designs for high-resolution, two-dimensional magnetic recording [37].

There are currently neither explicit nor approximate expressions for the potential and fields for asymmetrical magnetic recording heads. Therefore the explicit functional dependence of the corresponding magnetic fields' magnitude, gradient, and wavelength response on the head parameters (such as θ, g and d) is not well understood. The difficulty in deriving explicit solutions for the potentials and fields of asymmetrical heads arises from the fact that this geometry does not conform to conventional coordinate systems, for which formal methods of solution can be applied. Implicit, conformal mapping solutions were previously derived exactly for asymmetrical heads, but only for limited (rational) corner angles [8, 9]. Conformal mapping solutions require numerical inversion to explicitly determine the vector fields in the space surrounding the head surface, and are thus not practical to use in head design and optimisation studies, nor in more complex simulations of the record and readout processes. This chapter provides a detailed investigation of one method of deriving analytical expressions for the magnetic scalar potential and fields for asymmetrical magnetic recording heads without an underlayer, that is based on superposition of single corner structure solutions for any exterior corner inclination angle θ_0 (0° to 90°). The case when the soft magnetic underlayer (SUL) is present will be covered in the next chapters.

To study the validity of the approximate models and estimate the errors in the approximations, Laplace's equation was solved in two dimensions numerically using

finite-element on Comsol Multiphysics®. The geometry and boundary conditions used in the finite-element simulations follows from Figure 3.1, with the simulation space terminated by zero potential planes at very large distances from the gap region to model semi-infinite head structures. Adaptive and progressive mesh refinement was employed to increase the mesh resolution in the (tilted) corner regions for accuracy and convergence of the solution. The closeness of the approximate potential and field models to the more accurate finite-element calculations is estimated using the absolute root-mean-square deviation (RMSD) which is defined in equation (2.16) in chapter 2 normalised by the extrema in the potential or field magnitudes to estimate the percentage deviation.

Increasing the exterior angle θ_0 increases the magnetic field in the acute head corner, leading to saturation in that corner. Pole corner saturation in tilted corners will be discussed in the discussion chapter of this thesis.

In section 3.2 of this chapter, Laplace's equation is solved exactly for the scalar magnetic potential near a single two-dimensional corner in polar coordinates Section in 3.4 will evaluate the error involved in the superposition approximations by drawing upon comparisons with finite-element calculations and exact available solutions (for some corner angles).

3.2 Potential near a two-dimensional corner

The focus here will be on the solution of Laplace's equation in Polar coordinates as defined in (2.7). The use of Polar coordinates is due to the tilted inner (gap) surfaces of the 2D asymmetrical head structure that are identified through polar angle θ.

Laplace's equation in 2D is repeated here for convenience:

$$\frac{1}{\rho}\frac{\partial}{\partial\rho}(\rho\frac{\partial u}{\partial\rho})+\frac{1}{\rho^2}\frac{\partial^2 u}{\partial\theta^2}=0 \tag{3.1}$$

where $\rho=\sqrt{x^2+y^2}$ and $\theta = tan^{-1}(\frac{y}{x})$. Using the method of separation of variables, the general solution to Laplace's equation in (3.2) for small distances near the corner can be shown to be:

$$u(\rho,\theta)=a_0+\rho^k(A\cos(k\theta)+B\sin(k\theta)) \tag{3.2}$$

where a_0, k, A, and B are constants to be determined from application of boundary conditions. The boundary conditions are applied next to derive solutions for a left and a right corner structures to represent the poles of the asymmetrical head. These solutions will then be superposed to arrive at an approximate solution for the asymmetrical head.

3.2.1 The potential for the left pole

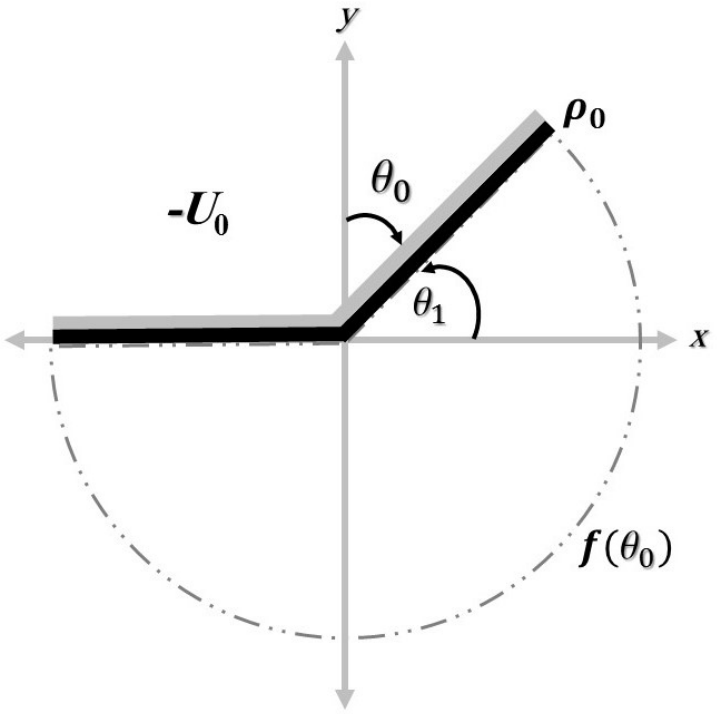

Figure 3.2 The geometry of the left pole and associated boundary conditions.

From Figure (3.2), the boundary conditions can be formulated as:

$$u_L = -U_0 \text{ for } \theta = \pi \text{ for all } \rho > 0 \tag{3.3}$$

$$u_L = -U_0 \text{ for } \theta = -\theta_0 \text{ for all } \rho > 0 \tag{3.4}$$

$$u_L = f(\theta) \text{ for } -\theta_0 \leq \theta \leq \pi \text{ at } \rho = \rho_0 \tag{3.5}$$

where $\theta_0 = \frac{\pi}{2} - \theta_1$

$$u_L = U_0 \text{ for } \rho \to 0 \text{ (near field)} \tag{3.6}$$

Application of the outlined boundary conditions yields the particular solution as:

$$u_L = U_0 + \rho^k B\, sin(k\theta - k\pi) \tag{3.7}$$

Applying the boundary condition in (3.4) allows the determination of the eigen values:

$$k = \frac{n\pi}{\theta_0 + \pi} \tag{3.8}$$

Adding all solutions in equation (3.7)

$$u_L = U_0 + \sum_{m=1}^{\infty} A_m\, \rho^{\frac{m}{\alpha}}\, sin\left(\frac{m(\theta - \pi)}{\alpha}\right) \tag{3.9}$$

where $\alpha = \frac{\pi}{\theta_0 + \pi}$

Applying boundary condition (3.5) to (3.9) gives:

$$f(\theta) = U_0 + \sum_{m=1}^{\infty} A_m \rho_0^{\frac{m}{\alpha}} sin\left(\frac{m(\theta-\pi)}{\alpha}\right) \tag{3.10}$$

To determine the coefficients A_m, the potential is assumed to vanish at $\rho = \rho_0$ so that $f(\theta) = 0$. Thus using the orthogonal property of the Fourier series [71] by multiply both sides by $sin\left(\frac{n(\theta-\pi)}{\alpha}\right)$ and integrating over $-\theta_0 < \theta < \pi$ yields:

$$\begin{aligned} &-U_0 \int_{-\theta_0}^{\pi} sin\left(\frac{n(\theta-\pi)}{\alpha}\right) d\theta \\ &= \sum_{m=1}^{\infty} A_m \rho_0^{\frac{m}{\alpha}} \int_{-\theta_0}^{\pi} sin\left(\frac{n(\theta-\pi)}{\alpha}\right) sin\left(\frac{m(\theta-\pi)}{\alpha}\right) d\theta \end{aligned} \tag{3.11}$$

The term on the left hand side of (3.11) can be evaluated as:

$$-U_0 \int_{-\theta_0}^{\pi} sin\left(\frac{n(\pi-\theta)}{\alpha}\right) d\theta = \frac{-U_0\alpha}{n} ((-1)^n - 1) \tag{3.12}$$

The term on the right hand side of (3.11) can be evaluated as:

$$\int_{-\theta_0}^{\pi} sin\left(\frac{n(\pi-\theta)}{\alpha}\right) sin\left(\frac{m(\pi-\theta)}{\alpha}\right) d\theta \begin{cases} = 0 & if\ m \neq n \\ = \dfrac{\alpha(\pi-\theta_0)}{2} & if\ n = m \end{cases} \tag{3.13}$$

Substituting (3.12) and (3.13) into (3.11) yields:

$$\frac{-U_0\alpha}{n}\left((-1)^n-1\right)=\sum_{m=1}^{\infty}A_m\,\rho_0^{\frac{m}{\alpha}}\,\frac{\alpha(\pi-\theta_0)}{2} \tag{3.14}$$

Thus the coefficients A_m are given by:

$$A_m=\frac{-2U_0\left((-1)^n-1\right)}{n\pi\,\rho_0^{\frac{m}{\alpha}}}\begin{cases}=0 & if\ n\ \ even\\ =\dfrac{4U_0}{n\pi\,\rho_0^{\frac{m}{\alpha}}} & if\ n\ \ odd\end{cases} \tag{3.15}$$

Then, the potential can be written as:

$$u_L=U_0+\frac{4U_0}{\pi}\sum_{m=1}^{\infty}\frac{\rho^{\frac{m}{\alpha}}}{m\,\rho_0^{\frac{m}{\alpha}}}\sin\left(\frac{m(\theta-\pi)}{\alpha}\right) \tag{3.16}$$

Equation (3.16) can be re-written in the form:

$$u_L=U_0+\frac{4U_0}{\pi}\sum_{m=1}^{\infty}\frac{1}{m}\left(\frac{\rho}{\rho_0}\right)^{\frac{m}{\alpha}}\sin\left(\frac{m(\theta-\pi)}{\alpha}\right) \tag{3.17}$$

By setting $P = (\frac{\rho}{\rho_0})^{\alpha}$ and $Z = \frac{(\theta-\pi)}{\alpha}$, equation (3.17) becomes:

$$u_L = U_0 + \frac{4U_0}{\pi}\sum_{m=1}^{\infty}\frac{P^{2m-1}}{(2m-1)}sin((2m-1)Z) \tag{3.18}$$

The summation in (3.18) can be evaluated exactly as follows:

$$\sum_{m=1}^{\infty}\frac{P^{2k-1}\,sin((2k-1)(Z))}{(2k-1)} = \frac{1}{2}tan^{-1}(\frac{2P\,sin(x)}{1-P^2}) \tag{3.19}$$

Substituting back in (3.18) gives:

$$u_L = U_0 + \frac{2U_0}{\pi}tan^{-1}\left(\frac{2(\frac{\rho}{\rho_0})^{\alpha}\,sin\left(\frac{(\theta-\pi)}{\alpha}\right)}{1-(\frac{\rho}{\rho_0})^{\frac{2}{\alpha}}}\right) \tag{3.20}$$

3.2.2 The potential for the right pole

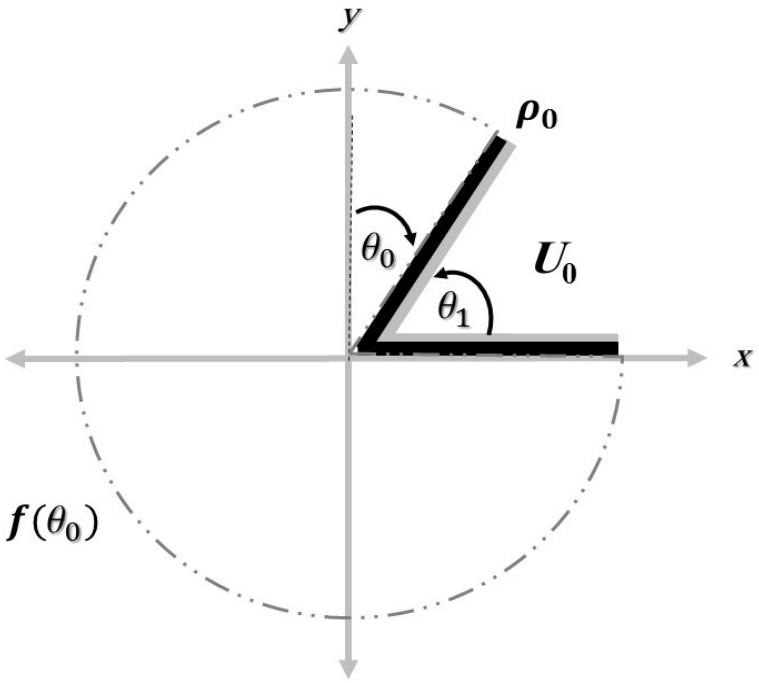

Figure 3.3 The geometry of the right pole and associated boundary conditions.

From Figure (3.3), the boundary conditions can be written as:

$$u_R = U_0 \text{ for } \theta = 0, \text{ for } \rho > 0 \tag{3.21}$$

$$u_R = U_0 \text{ for } \theta = 2\pi - \theta_0, \text{ for } \rho > 0 \tag{3.22}$$

$$u_R = f(\theta) \text{ for } 0 < \theta < 2\pi - \theta_0, \rho = \rho_0 \tag{3.23}$$

where $\theta_0 = \frac{\pi}{2} - \theta_1$

Applying the boundary condition (3.21) in (3.2) yields

$$u_R = U_0 + \sum_{m=1}^{\infty} B_m \rho^{\frac{m}{\beta}} \sin\left(m\frac{\theta}{\beta}\right) \tag{3.24}$$

where $\beta = \frac{\pi}{2\pi-\theta_0}$

Application of the boundary condition in (3.22) gives:

$$f(\theta) = U_0 + \sum_{m=1}^{\infty} B_m \rho^{\frac{m}{\beta}} \sin\left(m\frac{\theta}{\beta}\right) \tag{3.25}$$

To determine the coefficients A_m, the potential is assumed to vanish at $\rho = \rho_0$ so that $f(\theta) = 0$. Thus using the orthogonal property of the Fourier series [71] by multiplying both sides by $sin\left(n\frac{\theta}{\beta}\right)$ and integrating over $0 \leq \theta \leq \beta$ yields:

$$-U_0 \int_0^{\alpha} sin\left(n\frac{\theta}{\beta}\right) d\theta = \sum_{m=1}^{\infty} B_m \rho^{\frac{m}{\beta}} \int_0^{\alpha} sin\left(n\frac{\theta}{\beta}\right) sin\left(m\frac{\theta}{\beta}\right) d\theta \tag{3.26}$$

Carrying out the integrations following the previous section, the coefficients B_m were found to be:

$$B_n = \frac{-2U_0}{n\pi\,\rho_0^{\frac{n}{\beta}}}\,(1-(-1)^n) = \begin{cases} 0 & when\ n\ even \\ \dfrac{-4U_0}{n\pi\,\rho_0^{\frac{n}{\beta}}} & when\ n\ odd \end{cases} \tag{3.27}$$

Thus the potential for the right pole (corner) now becomes:

$$u_R = U_0 - \frac{2U_0}{\pi}\sum_{m=1}^{\infty}\frac{(1-(-1)^m)}{m}\left(\frac{\rho}{\rho_0}\right)^{\frac{m}{\beta}}\sin\left(m\frac{\theta}{\beta}\right) \tag{3.28}$$

By setting $P = (\frac{\rho}{\rho_0})^{\beta}$ and $Z = \frac{\theta}{\beta}$ equation (3.28) is re-written as:

$$u_R = U_0 - \frac{4U_0}{\pi}\sum_{m=1}^{\infty}\frac{P^{2m-1}}{(2m-1)}\sin((2m-1)Z) \tag{3.29}$$

The summation in (3.29) can be evaluated exactly as follows [108] :

$$\sum_{m=1}^{\infty}\frac{P^{2k-1}\sin\big((2k-1)(Z)\big)}{(2k-1)} = \frac{1}{2}tan^{-1}\left(\frac{2P\sin(x)}{1-P^2}\right) \tag{3.30}$$

Using equation (3.30) in (3.29) gives the solution for the right corner:

$$u_R = U_0 - \frac{2U_0}{\pi} tan^{-1}\left(\frac{2(\frac{\rho}{\rho_0})^{\beta} \sin\left(\frac{\theta}{\beta}\right)}{1 - (\frac{\rho}{\rho_0})^{\frac{2}{\beta}}}\right) \tag{3.31}$$

3.3 Superposition of corner potentials

The two modelled corners in the previous section can be conceptually used to model the two semi-infinite poles of a gapped head structure. This can be achieved by translating each corner from the origin by a distance along the *x*-axis equivalent to half of the head gap length. In this case, the potential of the gapped head structure may be determined from the superposition of the potential at each corner. Deriving the surface potential of the gapped head structure this way, it may then be possible to determine the potential and fields everywhere beyond the head surface by substituting this surface potential into the appropriate Green's function defined in chapter 2 and carrying out the convolution.

Since the focus here is on the potential and fields near corners, then for sufficiently small distances, ρ, near the corner only the first term in the potential series solution can be used to simplify the expressions for the corner potentials [58].

The superposition of the potential at each corner is evaluated for full series solution form, and first term for symmetrical head (θ_0=0^o) using the equations (3.31) and (3.20) as shown in Figure 3.4, which is also compared with the potential of Thin-film head.

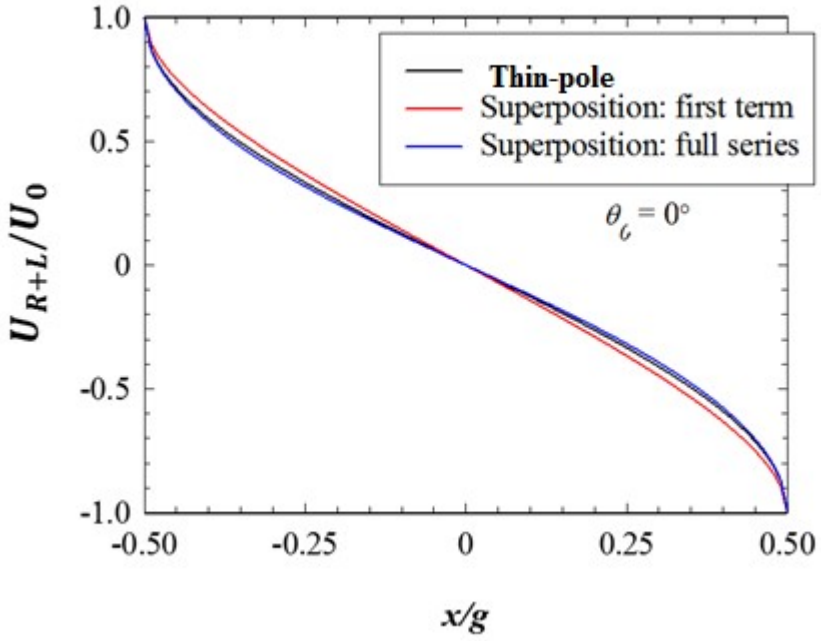

Figure 3.4 Superposition potential Symmetrical head plots.

Figure 3.4 shown a very good agreement between the full series term and the first term in the Fourier series solution of the corner potential therefore provides sufficient accuracy for modelling potentials and fields near corners. Moreover and as will be shown later in this chapter, the first term solution allows the derivation of exact and closed-form solutions for the magnetic fields from asymmetrical heads. Hence the surface potentials of the corners are written using only the first terms in their Fourier series solution in (3.9) and (3.24), which will be used throughout this thesis and are given by:

$$u_L \cong -U_0 + A\rho^{\alpha}\sin(\alpha(\theta-\pi)) \tag{3.32}$$

$$u_R \cong U_0 - B\rho^{\beta}\sin(\beta\theta) \tag{3.33}$$

where $\alpha = \frac{\pi}{\pi + \theta_0}$, and $\beta = \frac{\pi}{2\pi - \theta_0}$.

In addition to translating the two corners by ±g/2 to model the gapped head structure, another important requirement for the valid application of superposition is that the surface potential of one corner vanishes at the other corner. This is to prevent disturbing the constant potentials of the corner surfaces (held at ±U_0). Thus the coefficients A and B for each pole corner are determined by stipulating that the potential at a distance g from each corner is zero, which yields:

$$A = \frac{-U_0 g^{-\alpha}}{\sin(\alpha(\theta - \pi))} \tag{3.34}$$

$$B = \frac{U_0 g^{-\beta}}{\sin(\beta\theta)} \tag{3.35}$$

The surface potential for each corner is then given by:

$$u_L = -U_0 - A\left|x + g/2\right|^{\alpha} \sin(\alpha\pi) \tag{3.36}$$

$$u_R = U_0 - B\left|x - g/2\right|^{\beta} \sin(\beta\pi) \tag{3.37}$$

Superposing the surface potentials of the translated corners provides the following approximation for the surface p otential of the gapped head:

$$u_{L+R} = -U_0 - A\left|\frac{g}{2} + x\right|^{\alpha} \sin(\alpha\pi) + U_0 - B\left|\frac{g}{2} - x\right|^{\beta} \sin(\beta\pi) \qquad (3.38)$$

where $-g/2 \le x \le g/2$.

The purpose of evaluating the surface potential at $y = 0$ is so that it can be convolved with the appropriate two-dimensional Green's function to evaluate the potential and fields everywhere beyond the head surface. In this case, evaluation of the convolution involves integration along the surfaces of the two poles and over the gap region. Thus it would be simpler to work with surface fields rather than surface potentials when convolving with Green's functions since the integration is only over the gap region (surface fields along the poles are zero). Thus the focus henceforth in this chapter is on using the surface fields. The horizontal component of the surface field is determined from the gradient of the surface potential:

$$H_x^s(x,0) = -\frac{du_R}{dx} - \frac{du_L}{dx} \qquad (3.39)$$

Substituting the surface potentials (3.38) yields the surface field:

$$H_x^s = -A\alpha \left|x + \frac{g}{2}\right|^{\alpha-1} sin(\alpha\pi) + B\beta \left|x - \frac{g}{2}\right|^{\beta-1} sin(\beta\pi) \tag{3.40}$$

3.3.1 Horizontal and Vertical field components

The magnetic fields everywhere beyond the head surface can be determined using the Green's function solution of Laplace's equation as defined in (2.14) convolved with the prescribed surface field $H_x^s(x',0)$ at $y = 0$ [65]:

$$H_x(x,y) = \frac{y}{\pi}\int_{-\infty}^{\infty} \frac{H_x^s(x',0)}{(x'-x)^2 + y^2} dx' \tag{3.41}$$

$$H_y(x,y) = \frac{1}{\pi}\int_{-\infty}^{\infty} H_x^s(x',0)\ \frac{(x'-x)}{(x'-x)^2 + y^2} dx' \tag{3.42}$$

Here, the complex representation is used to evaluate the x and y field components to simplify the mathematical treatments in an effective manner. Since,

$$\frac{y}{(x'-x)^2 + y^2} = \frac{1}{2j}\left[\frac{1}{x'-x-jy} - \frac{1}{x'-x+jy}\right] \tag{3.43}$$

then (3.41) can be written as:

$$H_x(x,y) = \frac{1}{2\pi}\left[\int_{-\infty}^{\infty} \frac{H_x^s(x',0)}{x'-x-jy}\,dx' - \left(\int_{-\infty}^{\infty} \frac{H_x^s(x',0)}{x'-x-jy}\,dx'\right)^*\right] \tag{3.44}$$

where $\left(\int_{-\infty}^{\infty} \frac{H_x^s(x',0)}{x'-x-jy}\,dx'\right)^*$ is the complex conjugate and hence,

$$H_x(x,y) = \frac{1}{\pi}\ \text{Imag}\left(\int_{-\infty}^{\infty} \frac{H_x^s(x',0)}{x'-x-jy}\,dx'\right) \tag{3.45}$$

Similarly, since

$$\frac{(x'-x)}{(x'-x)^2+y^2} = \frac{1}{2}\left[\frac{1}{x'-x-jy} + \frac{1}{x'-x+jy}\right] \tag{3.46}$$

Then,

$$H_y(x,y) = \frac{1}{\pi}\ \text{Real}\left(\int_{-\infty}^{\infty} \frac{H_x^s(x',0)}{x'-x-jy}\,dx'\right) \tag{3.47}$$

Using (3.40) in (3.45) gives,

$$H_x(x,y) = \text{Imag}\left(-A\alpha\,\frac{\sin(\alpha\pi)}{\pi} I_\alpha + B\beta\,\frac{\sin(\beta\pi)}{\pi} I_\beta\right) \tag{3.48}$$

where

$$I_\alpha = \int_{-\frac{g}{2}}^{\frac{g}{2}} \frac{\left|x+\frac{g}{2}\right|^{\alpha-1}}{x'-x-jy}\,dx' \tag{3.49}$$

$$I_\beta = \int_{-\frac{g}{2}}^{\frac{g}{2}} \frac{\left|x-\frac{g}{2}\right|^{\beta-1}}{x'-x-jy}\,dx' \tag{3.50}$$

Similarly, the y-component of the field can be written as:

$$H_y(x,y) = \text{Real}\left(-A\alpha\,\frac{\sin(\alpha\pi)}{\pi} I_\alpha + B\beta\,\frac{\sin(\beta\pi)}{\pi} I_\beta\right) \tag{3.51}$$

In order to evaluate *Iα* and *Iβ* in (3.49) and (3.50) respectively, the Hurwitz–Lerch Zeta function has been used, which is defined as [109]:

$$\Phi(z,s,a) = \frac{1}{\Gamma(s)} \int_0^\infty \frac{t^{s-1}\, e^{-at}}{1 - ze^{-t}}\, dt \tag{3.52}$$

where, $\Gamma(s)$ is the Gamma function. When s = 1, the Zeta function becomes:

$$\Phi(z,1,a) = \int_0^\infty \frac{e^{-at}}{1 - ze^{-t}}\, dt \tag{3.53}$$

The integral $I\alpha$ in (3.49) can be evaluated by using the substitution $x' = -t + \frac{g}{2}$ to yield:

$$I_\alpha = -\int_0^g \frac{t^{\alpha-1}}{t - z_1} dt \tag{3.54}$$

where $z_1 = \frac{g}{2} - x - jy$. Similarly, using the substitution $x' = t - \frac{g}{2}$ to evaluate I_β in (3.50) gives:

$$I_\beta = \int_0^g \frac{t^{\beta-1}}{t - z_2} dt \tag{3.55}$$

where $z_2 = \frac{g}{2} + x + jy$.

The integrals I_α and I_β were determined using Mathematica ®, and can be written in terms of the Hypergeometric function *2F1* [109] as:

$$I_\alpha = -\frac{(g-z_1)^\alpha}{\alpha z_1}\,{}_2F_1\left(-\alpha,-\alpha;1-\alpha,\frac{z_1}{z_1-g}\right)+\frac{g^\alpha}{\alpha z_1}-(-z_1)^{\alpha-1}\frac{\pi}{\sin(\alpha\pi)} \qquad (3.56)$$

$$I_\beta = \frac{(g-z_2)^\beta}{\beta z_2}\,{}_2F_1\left(-\beta,-\beta;1-\beta,\frac{z_2}{z_2-g}\right)-\frac{g^\beta}{\beta z_2}+(-z_2)^{\beta-1}\frac{\pi}{\sin(\beta\pi)} \qquad (3.57)$$

Equations (3.48) and (3.51) are used next to evaluate and plot the fields beyond the surface of asymmetrical heads.

3.4 Results

3.4.1 Surface potential

The surface potential derived from superposition in (3.38) is plotted in Figure 3.5 (dashed lines) for a number of exterior corner angles and compared with the accurate finite-element calculations using COMSOL Multiphysics® (solid lines).

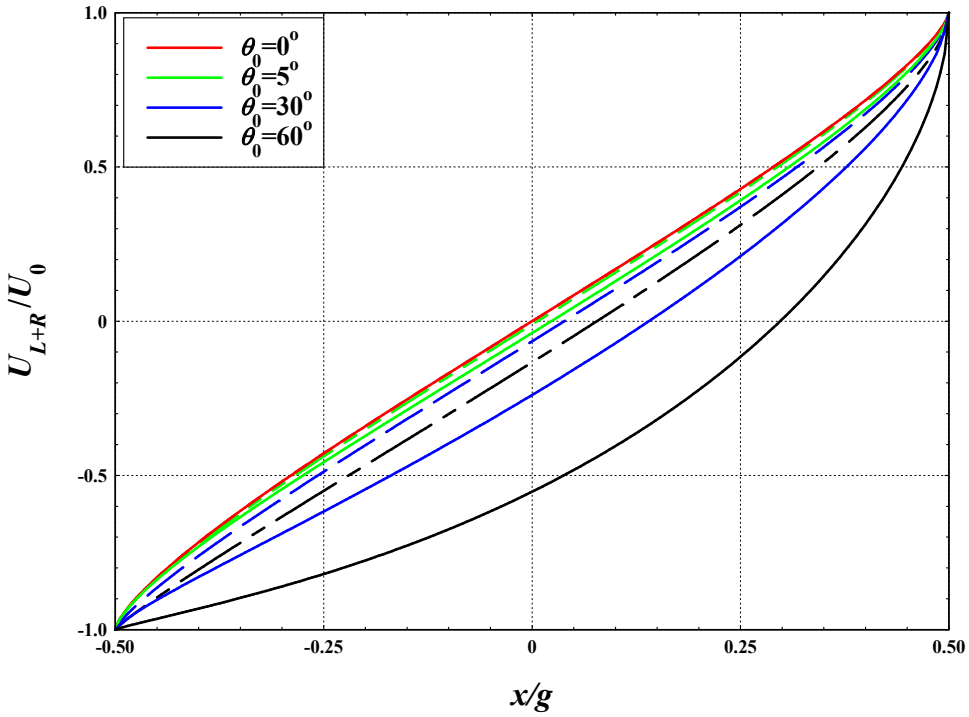

Figure 3.5 Calculated gap surface potential for a range of different corner angles $0 \leq \theta_0 \leq 60$ using finite-element solution of Laplace's equation (solid lines). The dashed lines are the approximate surface potential calculated using (3.38).

Figure 3.6 shows the calculated RMSD between the approximate gap potential in (3.38) and the finite-element calculations, normalised by the maximum change of potential in the gap ($2U_0$) as a function of the interior corner angle (θ_0). It can be seen that the RMSD increases almost linearly with increasing inclination angle.

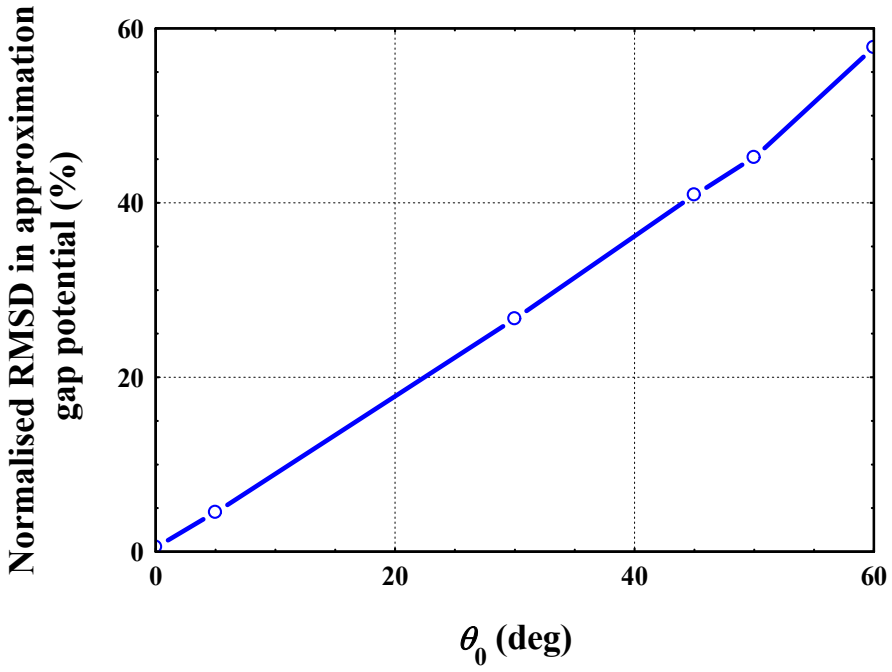

Figure 3.6 The RMSD between the superposition of approximate gap potential in (3.38) and the finite-element calculations by COMSUL Multiphysics®.

Figure 3.5 shows excellent agreement between the surface potential calculated using superposition and the finite-element/exact solutions [67] when $\theta_0 = 0^o$ (right-angled, symmetrical head), with RMSD ~ 0.5%. With increasing θ_0, Figures 3.6 and 3.7 illustrate that the superposition approximation continues to provide good/acceptable agreement with the calculated gap surface potential from finite-element in the range of $0 \leq \theta_0 \leq 30$ with maximum RMSD of ~ 27%. The error in the superposition-based approximation increases dramatically for θ_0 greater than 30°. The increase of RMSD in potential in Figure 3.7 provides an indication of the range of θ_0 for which the superposition process provides an acceptable accuracy, and next the RMSD in magnetic field will provide another qualifier.

3.4.2 Magnetic Fields

Equations (3.48) and (3.51) are used to evaluate the fields everywhere beyond the head surface using the surface field expression in (3.38) based on superposition. The normalised x and y field components of the approximate fields at different spacings from the head surface and $H_0 = 2U_0/g$ is the x-component of the deep-gap field are plotted as dashed lines in the following figures and compared with the finite-element calculations obtained using COMSOL Multiphysics® and indicated with solid lines. The normalised (by the peak field) RSMD is used to estimate the percentage differences between the approximation and the finite-element calculations.

For the right angled head with $\theta_0 = 0°$, the x and y field components at different spacings from the head surface are shown in Figure 3.7. This figure shows that the fields are symmetrical with almost perfect agreement between the theoretical, superposition-based calculations, and the finite-element solution where the RMSD is less than 1% (see Table 3.1). This figure again demonstrates that the superposition method provides an accurate description of the potential and fields for symmetrical heads. Table 3.1 shows the RMSD between the superposition of the normalised x and y field components and the finite-element calculations for $\theta_0 = 0^o$. This table also shows that the y field component in the approximation agrees more to the finite-element data.

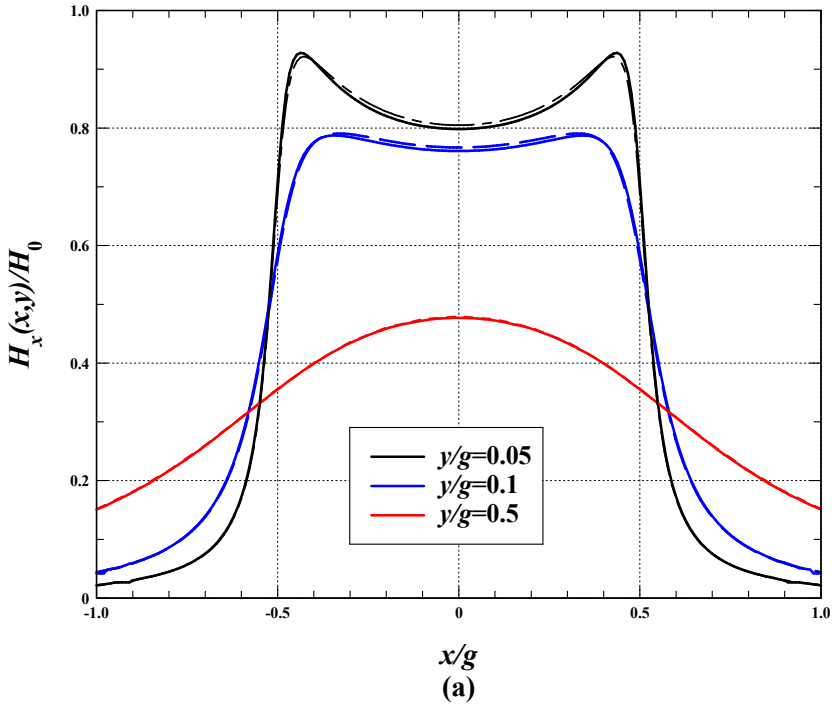

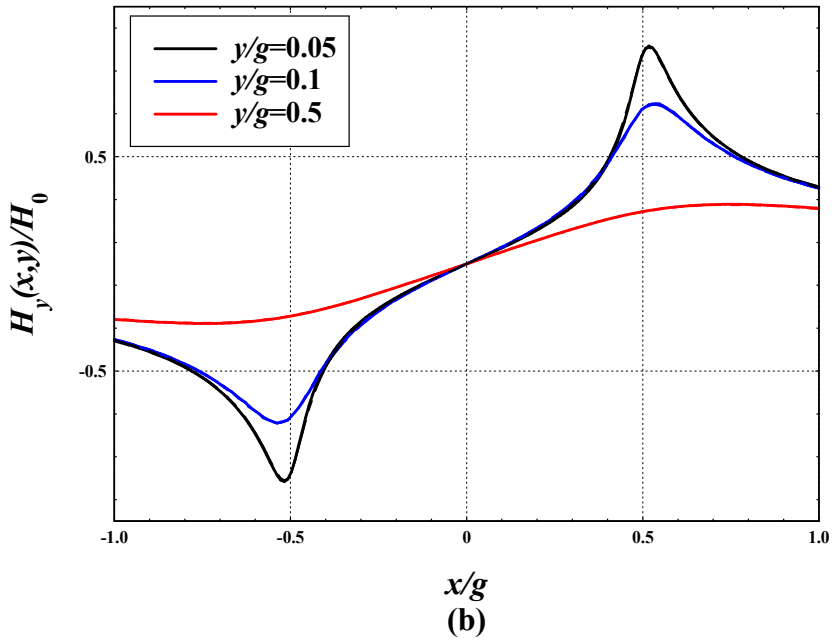

Figure 3.7 (a) Normalised *x*-component (b) y-component field distribution for the symmetrical head for interior corner angle θ_0=0° at *y*/*g*=0.05, 0.1, and 0.5 (calculated using finite-element (solid lines) and using the approximate models in equations (3.48) and (3.51) (dashed lines)).

Table 3.1 RMSD percentages between the superposition of the normalised *x* and *y* components of fields and the finite-element calculations for $\theta_0 = 0^o$

y/g	% RMSD for H_x	% RMSD for H_y
0.05	0.96	0.38
0.1	0.53	0.28
0.5	0.37	0.26

The *x* and *y* field distributions for $\theta_0 = 5°$ in the asymmetric head at different spacing from the head surface are shown in Figure 3.8. In here the fields are becoming asymmetric with increasing fields in the right corner. The agreement between the approximations (dashed lines) and the finite-element calculations using COMSOL Multiphysics® (solid lines) is very good. The *y* component of the head field reflects the magnetic charge distribution normal to the head surface, and therefore increases near the right (acute) corner. The calculated deviations of the approximate *x* and *y* field components are illustrated in Table 3.2, where again the *y* field component in the approximation agrees more to the finite-element data. Table 3.2 demonstrates very good agreement between the approximation model and the FEM. In general, the error in the approximate fields decreases for increases in head spacing ($y/g \geq 0.5$).

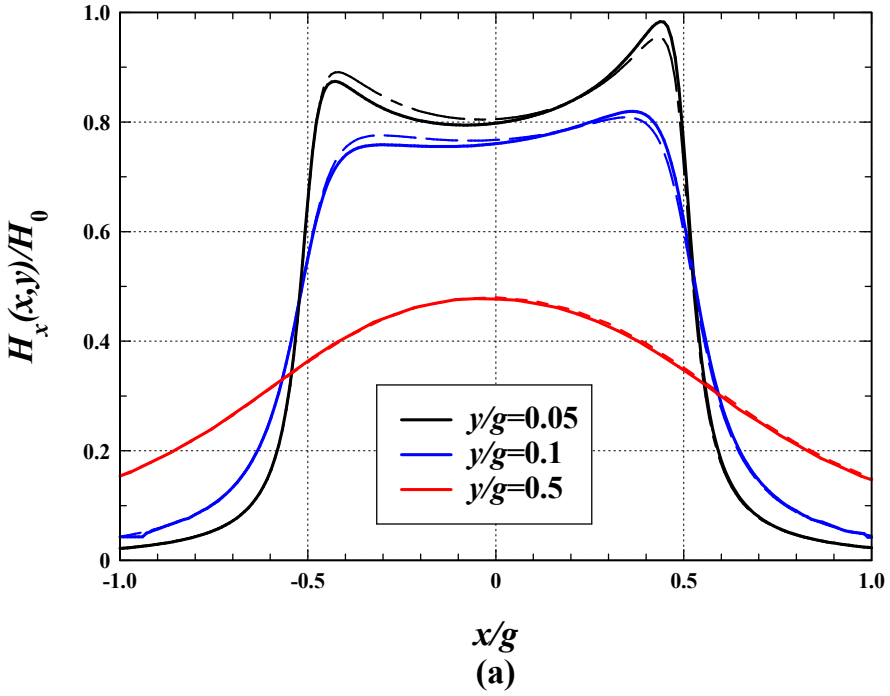

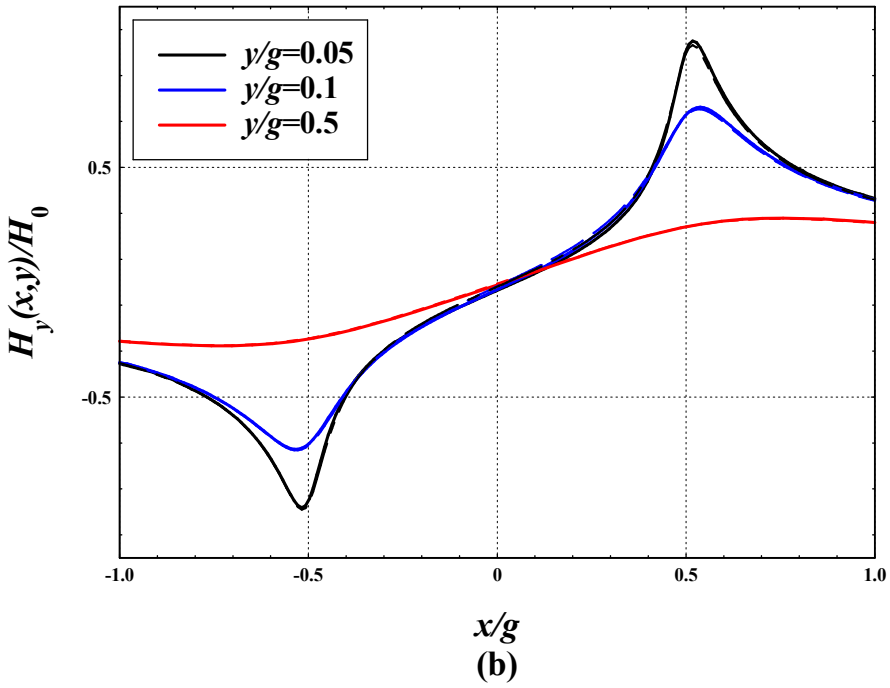

Figure 3.8 (a) Normalised *x*-component (b) *y*-component field distributions for the asymmetrical head for interior corner angle θ_0=5° at *y*/*g*=0.05, 0.1, and 0.5 (calculated using finite-element (solid lines) and using the approximate models in equations (3.48) and (3.51) (dashed lines)).

Table 3.2 RMSD percentages between the superposition of the normalised *x* and *y* components of fields and the finite-element calculations for $\theta_0 = 5^o$

y/g	% RMSD for H_x	% RMSD for H_y
0.05	4.06	1.96
0.1	3.56	2.10
0.5	2.09	1.78

For $\theta_0 = 30°$, the *x* and *y* field components are shown in Figure 3.9 illustrating the continued increase in head field magnitudes near the right corner. The agreement between the approximation (dashed lines) and the finite-element calculations (solid lines) is decreased as shown in Table 3.3, following the increased deviation exhibited in the surface potential with angle illustrated in the previous section. Moreover and following the observations for the previous corner angles, the approximation shows better agreement to the finite-element data for the *y* field component (see Table 3.3).

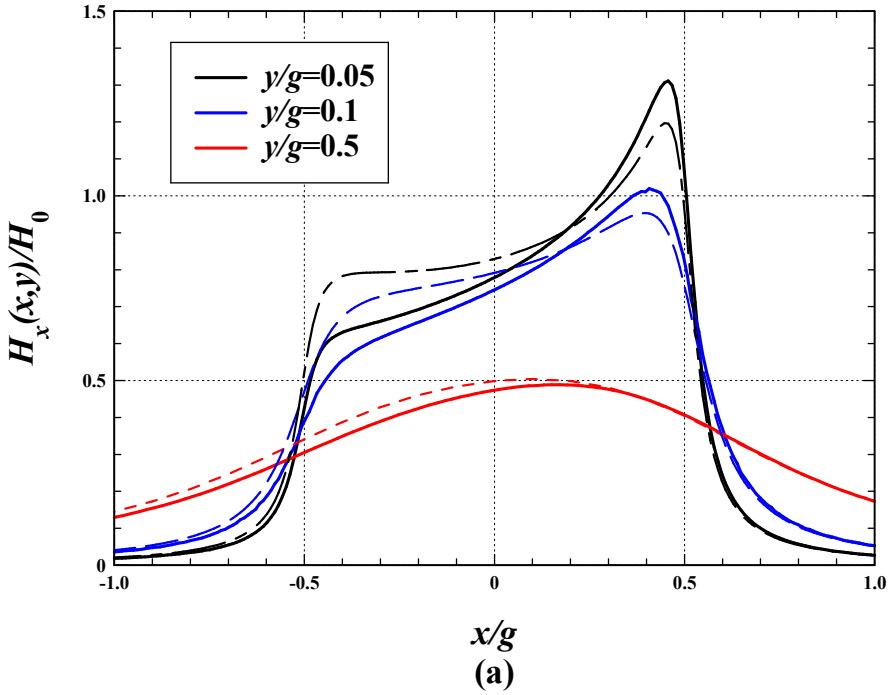

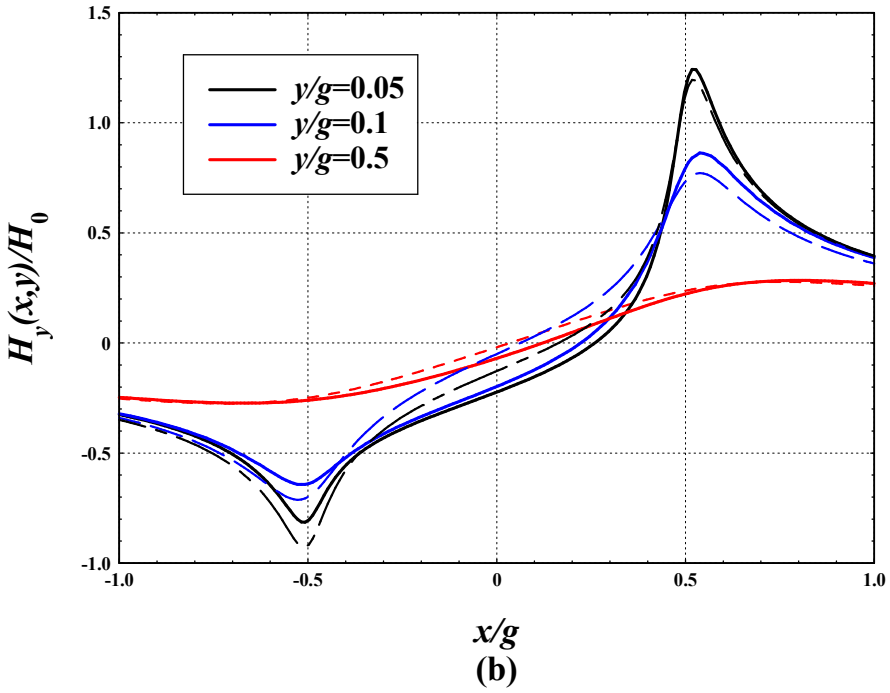

Figure 3.9 (a) Normalised *x*-component (b) *y*-component field distributions for the asymmetrical head for interior corner angle θ_0=30° at *y*/*g*=0.05, 0.1, and 0.5 (calculated using finite-element (solid lines) and using the approximate models in equations (3.48) and (3.51) (dashed lines)).

Table 3.3: RMSD percentages between the superposition of the normalised *x* and *y* components of fields and the finite-element calculations for $\theta_0 = 30^o$

y/g	% RMSD for H_x	% RMSD for H_y
0.05	18.89	11.98
0.1	19.68	13.15
0.5	13.08	11.16

The *x* and *y* field components for $\theta_0 = 45°$ in the asymmetric head at different spacing from the head surface are shown in Figure 3.10. The agreement between the approximations (dashed lines) and the finite-element calculations using COMSOL Multiphysics® (solid lines) is acceptable. The calculated deviation of the approximate *x* and *y* field components is illustrated in Table 3.4 that shows an increasing error between the superposition-based approximation and the FEM calculations. Moreover, and in line with previous calculations at smaller angles, the approximate H_y exhibit less RMSD than H_x. In general, the left corner still shows very good agreement for both the vertical and horizontal components.

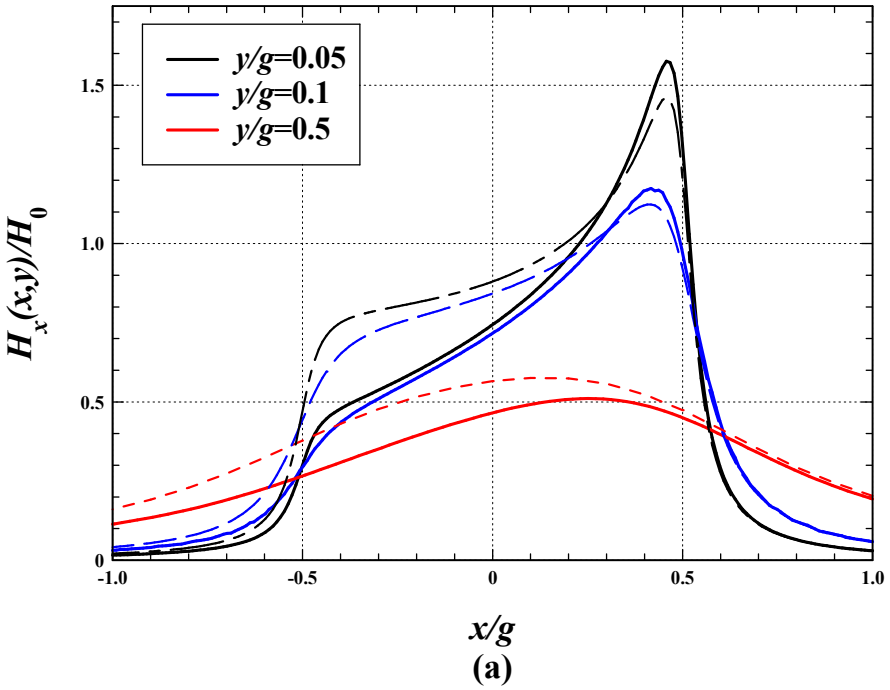

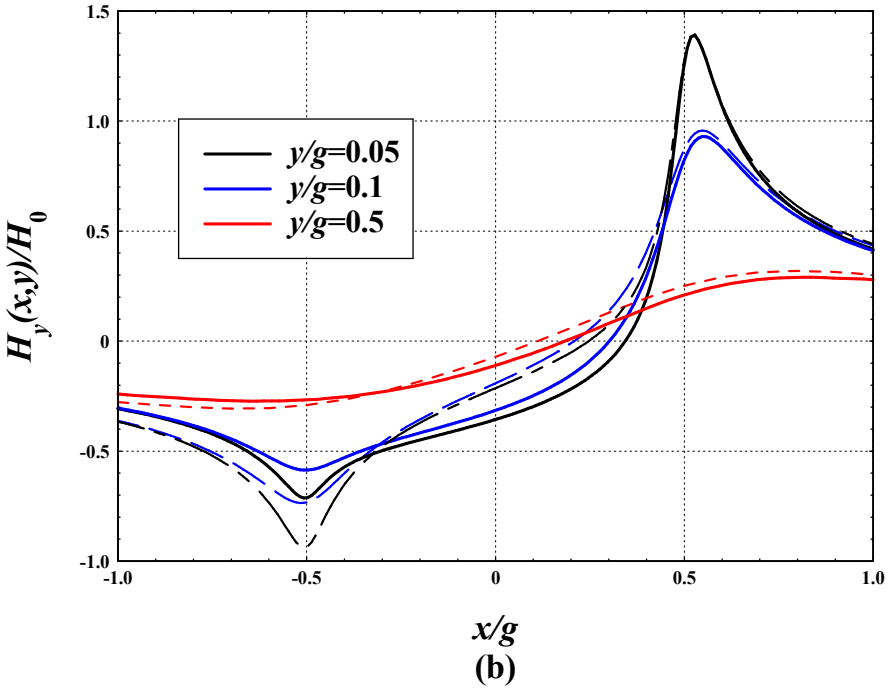

Figure 3.10 (a) Normalised *x*-component (b) *y*-component field distributions for the asymmetrical head for interior corner angle θ_0=45° at *y*/*g*=0.05, 0.1, and 0.5 (calculated using finite-element (solid lines) and using the approximate models in equations (3.48) and (3.51) (dashed lines)).

Table 3.4: RMSD percentages between the superposition of the normalised *x* and *y* components of fields and the finite-element calculations for $\theta_0 = 45^o$

y/g	% RMSD for H_x	% RMSD for H_y
0.05	26.14	19.21
0.1	28.15	21.19
0.5	22.05	18.36

The *x* and *y* field components for $\theta_0 = 60°$ in the asymmetric head at different spacings from the head surface are shown in Figure 3.11, which shows further increases in the field magnitudes near the left corner. The agreement between the approximate model (dashed lines) and the finite-element calculations (solid lines) is still very good at the right corner, while there is more disagreement near the left corner. The calculated deviations of the approximate *x* and *y* field components are listed in Table 3.5, showing percentage deviations approaching 40%.

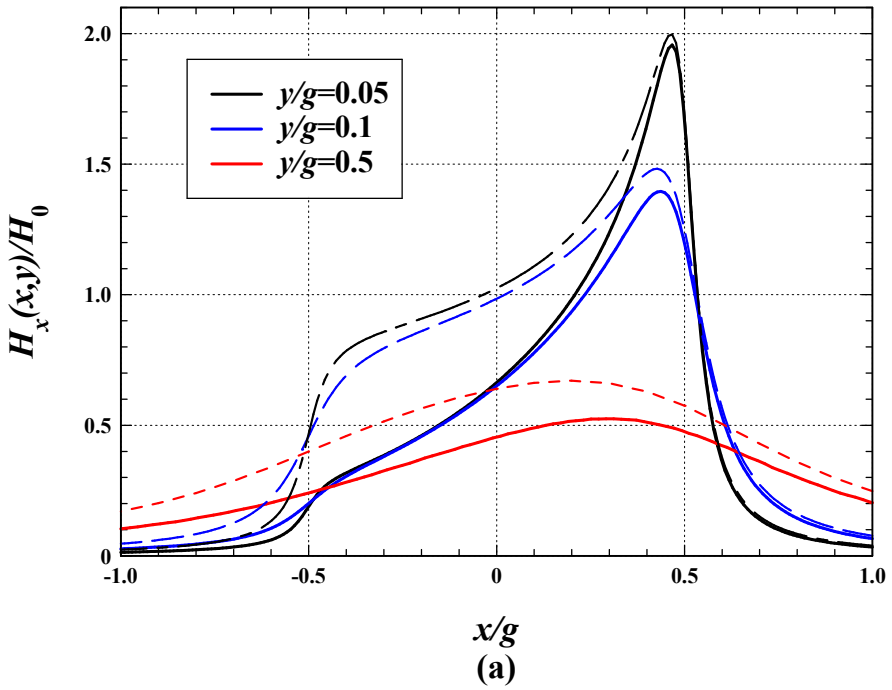

(a)

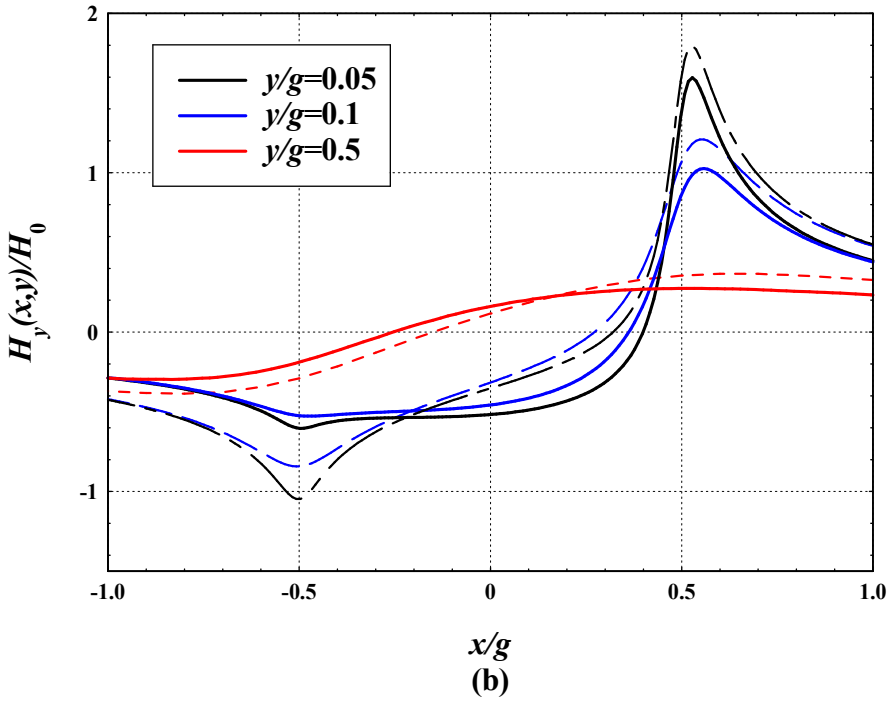

Figure 3.11 (a) Normalised *x*-component (b) *y*-component field distributions for the asymmetrical head for interior corner angle θ_0=60° at *y/g*=0.05, 0.1, and 0.5 (calculated using finite-element (solid lines) and using the approximate models in equations (3.48) and (3.51) (dashed lines)).

Table 3.5: RMSD percentages between the superposition of the normalised *x* and *y* components of fields and the finite-element calculations for θ_0= 60°.

y/g	% RMSD for H_x	% RMSD for H_y
0.05	33.82	29.23
0.1	38.39	33.11
0.5	38.63	30.10

Therefore, the validity of the model will be not considered for θ_0> 45°

Figure 3.12 plots the calculated RMSD between the calculated *x* and *y* field components using the approximations defined in (3.48) and (3.51) and the finite-element calculations as a function of the exterior corner angle θ_0. These plots confirm the increase in the error in the superposition approximation with increasing asymmetry in the head structure

(increasing exterior corner angle), particularly for corner angles $\theta_0 > 30$. As illustrated in the field plots, the largest disagreement between the approximate fields and finite-element calculations is mainly localised near the obtuse head corner.

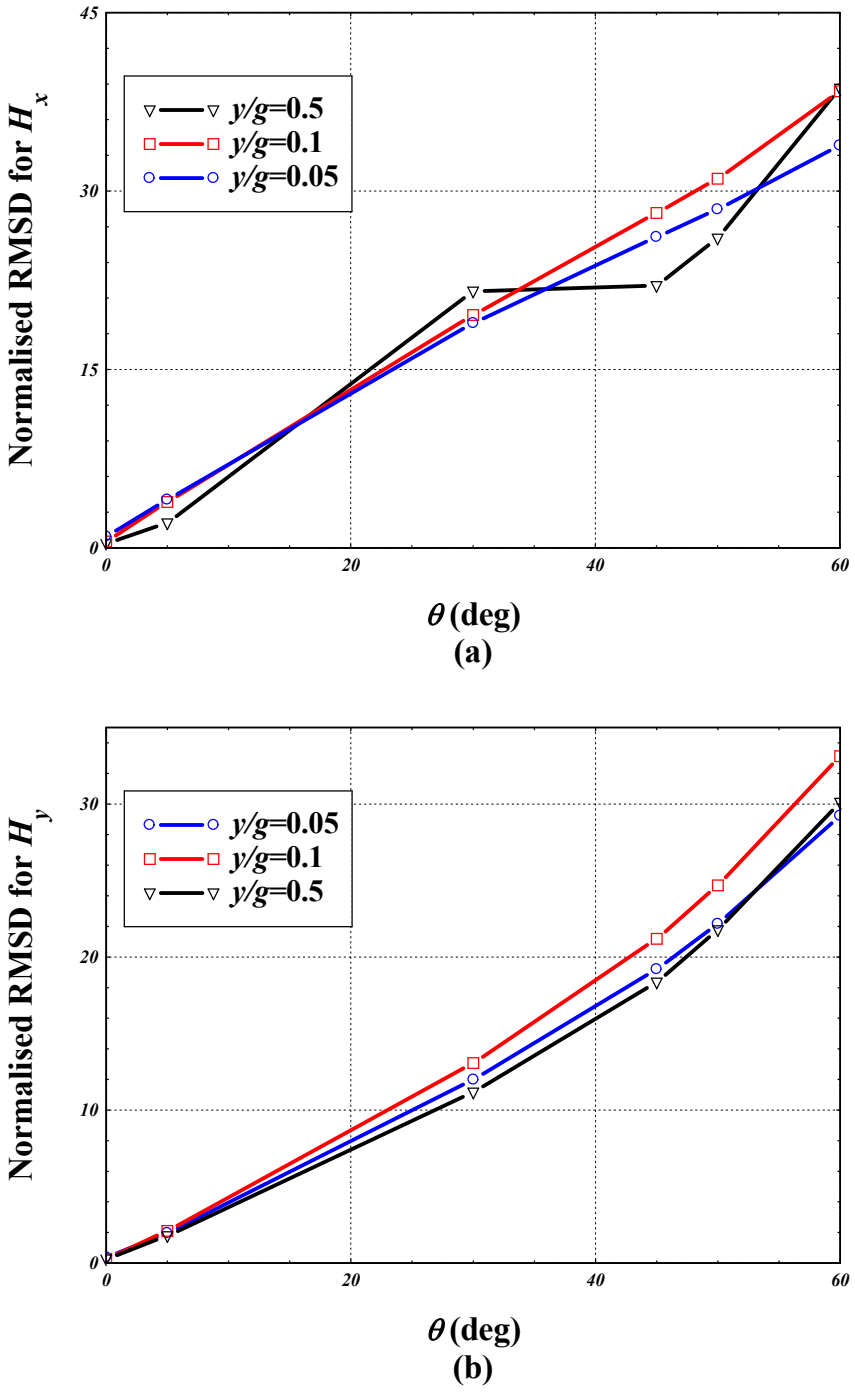

Figure 3.12 The RMSD for (a) *x* component (b) *y* field components distribution between the approximation method calculations and the finite-element calculations.

This may be explained by the increased charge density and concentration near the acute (right) pole corner of the head, which is well described by the single corner model developed in this work. This in turn led to the increase in field magnitudes near that corner and consistent good agreement with the finite-element calculations with continued increase in exterior angle θ_0. On the other hand, the surface charge distribution near the left (obtuse) corner becomes more spread out over the surface with increasing θ_0, which is not captured sufficiently by the existing model which takes account the surface charge contribution up to one gap length from the corner edge. This unequal charge distribution in the superposition model for the asymmetrical head leads to the error observed in the potential and field calculations. This matter will be elaborated on in more detail in the discussion chapter of this thesis.

Chapter 4: Modelling Asymmetric Magnetic Recording Heads with Soft Underlayer Using Superposition

The scalar magnetic potential for a single corner was derived in the previous chapter. Superposition was then applied to add the contribution of the magnetic polarisation of two corners to model the surface potential and magnetic fields of two-dimensional, asymmetrical gapped head structures in the absence of a soft underlayer (SUL). As indicated in chapter 2, the presence of a SUL leads to an increase in the vertical component of the magnetic field, which is exploited mainly in perpendicular recording [53]. For two-dimensional gapped head structures with right-angled corners, the magnetic potentials and fields in the presence of a SUL are modelled mainly by convolving the approximate linear gap surface potential with the appropriate Green's function as indicated in chapter 2 [54]. Exact solutions to Laplace's equation for this problem were derived by Wilton [110] in the form of an infinite Fourier series that required the solution of an infinite system of equations to determine the Fourier coefficients. Implicit conformal mapping solutions were also derived for this geometry [53, 54], which require numerical inversion.

For the asymmetrical gapped head structure with a SUL, only a conformal mapping solution has been derived in literature [55]. Thus there are currently no exact or approximate explicit solutions for the potentials and fields for this asymmetrical geometry with an underlayer. In this chapter the surface potentials or fields for asymmetric heads derived from superposition in chapter are convolved with the Green's function solution of Laplace's equation in the presence of an underlayer (derived in Chapter 2). The error involved in this method of approximation is estimated using the RMS deviation from exact solutions using the finite-element method.

4.1 Magnetic fields using convolution of surface potentials/fields with Green's functions

4.1.1 Mathematical description

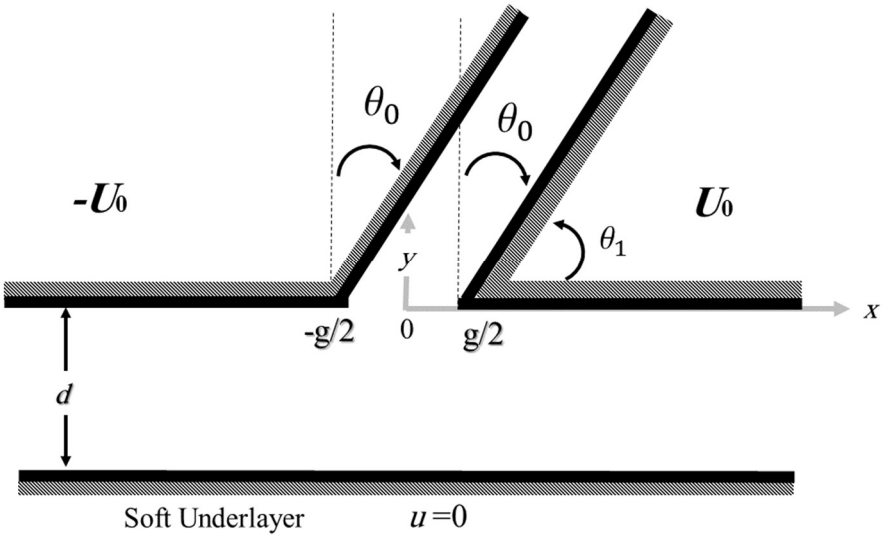

Figure 4.1 Two-dimensional asymmetrical ring head geometry, with gap length *g* and exterior corner inclination angle θ_0 ($\theta_0 = \frac{\pi}{2} - \theta_1$). The poles are assumed to have infinite permeability with potentials $\pm U_0$, at a distance *d* from a soft magnetic underlayer (SUL) held at zero potential.

Figure 4.1 shows an asymmetrical head with underlayer where the pole pieces are assumed to be infinitely permeable with constant potentials $\pm U_0$ separated by a semi-infinite gap of width *g* at a distance *d* from an infinite permeability underlayer held at zero potential. The magnetic potential satisfies Laplace's equation in the exterior region to the poles and the infinitely permeable underlayer.

From Figure 4.1, the potential between the head and underlayer is subject to the following boundary conditions:

$$u = -U_0 \text{ for } x \leq -g/2, \text{ at } y=0 \tag{4.1}$$

$$u = U_0 \text{ for } x \geq g/2, \text{ at } y=0 \tag{4.2}$$

$$u = 0 \text{ at } y = d \tag{4.3}$$

As shown in chapter 2, the general solution to Laplace's equation for the magnetic potential when the potential is known along the head surface is given by [57]:

$$u^r(x,y) = \frac{1}{2d}\sin(\frac{\pi y}{d}) \int_{-\infty}^{\infty} \frac{u(\acute{x},0)}{\cosh\left(\frac{(\acute{x}-x)\pi}{d}\right) - \cos\left(\frac{\pi y}{d}\right)}\, d\acute{x} \tag{4.4}$$

for $0<y<d$. The surface potential $u(\acute{x},0)$ in (4.6) for asymmetrical heads with underlayer is not known theoretically or experimentally in literature, so the surface potential in the absence of the SUL is normally used instead. The corresponding two-dimensional field components are then obtained from the gradient of the potential:

$$H_x^r(x,y) = \frac{-\partial u}{\partial x} = \\ = \frac{-\sin(\pi y/d)}{2d} \int_{x'=-\infty}^{\infty} \frac{H_x^r(x',0)}{\cos(\pi y/d) - \cosh(\pi(x'-x)/d)} dx' \tag{4.5}$$

$$H_y^r(x,y) = \frac{-\partial u}{\partial y}$$

$$= \frac{1}{2d} \int_{x'=-\infty}^{\infty} \frac{H_x^r(x',0)\sinh(\pi(x'-x)/d)}{\cos(\pi y/d) - \cosh(\pi(x'-x)/d)} dx' \tag{4.6}$$

As discussed in chapter 2, it is normally easier to work with the magnetic fields using equations (4.5) and (4.6) since the integrals are only evaluated over the gap length (the surface fields are zero over the head poles). Nevertheless, equations (4.5) and (4.6) can only be integrated exactly for limited functional descriptions of the surface potential/field; in particular the case of linear gap potential (or constant surface field) allows the derivation of an exact solution for the magnetic fields between the head surface and SUL. Otherwise it is not possible to evaluate these integrals analytically.

The effect of the infinite permeability, zero potential underlayer is to produce an image of the magnetic head with equal but opposite magnetic surface charge/scalar potential that is placed at a distance $2d$ from the original head surface as illustrated in Figure 4.1. Thus the magnetic scalar potential or field between the original head surface and underlayer (i.e. $0 < y < d$) may be determined from the algebraic sum (superposition) of the magnetic potentials or fields from the original head (without an underlayer) and its image. This superposition process must also take into account the infinite number of images created in turn by the surfaces of the head and its image placed at multiples of $2d$. The contribution of the infinite set of images is already taken into account in the Green's function formulation in (4.5) and (4.6). This can be illustrated by writing the Green's functions in the form of infinite series using [108]:

$$\frac{1}{2d}\frac{\sin(\pi y/d)}{\cosh(\pi\bar{x}/d)-\cos(\pi y/d)}=\frac{1}{\pi}\sum_{n=-\infty}^{+\infty}\frac{(y+2nd)}{(y+2nd)^2+\bar{x}^2} \tag{4.7}$$

$$\frac{1}{2d}\frac{\sinh(\pi\bar{x}/d)}{\cosh(\pi\bar{x}/d)-\cos(\pi y/d)}=\frac{1}{\pi}\sum_{n=-\infty}^{+\infty}\frac{\bar{x}}{(y+2nd)^2+\bar{x}^2} \tag{4.8}$$

where $\bar{x}=x'-x$. Thus the head magnetic fields in the presence of a SUL can be written as the superposition of multiple images from heads without a SUL as (following equations (3.48) and (3.51) in chapter 2:

$$H_x^{SUL}(x,y)=-\sum_{n=-\infty}^{+\infty}H_x(x,y+2nd) \tag{4.9}$$

$$H_y^{SUL}(x,y)=\sum_{n=-\infty}^{+\infty}H_y(x,y+2nd) \tag{4.10}$$

Equations (4.9) and (4.10) can thus be used to determine the head magnetic fields in the presence of a SUL if the magnetic fields without an underlayer are available analytically or numerically. However the accuracy of this approach is limited by the accuracy of the analytical expression or numerical values of the magnetic fields H_x and H_y. Moreover, large number of images must be evaluated in the above summation when the head-to-underlayer separation is reduced (when $d/g < 0.5$ approximately). As a result, it would be more accurate to use the convolution integrals in (4.5) and (4.6), which account for an

infinite set of image fields, to evaluate the magnetic fields in the presence of an underlayer numerically with little numerical overhead using the Matlab's '*quadgk*' function (adaptive Gauss-Kronrod quadrature).

It is also important to note that equations (4.4) - (4.6) describe an infinite set of field reflections between two parallel surfaces [54]; one at $y = d$ (underlayer) and the other at $y = 0$ with a prescribed surface potential/field. Thus these expressions and the corresponding potentials and fields do not take into account the presence of a gap and the reaction of the underlayer on modifying the gap surface potential. As a result, the derived solutions using the surface potentials/fields in absence of a SUL used in equations (4.4) - (4.6) are expected to be accurate for only increasing separations between the head surface and underlayer (approximately $d/g > 0.5$ as will be shown in chapter 5). In Chapter 5, a new general method based on the sine integral transform is derived that allows to model the reaction of a SUL on the surface potential of any head structure, thus providing sufficient accuracy for closer head-to-underlayer separations $d/g < 0.5$.

The x and y field components are calculated next using the surface field of the asymmetrical head derived using superposition in (3.40), to estimate the error in the approximate calculations and as functions of the head-to-underlayer parameters.

4.2 Results

In the following, the calculated magnetic fields using equations (4.5) and (4.6) (dashed lines) are normalised by the deep gap field for the right angled head ($H_0 = 2U_0/g$) and the

integrations are carried out using the Matlab quaderature function *quadgk*. The calculated fields are compared with finite-element solutions (solid lines) of Laplace's equation for the same head geometry in Comsol Multiphysics.

For the right angled head with $\theta_0 = 0°$, the x and y field components at a spacing $y/g = 0.1$ from the head surface and for three different head-to-underlayer distances are shown in Figure 4.2. This figure shows that the fields are symmetrical with very good agreement between the theoretical, superposition-based calculations (dashed lines), and the finite-element solution. This figure also shows that the error in the theoretical approximations reduces with increasing $d/g > 0.5$. Table 4.1 shows the RMSD between the superposition of the normalised x and y field components and the finite-element calculations for $\theta_0 = 0^o$. This table also shows that the y field component in the approximation agrees more to the finite-element data.

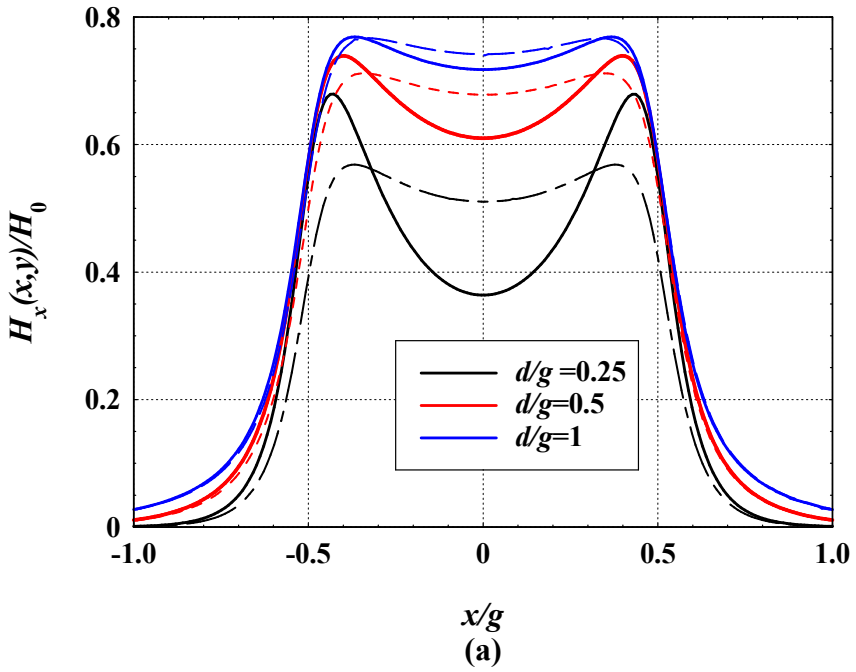

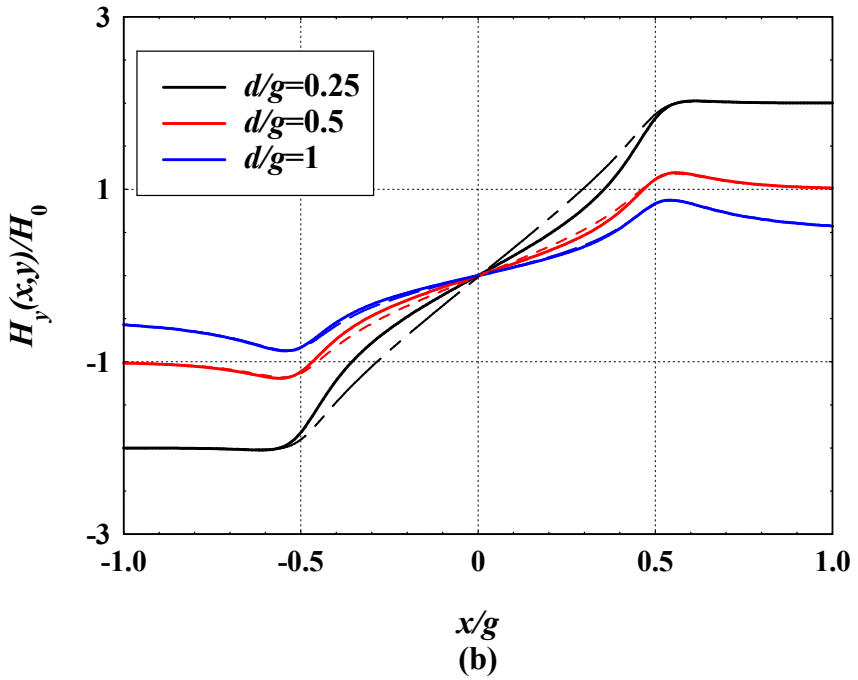

Figure 4.2 (a) Normalised *x* field component, and (b) *y* field component for the asymmetrical head in the presence of a SUL for inclination angle θ_0=0°, calculated at a distance *y/d* = 0.1 from the head surface. Solid lines are the finite-element calculations, and the dashed lines are from the approximate theoretical model in (4.5) and (4.6).

Table 4.1 Percentage RMSD between the normalised theoretical and exact (finite-element) *x* and *y* field components and the finite-element calculations for θ_0= 0°

	% RMSD for H_x	% RMSD for H_y
***d/g*=1**	1.78	2.71
***d/g*=0.5**	5.05	6.15
***d/g*=0.25**	12.38	11.64

For θ_0= 30°, the *x* and *y* field components are shown in Figure 4.3 illustrating the continued increase in head field magnitudes near the right (acute) corner due to increased charge density near that corner. This figure also illustrates the increased deviation between the theoretical fields (dashed lines) and exact fields calculated using finite-

elements (solid lines). This increase in RMSD with increasing θ_0 is shown in Table 4.2 and in line with the increase in error in the surface potential approximation without a SUL (based on superposition) with increasing corner exterior angle for asymmetrical heads (see Chapter 3). Moreover and following the observations for the previous corner angles, the approximation shows better agreement to the finite-element data for the y field component (see Table 4.2).

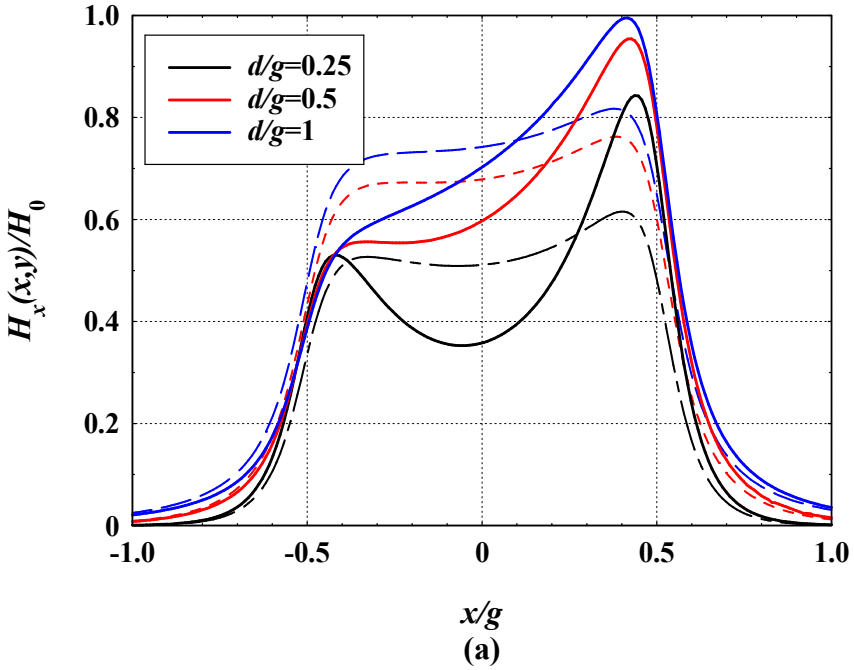

(a)

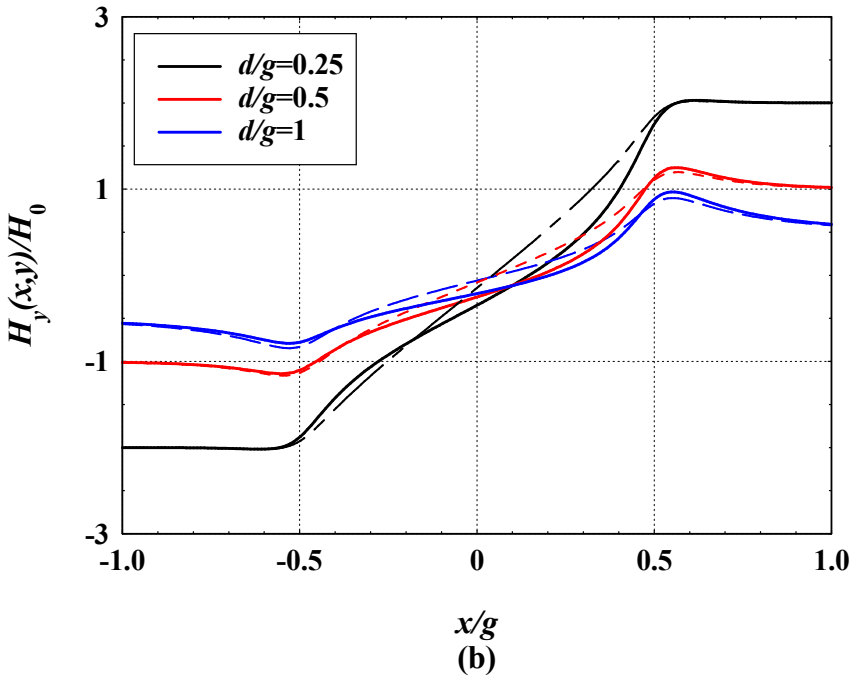

Figure 4.3 (a) Normalised *x* field component, and (b) *y* field component for the asymmetrical head in the presence of a SUL for inclination angle θ_0=30°, calculated at a distance *y/d* = 0.1 from the head surface. Solid lines are the finite-element calculations, and the dashed lines are from the approximate theoretical model in (4.5) and (4.6).

Table 4.2 Percentage RMSD between the normalised theoretical and exact (finite-element) *x* and *y* field components and the finite-element calculations for θ_0= 30°

	% RMSD for H_x	% RMSD for H_y
***d/g*=1**	8.03	4.74
***d/g*=0.5**	8.19	8.54
***d/g*=0.25**	17.69	13.63

The *x* and *y* field components for θ_0= 45° in the asymmetric head with an underlayer are shown in Figure 4.4. The agreement between the approximations (dashed lines) and the finite-element calculations (solid lines) continues to decrease as expected following the error in the surface potential approximation using superposition. The calculated

deviations of the approximate x and y field components is illustrated in Table 4.3 that shows the increasing RMSD between the superposition-based approximation and the FEM calculations. Moreover and in line with previous calculations at smaller angles, the approximate H_y exhibit less RMSD than H_x.

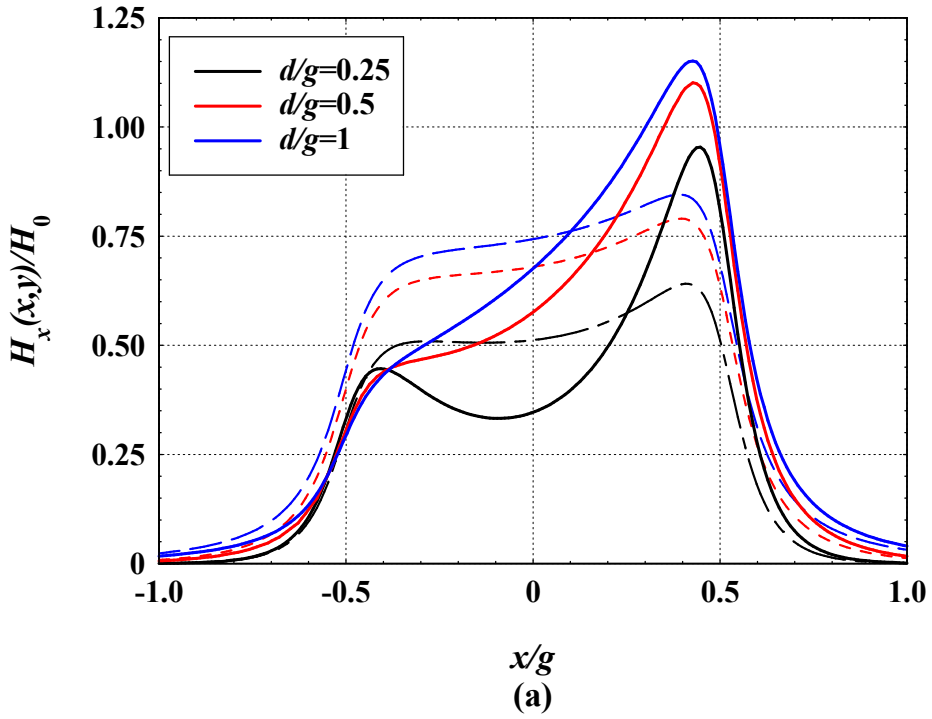

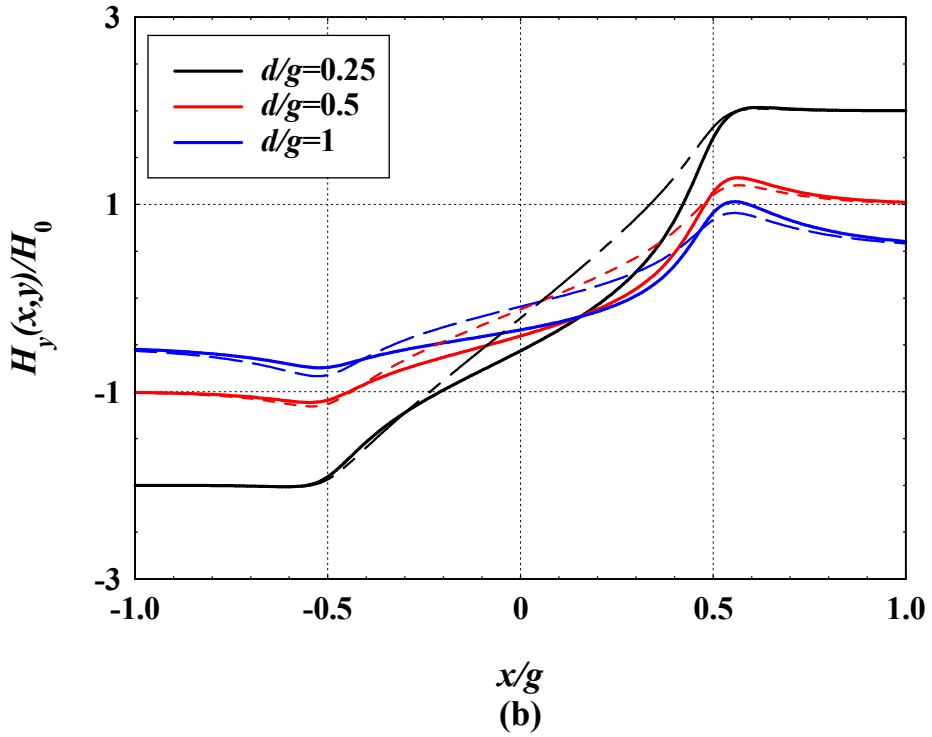

Figure 4.4 (a) Normalised *x* field components, and (b) *y* field components for the asymmetrical head in the presence of a SUL for inclination angle θ_0=45°, calculated at a distance *y/d* = 0.1 from the head surface. Solid lines are the finite-element calculations, and the dashed lines are from the approximate theoretical model in (4.5) and (4.6).

Table 4.3 Percentage RMSD between the normalised theoretical and exact (finite-element) *x* and *y* field components and the finite-element calculations for θ_0= 45°

	% RMSD for H_x	% RMSD for H_y
***d/g*=1**	11.09	5.51
***d/g*=0.5**	19.74	9.76
***d/g*=0.25**	22.39	15.32

The *x* and *y* field components for θ_0= 60° in the asymmetric head when the soft underlayer is present and located at three different spacings *d*/*g*= 0.25, 0.5 and 1 are shown in Figure 4.5, which illustrates further deviation between the approximate solutions (dashed lines)

and exact finite-element calculations (solid lines). The calculated deviations of the approximate x and y field components are listed in Table 4.4, showing percentage deviations approaching 30%for H_x and about 22% for H_y.

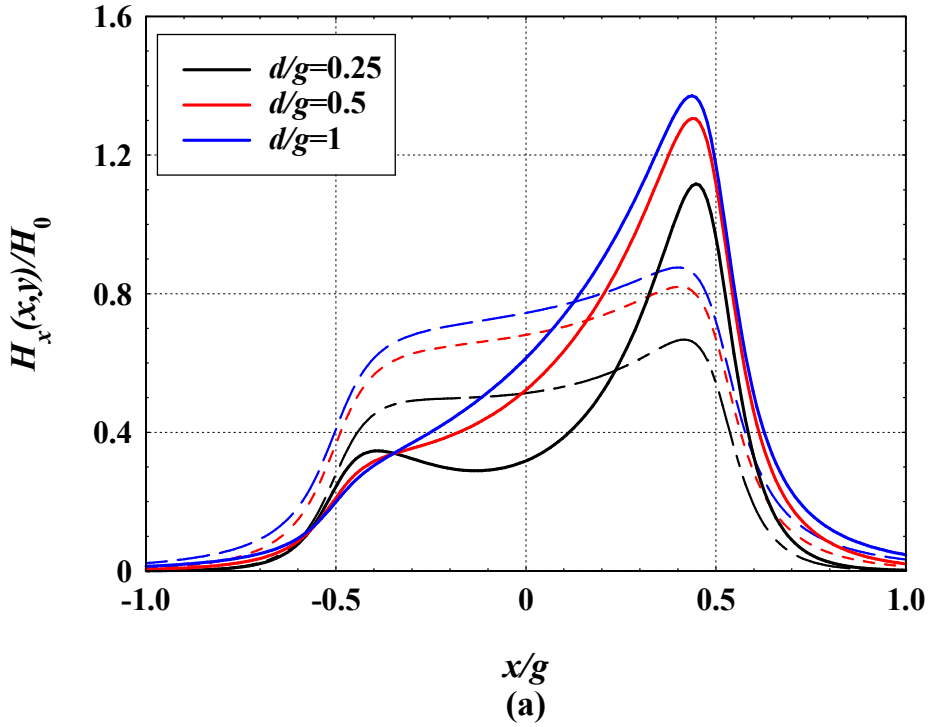

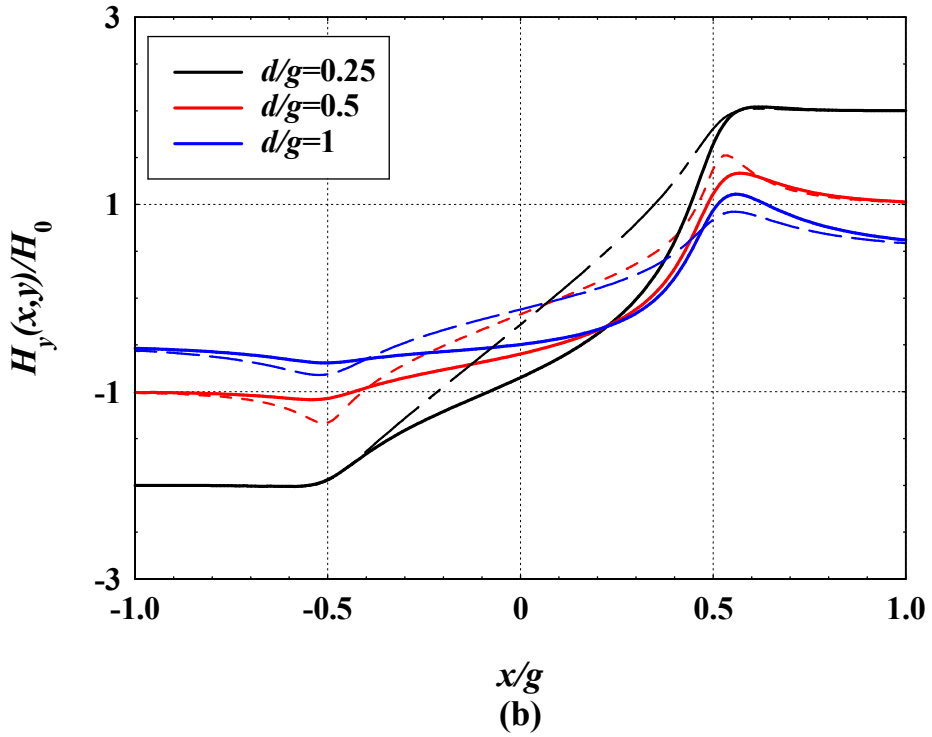

Figure 4.5 (a) Normalised *x* field components, and (b) *y* field components for the asymmetrical head in the presence of a SUL for inclination angle θ_0=60°, calculated at a distance *y/d* = 0.1 from the head surface. Solid lines are the finite-element calculations, and the dashed lines are from the approximate theoretical model in (4.5) and (4.6).

Table 4.4 Percentage RMSD between the normalised theoretical and exact (finite-element) *x* and *y* field components and the finite-element calculations for θ_0= 60°

	% RMSD for H_x	% RMSD for H_y
***d/g*=1**	13.94	10.07
***d/g*=0.5**	17.47	12.47
***d/g*=0.25**	32.99	22.96

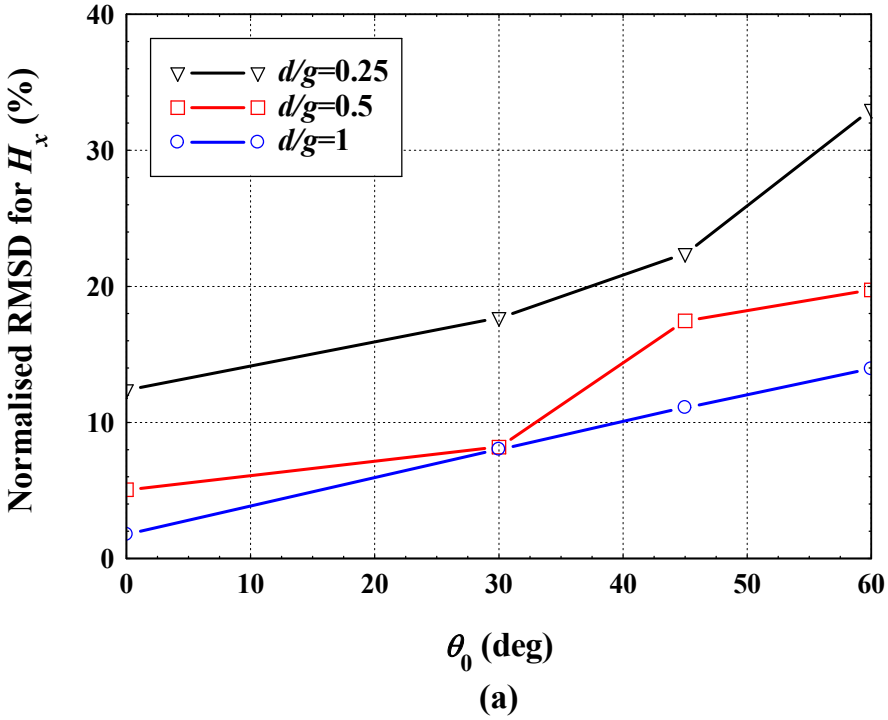

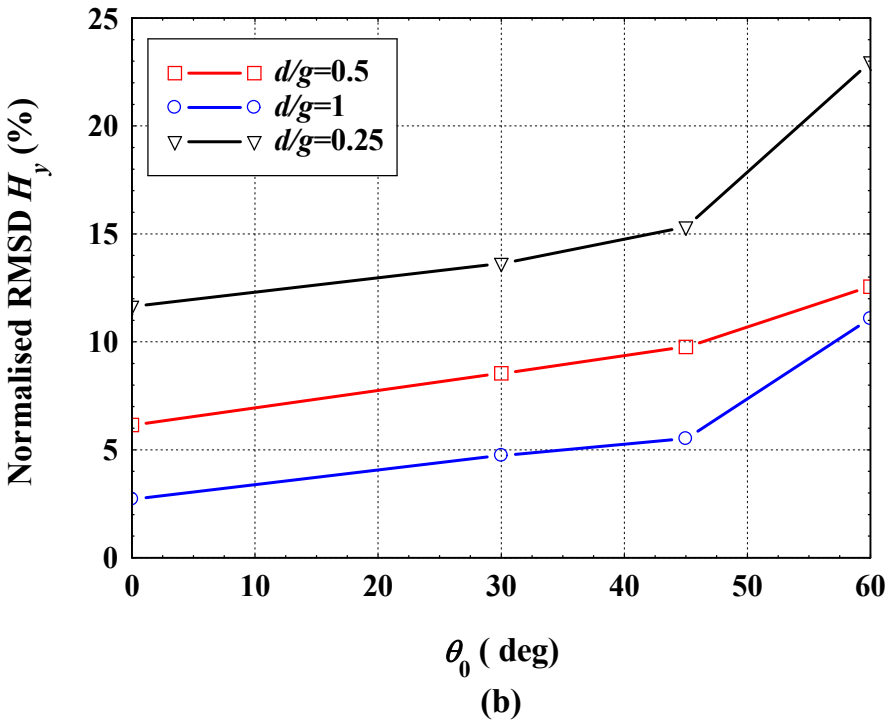

Figure 4.6 The RMSD for field (a) *x*-components (b) *y*-components between the approximation method calculations and the finite-element calculations at *y*/*g*=0.1 for head-to-underlayer distances *d*/*g*=0.25, 0.5, and 1.

The RMSD or error in the approximate field calculations as functions of the corner angle is summarised in Figure 4.6. This figure along with the field plots in Figures 4.2 - 4.5 illustrate the increased error in the approximation with increasing corner angle. The discrepancy between approximate field and finite-element calculations in the gap region is caused by using the surface field approximation (based on superposition) for the head without underlayer. Figure 4.5 also illustrates the reduction in the error of the approximation for increased head-to-underlayer separations $d/g > 0.5$. More generally, figure 4.5 shows that there is less error in the vertical field approximation H_y compared to the horizontal field component H_x.

Chapter 5: Magnetic Potential and Fields of 2D Asymmetrical Magnetic Recording Heads Based on Fitting to Finite-Element Calculations

5.1 Introduction

In deriving the magnetic potential and fields of two-dimensional asymmetrical magnetic recording heads in chapters 3 and 4, the method of superposition of single corner potentials and fields was utilised. This superposition-based approach provided a plausible analytical model of the scalar magnetic surface potential of asymmetrical heads, but its accuracy degrades with reducing the interior gap corner angle of the head. This limits the applicability of the superposition based model to asymmetrical heads with modest degree of asymmetry. In this chapter, a detailed and comprehensive investigation is carried out on another method of modelling the magnetic scalar potential and fields from asymmetrical heads with and without a soft magnetic underlayer (SUL) for any exterior corner inclination angle θ (0° to 90°).

The method adopted for the derivation here assumes a plausible rational function approximation for the surface potential in the gap region with adjustable coefficients that are determined from fitting to finite-element numerical solutions of Laplace's equation for the asymmetrical head, following the approach of Szczech *et. al.* [111]. This simplified rational function approximation is then convolved with the appropriate Green's functions to determine the potential and fields everywhere beyond the head surface.

In the presence of a SUL, a new general and approximate theory, based on the integral transform method, is derived for any two-dimensional head structure to approximate the reaction of the high permeability underlayer on the known head surface potential in the absence of the underlayer. This modified surface potential is then convolved with the two-dimensional Green's function for the head/underlayer combination to determine the fields everywhere beyond the head surface. The Fourier transform of the asymmetrical head surface field, in the presence and absence of a SUL, is also derived exactly to study the effect of corner angle inclination on the wavelength response of asymmetrical heads.

The developed analytical expressions for the surface potential and fields are general and can be easily combined through superposition to derive the fields of more complex asymmetrical head structures (such as shielded single-pole heads) with multiple gaps, and incorporated into studies and simulations of the recording and readout processes without much processing overhead.

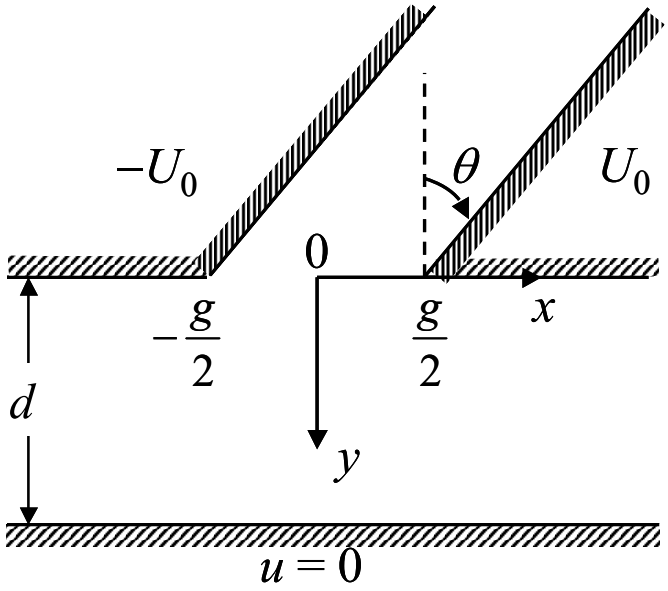

Figure 5.1 Two-dimensional geometry of the asymmetrical head, with gap length *g* and exterior corner inclination angle θ. The poles are assumed to have infinite permeability with potentials $\pm U_0$, at a distance *d* from a soft magnetic underlayer (SUL) held at zero potential. To model two-dimensional heads without an underlayer, the SUL is removed with $d \to \infty$.

This chapter will begin with the derivation of the rational function approximation for the surface potential for two-dimensional asymmetrical heads in the absence of a SUL. The surface potential is then used along with the two-dimensional Green's functions derived in chapter 2 to arrive at expressions for the magnetic fields beyond the head surface. The Fourier transform of the surface fields is derived to explore the effect of asymmetry on the wavelength content of the fields. The translated sine transform is later defined and applied to derive an expression describing the reaction of an underlayer on any general, functional description of a surface potential in the absence of an underlayer, and then applied to the asymmetrical head to predict the potential and fields. Finally, the Fourier transform of the surface fields in the presence of an underlayer is derived to explore the effect of asymmetry on the wavelength content of the fields. The validity of the

approximate magnetic potential and field models, their limitations and improvements are discussed in the relevant sections of the chapter.

5.2 Surface potential, and magnetic fields for asymmetrical magnetic recording heads without underlayer

5.2.1 Surface potential approximations

In this section an approximate expression is derived for the surface magnetic potential for asymmetrical heads without a SUL. This will be later convolved with the Green's function for the magnetic head geometry to determine the fields everywhere beyond the head surface.

The gap surface potential for an asymmetrical head calculated using finite-elements is shown Figure 5.2 for a number of exterior corner angles θ. For right-angled corners (θ = 0°), the gap potential is symmetrical with increasing gradient (and therefore fields) near the gap corners at $\pm g/2$ [106]. Increasing θ increases the asymmetry in the potential due to the increased magnetic surface charge density in the acute corner at $x = g/2$, and shifts the zero-crossing of the potential towards this corner. This displacement of the potential zero-crossing leads to a reduction in the effective gap length of the head. In the limit where $\theta \rightarrow 90°$, the effective gap length reduces to zero towards the right corner with a step change in the surface potential at $x = g/2$, leading to the narrow gap or far field potential distribution [54].

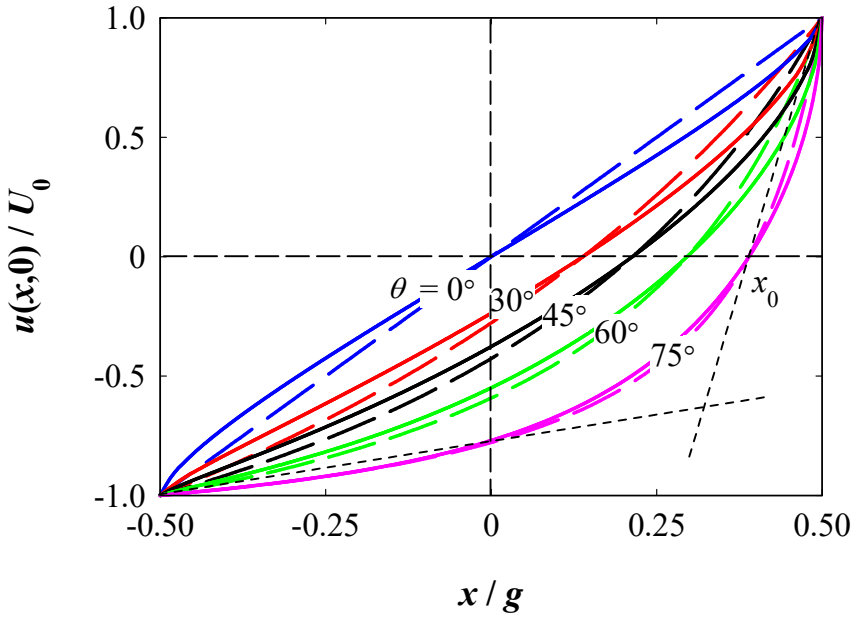

Figure 5.2 Calculated gap surface potential using finite-elements (solid lines) and the approximate surface potential in (5.2) and (5.3) (dashed lines) for different corner angles. The dotted straight lines highlight the approximate hyperbolic locus of the asymmetrical potential, and were used as guides to derive the rational function approximation for the potential.

The surface gap potential determined by finite-elements in Figure 5.2 may be characterised by both: (i) a shift in the zero-crossing, x_0, of the potential, and (ii) scaling of the potential magnitude and gradient near the origin, with changes in exterior corner angle θ. This surface gap potential approximately traces a hyperbola joining the two intersecting straight dashed lines indicated in Figure 5.2 (shown for $\theta = 75°$ as an example). Thus, the gap surface potential may be described using the following rational function:

$$u(x,0) = a + \frac{b}{c + x} \tag{5.1}$$

The constants a, b and c were determined by requiring that the potential satisfies the conditions $u = \pm U_0$ at $x = \pm g/2$, and that the potential vanishes at $x = x_0$ where x_0 is a function of θ. This yields the following approximate surface potential:

$$u(x,0) = \begin{cases} -U_0 & x < -g/2 \\ \dfrac{g}{2}\dfrac{U_0(x - x_0)}{(g^2/4 - x_0 x)} & -g/2 \le x \le g/2 \\ U_0 & x > g/2 \end{cases} \qquad (5.2)$$

The potential in (5.2) is continuous and differentiable over the gap length, therefore satisfying the continuity requirement of the potential and fields in the gap. When $\theta = 0°$(and $x_0 = 0$) the head is symmetrical, and the gap potential in (5.2) reduces to the linear (Karlqvist) approximation [57]. As $\theta \rightarrow 90°$ (and $x_0 = g/2$), equation (5.2) produces a step function change in the potential along the head surface at $x = g/2$ to model the narrow gap head.

The dependence of the shift in the zero-crossing of the gap potential, x_0, on corner angle θ was determined from the finite-element calculations and is shown in Figure5.3 (open circles). The tangent function was found to provide the best least-squares fit to this dependence using the following fitting parameters:

$$\frac{x_0}{g} = 0.564 \tan(0.462\theta) \quad 0 \le x_0 \le g/2, \qquad 0 \le \theta \le \pi/2 \qquad (5.3)$$

Equation (5.3) is illustrated in Figure5.3 (solid line) with a very small absolute RMS deviation of 3.71×10^{-4} from the finite-element data. Therefore (5.3) will be used subsequently in this analysis for the determination of x_0 for a given corner angle θ.

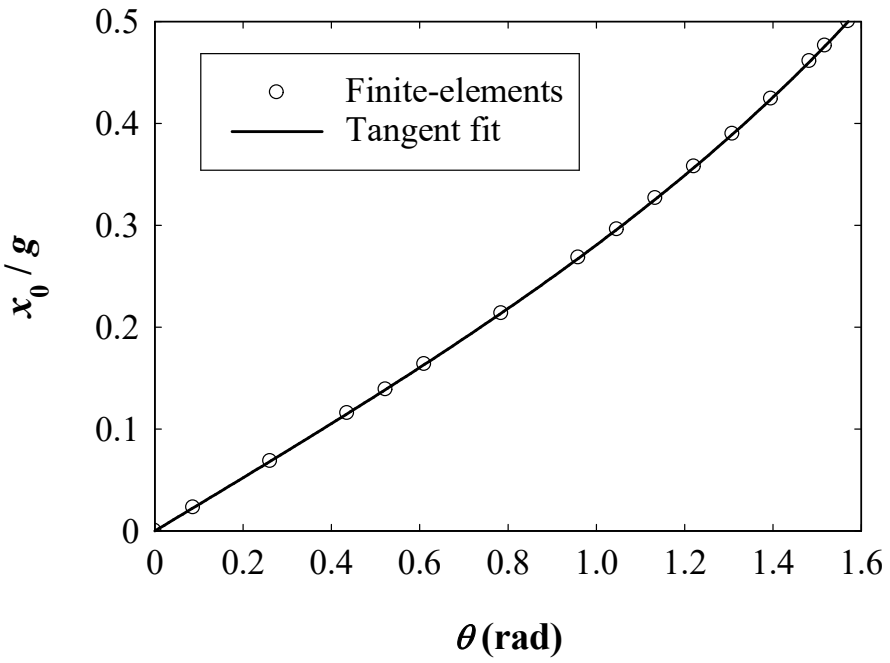

Figure 5.3 Dependence of the zero-crossing shift of the gap potential, x_0, on the corner angle θ, determined from the finite-element solution of Laplace's equation (circles). The solid line shows the least-squares fitting to the finite-element data using the tangent function with best fit parameters: $x_0/g = 0.564 \tan(0.462\theta)$.

The approximate surface gap potential in (5.2) is plotted in Figure 5.2 (dashed lines) using the calculated values of x_0 from (5.3), showing good agreement with the finite-element potential for different values of θ. Figure 5.4 shows the RMSD between the approximate potential and finite-element calculations, normalised by the maximum change in the gap potential ($2U_0$), as a function of exterior corner angle. For small θ, the RMSD is 3.3% which is consistent with the error in the Karlqvist approximation for symmetrical heads.

The RMSD reduces (and therefore accuracy increases) with increasing θ and correctly vanishes as $\theta \to 90°$ (narrow gap limit). Another advantage of the surface potential approximation in (5.2) is that it enables the derivation of exact, and relatively simple, closed-form solutions for the potential and fields everywhere beyond the head surface as illustrated later in this chapter.

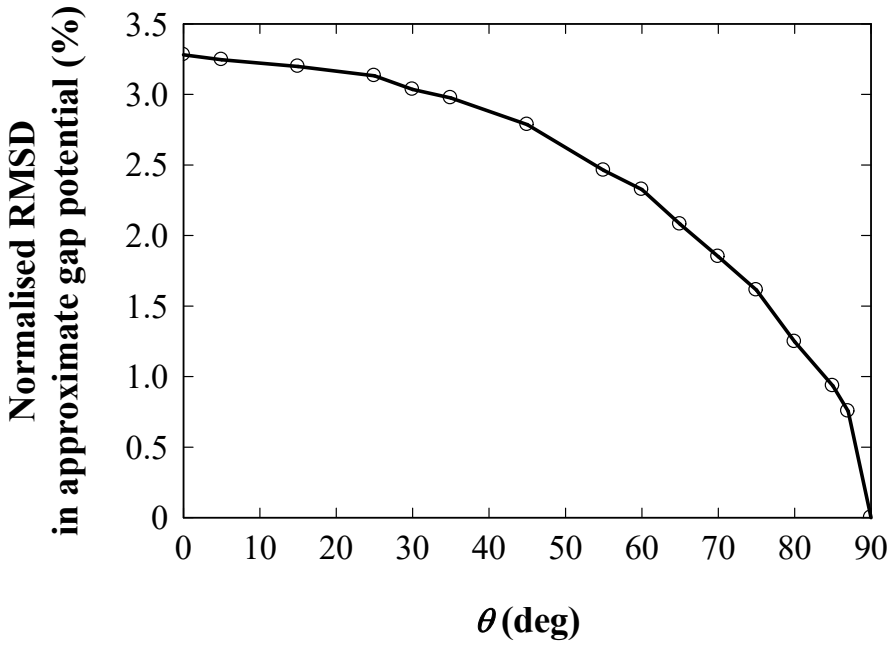

Figure 5.4 The RMSD between the approximate gap potential in (5.2) and the finite-element calculations, normalised by maximum change of potential in the gap ($2U_0$), as a function of the exterior corner angle θ. This plot shows the increase in accuracy of the rational function approximation for the surface potential with increasing θ.

5.2.2 Head magnetic fields

The magnetic surface potentials derived in the previous section will now be convolved with the Green's function for the asymmetrical head to determine the potential and fields everywhere beyond the head surface. Determining the magnetic fields directly using the surface fields rather than potentials, however, is easier mathematically as previously indicated with the convolution integrals evaluated only over the gap region (since the surface fields vanish over the infinitely permeable poles). This is the approach adopted in this section. Extensive use will be made of the Fourier transform, its inverse and the Green's functions solutions of Laplace's equation defined and derived in Chapter 2.

For the asymmetrical head considered in this work, the magnetic field along the head surface is determined from the gradient of the surface potential in (5.2) which is given by:

$$H_x(x,0) = \frac{-\partial u(x,0)}{\partial x} = \frac{-gU_0}{2}\frac{(g^2/4 - x_0^2)}{(g^2/4 - x_0 x)^2} \tag{5.4}$$

Substituting (5.4) into (2.41), and integrating over the gap length yields exactly the *x*-component of the magnetic field everywhere beyond the head surface as:

$$
\begin{aligned}
H_x(x,y) = \frac{-g^2 H_0}{4\pi}\Bigg\{ & \frac{x_0^2 y}{g/4\left((g^2/4 - x_0 x)^2 + x_0^2 y^2\right)} \\
& + \frac{\left(g^2/4 - x_0^2\right)}{\left(\left(g^2/4 - x_0 x\right)^2 + x_0^2 y^2\right)^2} \\
& \times \Bigg[h_x^k(x,y)\left(\left(g^2/4 - x_0 x\right)^2 - x_0^2 y^2\right) \\
& + x_0 y\left(g^2/4 - x_0 x\right)\left[h_y^k(x,y) + \ln\left(\frac{(g/2 + x_0)^2}{(g/2 - x_0)^2}\right)\right]\Bigg]\Bigg\}
\end{aligned}
\tag{5.5}
$$

while substituting (5.4) into (3.42) yields exactly the *y*-component of the magnetic field as:

$$
\begin{aligned}
H_y(x,y) = \frac{-g^2 H_0}{2\pi}\Bigg\{ & \frac{-x_0\left(g^2/4 - x_0 x\right)}{g/2\left((g^2/4 - x_0 x)^2 + x_0^2 y^2\right)} \\
& + \frac{\left(g^2/4 - x_0^2\right)}{\left(\left(g^2/4 - x_0 x\right)^2 + x_0^2 y^2\right)^2} \\
& \times \Bigg[x_0 y\left(g^2/4 - x_0 x\right) h_x^k(x,y) - \frac{1}{4}\left(\left(g^2/4 - x_0 x\right) - x_0^2 y^2\right) \\
& \times \left[h_y^k(x,y) + \ln\left(\frac{(g/2 + x_0)^2}{(g/2 - x_0)^2}\right)\right]\Bigg]\Bigg\}
\end{aligned}
\tag{5.6}
$$

where:

$$
h_x^k(x,y) = \tan^{-1}\left(\frac{x + g/2}{y}\right) - \tan^{-1}\left(\frac{x - g/2}{y}\right)
$$

$$
h_y^k(x,y) = \ln\left[\frac{(x - g/2)^2 + y^2}{(x + g/2)^2 + y^2}\right]
$$

are the normalised field components for the symmetrical (right-angled) head with linear gap potential (Karlqvist approximations), and $H_0 = 2U_0/g$ is the x-component of the deep-gap field. The first terms on the right-hand-side of (5.5) and (5.6) describe the increase in surface charge density on the right corner with increasing exterior angle θ, and correctly yield the narrow gap fields as $\theta \rightarrow 90^o$ (and $x_0 \rightarrow g/2$). Similarly, equations (5.5) and (5.6) correctly reduce to the Karlqvist field approximations when the head is symmetrical at $\theta = 0^o$ (and hence $x_0 = 0$). Moreover, examination of equations (5.5) and (5.6) reveal that the fields of asymmetrical heads (in the absence of an underlayer) may approximately be constructed from a weighted sum of the x and y components of the magnetic fields of the symmetrical (right-angled) head and the narrow gap head, where the weights are functions of the exterior corner angle θ.

The x and y field components for the asymmetrical head are plotted in Figure 5.5 for different corner angles at $y/g = 0.05$, calculated using equations (5.5) and (5.6) (dashed lines) and compared with the finite-element calculations from Comsol Multiphysics® (solid lines). Figure 5.5 shows the increase in asymmetry in both H_x and H_y with increasing θ, resulting from the increase in surface charge density and potential gradient near the acute corner of the head ($x = g/2$) with increasing θ. The increased asymmetry leads to reduction in the effective head gap length towards the right corner ($x_0 \rightarrow g/2$), consequently causing the increase in the magnitude of the fields and narrowing of their distributions in this region.

The approximate fields calculated using (5.5) and (5.6) correctly capture the asymmetry in the magnetic fields and dependence of both magnitude and distribution on exterior

corner angle θ as illustrated in Figure 5.5 (dashed lines), with some deviation from the finite-element calculations near the centre of the gap and corners for small values of θ.

Table 5.1 RMSD percentages between the normalised *x* and *y* components fields and the finite-element calculations for a range of inclination angles

θ	**% RMSD for H_x**	**% RMSD for H_y**
15°	9.00	5.00
45°	6.00	4.50
75°	1.70	1.70

This reduction of error in the approximate fields with increasing θ is consistent with the reduction in the error of the derived surface potential in (5.2) with increasing θ as illustrated in Figure 5.4. The largest RMS deviation at small value of θ is in line with the accuracy expected of the linear (Karlqvist) gap potential approximation for symmetrical heads where the contribution of the magnetic charges on the pole surfaces is underestimated [72].

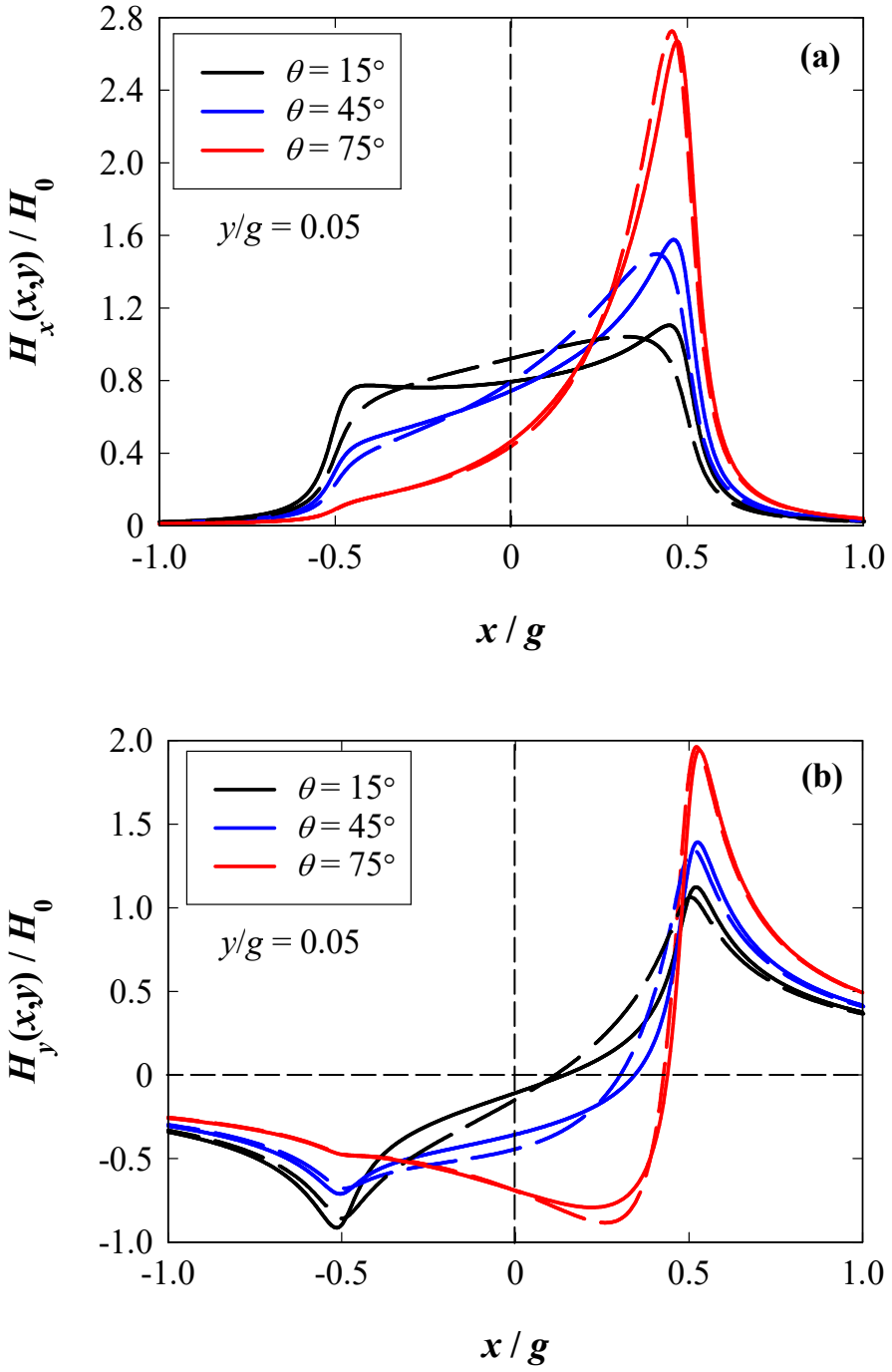

Figure 5.5 (a) Normalised *x*-component of the magnetic field, and (b) normalised *y*-component of the magnetic field for the asymmetrical head for different exterior corner angles θ, calculated using finite-elements (solid lines) and using the approximate models in equations (5.5) and (5.6) (dashed lines). The fields were calculated in close proximity to the head surface at $y/g = 0.05$.

At increasing distances from the head surface, the magnetic fields decrease in amplitude and their distributions broaden as illustrated in Figure 5.6. The increase in y/g is accompanied by increased agreement between the approximate fields calculated using (5.5) and (5.6) and the finite-element calculations as demonstrated in Figure 5.6, for $\theta =$ 45° as a representative example. The normalised RMSD between the approximate and exact (finite-element) H_x is 6% for $y/g = 0.05$ and reduces to 1.6% for $y/g = 0.5$. Similarly, the normalised RMSD for H_y continues the decrease with increasing θ at 4.5% for $y/g =$ 0.05, and down to 1% for $y/g = 0.5$.

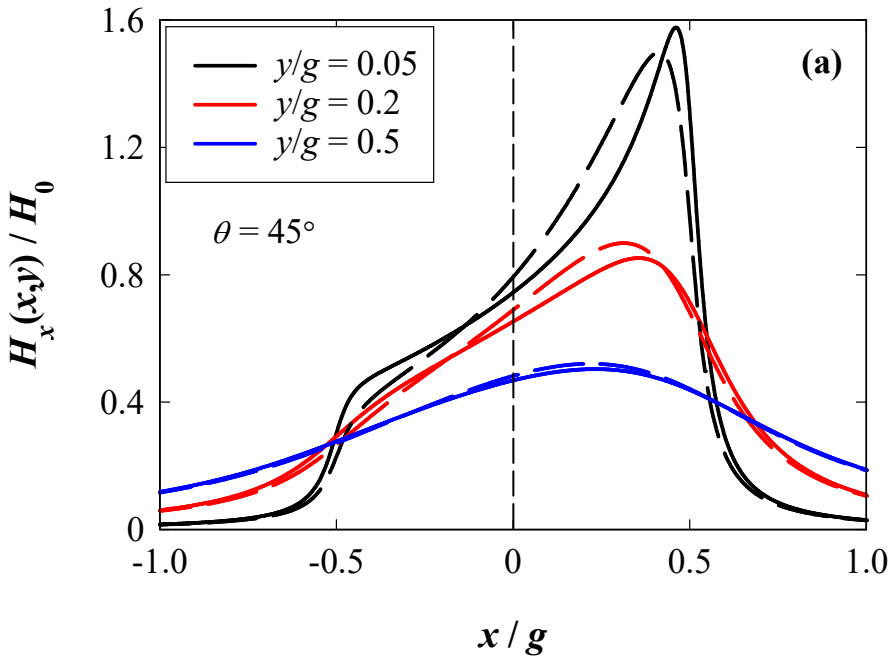

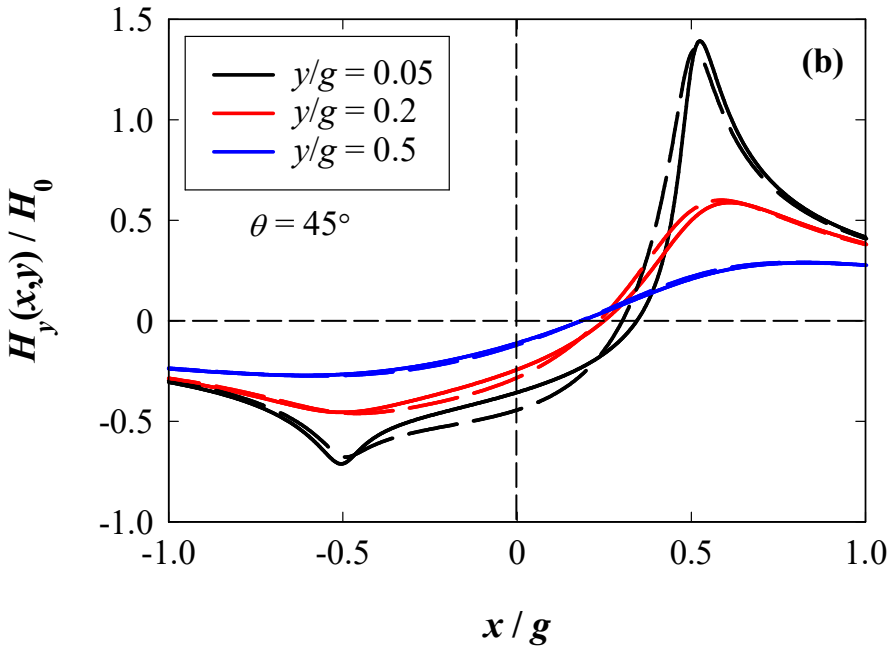

Figure 5.6 (a) Normalised *x* field component, and (b) *y* field component for the asymmetrical head for exterior corner angle $\theta = 45°$, calculated using finite-elements (solid lines) and using the approximate models in equations (5.5) and (5.6) (dashed lines) for increasing spacing *y*/*g* from the head surface.

5.2.3 Fourier transform of surface fields

The magnetic fields everywhere beyond the head surface were determined in Section 5.2.2 from the convolution of the head surface field with the Green's function for the two-dimensional geometry indicated in Figure 5.1. The wavelength content of the magnetic fields is primarily determined by the Fourier transform of the surface field, before being filtered by spacing losses when moving away from the head surface. Thus the surface field transform provides details on the wavelength content of the magnetic fields without any spacing losses, and will be determined next for the asymmetrical head without underlayer. These surface field transforms are also valuable for the numerical evaluation of the magnetic fields using the inverse Fourier transform.

The x-component of the magnetic field along the surface of the asymmetrical head is derived from the gradient of the potential in (5.2) and is given by:

$$H_x(x,0) = \frac{-g^2 H_0}{4} \frac{(g^2/4 - x_0^2)}{(g^2/4 - x_0 x)^2} \tag{5.7}$$

The surface field in (5.7) reveals the two connected characteristics of the surface potential and fields for asymmetrical heads: namely the shift of the zero-crossing of the potential and therefore field locations with the change in corner angle θ (through x_0), and the scaling of x-axis by x_0 which affects the magnitude and the width of the distribution of the fields with the change in θ. Both of these effects contribute to the reduction of effective gap length and narrowing of field distributions towards the acute head corner, as illustrated previously.

Evaluating the Fourier transform of the surface field in (5.7) yields:

$$\begin{aligned} H_x(k,0) = \frac{-gH_0}{2x_0} \Bigg\{ & \left[-2x_0 \cos\left(\frac{kg}{2}\right) + jg \sin\left(\frac{kg}{2}\right) \right] \\ & + j\frac{kg}{2x_0}\left(\frac{g^2}{4} - x_0^2\right) e^{\frac{-jkg^2}{4x_0}} \\ & \times \left[\mathrm{Ei}\left(j\frac{kg}{2x_0}\left(\frac{g}{2} - x_0\right)\right) - \mathrm{Ei}\left(j\frac{kg}{2x_0}\left(\frac{g}{2} + x_0\right)\right)\right] \Bigg\} \end{aligned} \tag{5.8}$$

where Ei is the exponential integral function [112]. The Fourier transform in (5.8) is complex due to the asymmetrical nature of the fields. Figure 5.7 shows the calculated magnitude of the Fourier transform in (5.8) for different exterior corner angles. At $\theta =$ 0°, the spectrum is the well-known Sinc function describing the Fourier transform of the constant (Karlqvist) surface field over the gap region, with nulls at exact multiples of the gap length. Increasing the exterior angle θ reduces the effective gap length of the head and narrows the field spatial distribution, therefore increasing the magnitude of the spectrum at shorter wavelengths (higher k), and diluting the gap nulls. The broadening of the spectrum continues with increasing θ until the narrow gap (or far field) limit is attained at $\theta = 90°$, corresponding to infinitely small gap length and infinitely narrow surface field distribution, which is represented by the constant spectrum in Figure 5.7.

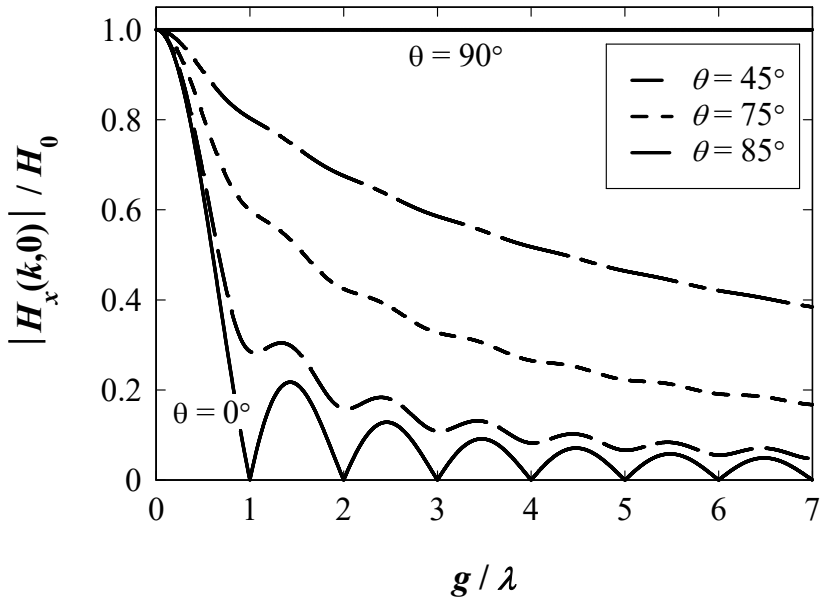

Figure 5.7 Normalised head surface field transform as a function of exterior corner angle θ. The solid lines show the spectra of symmetrical heads including the Karlqvist head ($\theta = 0°$) and the narrow gap head ($\theta = 90°$).

5.3 Surface potential, and magnetic fields for asymmetrical magnetic recording heads with underlayer

5.3.1 Modelling the reaction of the underlayer

The presence of a SUL modifies the magnetic circuit of the head and the distribution of the head surface potential [65]. The reaction of the underlayer on the surface potential for an asymmetrical head with $\theta = 45°$ is illustrated in Figure 5.8, calculated using finite-elements (solid lines) for different head-to-underlayer spacings. This figure shows that the effect the underlayer is more prominent for small head-to-underlayer separations $d/g < 0.5$, resulting in the reduction of the surface potential and its gradient in the gap central region, while increasing the potential gradient near the gap corners. With increasing the head-to-underlayer separation to values of $d/g > 0.5$, the surface potential rapidly approaches the surface potential without an underlayer. The same behaviour applies to other exterior corner angles, with the added displacement of the zero-crossing of the potential towards the acute corner with increasing θ, as previously described for the case without an underlayer.

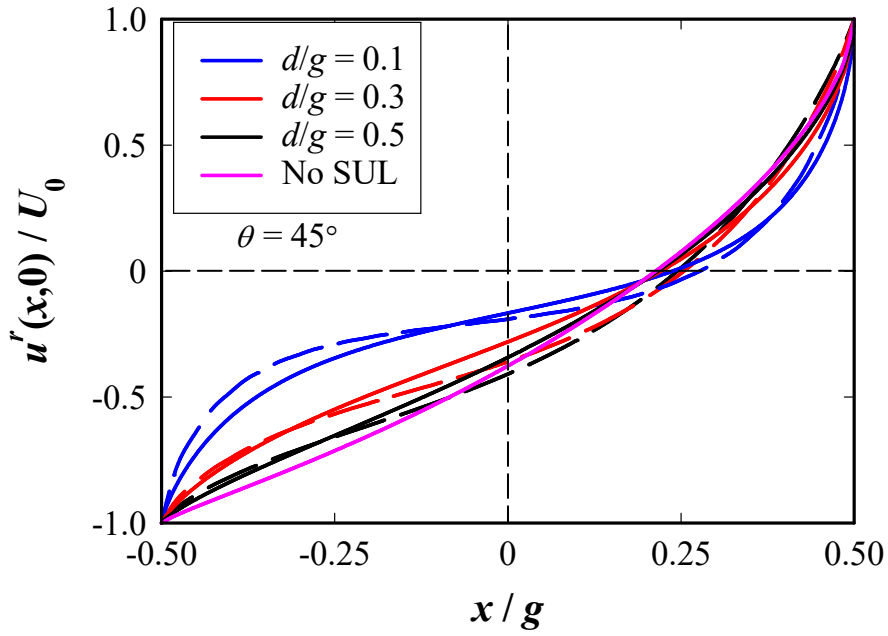

Figure 5.8 Normalised surface potential for an asymmetrical head with corner angle of 45° in the presence of a SUL, calculated using finite-elements (solid lines) and using the Fourier integral transform approximation in this chapter (dashed lines). The surface potential without a SUL, calculated using finite-elements, is shown for comparison.

Modelling the reaction of the underlayer on the head surface potential is complex due to the presence of finite-boundaries in this problem. Theoretical developments commonly use the surface potential or surface field of magnetic heads in the absence of the underlayer, as an approximation, along with the appropriate Green's functions to determine the potential and fields everywhere beyond the head surface (for example [54]). It will be shown in this chapter that this approximation is only valid for head-to-underlayer separations of $d/g > 0.5$. The only satisfactory theoretical treatment available to this boundary value problem is for symmetrical, right-angled corner heads, and involved solutions in the form of infinite Fourier series [43]. The coefficients of the Fourier series solution are determined implicitly from the numerically intensive solution of a truncated, infinite system of linear equations with terms requiring numerical

integration. The study of the authors in [43] also highlighted that the approximation of using the surface potential or field in the absence of the underlayer represent only the first-order term of the complete and accurate solution for this problem. For asymmetrical heads, only a conformal mapping solution was derived for rational corner angles [55], which also requires numerical inversion. In here, a simplified and explicit general theoretical treatment of this boundary value problem is presented to determine the effect of an underlayer on the surface potential of an arbitrary head structure, requiring only the functional description of the surface potential in the absence of the underlayer.

The theoretical treatment starts by assuming the simplified, two-region, boundary value problem shown in Figure 5.9 to represent the gap region of a general magnetic head (in region 1) at close proximity d to a SUL beyond the head surface (region 2). This model is similar to the 'slot' approximation proposed in [66] for the symmetrical ring-head, but generalised here to model any gapped head structure. To simplify the mathematical development and to a very good approximation for small head-to-underlayer separations, the potential on either side of the gap corners is assumed to vary linearly between the head and underlayer, and vanishes at the SUL surface ($y = d$) as indicated in Figure 5.9.

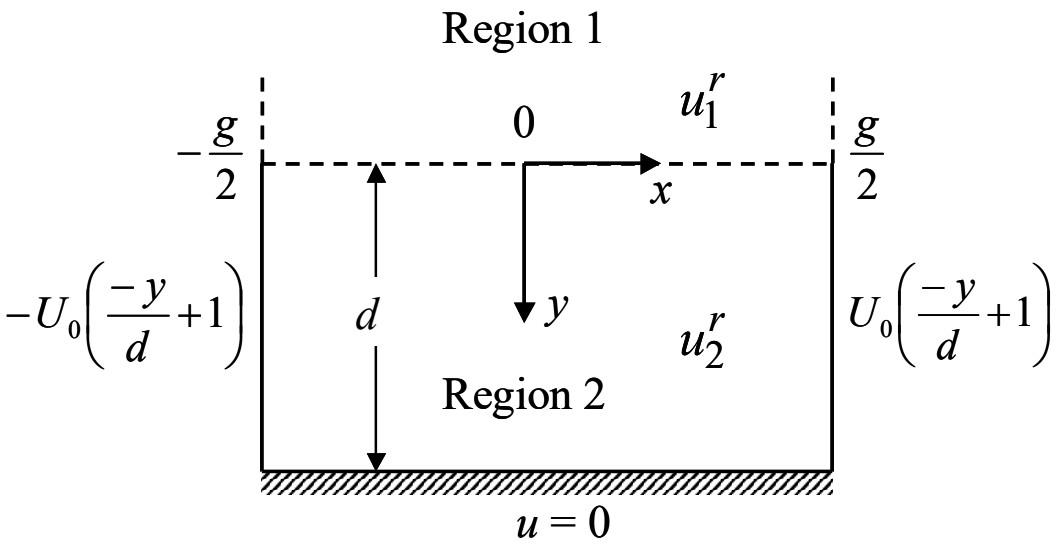

Figure 5.9 Theoretical boundary value problem of the gap region for a general magnetic head with arbitrary surface potential distribution a distance *d* from a SUL, used to derive a closed form distribution of the resulting surface potential in response to the SUL. Region 1 represents the magnetic head gap/surface, and Region 2 is the area beyond the head surface.

Solving Laplace's equation through variable separation in Region 2 (beyond the head surface) subject to the boundary conditions indicated in Figure 5.9, yields the following Fourier series solution for the potential in the presence of an underlayer:

$$u_2^r(x,y) = U_0 \frac{2x}{g}\left(\frac{-y}{d}+1\right) + \sum_{m=1}^{\infty} B_m \sin\left(\kappa_m (x-g/2)\right)\left[e^{-\kappa_m y} - e^{\kappa_m (y-2d)}\right] \qquad -g/2 \le x \le g/2 \qquad (5.9)$$

where the eigenvalues $\kappa_m = m\pi/g$ satisfy the boundary conditions, and eigenfunctions $\sin\left(\kappa_m (x-g/2)\right)$ were chosen to include translation along the *x*-axis to account for even and odd harmonics in the solution to describe the asymmetry in potential.

In Region 1, the magnetic head potential is assumed to have the general Fourier series solution:

$$u_1^r(x,y) = u'(x,y) + \sum_{m=1}^{\infty} A_m \sin\left(\kappa_m (x - g/2)\right) e^{\kappa_m y} \quad -g/2 \le x \le g/2 \qquad (5.10)$$

where $u'(x,y)$ is the head potential distribution in the absence of the underlayer, satisfying the boundary conditions indicated in Figure 5.9 at the head surface. The second, translated Sine series term in (5.10) models the reaction of the underlayer and represents a series of correction terms to the potential $u'(x,y)$, with coefficients A_m that are functions of the corner angle θ and head-to-underlayer separation d. Again, the translated eigenfunctions are chosen to model the asymmetry in the potential and, together with the eigenvalues $\kappa_m = m\pi / g$, satisfy the boundary conditions at the interface $y = 0$. The assumed y-dependence in the Fourier series term in (5.10) follows the exponential decay of fields and potentials expected inside two-dimensional permeable head structures.

The coefficient A_m and B_m in (5.9) and (5.10) are determined by forcing continuity of the potentials (i.e. $\acute{u}_1^r = \acute{u}_2^r$) and normal fields (i.e. $-\partial \acute{u}_1^r / \partial y = -\partial \acute{u}_2^r / \partial y$) at the interface $y = 0$. Multiplying the two continuity equations by $\sin\left(\kappa_n (x - g/2)\right)$ and integrating over the gap length $\pm g/2$, noting the orthogonality of the translated Sine function:

$$\int_{x=-g/2}^{g/2} \sin\left(\kappa_m (x-g/2)\right)\sin\left(\kappa_n (x-g/2)\right)dx = \begin{cases} 0 & m \neq n \\ g/2 & m = n \end{cases}$$

yields two algebraic equations, which can be solved exactly to reveal the following Fourier coefficients:

$$A_n = -\overline{u'}\frac{\left(1+e^{-2\kappa_n d}\right)}{g} - \left[\frac{\partial \overline{u'}}{\partial y}\right]_{y=0}\frac{\left(1-e^{-2\kappa_n d}\right)}{\kappa_n g} + \frac{\bar{v}}{g/2}\left[1-\frac{1}{2}\left(1+\frac{1}{\kappa_n d}\right)\left(1-e^{-2\kappa_n d}\right)\right] \tag{5.11}$$

$$B_n = \frac{\overline{u'}}{g} - \frac{1}{\kappa_n g}\left[\frac{\partial \overline{u'}}{\partial y}\right]_{y=0} - \frac{\bar{v}}{g}\left(1+\frac{1}{\kappa_n d}\right) \tag{5.12}$$

where the overlines indicate integral transforms defined by:

$$\bar{u}(k_n, 0) = \int_{x=-g/2}^{g/2} u(x,0)\sin\left(\kappa_n (x-g/2)\right)dx \tag{5.13}$$

$$\left.\frac{\partial \overline{u'}(\kappa_n)}{\partial y}\right|_{y=0} = \int_{x=-g/2}^{g/2} \left.\frac{\partial u'}{\partial y}\right|_{y=0} \sin\left(\kappa_n (x-g/2)\right)dx \tag{5.14}$$

$\bar{v}$ is the integral transform of the linear gap potential term at $y = 0$, that evaluates exactly to:

$$\bar{v}(\kappa_n,0)=\int_{x=-g/2}^{g/2}\left(\frac{2U_0x}{g}\right)\sin\left(\kappa_n(x-g/2)\right)dx=-\frac{U_0}{\kappa_n}\left[1+(-1)^n\right] \tag{5.15}$$

To maintain consistency with the geometry in Figure 5.9, $\partial\overline{u'}/\partial y$ in (5.11), and (5.12) is determined from the Fourier integral transform of Laplace's equation as detailed in the Appendix A. This provides the integral transform of the derivative of the surface potential as:

$$\left.\frac{\partial\overline{u'}}{\partial y}\right|_{y=0}=-\kappa_m(\overline{u'}-\bar{v}) \tag{5.16}$$

which upon substitution in (5.11), and (5.12) yields the simplified Fourier coefficients:

$$A_n=\frac{-2e^{-2\kappa_n d}}{g}\left(\overline{u'}-\bar{v}\right)+\frac{\bar{v}}{g\kappa_n d}\left(e^{-2\kappa_n d}-1\right) \tag{5.17}$$

$$B_n=\frac{2}{g}\left(\overline{u'}-\bar{v}\right)-\frac{\bar{v}}{g\kappa_n d} \tag{5.18}$$

This completes the formal solution of the boundary value problem described in Figure 5.9. The closed-form, explicit Fourier series representation of the potentials in (5.9) and (5.10) and their coefficients in (5.17), and (5.18) can be used to model the surface potential and fields of general two-dimensional head structures. Moreover, the potentials in (5.9) or (5.10) evaluated at y = 0 along with the coefficient in (5.17), and (5.18) correctly produce the surface potential in the absence of the underlayer in (5.2) as $d\to\infty$.

The Fourier coefficients in (5.17), and (5.18) are functions of the head-to-underlayer separation d, the exterior corner angle θ (through x_0), and head gap length g. Determination of these coefficients requires only knowledge of the surface potential distribution in the absence of an underlayer, which is readily available.

For the asymmetrical head considered here, the surface potential in the presence of the underlayer can now be determined by substituting $u'(x,0) = u(x,0)$ from (5.2) into (5.9) (or (5.10)) and evaluating the series coefficients in (5.17), and (5.18). The integral transform of the surface potential of the asymmetrical head (needed for the evaluation of the coefficients) can be integrated exactly in (5.13) and is given by:

$$\begin{aligned}\overline{u'}(\kappa_n,0) = \frac{gU_0}{2x_0^2}\Big\{&-x_0\left(-1+(-1)^n\right)/\kappa_n \\ &+\left(g^2/4-x_0^2\right)\times\left[\sin(\alpha)\left(-\mathrm{Ci}(\alpha)+\mathrm{Ci}(\beta)\right)-\cos(\alpha)\left(-\mathrm{Si}(\alpha)+\mathrm{Si}(\beta)\right)\right]\Big\}\end{aligned} \tag{5.19}$$

where $\alpha = g\kappa_n(g/2-x_0)/2x_0$, $\beta = g\kappa_n(g/2+x_0)/2x_0$, $\bar{v}$ is defined in (5.15), and Si and Ci are the sine and cosine integrals respectively [112].

Figure 5.8 illustrates the calculated surface potential for the asymmetrical head with an underlayer for corner angle θ = 45° using (5.9) (or equally (5.10)) (dashed lines) for different head-to-underlayer separations. There is very good agreement between the approximate potential calculated using (5.9) or (5.10) and the finite-element calculations in Figure 5.8, with maximum normalised RMSD of about 2.8%, that is consistent for other head corner angles. The rate of convergence of the Fourier coefficients in (5.17),

and (5.18) depends on the head-to-underlayer separation d, and on the corner angle θ. For head-to-underlayer separations of $d/g \geq 0.5$, the coefficients converge rapidly and 20 terms (coefficients) were found sufficient, for any θ, in evaluating the surface potential in (5.9) (or equally (5.10)). More terms are necessary for head-to-underlayer separation of $d/g < 0.5$, with up to 40 terms needed for the evaluation of the surface potential at $d/g = 0.1$ in Figure 5.8. The number of required series terms can increase with increasing corner inclination θ, to correctly sample larger gradients (short wavelength behaviour) in the potential and fields at the acute corner.

5.3.2 Head magnetic fields

In previous section, the magnetic surface potentials is derived, these will be used next convolved with the Green's function for the asymmetrical head to determine the potential and fields everywhere beyond the head surface using the surface fields.

In the presence of a SUL, the particular solution of Laplace's equation as defined in (2.14) subject to a prescribed potential u^r (function of the head-to-underlayer spacing d and corner angle θ) at $y = 0$, and a vanishing potential at the surface of the underlayer ($y = d$), was defined previously in chapter 2 in (2.26).

Thereafter, the superscript 'r' will be used to indicate potentials and fields in the presence of a SUL. Following the analysis of the previous section, it is more convenient mathematically to work with magnetic fields rather than potentials, and therefore the

gradient of the potential in (5.10) is taken to produce the Fourier transform of the magnetic fields:

$$H_x^r(k,y) = -H_x^r(k,0)\frac{\sinh(k(y-d))}{\sinh(kd)} \tag{5.20}$$

$$H_y^r(k,y) = jH_x^r(k,0)\frac{\cosh(k(y-d))}{\sinh(kd)} \tag{5.21}$$

where $H_x^r(k,0)$ is the surface field transform. Evaluating the inverse Fourier transforms of (5.20), and (5.21) using the convolution property of Fourier transforms yields the convolution integrals defined in chapter 2 in (2.29) and (2.30).

The field expressions in (2.29), and (2.30) account for the infinite reflections of the magnetic fields between the high permeability head surface and underlayer [54], and the effect of the gap and the reaction of the underlayer on the surface field are included in the surface field $H_x^r(x,0)$. For the asymmetrical head considered here, the surface field $H_x^r(x,0)$ can be derived from the gradient of the potential in (5.11) (or equally (5.9), and (5.10)). Choosing (5.9) due to the mathematical simplicity of the first linear term in the expression, and evaluating the derivative with respect to *x* yields the surface field:

$$H_x^r(x,0) = -H_0 - \sum_{m=1}^{\infty} \kappa_m B_m \cos(\kappa_m(x-g/2))(1-^{-2\kappa_m d}) \qquad -g/2 \le x \le g/2 \tag{5.22}$$

where $H_0 = 2U_0/g$, and the coefficient B_m are given explicitly in (5.18). It is possible to integrate (2.29), and (2.30) exactly using the surface field distribution in (5.22), however the solution is intractable and in terms of the hypergeometric series function. The magnetic fields in (2.29), and (2.30) can be numerically evaluated more conveniently and quickly using the inverse Fast Fourier Transform from equations (2.29), and (2.30). Alternatively, and in this chapter, the fields in (2.29), and (2.30) were more easily integrated numerically over the gap length using the surface field in (5.22).

Figure 5.10 shows the magnetic fields for the asymmetrical head for different degrees of corner asymmetry with head-to-underlayer separation d/g = 0.2, calculated at a head spacing y/g = 0.1 using finite elements (straight lines) and the theoretical models in (2.29), (2.30) and (5.22) (dashed lines). The presence of the soft underlayer enhances H_y at the expense of H_x, with H_x confined to the pole corners as indicated in Figure 5.10(a). Following a similar pattern to the head fields without an underlayer, the increase in the exterior corner angle θ increases the asymmetry in the magnetic fields in general, and particularly increases the magnitude of H_x near the acute corner (at $x = g/2$). With increases in θ, the zero-crossing in H_y shifts towards the right corner as shown in Figure 5.10(b) following the shift in the surface potential. Beyond the head corners and over the pole regions, H_y tends to a constant magnitude that depends only on the ratio of d/g as demonstrated in Figure 5.10(b). This dependence can be easily derived from (2.30) by evaluating the limit $x \to \pm\infty$, thus reducing the convolution integral to $1/2d\int_{x'=-g/2}^{g/2} H_x^r(x',0)dx'$. Substitution of (5.22) and integration yields the constant normalised field $H_y^r / H_0 \approx \pm g/2d$ (i.e. H_y over the head poles is determined by the first, long wavelength, term of the surface field in (5.22)).

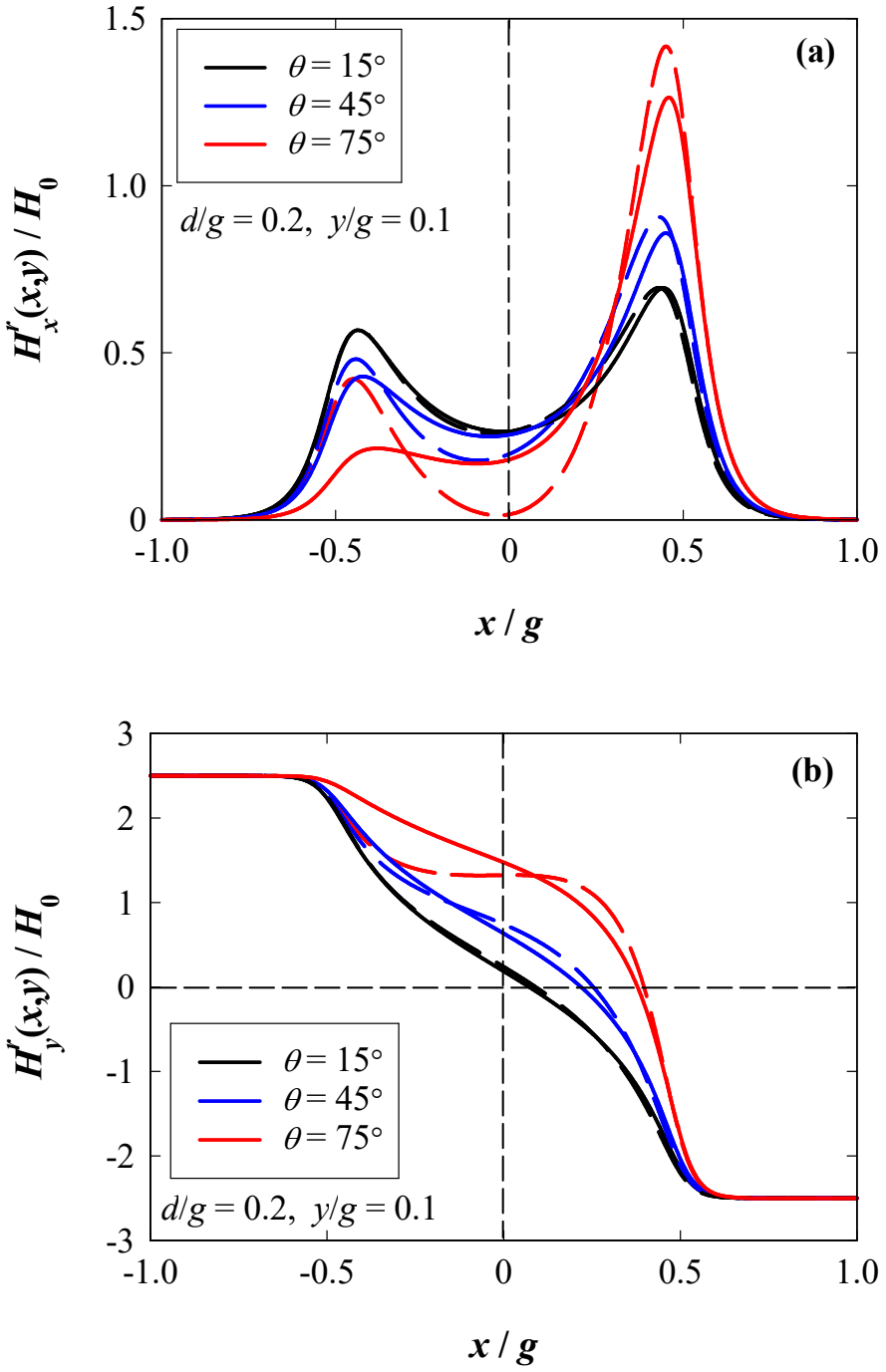

Figure 5.10 (a) Normalised *x* field component, and (b) *y* field component for the asymmetrical head in the presence of a SUL for different corner angles θ, calculated for a head-to-underlayer separation *d/g* = 0.2 at distance *y/d* = 0.1 from the head surface. Solid lines are the finite-element calculations, and the dashed lines are from the theoretical model in (2.29), and (2.30) and using the surface field distribution from (5.22). The calculated *y*-component of the magnetic field tends correctly to the normalised field value of $H_y^r / H_0 \approx \pm g/2d$ =±2.5 over the pole regions (| *x* | >g/2).

Table 5.2 RMSD percentages between the normalised *x* and *y* components fields and the finite-element calculations for a range of inclination angles

θ	% RMSD for H_x^r	% RMSD for H_y^r
15°	2.50	0.70
45°	4.50	1.50
75°	7.00	4.40

The deviation of the approximate field models from the accurate finite-element calculations in Figure 5.10 is mainly confined to the central region of the gap. This is where the surface potential in (5.9) or (5.10), derived based on the approximate boundary value problem described in Figure 5.9, predict a lower surface potential gradient (see Figure 5.8) and therefore fields in that region compared to the finite-element solution.

The dependence of the magnetic fields on the head-to-underlayer separation is depicted in Figure 5.11 for a fixed corner angle $\theta = 45°$. For small $d/g < 0.5$, H_x^r is confined and has maxima near the head corners as indicated in Figure 5.11(a). Increasing the head-to-underlayer separation enhances the magnitude of H_x^r at the acute pole corner, and beyond $d/g > 0.5$ causes only modest changes to the magnetic fields as they become comparable to the fields without an underlayer. The normalised RMS derivation between the approximation in H_x and finite-element calculations starts at 5% for $d/g = 0.2$, and reduces to 4% with increased head-to-underlayer spacing at $d/g = 1$. For increasing values of $d/g > 0.5$, H_y^r decreases in amplitude, and the fields beyond the pole corners fall to zero following the behaviour of the fields in the absence of the underlayer as indicated in Figure 5.11(b). The RMS deviation between the approximate and exact H_y^r fields in this

case is 1.5% at d/g = 0.2 and increases to 2.7% for d/g = 1 in line with the previously estimated RMS deviation values in the absence of the underlayer.

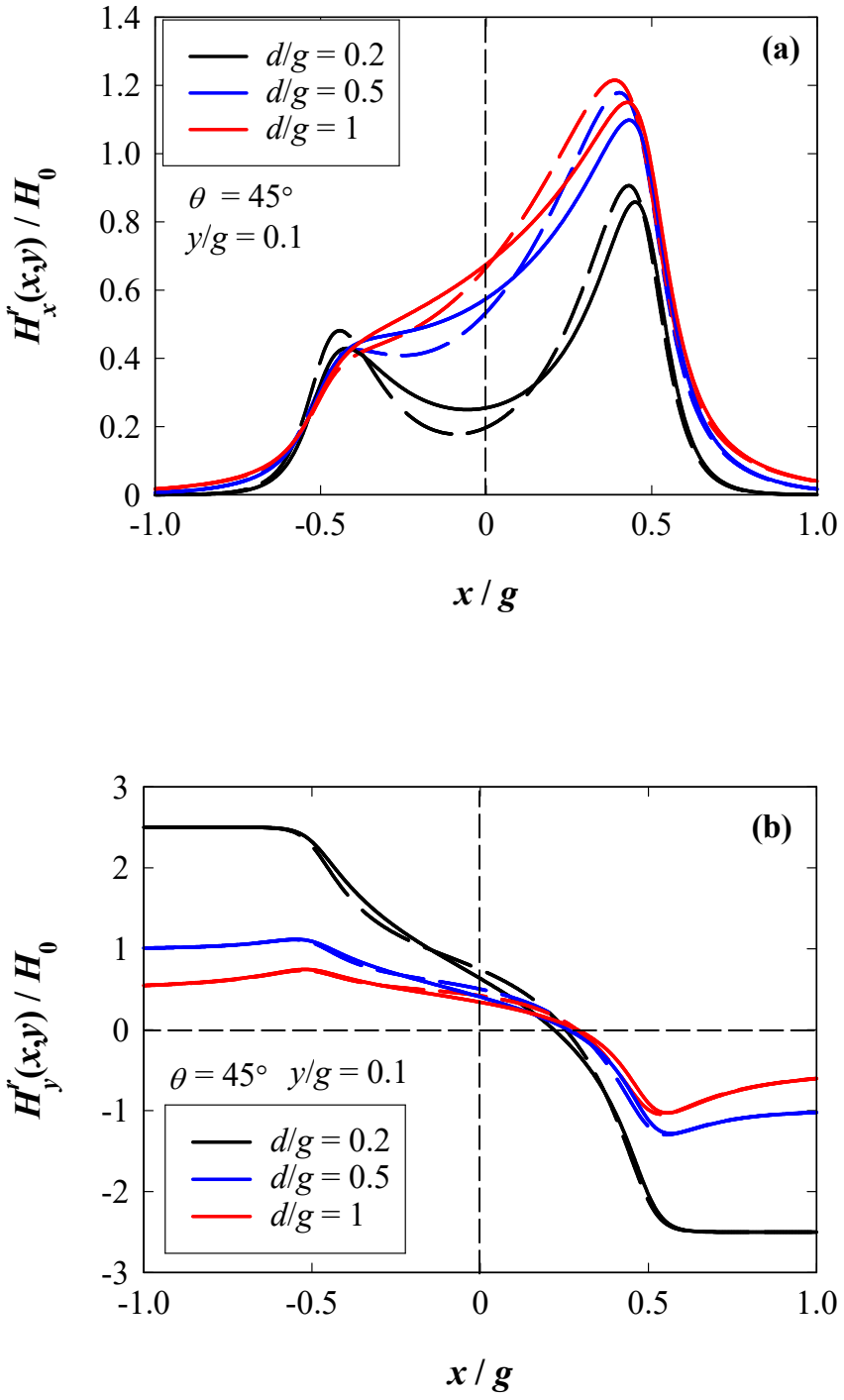

Figure 5.11 (a) Normalised *x* field component, and (b) *y* field component for the asymmetrical head in the presence of a SUL, for exterior corner angle θ= 45°. Solid lines are for the finite-element calculations, and the dashed lines are from the theoretical model in (2.29), and (2.30) and using the surface field from (5.22).

5.3.3 Fourier transform of surface fields

For the case when an SUL is present, the magnetic fields everywhere beyond the head surface were determined in Section 5.3.2. The equations (2.29) and (2.30) show that the wavelength content of the magnetic fields is primarily determined by the Fourier transform of the surface field, before being filtered by spacing losses when moving away from the head surface.

The presence of a soft underlayer causes an enhancement of H_y^r, making it of practical importance for magnetic recording. Nevertheless, the *x*-component of the surface field $H_x^r(k,0)$ still decides the surface wavelength spectrum of H_y^r as indicated by equation (5.21). Convolving $H_x^r(k,0)$ with the low-pass filter term 1/tanh(*kd*) in (5.21) further enhances the short wavelengths in the spectrum therefore increasing the magnitude of H_y^r over the head poles with reduction in head-to-underlayer separation *d* as shown in Figure 5.10(b). $H_x^r(k,0)$ can be determined from the gradient of (5.9) (or equally (5.10)) at $y = 0$. For mathematical convenience, the surface field in (5.22) will be used again, with Fourier transform given by:

$$H_x^r(k,0) = -gH_0 \frac{\sin(kg/2)}{(kg/2)} - 2k\sum_{m=1}^{\infty} j^m \kappa_m B_m (1 - e^{-2\kappa_m d}) \frac{\sin\left(g/2(k+\kappa_m)\right)}{k^2 - \kappa_m^2} \tag{5.23}$$

The surface field spectrum in (5.23) follows the same dependence on exterior corner angle θ as that indicated in Figure 5.7 in the absence of an underlayer, and will not be illustrated here. Specifically, the width and therefore wavelength content of the spectrum in (5.23) also increases with increasing θ, due to the reduction in effective gap and narrowing of field distributions. The effect of the head-to-underlayer spacing on head surface transform in (5.23) is illustrated in Figure 5.12 for $\theta = 45°$. Reducing the head-to-underlayer separation results in displacement of the gap-nulls toward larger wavelengths (smaller k) and increases in the amplitude of the ripples in the spectrum. This behaviour persists for all other corner angles.

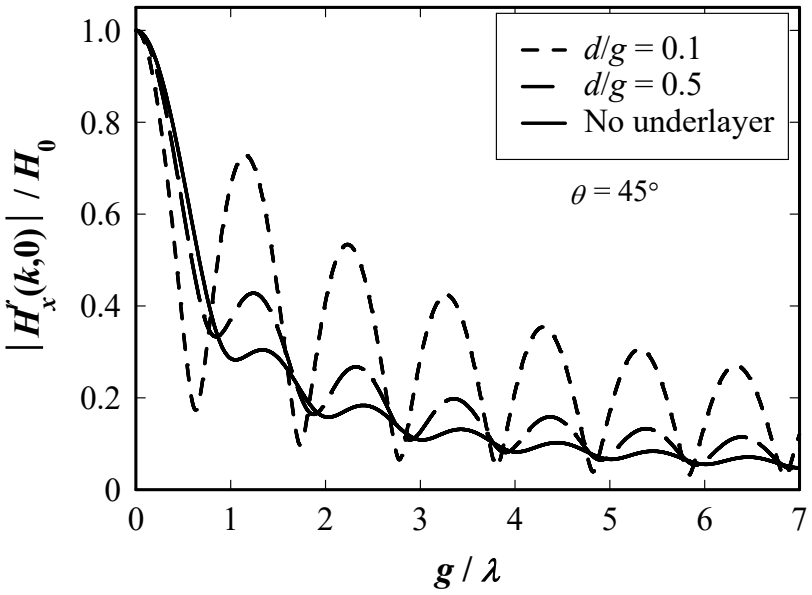

Figure 5.12 Normalised head surface field transforms for an asymmetrical head for $\theta = 45°$ at different head-to-underlayer spacings.

Chapter 6: Modelling Symmetric Magnetic Recording Heads With and Without an Underlayer Using Superposition of Corner Potentials

6.1 Introduction

In chapter 3 of this thesis, the scalar magnetic potential near a single two-dimensional corner was derived exactly. It was also shown in this chapter that it is possible to model two-dimensional asymmetrical heads by including the contribution of two corners separated from each other by a distance equal to the gap length, and held at equal and opposite potentials, through superposition. The derived approximate potentials and corresponding fields demonstrated good agreement with exact solutions and finite-element calculations. However, it was found in chapters 3 and 4 (in the presence of a SUL) that the error in this approximation increases with increasing head asymmetry, indicating that the increased error is associated with the increased mismatch between the charge density distributions on each of the head poles. This can be understood by inspection of Figure 3.1 as an example, where the left (obtuse) pole surfaces have less charge concentration near the corner compared to the right (acute) pole surfaces, over the same extent of the pole surfaces (which is taken in this thesis to be equal to the gap length i.e. $\rho = g$). This observation suggests that the method of superposition would be more applicable if the magnetic charge density or charge concentration is equal on both pole surfaces, which happens in the case of symmetrical head structures as shown in Figure 6.1.

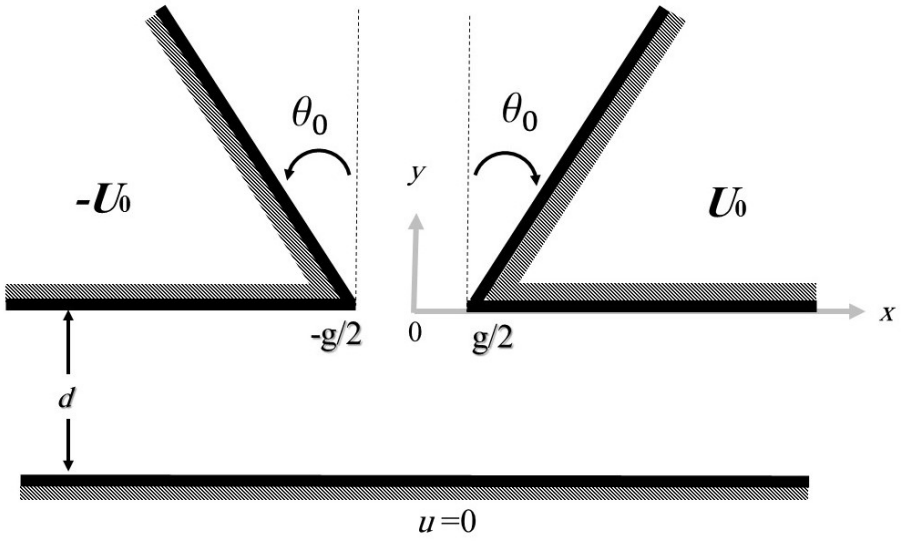

Figure 6.1 Two-dimensional geometry of the symmetrical head, with gap length *g* and exterior corner inclination angle θ_0. The poles are assumed to have infinite permeability with potentials $\pm U_0$, at a distance *d* from a soft magnetic underlayer (SUL) held at zero potential. To model two-dimensional heads without an underlayer, the SUL is removed with $d \to \infty$.

In this chapter, the potential and field expressions derived in chapters 3 and 4 for asymmetrical heads in the absence and presence of a SUL respectively, are utilised to evaluate the surface potential and fields of two-dimensional symmetrical magnetic recording heads for a range of exterior corner inclination angle θ_0 (0° to 90°) as indicated in Figure 6.1. This is to investigate the applicability of the method of superposition of corner potentials to asymmetrical structures and estimate the error in this approximation.

6.2 Surface potential

Following chapter 3, the gap surface potential is derived, to a good approximation, from the superposition of the first terms in the Fourier series solution of corner potentials as indicated by equations (3.36) and (3.37). The surface potential is thus given by:

$$u(x,0) \approx U_0 \left| \frac{x+g/2}{g} \right|^{\frac{\pi}{3\pi/2+\theta_0}} - U_0 \left| \frac{x-g/2}{g} \right|^{\frac{\pi}{3\pi/2+\theta_0}} \tag{6.1}$$

and the corresponding surface field (from the gradient of the surface potential above) is:

$$H_x(x,0) = \frac{-du}{dx} = \frac{-U_0}{g}\left(\frac{\pi}{3\pi/2+\theta_0}\right) \times \left\{ \left| \frac{x+g/2}{g} \right|^{\left(\frac{\pi}{3\pi/2+\theta_0}\right)-1} + \left| \frac{x-g/2}{g} \right|^{\left(\frac{\pi}{3\pi/2+\theta_0}\right)-1} \right\} \tag{6.2}$$

The gap surface potential for the symmetrical head shown in Figure 6.1 calculated using equation (6.1) is shown Figure 6.2 for a range of exterior corner angles θ_0, compared with the finite-element calculations using COMSOL Multiphysics®. The gap potential for all considered angles are symmetrical with increasing gradient (and therefore fields) near the gap corners at $\pm g/2$ [106] as θ_0 increases (See Figure 6.2).

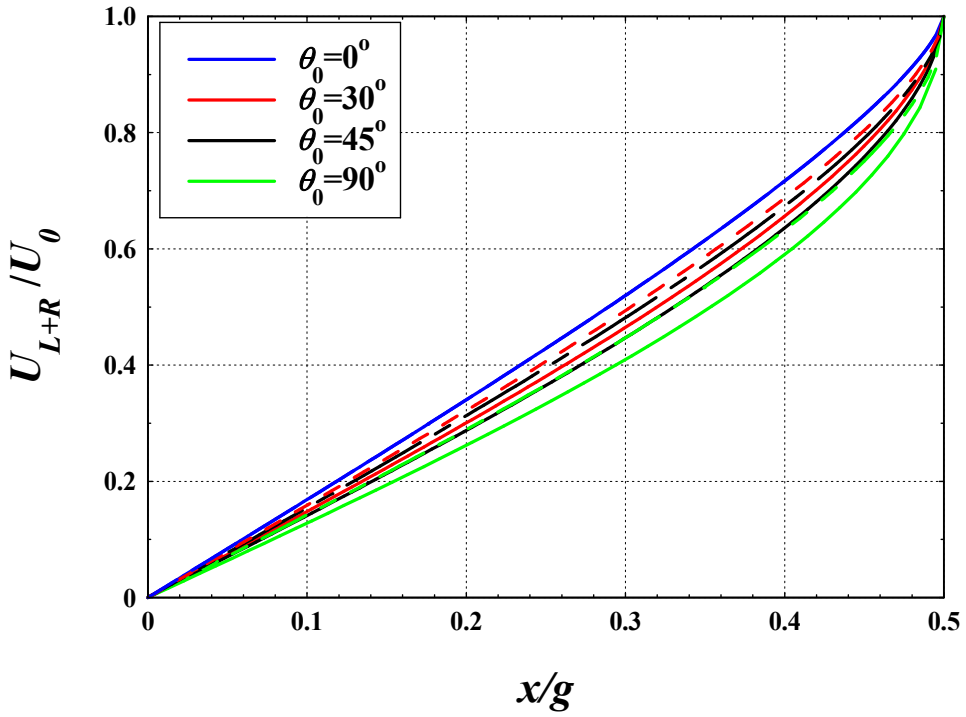

Figure 6.2 Calculated gap surface potential using finite-elements (solid lines) and the approximate surface potential in (6.1) (dashed lines) for a range of inclination angles $0^o \le \theta_0 \le 90^o$.

Figure 6.2 shows excellent agreement between the surface potential calculated using superposition and the finite-element/exact solutions [67], with RMSD of 0.5% when when $\theta_0 = 0^o$ (right-angled corners) and increasing to maximum of less than 4% for $\theta_0 = 90^o$ as indicated in Figure 6.3. These results provide clear evidence of the validity of the superposition of corners approximation particularly in modelling the potentials and fields of symmetrical structures.

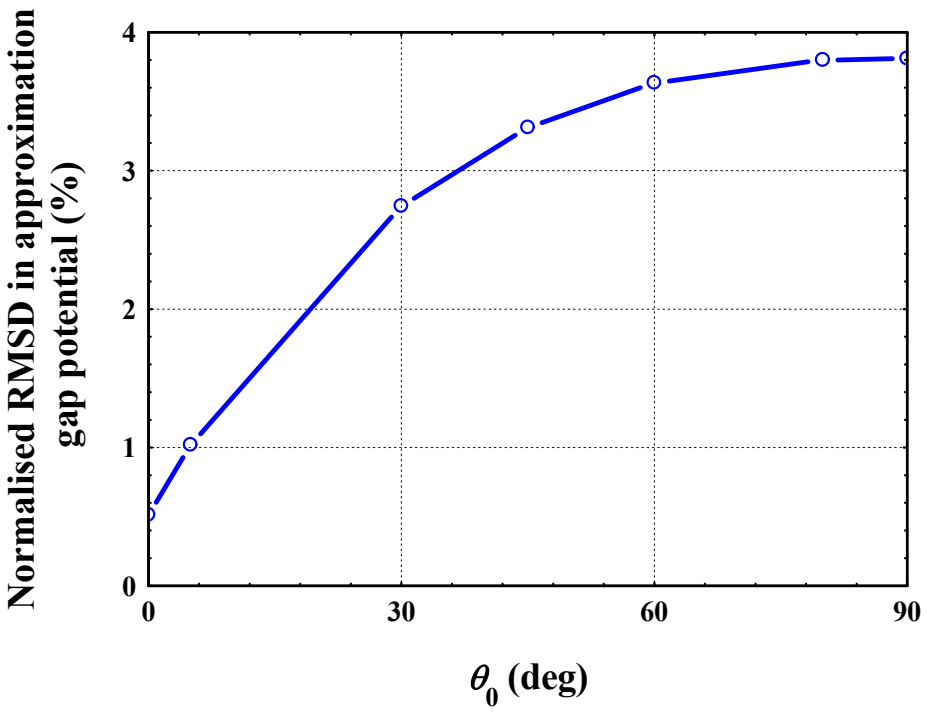

Figure 6.3 The RMSD between the approximate gap potential in (6.1) and the finite-element calculations, normalised by maximum change of potential in the gap ($2U_0$), as a function of the exterior corner angle θ_0.

6.3 Magnetic fields for symmetrical head without SUL

The magnetic surface potential for the symmetrical head plotted above and given by equation (6.1) is now convolved with the Green's function for the two-dimensional, semi-infinite head geometry in equations (3.41) and (3.42) to determine the potential and fields everywhere beyond the head surface. The magnetic fields are normalised by the deep gap field for the right-angled head ($H_0 = 2U_0/g$) and compared with exact solutions and finite-element calculations using Comsol Multiphysics®.

The normalised x and y field components at $y/g = 0.1$ are plotted in Figure 6.4, where only half the field curves are displayed due to symmetry.

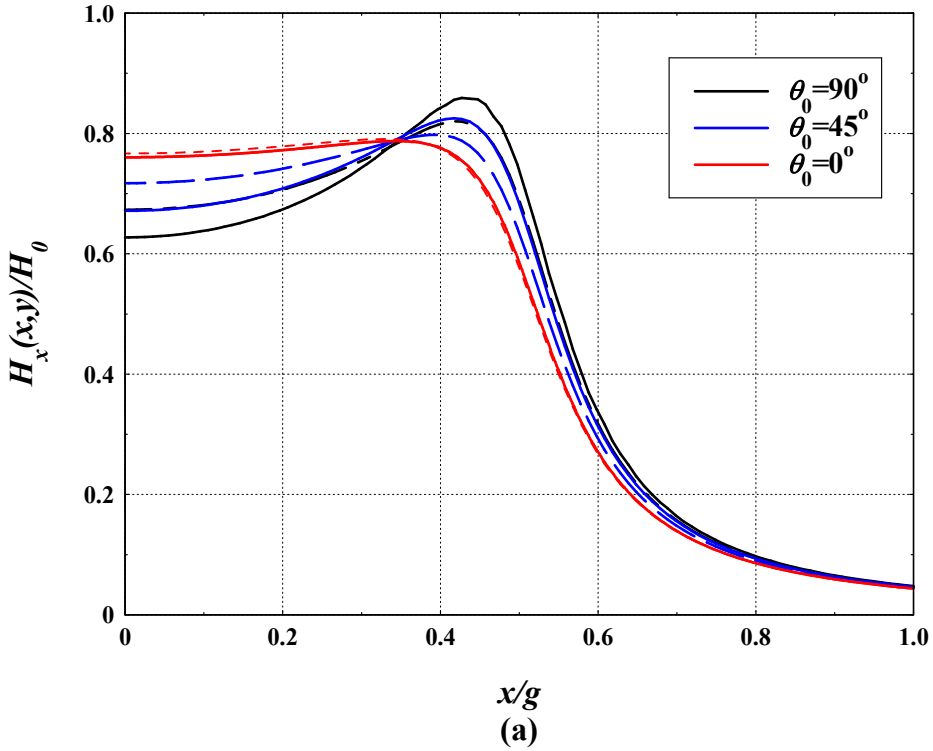

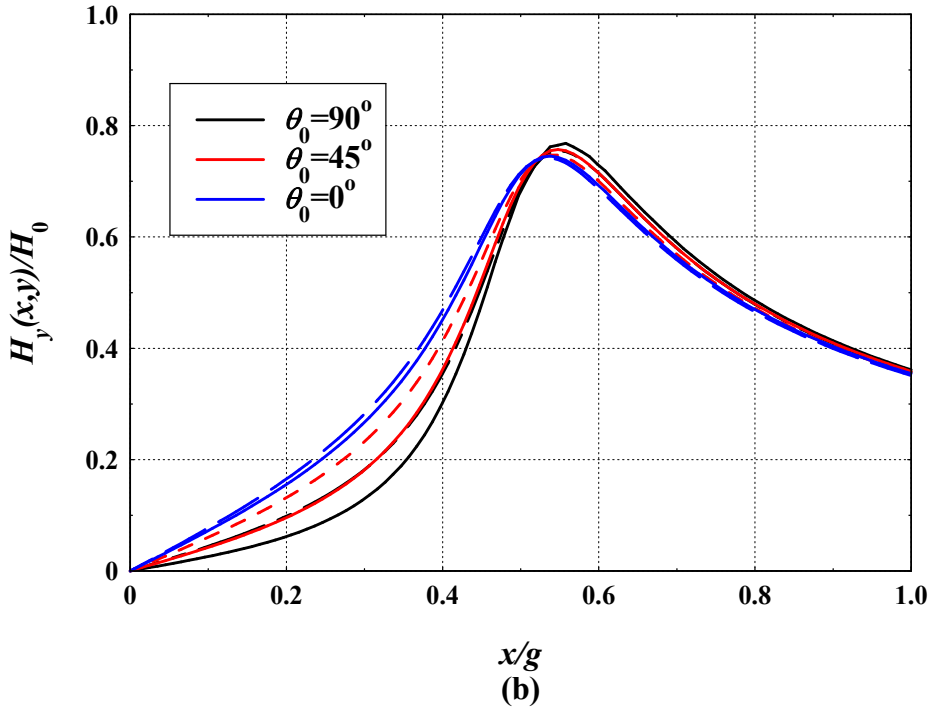

Figure 6.4 (a) Normalised *x*-component and (b) *y*-component field distribution for the symmetrical head for different interior corner angles at *y/g*=0.1 calculated using finite-element (solid lines) and using the superposition of corner potentials (dashed lines)).

In here the magnetic fields continue their symmetrical behaviour with increasing magnitude in the corner regions as θ_0 increases, in line with dependence of the potential spatial distribution on θ_0 illustrated in Figure 6.2. The agreement between the approximations (dashed lines) and the finite-element calculations using COMSOL Multiphysics® (solid lines) is excellent. The calculated deviations of the approximate *x* and *y* field components from the exact calculations are illustrated in Table 6.1, where the *y* field component in the approximation agrees more to the finite-element data. Table 6.1. In general, the error in the approximate fields decreases for decreases in θ_0, with maximum RMSD of less than (3.8% for H_x and 2% for H_y) for $\theta_0 = 90°$.

Table 6.1 Percentage RMSD between the theoretical *x* and *y* field components and the finite-element calculations at *y/g*=0.1.

θ_0	% RMSD for H_x	% RMSD for H_y
0°	0.53	0.28
5°	1.12	0.58
30°	2.84	1.52
45°	3.32	1.79
60°	3.52	1.87
90°	3.72	1.92

Closer to the head surface at *y/g*=0.05, the magnetic fields using the superposition of surface potentials/fields are plotted in Figure 6.5 and again demonstrate excellent agreement with the exact calculated fields. This agreement is illustrated in the RMSD values tabulated in Table 6.2 for different values of corner angles, with maximum value not exceeding 4%. Moreover and following the observations for the previous head separation, the approximation shows better agreement to the finite-element data for the *y* field component.

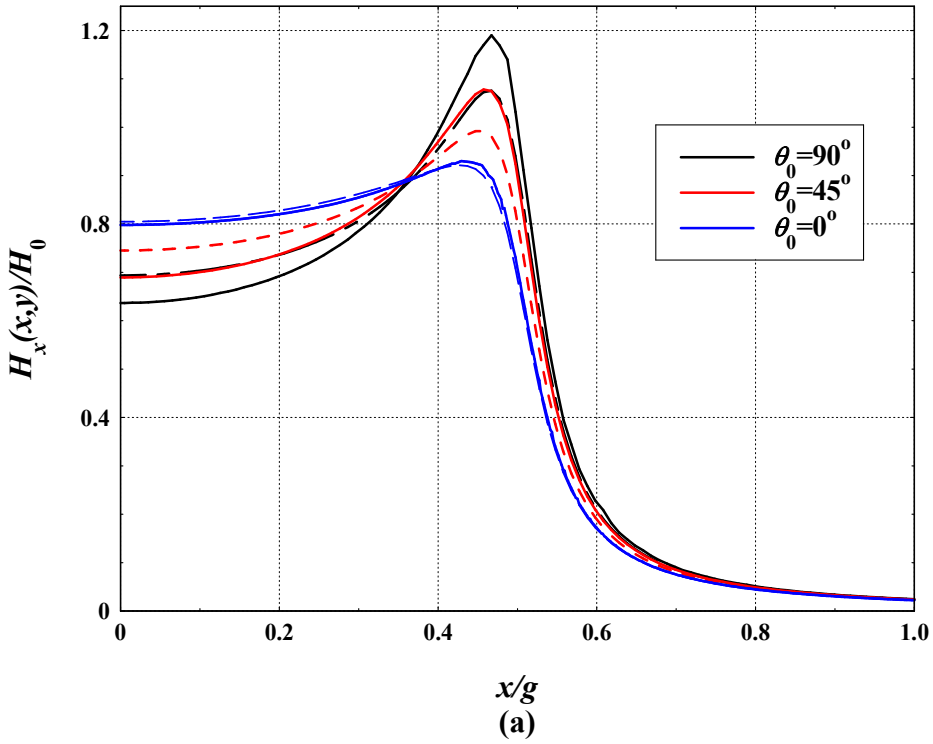

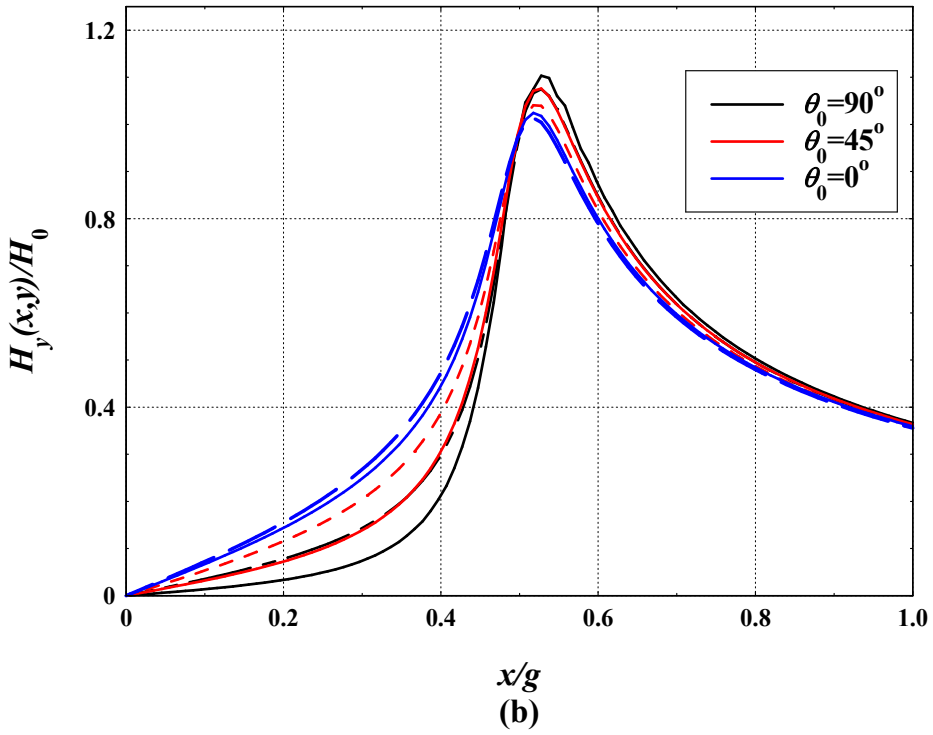

Figure 6.5 (a) Normalised *x*-component and (b) *y*-component field distributions for the symmetrical head for different interior corner angles at *y/g*=0.05 calculated using finite-element (solid lines) and using the superposition of corner potentials (dashed lines)).

Table 6.2 Percentage RMSD between the theoretical *x* and *y* field components and the finite-element calculations at *y/g*=0.05.

θ_0	% RMSD for H_x	% RMSD for H_y
0°	0.96	0.37
5°	1.39	0.62
30°	3.18	1.55
45°	3.64	1.81
60°	3.78	1.89
90°	3.84	1.81

The RMSD or error in the approximate field calculations as functions of the corner angle for *x* and *y* field components calculations at *y/g*=0.1, and 0.05 is summarised in Figure 6.6.

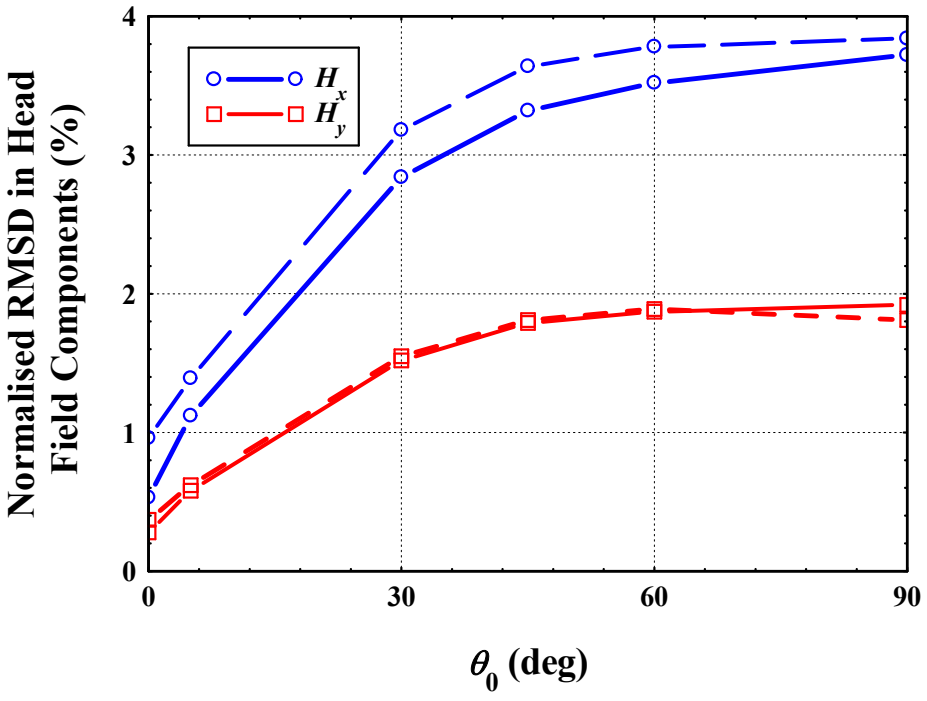

Figure 6.6 The RMSD for field (a) *x*-components (b) *y*-components between the approximation method calculations and the finite-element calculations at *y/g*=0.1 (solid lines) and at *y/g*=0.05 (dashed lines).

6.4 Magnetic fields for symmetrical head with SUL

The magnetic surface potentials plotted for symmetrical head without underlayer above is now convolved with the Green's function for the semi-infinite two-dimensional geometry in the presence of an underlayer given by equations (4.5) and (4.6). This is to evaluate the fields everywhere beyond the head surface using the surface field expression in (6.2) based on superposition $0° \le \theta_0 \le 90°$.

The convolution integrations in (4.5) and (4.6) are carried out using the Matlab quaderature function *quadgk* then plotted as dashed lines in the following figures and compared with finite-element calculations obtained using COMSOL Multiphysics® and indicated with solid lines. The normalised (by the peak field values) RSMD is used to estimate the percentage differences between the approximation and the finite-element calculations.

For the right angled head with $\theta_0 = 0°$, the x and y field components at a spacing of $y/g = 0.1$ from the head surface and head-to-underlayer distance $d/g=1$ are shown in Figure 6.7 for a range of inclination angles $0^o \le \theta_0 \le 90^o$. At this head-to-underlayer separation, the convolution integrations using the surface fields for the head without an underlayer are accurate as described in chapter 4, allowing focus on studying the error in the superposition approximation rather than on the Green's function solution. This figure shows that the fields are symmetrical with very good agreement between the theoretical, superposition-based calculations (dashed lines), and the finite-element solution (solid lines) with increasing magnitude towards the gap corners with increasing θ_0. Table 6.3 shows the RMSD between the superposition of the normalised x and y field components and the finite-element calculations, and indicates that the errors in the theoretical approximations do not exceed 2.8% for H_y and 5% for H_x. This table also shows that the y field component in the approximation agrees more to the finite-element data.

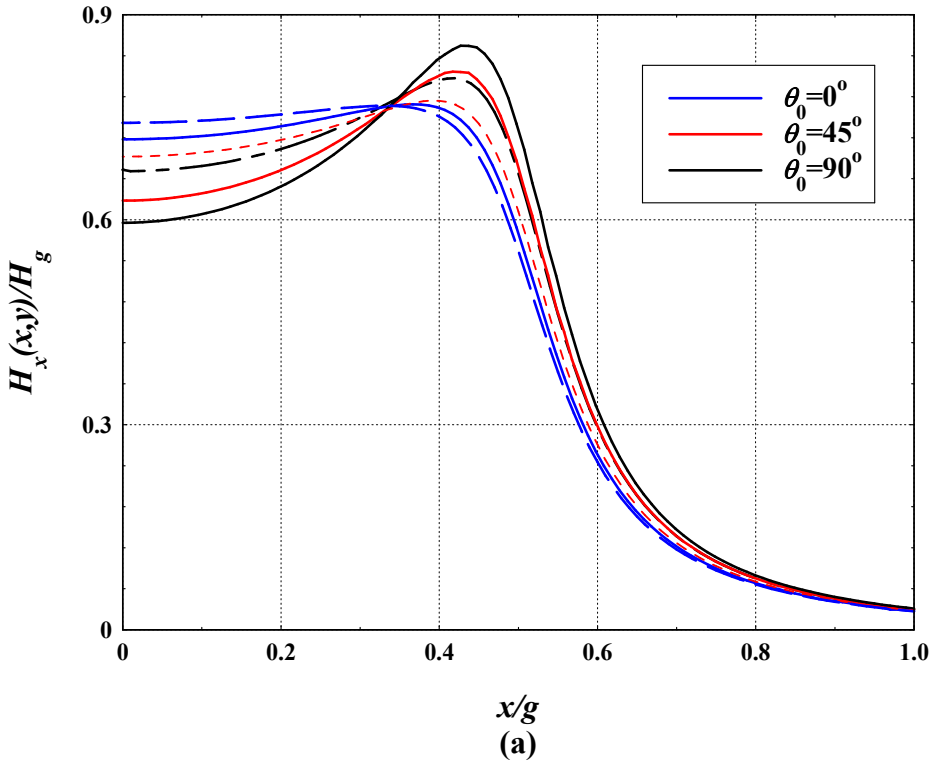

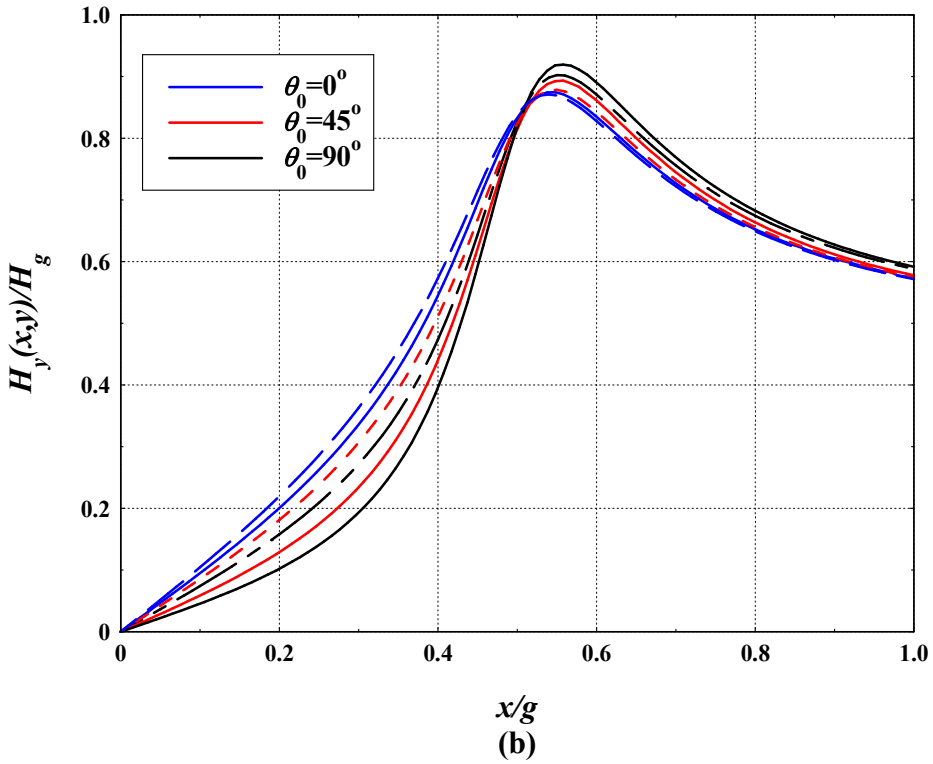

Figure 6.7 (a) Normalised *x*-component and (b) *y*-component field distributions for the symmetrical head for different interior corner angles at *y/g*=0.1 calculated using finite-element (solid lines) and using the superposition of corner potentials (dashed lines)).

Table 6.3 Percentage RMSD between the theoretical *x* and *y* field components and the finite-element calculations at *y/g*=0.1.

θ_0	% RMSD for H_x	% RMSD for H_y
0°	1.85	0.81
5°	2.90	1.29
30°	4.07	1.84
45°	4.47	2.03
60°	4.72	2.18
80°	4.61	2.17
90°	4.59	2.15

The calculations are repeated for *y/g*=0.05 and the *x* and *y* field components for head-to-underlayer separation of *d/g*=1 are shown in Figure 6.8. This figure again shows that the fields are symmetrical with excellent agreement between the theory and numerical calculations. Table 6.4 shows the RMSD between the approximation of the normalised *x* and *y* field components and the finite-element calculations. This table also shows that the errors between the *y* field component in the approximation and the finite-element has not reached 2.3%, while the *x* field component shows an increasing disagreement with increasing θ_0.

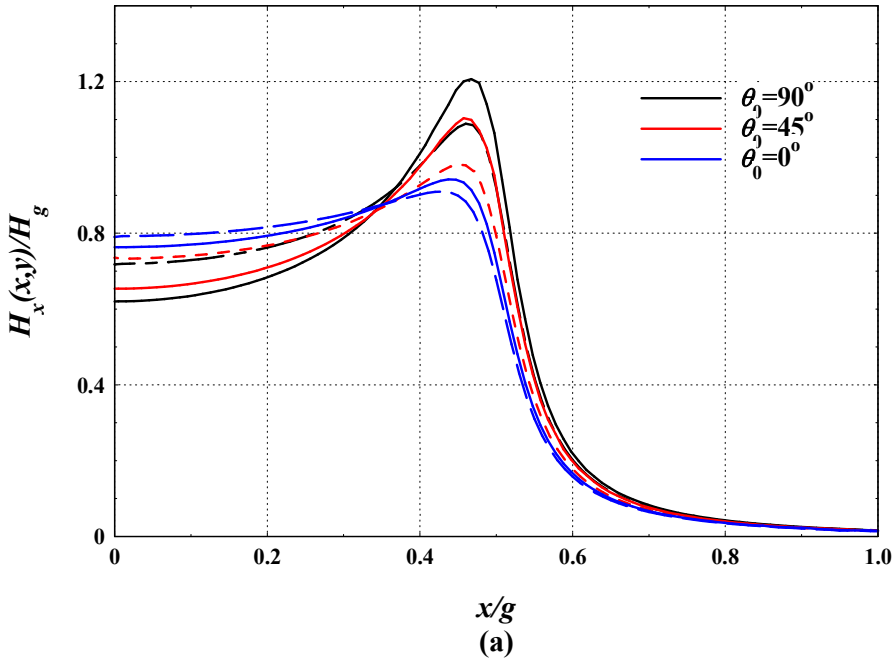

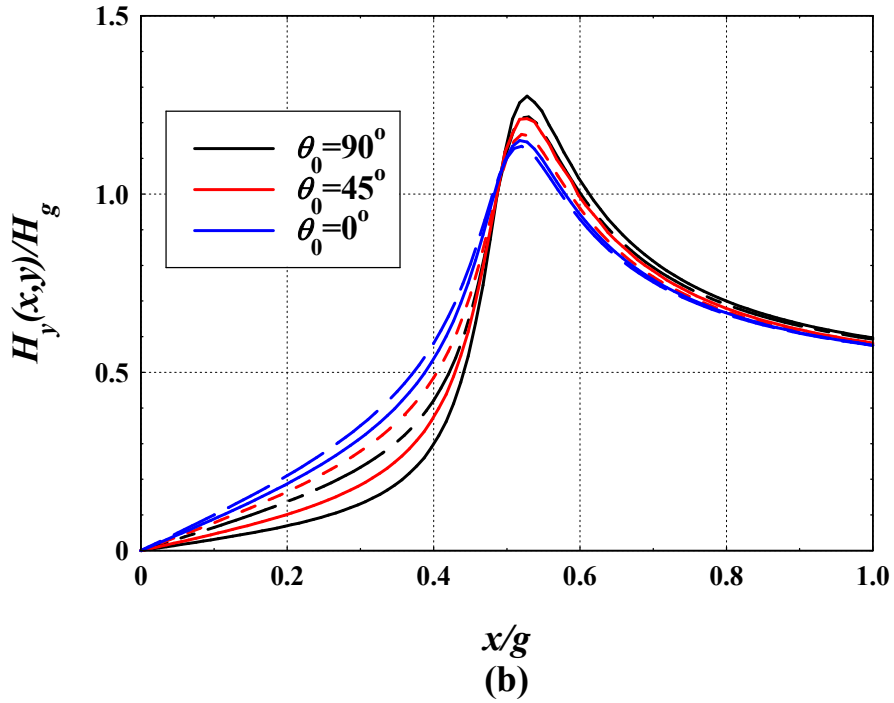

Figure 6.8 (a) Normalised *x*-component and (b) *y*-component field distribution for the symmetrical head for different interior corner angles at *y/g*=0.05 calculated using finite-element (solid lines) and using the superposition of corner potentials (dashed lines)).

Table 6.4 Percentage RMSD between the theoretical *x* and *y* field components and the finite-element calculations at *y*/*g*=0.05.

θ_0	% RMSD for H_x	% RMSD for H_y
0°	2.23	0.91
5°	3.23	1.36
30°	4.43	1.95
45°	4.78	2.16
60°	4.97	2.29
80°	4.75	2.27
90°	4.74	2.26

The RMSD or error in the approximate field calculations as functions of the corner angle for *x* and *y* field components calculations at *y*/*g*=0.1, and 0.05 for head-to-underlayer distances *d*/*g*=1 is summarised in Figure 6.9.

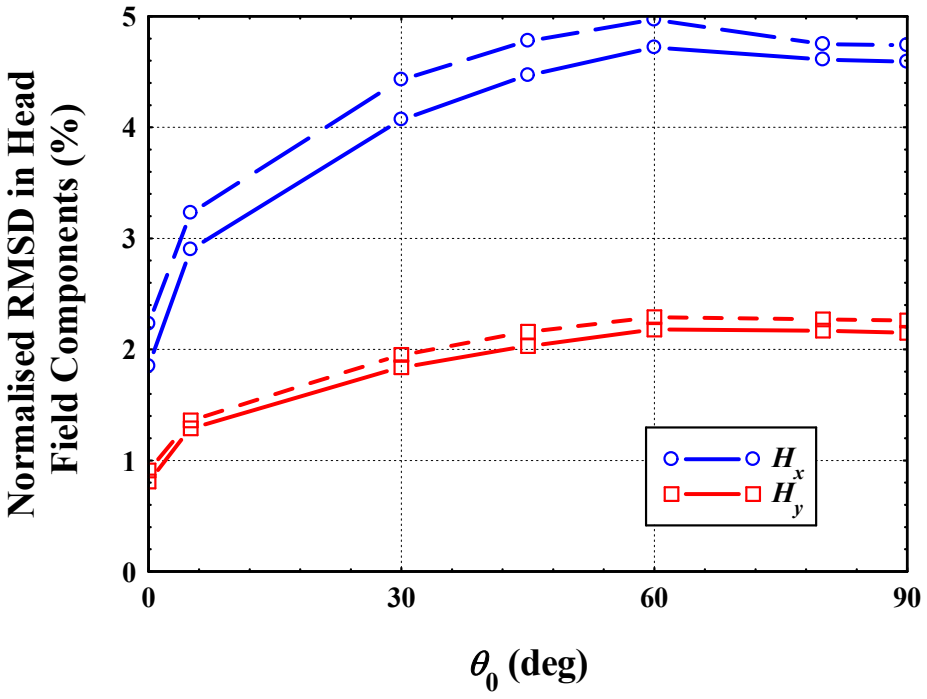

Figure 6.9 The RMSD for field (a) *x*-components (b) *y*-components between the approximation method calculations and the finite-element calculations at *y*/*g*=0.1 (solid lines) and at *y*/*g*=0.05 (dashed lines) for head-to-underlayer distances *d*/*g*=1.

Chapter 7: Conclusions and future work

To meet the ever increasing demand for information storage, recent advances in recording technologies have focused on the question of 'How to increase the areal densities of HDD storage?' using such methods as Heat Assisted Magnetic Recording, Patterned Media, Shingled and Two-Dimensional Magnetic Recording. Due to the highly competitive race between HDD developers, efforts to develop and increase magnetic recording capacities and the aim of reaching higher areal density will continue.

The magnetic head is considered an effective and important part of magnetic recording systems, where its geometry and dimensions determine the magnitude and distribution of the fringing gap fields and their gradients. Hence, the design of magnetic heads has a direct impact on the achievable storage density of magnetic recording systems. As part of the natural evolution of magnetic recording head technology and optimisation of their geometry and dimensions (including shielding), asymmetrical head structures appeared as good candidates to increase the recording resolution in longitudinal and perpendicular recording. This can be understood by examining the magnetic surface charge density near a single corner which is equal to the normal component of the surface field H_θ, and hence $\boldsymbol{M} \cdot \boldsymbol{n} = H_\theta = -1/\rho \, \partial u / d\theta$ where $\boldsymbol{n}$ is the vector normal to surface. Using the first term in the series expansion of the potential near a corner in Chapter 3 for simplicity and evaluating along one of the surfaces yields a surface charge density $\boldsymbol{M} \cdot \boldsymbol{n} \ \alpha \ \rho^{\frac{\pi}{3\pi/2+\theta_0}-1}$, where ρ is the distance from the corner apex. For increasing $\theta_0 > 0°$, the exponent in the surface charge

density is negative and sufficiently large to maintain the charge density concentration near the acute corner. This leads to increased field gradients near the acute pole corner in the gap region to further enhance the recording resolution of magnetic heads. While conventional two-dimensional magnetic heads, including the ring-type, finite-pole thin-film and single pole head structures mostly produce symmetrical fringing fields in the gap or pole corner regions.

While the field theory of conventional, right-angled symmetrical head structures is well established and enjoyed considerable success since the early 1950s, an analytical field theory of asymmetrical heads or symmetrical heads with tilted gap corners in general is lacking. The aim of this research is therefore to develop mathematical methods that enable the analytical modelling of the magnetic scalar potentials and magnetic fields from general symmetrical and asymmetrical magnetic recording heads with tilted gap corners, in the absence and presence of a soft magnetic underlayer. Thus providing, where possible, relatively simple closed-form solutions for the magnetic potentials and fields, that can be used in more detailed numerical simulations of the magnetic recording and readout processes with little computational overhead, and to understand the operation and help in the design of high performance magnetic recording heads.

The main assumptions used in this research is that the head structures are two-dimensional and semi-infinite (along the pole faces and through the thickness). This also follows the assumption that the head gap length is much shorter than other

dimensions in the head. The modelled potentials and fields are determined through solution of Laplace's equation, and therefore are static boundary value problems, and the magnetisation switching dynamics in the head are ignored. With inclined gap corners, the effect of corner saturation is expected to become more important. Saturation of corner regions reduces the permeability in these regions, leading to increases in the effect head gap length and increases in head separation due to the loss of the magnetic material in the gap corner regions. These effects cause degradation in the gradients of writing fields and performance of recording heads, particularly for small head to medium separations. Pole corner saturation in symmetrical and asymmetrical heads is beyond the scope of study, and was examined numerically using finite-elements in [52], by examining and comparing the fields from low saturation, asymmetrical *MnZn* heads modelled in two-dimensions with infinite permeability cores (assumption used in this work), and with linear and non-linear B-H core characteristics. Saturation was induced with a magnetomotive force corresponding to a deep-gap field greater than half the saturation magnetisation of the core material [113]. Their study showed that while the distributions of the magnetic fields from these different models are very similar, severe saturation occurred for inclination angles $\theta_0 > 45°$ in the linear and non-linear head material models, causing large reductions in the magnitude of the fields near the acute corner of the head (when compared to the infinite permeability model). With higher saturation core material and careful control over the core magnetic fields, it is expected that the theory presented in this work would be applicable to two-dimensional heads with a wider range of exterior corner angles of $\theta_0 > 45°$.

7.1 Conclusions and Contribution to Knowledge

The aim of this project was to develop mathematical methods and model corner-type heads, and derive approximate solutions for the fields from symmetrical and asymmetrical heads without a SUL, and with a SUL. Two methods were developed in this thesis to provide analytical solutions to this boundary value problem: in the first approach, the potential near a corner was derived exactly (explicitly), followed by application of superposition of the potentials and fields of two corners at equal but opposite magnetic potential and displaced from each other by a distance equal to the gap length to model symmetrical and asymmetrical heads fields. The second developed method uses a rational function to approximate the surface potential of asymmetrical head with adjustable parameters which were determined from fitting to finite-element simulations. The rational function approximation enabled the derivation of exact and closed-form solutions for the fields from asymmetrical head at any gap corner orientation. To overcome the limitations of current methods of modelling the effect of soft magnetic underlayers, a new theory based on the sine integral transform was developed in this thesis. This theory models the reaction of a soft magnetic underlayer on the surface potential and fields of any two-dimensional head structure, requiring only the surface potential or field in the absence of an underlayer as input, which is readily available. Through this theoretical framework and analysis, this research also delivers a quantitative understanding of magnetic fields produced by tilted gap corner heads (asymmetrical and symmetrical) and their correlation to the corner angles.

7.1.1 Superposition Technique

In chapter 3 of this thesis, the magnetic scalar potential near a corner was derived exactly from solution of Laplace's equation in polar coordinates. At sufficiently close distances from the corner, the first term in the series expansion of the solution was taken to very good approximation, and superposition of the potentials of two corners was used to derive approximate, closed-form analytical expressions for the potential and fields from asymmetrical two dimensional heads structures in the absence of a soft underlayer. The results show a very good agreement to finite-element calculations on Comsol Multiphysics (estimated using the normalised root-mean-square deviation (RMSD)), confirming the validity of the superposition approximation to the range of exterior corner angles $0^{o}<\theta_0< 45^{o}$ with maximum RMSD of 28% for H_x, and 21% for H_y. Further increases in the exterior corner angle increases the mismatch between the magnetic charge density distributions on both head pole surfaces considered in the approximation, and leading to large deviation and error in this approximation. In general, it was found that the *y* component of the magnetic field evaluated using superposition show more agreement to the finite-element/exact solutions.

The derived surface potential and field was also convolved with the Green's function corresponding to the two-dimensional semi-infinite geometry bounded by two parallel planes corresponding to the head surface and a zero potential soft magnetic underlayer. This convolution accounts for the contribution of infinite number of images fields from the high permeability surfaces/image planes in this structure (or in other words an infinite number reflected fields between the two parallel planes). The

magnetic fields for asymmetrical and symmetrical heads in the presence of a SUL where therefore calculated in chapters 4 and 6, and their agreement with finite-element simulations were consistent with the calculations in chapter 3 without the underlayer for the range of exterior gap corner angles $0^o<\theta_0< 45^o$. This convolution integration does not model the reaction of the underlayer on the surface potential/fields used in the solution (normally for structures without an underlayer) and therefore was found to be valid for head-to-underlayer separations $d/g > 0.5$.

In chapter 6, the method of superposition of corner potential/fields was applied to two-dimensional symmetrical heads, and derived surface potential was in excellent agreement with exact solutions and with finite-element calculations for all range of exterior corner angles $0^o< \theta_0< 90^o$ with maximum RMSD of 5%, in presence and absence of an underlayer. This remarkable agreement may be explained by the equal amount of magnetic surface charge density contribution from both pole corners in the superposition process. Moreover, this also indicates that, within the range of corner angles above, that the charge density contribution within one gap length from each corner is sufficient to accurately model the magnetic potentials and fields near corners.

7.1.2 Rational function approximation

Chapter 5 was concerned with the detailed theoretical derivation of relatively simple closed-form approximations for the scalar magnetic surface potential and fields from two-dimensional asymmetrical magnetic heads and their Fourier transforms,

applicable to any arbitrary corner inclination angle. A rational mathematical function with adjustable coefficients was used to approximate the surface potential of asymmetrical heads. The adjustable coefficients describe the shift in the zero-crossing of the surface potential and change in curvature with corner angle. The adjustable coefficients were determined with high accuracy by fitting to finite-element calculations. The corresponding rational function approximation was found to reduce to the linear gap surface approximation for right-angled corners (with maximum error), and increases in accuracy with increasing asymmetry. Convolving this rational function approximation with the Green's function for two-dimensional semi-infinite structures without an underlayer, yielded closed-form solutions for the magnetic fields in the form of the superposition of horizontal and vertical Karlqvist field components, in addition to narrow gap head field components accounting for the reduction in the effective head gap length with increasing asymmetry towards the acute gap corner. Following the surface potential approximation, the accuracy of the derived expressions for the magnetic fields increase with increasing asymmetry, as confirmed by comparison to finite-element calculations.

7.1.3 Modelling the reaction of the underlayer

A new general theory based on the translated Sine Fourier series was developed to model and study the reaction of a soft magnetic underlayer (SUL) on the surface potential of any magnetic head structure and for $d/g < 0.5$, and applied to asymmetrical head structures. The input to this model is a mathematical description of the surface potential or field of any two-dimensional head structure in the absence of an underlayer, which is readily available. The reaction of underlayer is then

determined as an infinite sine series of correction terms to the supplied surface potential/field without an underlayer, whose coefficients are determined exactly and are functions of the head-to-underlayer separation and gap corner angle. The corrected surface potential/field for the reaction of the underlayer were then convolved numerically with the Green's function description for the underlayer to calculate the magnetic fields, which were in very good agreement with finite-element calculations particularly for head-to-underlayer separations $d/g < 0.5$. For increase underlayer separations, the set of correction terms tend to a small and negligible value, and the calculated fields are in agreement with the Green's function analysis in chapter 4.

7.1.4 Analysis of magnetic fields from tilted gap heads

The theory developed in this thesis provides quantitative understanding of the behaviour of the magnetic fields from two-dimensional gapped head structures with tilted gap corners. In asymmetrical heads, the zero-crossing of the surface gap potential shifts towards the acute pole corner with increase in its gradient near that corner. This leads to reduction in the effective head gap length towards the acute corner with increasing magnitude and gradient of the magnetic fields and narrowing of their distributions in this region. The narrowing of the effective gap length in this case increases the spatial bandwidth of the head and increasing its resolution (hence the suggestion of using such heads for high density inductive readout in the past [114]). The presence of an underlayer in asymmetrical heads has small effect on the zero-crossing of the surface potential but further reduces its gradient in the gap central region and enhances it in the acute gap corner region. This leads to further increases

in the magnitude and gradient of the magnetic fields in the acute corner region (in particular the *y*-component of the magnetic field), and reduction of their magnitude and gradient towards the gap centre.

With equal contributions of surface charge densities in symmetrical heads, the surface potential was found to decrease in gradient in the central gap region, with increasing gradient towards the gap corners. This increase in field gradient increases the magnitude of the magnetic fields and their gradients in the gap regions. At the same time, the increase in gradient of surface potential at the corners increases the effective head gap length, leading to reductions in the field magnitudes in the gap region and reduction in the wavelength content of the head. Nevertheless, it was found that the above changes in surface potential and corresponding magnetic fields are modest as the gap corner angle spans the whole range of angles $0^o < \theta_0 < 90^o$. This may go some way in explaining the success of the simplified head fields theories (such as Karlqvist's) in modelling a wide range of practical symmetrical magnetic recording head structures and closely predicting their experimental performances despite the varying manufacturing conditions and their tolerances that lead to non-ideal or symmetrical head geometries.

7.2 Future Work

The analyses of asymmetrical head geometry can be also extended to produce mathematical models of more complex, shielded corner-type heads with multiple gaps

(analytically and numerically), and optimise the shielded head design to maximise field gradients.

Due to the remarkable success of the superposition method for predicting the potentials and field of symmetrical heads, it would be interesting to investigate the applicability of this approach to other symmetrical head structures such as the parallel plate head, the tilted plate head and the tilted pole head structures.

With inclined gap corners, the effect of corner saturation on the produced magnetic fields becomes very important, and corner saturation in this case must be characterised as a function of gap corner angle. This can be carried out by solving a vector potential boundary value problem, with non-linear B-H characteristics described using a functional dependence of the permeability of the core material on driving fields [113]. The simulations must be carried out for a range of gap corner angles and deviations from the linear behaviour can be used to characterise the fields required for the onset of saturation as a fraction of the core material saturation magnetisation.

Appendices

A. Solution of Laplace's equation using the translated Sine transform

Laplace's equation in two-dimensions for the scalar magnetic potential u for the geometry shown in Figure 5.9 in the absence of the underlayer (i.e. $d \to \infty$) is given by:

$$\frac{\partial^2 u}{\partial x^2} + \frac{\partial^2 u}{\partial y^2} = 0$$

Taking the translated Sine integral transform of Laplace's equation, defined for $u(x,y)$ as:

$$\overline{u'}(\kappa_n, y) = \int_{x=-g/2}^{g/2} u'(x,y) \sin\left(\kappa_n (x - g/2)\right) dx$$

and applying successive integration by parts, observing the boundary conditions indicated in Figure 5.9 with eignvalues $\kappa_n = n\pi / g$, reduces Laplace's equation to the ordinary differential equation:

$$\frac{\partial^2 \overline{u'}}{\partial y^2} - \kappa_n^2 \left(\overline{u'} - \overline{v}\right) = 0 \qquad \text{(A.1)}$$

where the eigenvalues $\kappa_n = n\pi/g$ and eigenfunctions $\sin(\kappa_n(x-g/2))$ satisfy the boundary conditions shown in Figure 5.9, and allow asymmetrical description of $u'(x,0)$ in the transform. $\bar{v}$ is the integral transform of the linear gap potential at $y = 0$, and is defined by:

$$\bar{v}(\kappa_n,0) = \int_{x=-g/2}^{g/2} \left(\frac{2U_0 x}{g}\right) \sin(\kappa_n (x - g/2)) dx$$

The general solution to (A.1) is given by:

$$\overline{u'}(\kappa_n, y) = Ce^{\kappa_n y} + De^{-\kappa_n y} + \bar{v} \qquad \text{(A.2)}$$

where C and D are the constants of the integration. Application of the boundary conditions that $\overline{u'}$ vanishes as $y \to \infty$, with prescribed surface potential $\overline{u'}(\kappa_n,0)$ at $y = 0$ yields the particular solution of (A.2) as:

$$\overline{u'}(\kappa_n, y) = \left(\overline{u'}(\kappa_n,0) - \bar{v}\right)e^{-\kappa_n y} + \bar{v} \qquad \text{(A.3)}$$

The normal derivative of the integral transform of the potential is therefore given by:

$$\frac{\partial \overline{u'}(\kappa_n, y)}{\partial y} = -\kappa_n \left(\overline{u'}(\kappa_n,0) - \bar{v}\right)e^{-\kappa_n y} \qquad \text{(A.4)}$$

B. Publication

Mustafa M. Aziz, Ammar I. Edress, and C. David Wright, ‘Approximate Expressions for the Magnetic Potential and Fields of Two-Dimensional’, Asymmetrical Magnetic Recording Heads’. IEEE Trans. Magn. vol.52, no.2, pp. 1-12, Feb. 2016.

Approximate Expressions for the Magnetic Potential and Fields of 2-D, Asymmetrical Magnetic Recording Heads

Mustafa M. Aziz, Ammar I. Edress, and C. David Wright

College of Engineering, Mathematics and Physical Sciences, University of Exeter, Exeter EX4 4QF, U.K.

A 2-D asymmetrical magnetic head is characterized by the parallel inclination of the semi-infinite, inner gap walls, and where the gap length and head-to-underlayer separation are small compared with the other dimensions in the head. With head corner inclination, these structures contribute to the reduction in the effective gap length of the head and, therefore, the increase in the field magnitude and narrowing of the field distributions near the acute gap corner. Asymmetrical heads were, therefore, proposed for increasing the writing and readout resolutions in gapped magnetic head structures. There are currently no explicit or approximate analytical solutions for the potential and fields from 2-D asymmetrical magnetic heads. This paper is concerned with the detailed theoretical derivation of relatively simple closed-form approximations for the scalar magnetic potential and fields from 2-D asymmetrical magnetic heads and their Fourier transforms, applicable to any arbitrary corner inclination angle. A general theory based on the translated sine Fourier series is developed to model and study the reaction of a soft magnetic underlayer on the surface potential of any magnetic head structure, and applied to the asymmetrical head. The approximate potential and field expressions derived in this paper demonstrated a very good agreement with the finite-element calculations of the 2-D asymmetrical heads.

Index Terms—**Asymmetrical heads, Fourier series, Laplace's equation, magnetic fields, magnetic recording.**

I. Introduction

THE MAGNETIC head is an integral part of magnetic recording systems. The head geometry and dimensions determine the magnitude and distribution of the fringing gap fields and their gradients, therefore affecting the size and shape of the recorded magnetization pattern in the magnetic medium during recording, and the resolving performance of the head in readout [1]. The design of magnetic heads, therefore, has a direct impact on the achievable storage density of the magnetic recording systems.

The conventional 2-D magnetic heads, including the ring-type, finite-pole thin-film, and single-pole head structures, have symmetrical pole geometry and produce mostly symmetrical fringing fields in the gap or pole corner regions. Asymmetric heads differ by rotating, in parallel, the pole corners in the gap region through exterior angle θ, as indicated in two-dimensions in Fig. 1, where the x-axis is the direction along the head/medium motion and the y-axis is normal to the head surface. In this 2-D geometry, the cross-track direction (along z-axis) is assumed much larger in extent compared with the gap length g and the head-to-underlayer separation d.

The significance of the asymmetrical head shown in Fig. 1 arises from the increased magnetic charge density in the acute head corner [2]. This leads to an increase in the magnitude of the magnetic fields in this region and narrowing of their distributions, as will be shown later in this paper. Asymmetric heads were, therefore, proposed for increasing the recording resolution in longitudinal and perpendicular recording due to the increased field gradients near the acute pole corner in the gap region [3]. Asymmetrical heads were also suggested as a method of increasing the readout resolution of the ring-type inductive heads and develop gap-null free heads [4], primarily through the natural reduction in the effective gap length of the head with the increase in θ enabling shorter recorded magnetization patterns in the recording medium to be resolved. Asymmetric head designs were also incorporated in perpendicular heads with tapering in both the main pole and side shields to increase the recording fields and their gradients and to reduce side fringing [5]. This tapered single-pole head structure with tapered shields, incorporating the asymmetric gapped geometry, were also investigated as part of corner-type head designs for high-resolution, 2-D magnetic recording [6].

There are currently neither explicit nor approximate expressions for the potential and fields for asymmetrical magnetic

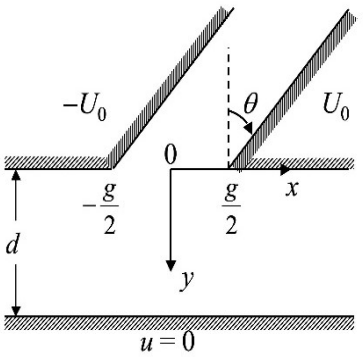

Fig. 1. 2-D geometry of the asymmetrical head, with gap length g and exterior corner inclination angle θ. The poles are assumed to have infinite permeability and, therefore, with equipotentials $\pm U_0$, at a distance d from an SUL held at zero potential. To model 2-D heads without an underlayer, the SUL is removed with $d \to \infty$.

Manuscript received August 9, 2015; revised September 23, 2015 and September 25, 2015; accepted October 13, 2015. Date of publication October 19, 2015; date of current version January 18, 2016. Corresponding author: M. M. Aziz (e-mail: m.m.aziz@exeter.ac.uk).

Color versions of one or more of the figures in this paper are available online at http://ieeexplore.ieee.org.

Digital Object Identifier 10.1109/TMAG.2015.2492947

recording heads. Therefore, the explicit functional dependence of the corresponding magnetic fields' magnitude, gradient, and wavelength response on the head parameters (such as θ, g, and d) is not well understood. The difficulty in deriving explicit solutions for the potentials and the fields of asymmetrical heads arises from the fact that the geometry does not conform to the conventional coordinate systems, for which the formal methods of solution can be applied. Implicit, conformal mapping solutions were previously derived exactly for asymmetrical heads, but only for limited (rational) corner angles [7], [8]. Conformal mapping solutions require numerical inversion to explicitly determine the vector fields in the space surrounding the head surface, and are thus not practical to use in head design and optimization studies, or in more complex simulations of the record and readout processes. This paper, therefore, provides, for the first time, detailed and comprehensive derivations of relatively simple analytical approximations for the magnetic scalar potential and fields from asymmetrical heads with and without a soft magnetic underlayer (SUL), for any exterior corner inclination angle θ (0°–90°).

Fields from magnetic heads can be derived from the solution of the boundary value problem involving Laplace's equation for the scalar magnetic potential, u, which in two dimensions is written as

$$\frac{\partial^2 u}{\partial x^2} + \frac{\partial^2 u}{\partial y^2} = 0 \tag{1}$$

using the assumption that the head pole pieces are infinitely permeable, thus providing the equipotential boundaries for this system. The magnetic fields $\boldsymbol{H}$ are then determined from the gradient of the potential $\boldsymbol{H} = -\nabla u$. It is generally difficult to derive explicit and exact solutions to Laplace's equation for the common 2-D magnetic head geometries directly. The rigorous approach has been to divide the head into rectangular regions inside the gap and beyond the head poles, and derive general solutions for the scalar potential in these regions in the form of an infinite Fourier series. Forcing the continuity of potentials and normal fields at the interfaces between these rectangular regions enables the determination of the Fourier coefficients. The few exact solutions derived in this way are for the conventional symmetrical (right-angled) head structures, including the ring-type head [9], [10], single-pole and perpendicular heads [11], [12], and their shielded varieties [13]. The Fourier coefficients [11], [14] in these series solutions are normally determined implicitly from the solution of a large system of linear equations and involve numerical integration, which complicates the evaluation of the magnetic potentials and fields. An alternative approach for mapping the magnetic fields from 2-D head structures involves explicitly specifying the potential or the field distribution along the head surface, and convolving this distribution with the appropriate Green's function for the specific geometry and boundary conditions of the problem to obtain the potential and fields everywhere beyond the head surface. The accuracy of this method relies heavily on the assumed surface potential or field. The well-known Karlqvist approximation [15], for example, assumes a linear gap surface potential following the potential deep inside the gap in a ring-type head, to predict simple and convenient closed-form expressions for the fields beyond the head surface. One approach that has been adopted for the determination of more accurate surface field distributions is through assuming a plausible rational function approximation for the surface fields in the gap region and beyond pole corners, with adjustable coefficients that are determined through fitting to computer models of the magnetic head (such as finite elements) (see [16]). These simplified rational function approximations are then convolved with the appropriate Green's functions to determine the fields everywhere beyond the head surface. In this paper, a combination of the aforementioned methods will be used to arrive at explicit and approximate closed-form expressions for the potential and fields for 2-D asymmetrical heads as outlined next.

Asymmetrical heads exhibit non-equal surface charge distributions in the pole corners, leading to asymmetry in the gap surface potential. In this paper, this asymmetry in head surface potential is modeled, in the absence of an SUL, using a rational function approximation, derived from the analysis of finite-element solution to Laplace's equation for this geometry at different corner angles θ in the range $0° \rightarrow 90°$. The approximate surface potential is then convolved with Green's function solution for the semi-infinite, 2-D geometry considered here to determine the potential and the fields everywhere beyond the surface of the head. In the presence of an SUL, a general and approximate theory, based on the integral transform method, for any 2-D gapped head structure is developed to approximate the reaction of the high-permeability underlayer on the known head surface potential in the absence of the underlayer. This modified surface potential is then convolved with the 2-D Green's function for the head/underlayer combination to determine the fields everywhere beyond the head surface. The Fourier transform of the asymmetrical head surface field, in the presence and the absence of an SUL, is also derived exactly to study the effect of corner angle inclination on the wavelength response of asymmetrical heads.

For the mathematics to remain analytical and tractable, the theory presented here is for 2-D head structures with infinite-cross-track width, and based on magnetostatics. Therefore, transient effects are neglected, and the effects of finite-track width of the head are not considered. Increasing the exterior angle θ increases the magnetic flux density in the acute head corner, leading to corner saturation that occurs at lower driving fields compared with right-angled corners. Pole saturation affects the gradient of the fields and degrades the recording performance especially at small head-to-recording medium separations [18]. Studying and modeling pole saturation in asymmetrical heads and in the SUL requires a full numerical treatment, which is beyond the scope and length of this paper. Corner saturation in asymmetrical heads was examined numerically using finite elements in two dimensions in [19] using linear and non-linear B–H models of the field dependence of permeability for low saturation MnZn ferrites. Saturation was induced with a deep-gap driving field greater than half the saturation magnetization of the core material [18]. Their study showed that severe saturation occurred for inclination angles $\theta > 40°$ causing large reductions in the magnitude of

the fields near the acute corner of the head (when compared with the infinite permeability model).

To study the validity of the approximate models and estimate the errors in the approximations, Laplace's equation was solved in two-dimensions numerically using finite elements on Comsol Multiphysics [17]. The geometry and boundary conditions used in the finite-element simulations follow from Fig. 1, with the simulation space terminated by zero-potential planes at very large distances from the gap region to model semi-infinite head structures in the absence of an underlayer, or with the zero potential plane at a distance d from the head surface in the presence of an underlayer. Adaptive and progressive mesh refinement was employed in the boundaries near the head corners to increase the mesh resolution in the (tilted) corner regions to accurately evaluate the potentials and fields.

In this paper, the closeness of the approximate potential and field models to the more accurate finite-element calculations is estimated using the absolute root-mean-square deviation (RMSD), defined as

$$\text{RMSD} = \sqrt{\frac{1}{N}\sum_{n=1}^{N}(\hat{f}_n - f_n)^2}$$

where $\hat{f}_n$ is the approximated model value, f_n is the finite-element data, and the summation is taken over N data points. The RMSD is a global, absolute measure with the same units as the potential or fields used in the estimation, with lower values indicating less deviation from the accurate finite-element simulations. The RMSD will, therefore, be normalized by the extreme in the potential or field magnitudes to estimate the percentage deviation.

This paper will begin with the derivation of the rational function approximation for the surface potential for 2-D asymmetrical heads in the absence of an SUL in Section II. The integral transform approach is used in this section to derive a general theory for modeling the reaction of the underlayer on the surface potential. The surface potentials are then used in Section III along with the 2-D Green's functions to derive expressions for the magnetic fields beyond the head surface. In Section IV and before concluding this paper, the Fourier transform of the surface fields is derived to explore the effect of asymmetry on the wavelength content of the fields. The validity of the approximate magnetic potential and field models, and their limitations and improvements are discussed in the relevant sections of this paper.

II. Surface Potential Approximations

In this section, approximate expressions are derived for the surface magnetic potential for asymmetrical heads with and without an SUL. These will be later convolved with Green's function for the magnetic head geometry to determine the potentials and fields everywhere beyond the head surface.

A. Without Underlayer

The gap surface potential for an asymmetrical head calculated using finite elements is shown in Fig. 2 for a number

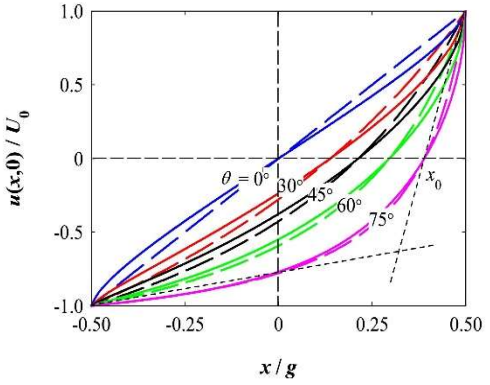

Fig. 2. Calculated gap surface potential using finite elements (solid lines) and the approximate surface potential in (2) and (3) (dashed lines) for different corner angles. The dotted straight lines highlight the approximate hyperbolic locus of the asymmetrical potential, and were used as guides to derive the rational function approximation for the potential.

of exterior corner angles θ. For right-angled corners ($\theta = 0°$), the gap potential is symmetrical with increasing gradient (and therefore fields) near the gap corners at $\pm g/2$ [1]. Increasing θ increases the asymmetry in the potential due to the increased magnetic surface charge density in the acute corner at $x = g/2$, and shifts the zero-crossing of the potential toward this corner. This displacement of the potential zero-crossing leads to a reduction in the effective gap length of the head. In the limit where $\theta \to 90°$, the effective gap length reduces to zero toward the right corner producing a step change in the surface potential at $x = g/2$, leading to the narrow gap or far field potential distribution [1].

The surface gap potential determined by finite elements in Fig. 2 may be characterized by both: 1) a shift in the zero-crossing, x_0, of the potential and 2) a scaling of the potential magnitude and gradient near the origin, with changes in exterior corner angle θ. This surface gap potential approximately traces a hyperbola joining the two intersecting straight dashed lines, as shown in Fig. 2 (shown for $\theta = 75°$ as an example). Thus, the gap surface potential may be described using the following rational function:

$$u(x,0) = a + \frac{b}{c+x}.$$

The constants a, b, and c were determined by requiring that the potential satisfies the conditions $u = \pm U_0$ at $x = \pm g/2$, and that the potential vanishes at $x = x_0$ where x_0 is a function of θ. This yields the following approximate surface potential:

$$u(x,0) = \begin{cases} -U_0 & x < -g/2 \\ \dfrac{g}{2}\dfrac{U_0(x-x_0)}{(g^2/4 - x_0 x)} & -g/2 \le x \le g/2 \\ U_0 & x > g/2. \end{cases} \quad (2)$$

The potential in (2) is continuous and differentiable over the gap length, therefore, satisfying the continuity requirement of the potential and fields in the gap. When $\theta = 0°$ (and $x_0 = 0$), the head is symmetrical, and the gap potential in (2) reduces

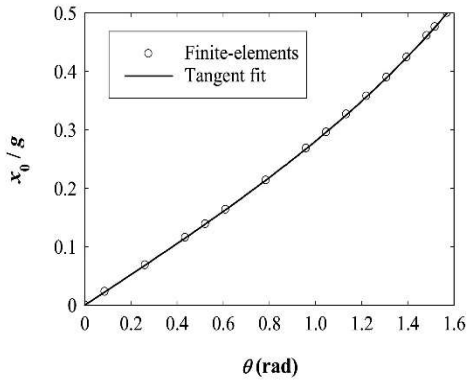

Fig. 3. Dependence of the zero-crossing shift of the gap potential, x_0, on the corner angle θ, determined from the finite-element solution of Laplace's equation (circles). Solid line: least squares fitting to the finite-element data using the tangent function with the best fit parameters: $x_0/g = 0.564\tan(0.462\theta)$.

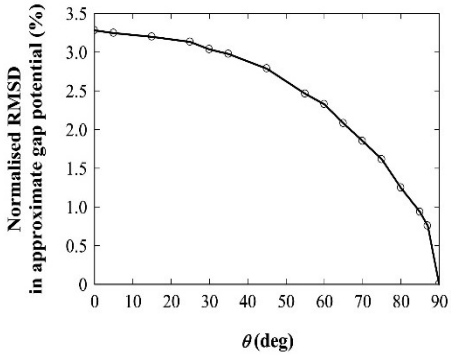

Fig. 4. RMSD between the approximate gap potential in (2) and the finite-element calculations, normalized by maximum change of potential in the gap ($2U_0$), as a function of the exterior corner angle θ. This plot shows the increase in the accuracy of the rational function approximation for the surface potential with increasing θ.

to the linear (Karlqvist) approximation [16]. As $\theta \to 90°$ (and $x_0 - g/2$), (2) produces a step function change in the potential along the head surface at $x = g/2$ to model the narrow-gap head.

The dependence of the shift in the zero-crossing of the gap potential, x_0, on corner angle θ was determined from the finite-element calculations and is shown in Fig. 3 (open circles). The tangent function was found to provide the best least-squares fit to this dependence using the following fitting parameters:

$$\frac{x_0}{g} = 0.564\tan(0.462\theta) \quad 0 \le x_0 \le g/2, \quad 0 \le \theta \le \pi/2. \quad (3)$$

Equation (3) is shown in Fig. 3 (solid line) with a very small absolute rms deviation of 3.71×10^{-4} from the finite-element data. Therefore, (3) will be used subsequently in this paper for the determination of x_0 for a given corner angle θ.

The approximate surface gap potential in (2) is plotted in Fig. 2 (dashed lines) using the calculated values of x_0 from (3), showing good agreement with the finite-element potential for different values of θ. Fig. 4 shows the RMSD between the approximate potential and finite-element calculations,

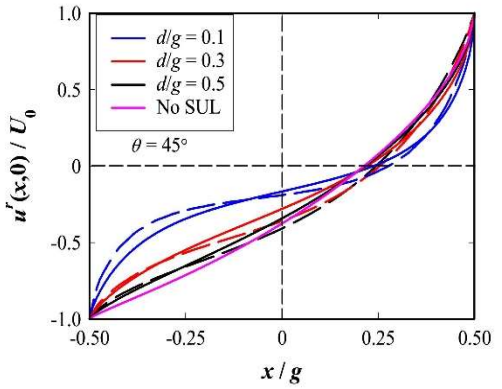

Fig. 5. Normalized surface potential for an asymmetrical head with corner angle of 45° in the presence of an SUL, calculated using finite elements (solid lines) and using the Fourier integral transform approximation in this paper (dashed lines). The surface potential without an SUL, calculated using finite elements, is shown for comparison.

normalized by the maximum change in the gap potential ($2U_0$), as a function of exterior corner angle. For small θ, the RMSD is 3.3% which is consistent with the error in the Karlqvist approximation for symmetrical heads. The RMSD reduces (and therefore accuracy increases) with increasing θ and correctly vanishes as $\theta \to 90°$ (narrow-gap limit). Another advantage of the surface potential approximation in (2) is that it enables the derivation of exact, and relatively simple, closed-form solutions for the potential and fields everywhere beyond the head surface, as illustrated later in this paper.

B. With Underlayer

The presence of an SUL modifies the magnetic circuit of the head and the distribution of the head surface potential [20]. The reaction of the underlayer on the surface potential for an asymmetrical head with $\theta = 45°$ is shown in Fig. 5, calculated using finite elements (solid lines) for different head-to-underlayer spacings. This figure shows that the effect of the underlayer is more prominent for small head-to-underlayer separations $d/g < 0.5$, resulting in the reduction of the surface potential and its gradient in the gap central region while increasing the potential gradient near the gap corners. With increasing the head-to-underlayer separation to the values of $d/g > 0.5$, the surface potential rapidly approaches the surface potential without an underlayer. The same behavior applies to other exterior corner angles, with the added displacement of the zero-crossing of the potential toward the acute corner with increasing θ, as previously described for the case without an underlayer.

Modeling the reaction of the underlayer on the head surface potential is complex due to the presence of finite boundaries in this problem. Theoretical developments commonly use the surface potential or surface field of magnetic heads in the absence of the underlayer, as an approximation, along with the appropriate Green's functions to determine the potential and fields everywhere beyond the head surface (see [21]). It will be shown, in this paper, that this approximation is only valid

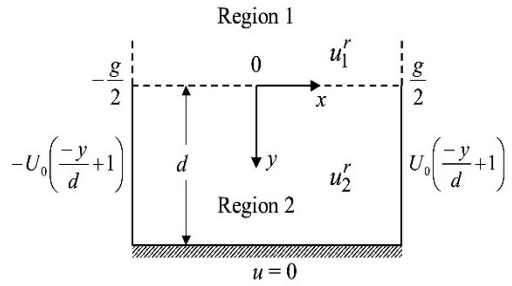

Fig. 6. Theoretical boundary value problem of the gap region for a general magnetic head with arbitrary surface potential distribution and a distance d from an SUL, used to derive a closed-form distribution of the resulting surface potential in response to the SUL. Region 1: magnetic head gap/surface. Region 2: area beyond the head surface.

for head-to-underlayer separations of $d/g > 0.5$. The only satisfactory theoretical treatment available to this boundary value problem is for symmetrical, right-angled corner heads, and involve solutions in the form of infinite Fourier series [11]. The coefficients of the Fourier series solution are determined implicitly from the numerically intensive solution of a truncated, infinite system of linear equations with terms requiring numerical integration. Their study [11] also highlighted that the approximation of using the surface potential or field in the absence of the underlayer represent only the first-order term of the complete and accurate solution for this problem. For asymmetrical heads, only a conformal mapping solution was derived for rational corner angles [9], which also requires numerical inversion. In here, a simplified and explicit general theoretical treatment of this boundary value problem is presented to determine the effect of an underlayer on the surface potential of an arbitrary head structure, requiring only the functional description of the surface potential in the absence of the underlayer.

The theoretical treatment starts by assuming the simplified, two-region, boundary value problem shown in Fig. 6 to represent the gap region of a general magnetic head (in Region 1) at close proximity d to an SUL beyond the head surface (Region 2). The geometry of this model is similar to the slot approximation proposed in [22] for the symmetrical ring-head, but generalized here to model any gapped head structure using the integral transform approach. To simplify the mathematical development and to a very good approximation for small head-to-underlayer separations, the potential on either side of the gap corners is assumed to vary linearly between the head and the underlayer, and vanishes at the SUL surface ($y = d$), as shown in Fig. 6.

Solving Laplace's equation through variable separation in Region 2 (beyond the head surface) subject to the boundary conditions indicated in Fig. 6 yields the following Fourier series solution for the potential in the presence of an underlayer:

$$u_2^r(x,y) = U_0\frac{2x}{g}\left(\frac{-y}{d}+1\right) + \sum_{m=1}^{\infty} B_m \sin(\kappa_m(x-g/2)) \times [e^{-\kappa_m y} - e^{\kappa_m(y-2d)}] \quad (4)$$

defined over $-g/2 \le x \le g/2$, where the eignvalues $\kappa_m = m\pi/g$ satisfy the boundary conditions, and the eigenfunctions $\sin(\kappa_m(x-g/2))$ were chosen to include translation along the x-axis to account for even and odd harmonics in the solution to describe the asymmetry in potential while satisfying the boundary conditions.

In Region 1, the magnetic head potential is assumed to have the general Fourier series solution

$$u_1^r(x,y) = \phi(x,y) + \sum_{m=1}^{\infty} A_m \sin(\kappa_m(x-g/2))e^{\kappa_m y} \quad (5)$$

over the gap region $-g/2 \le x \le g/2$, where $\phi(x,y)$ is the head potential distribution in the absence of the underlayer, satisfying the boundary conditions indicated in Fig. 6 at the head surface. The second, translated sine series term in (5) models the reaction of the underlayer and represents a series of correction terms to the potential $\phi(x,y)$, with coefficients A_m that are functions of the corner angle θ and head-to-underlayer separation d. Again, the translated eigenfunctions are chosen to model the asymmetry in the potential and, together with the eignvalues $\kappa_m = m\pi/g$, satisfy the boundary conditions at the interface $y = 0$. The assumed y-dependence in the Fourier series term in (5) follows the exponential decay of fields and potentials expected inside 2-D permeable head structures.

The coefficients A_m and B_m in (4) and (5) are determined by forcing the continuity of the potentials (i.e., $u_1^r = u_2^r$) and normal fields (i.e., $-du_1^r/dy = -du_2^r/dy$) at the interface $y = 0$. Multiplying the two continuity equations by $\sin(\kappa_n(x-g/2))$ and integrating over the gap length $\pm g/2$, noting the orthagonality of the translated sine function

$$\int_{x=-g/2}^{g/2} \sin(\kappa_m(x-g/2))\sin(\kappa_n(x-g/2))dx = \begin{cases} 0 & m \ne n \\ g/2 & m = n \end{cases}$$

yields two algebraic equations, which can be solved exactly to reveal the following Fourier coefficients:

$$A_n = -\bar{\phi}\frac{(1+e^{-2\kappa_n d})}{g} - \left[\frac{\partial\bar{\phi}}{\partial y}\right]_{y=0}\frac{(1-e^{-2\kappa_n d})}{\kappa_n g} + \frac{\bar{v}}{g/2}\left[1-\frac{1}{2}\left(1+\frac{1}{\kappa_n d}\right)(1-e^{-2\kappa_n d})\right] \quad (6a)$$

$$B_n = \frac{\bar{\phi}}{g} - \frac{1}{\kappa_n g}\left[\frac{\partial\bar{\phi}}{\partial y}\right]_{y=0} - \frac{\bar{v}}{g}\left(1+\frac{1}{\kappa_n d}\right) \quad (6b)$$

where the overlines indicate integral transforms defined by

$$\bar{\phi}(\kappa_n,0) = \int_{x=-g/2}^{g/2} \phi(x,0)\sin(\kappa_n(x-g/2))dx \quad (7a)$$

$$\left.\frac{\partial\bar{\phi}(\kappa_n)}{\partial y}\right|_{y=0} = \int_{x=-g/2}^{g/2} \left.\frac{\partial\phi}{\partial y}\right|_{y=0} \sin(\kappa_n(x-g/2))dx \quad (7b)$$

where $\bar{v}$ is the integral transform of the linear gap potential term at $y = 0$ that evaluates exactly to

$$\bar{v}(\kappa_n,0) = \int_{x=-g/2}^{g/2}\left(\frac{2U_0 x}{g}\right)\sin(\kappa_n(x-g/2))dx = -\frac{U_0}{\kappa_n}[1+(-1)^n]. \quad (8)$$

To maintain consistency with the geometry in Fig. 6, $\partial\bar{\phi}/\partial y$ in (6) is determined from the Fourier integral transform of Laplace's equation as detailed in the Appendix. This provides the integral transform of the derivative of the surface potential as

$$\left.\frac{\partial\bar{\phi}}{\partial y}\right|_{y=0} = -\kappa_m(\bar{\phi}-\bar{v}) \tag{9}$$

which upon substitution in (6) yields the simplified Fourier coefficients

$$A_n = \frac{-2e^{-2\kappa_n d}}{g}(\bar{\phi}-\bar{v}) + \frac{\bar{v}}{g\kappa_n d}(e^{-2\kappa_n d}-1) \tag{10a}$$

$$B_n = \frac{2}{g}(\bar{\phi}-\bar{v}) - \frac{\bar{v}}{g\kappa_n d}. \tag{10b}$$

This completes the formal solution of the boundary value problem described in Fig. 6. The closed form, explicit Fourier series representation of the potentials in (4) and (5) and their coefficients in (10), can be used to model the surface potential and fields of general 2-D head structures. Moreover, the potentials in (4) or (5) evaluated at $y = 0$ along with the coefficient in (10) correctly produce the surface potential in the absence of the underlayer in (2) as $d \to \infty$. The Fourier coefficients in (10) are functions of the head-to-underlayer separation d, the exterior corner angle θ (through x_0), and head gap length g. The determination of these coefficients requires only knowledge of the surface potential distribution in the absence of an underlayer, which is normally available.

For the asymmetrical head considered here, the surface potential in the presence of the underlayer can now be determined by substituting $\phi(x,0) = u(x,0)$ from (2) into (4) [or (5)] and evaluating the series coefficients in (10). The integral transform of the surface potential of the asymmetrical head (needed for the evaluation of the coefficients) can be integrated exactly in (7a) and is given by

$$\bar{\phi}(\kappa_n,0) = \frac{gU_0}{2x_0^2}\Big\{-x_0(-1+(-1)^n)/\kappa_n + \left(g^2/4 - x_0^2\right) \times\big[\sin(\alpha)(-\mathrm{Ci}(\alpha)+\mathrm{Ci}(\beta)) - \cos(\alpha)(-\mathrm{Si}(\alpha)+\mathrm{Si}(\beta))\big]\Big\} \tag{11}$$

where $\alpha = g\kappa_n(g/2-x_0)/2x_0$, $\beta = g\kappa_n(g/2+x_0)/2x_0$, $\bar{v}$ is defined in (8), and Si and Ci are the sine and cosine integrals, respectively [23].

Fig. 5 shows the calculated surface potential for the asymmetrical head with an underlayer for corner angle $\theta = 45°$ using (4) [or equally (5)] (dashed lines) for different head-to-underlayer separations. There is a very good agreement between the approximate potential calculated using (4) or (5) and the finite-element calculations in Fig. 5, with maximum normalized RMSD of about 2.8%, that is consistent for other head corner angles. The rate of convergence of the Fourier coefficients in (10) depends on the head-to-underlayer separation d, and on the corner angle θ. For head-to-underlayer separations of $d/g \geq 0.5$, the coefficients converge rapidly, and 20 terms (coefficients) were found sufficient, for any θ, in evaluating the surface potential in (4) [or equally (5)]. More terms are necessary for head-to-underlayer separation of $d/g < 0.5$, with up to 40 terms needed for the evaluation of the surface potential at $d/g = 0.1$ in Fig. 5. The number of required series terms can increase with increasing corner inclination θ, to correctly sample larger gradients (short wavelength behavior) in the potential and fields at the acute corner.

III. Head Magnetic Fields

The magnetic surface potentials derived in Section II will now be convolved with Green's function for the asymmetrical head to determine the potential and fields everywhere beyond the head surface. Determining the magnetic fields directly using the surface fields rather than potentials, however, is easier mathematically with the convolution integrals evaluated only over the gap region (since the surface fields vanish over the infinitely permeable poles). This is the approach adopted in this section. Extensive use will be made of the Fourier transform and its inverse for the derivation of Green's functions and field spectra in this paper. The Fourier transform and its inverse are defined, respectively, for the spatial function $f(x)$ by

$$F(k) = \int_{x=-\infty}^{\infty} e^{-jkx} f(x)dx \tag{12a}$$

$$f(x) = \frac{1}{2\pi}\int_{k=-\infty}^{\infty} e^{jkx} F(k)dk \tag{12b}$$

where $k = 2\pi/\lambda$ is the wavenumber at wavelength λ.

To derive the appropriate Green's functions for the asymmetrical head, the spatial Fourier transform of Laplace's equation in (1) is first taken to remove the x-dependence of the scalar potential. This yields the ordinary differential equation

$$\frac{\partial^2 u(k,y)}{\partial y^2} - k^2 u(k,y) = 0 \tag{13}$$

which is solved next for the appropriate boundary conditions in the absence and the presence of an SUL.

A. Without Underlayer

For this semi-infinite geometry (when $d \to \infty$ in Fig. 1), the boundary conditions are such that there is a prescribed surface potential, $u(k,0)$ at $y = 0$, and a vanishing potential as $y \to \infty$. This yields the classical spacing loss dependence of the potential (and fields) on one side of semi-infinite structures

$$u(k,y) = u(k,0)e^{-ky}. \tag{14}$$

To reduce the complexity of the mathematical derivations, the gradient of the potential in (14) is taken to produce the Fourier transforms of the magnetic fields

$$H_x(k,y) = H_x(k,0)e^{-ky} \tag{15a}$$

$$H_y(k,y) = j\,\mathrm{sgn}(k)H_x(k,0)e^{-ky} \tag{15b}$$

where H_x and H_y are the x-component and y-component of the magnetic field, respectively, $H_x(k,0)$ is the Fourier transform of the x-component of the surface field, and sgn is the signum function. Taking the inverse Fourier transform of (15) and invoking the convolution theorem of Fourier transforms yields the magnetic fields beyond the head surface

$$H_x(x,y) = \frac{y}{\pi}\int_{x'=-\infty}^{\infty} \frac{H_x(x',0)}{(x'-x)^2+y^2}dx' \tag{16a}$$

$$H_y(x,y) = \frac{-1}{\pi}\int_{x'=-\infty}^{\infty} \frac{H_x(x',0)(x'-x)}{(x'-x)^2+y^2}dx'. \tag{16b}$$

For the asymmetrical head considered in this paper, the magnetic field along the head surface is determined from the gradient of the surface potential in (2) which is given by

$$H_x(x,0) = \frac{-\partial u(x,0)}{\partial x} = \frac{-gU_0}{2}\frac{(g^2/4 - x_0^2)}{(g^2/4 - x_0 x)^2}. \quad (17)$$

Substituting (17) into (16a), and integrating over the gap length yields exactly the x-component of the magnetic field everywhere beyond the head surface as

$$\begin{aligned} H_x(x,y) &= \frac{-g^2 H_0}{4\pi}\left\{\frac{x_0^2 y}{g/4((g^2/4 - x_0x)^2 + x_0^2y^2)}\right. \\ &\quad + \frac{(g^2/4 - x_0^2)}{((g^2/4 - x_0x)^2 + x_0^2y^2)^2} \\ &\quad \times \left[h_x^k(x,y)((g^2/4 - x_0x)^2 - x_0^2y^2)\right. \\ &\quad + x_0y(g^2/4 - x_0x) \\ &\quad \left.\left. \times \left[h_y^k(x,y) + \ln\left(\frac{(g/2 + x_0)^2}{(g/2 - x_0)^2}\right)\right]\right]\right\} \quad (18) \end{aligned}$$

while substituting (17) into (16b) yields exactly the y-component of the magnetic field as

$$\begin{aligned} H_y(x,y) &= \frac{-g^2 H_0}{2\pi}\left\{\frac{-x_0(g^2/4 - x_0x)}{g/2((g^2/4 - x_0x)^2 + x_0^2y^2)}\right. \\ &\quad + \frac{(g^2/4 - x_0^2)}{((g^2/4 - x_0x)^2 + x_0^2y^2)^2} \\ &\quad \times \left[x_0y(g^2/4 - x_0x)h_x^k(x,y)\right. \\ &\quad - \frac{1}{4}((g^2/4 - x_0x) - x_0^2y^2) \\ &\quad \left.\left. \times \left[h_y^k(x,y) + \ln\left(\frac{(g/2 + x_0)^2}{(g/2 - x_0)^2}\right)\right]\right]\right\} \quad (19) \end{aligned}$$

where

$$h_x^k(x,y) = \tan^{-1}\left(\frac{x + g/2}{y}\right) - \tan^{-1}\left(\frac{x - g/2}{y}\right)$$

and

$$h_y^k(x,y) = \ln\left[\frac{(x - g/2)^2 + y^2}{(x + g/2)^2 + y^2}\right]$$

are the normalized field components for the symmetrical (right-angled) head with linear gap potential (Karlqvist approximations), and $H_0 = 2U_0/g$ is the x-component of the deep-gap field. The first terms on the right-hand side of (18) and (19) describe the increase in surface charge density on the right corner with increasing exterior angle θ, and correctly yield the narrow-gap fields as $\theta \to 90°$ (and $x_0 \to g/2$). Similarly, (18) and (19) correctly reduce to the Karlqvist field approximations when the head is symmetrical at $\theta = 0°$ (and hence $x_0 = 0$). Moreover, the examination of (18) and (19) reveals that the fields of asymmetrical heads (in the absence of an underlayer) may approximately be constructed from a weighted sum of the x-component and y-component of the magnetic fields of the symmetrical (right-angled) head and the narrow-gap head, where the weights are functions of the exterior corner angle θ.

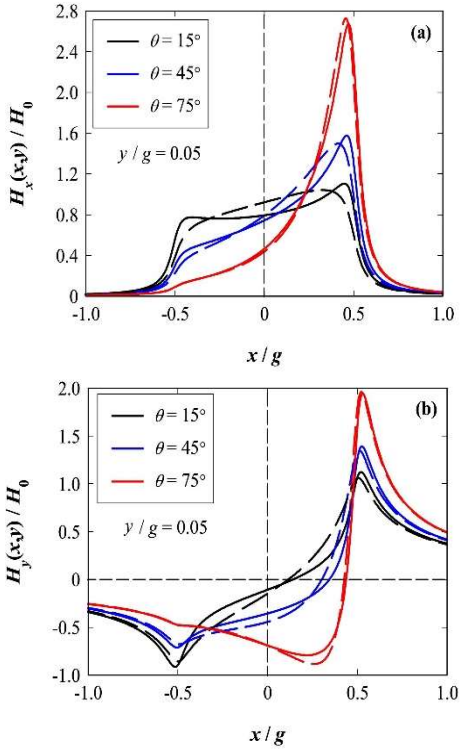

Fig. 7. (a) Normalized x-component of the magnetic field and (b) normalized y-component of the magnetic field for the asymmetrical head in the absence of an SUL for different exterior corner angles θ, calculated using finite elements (solid lines) and using the approximate models in (18) and (19) (dashed lines). The fields were calculated in close proximity to the head surface at $y/g = 0.05$.

The x- and y-field components for the asymmetrical head are plotted in Fig. 7 for different corner angles at $y/g = 0.05$, calculated using (18) and (19) (dashed lines) and compared with the finite-element calculations from Comsol Multiphysics (solid lines). Fig. 7 shows the increase in asymmetry in both H_x and H_y with increasing θ, resulting from the increase in surface charge density and potential gradient near the acute corner of the head ($x = g/2$) with increasing θ. The increased asymmetry leads to reduction in the effective head gap length toward the right corner ($x_0 \to g/2$), consequently causing the increase in the magnitude of the fields and narrowing of their distributions in this region.

The approximate fields calculated using (18) and (19) correctly capture the asymmetry in the magnetic fields and dependence of both magnitude and distribution on exterior corner angle θ, as shown in Fig. 7 (dashed lines), with some deviation from the finite-element calculations near the center of the gap and corners for small values of θ. For H_x in Fig. 7(a), the normalized deviation between the approximate and finite-element calculations is largest at 9% for $\theta = 15°$, reducing to 6% for $\theta = 45°$, and decreasing further to 1.7% for $\theta = 75°$. Fig. 7(b) shows that the approximate H_y generally

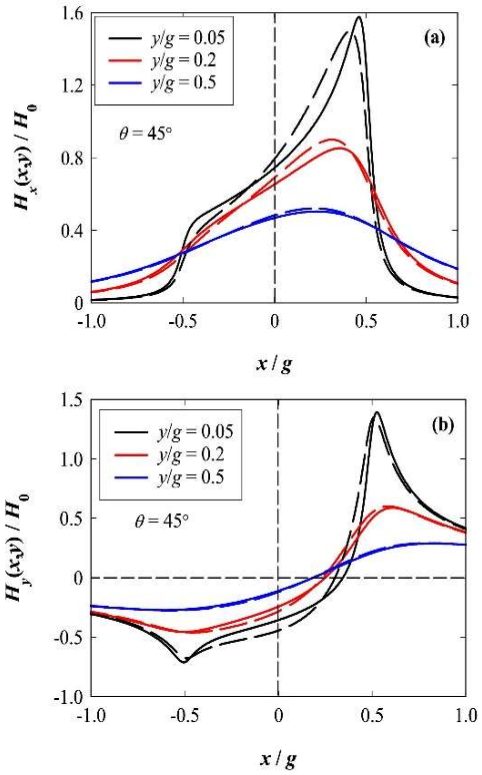

Fig. 8. (a) Normalized x-field component and (b) y-field component for the asymmetrical head in the absence of an SUL for exterior corner angle $\theta = 45°$, calculated using finite elements (solid lines) and using the approximate models in (18) and (19) (dashed lines) for increasing spacing y/g from the head surface.

exhibits closer agreement with the finite-element calculations with a normalized RMSD of 5% for $\theta = 15°$, reducing to 4.5% for $\theta = 45°$, and down to 1.7% for $\theta = 75°$. This reduction of error in the approximate fields with increasing θ is consistent with the reduction in the error of the derived surface potential in (2) with increasing θ, as shown in Fig. 4. The largest rms deviation at small value of θ is in line with the accuracy expected of the linear (Karlqvist) gap potential approximation for symmetrical heads where the contribution of the magnetic charges on the pole surfaces is underestimated [24].

At increasing distances from the head surface, the magnetic fields decrease in amplitude and their distributions broaden, as shown in Fig. 8. The increase in y/g is accompanied by increased agreement between the approximate fields calculated using (18) and (19) and the finite-element calculations, as shown in Fig. 8, for $\theta = 45°$ as a representative example. The normalized RMSD between the approximate and exact (finite element) H_x is 6% for $y/g = 0.05$ and reduces to 1.6% for $y/g = 0.5$. Similarly, the normalized RMSD for H_y continues the decrease with increasing θ at 4.5% for $y/g = 0.05$, and down to 1% for $y/g = 0.5$.

B. With Underlayer

In the presence of an SUL, the particular solution of Laplace's equation in (13) subject to a prescribed potential u^r (function of the head-to-underlayer spacing d and corner angle θ) at $y = 0$, and a vanishing potential at the surface of the underlayer ($y = d$), was found to be

$$u^r(k, y) = -u^r(k, 0)\frac{\sinh(k(y-d))}{\sinh(kd)}. \tag{20}$$

Thereafter, the superscript r will be used to indicate potentials and fields in the presence of an SUL. Following the analysis of Section III.A, it is more convenient mathematically to work with magnetic fields rather then potentials, and therefore, the gradient of the potential in (20) is taken to produce the Fourier transform of the magnetic fields:

$$H_x^r(k, y) = -H_x^r(k, 0)\frac{\sinh(k(y-d))}{\sinh(kd)} \tag{21a}$$

$$H_y^r(k, y) = jH_x^r(k, 0)\frac{\cosh(k(y-d))}{\sinh(kd)} \tag{21b}$$

where $H_x^r(k, 0)$ is the surface field transform. Evaluating the inverse Fourier transforms of (21) using the convolution property of Fourier transforms yields the convolution integrals

$$H_x^r(x, y) = \frac{-1}{2d}\int_{x'=-\infty}^{\infty} \frac{\sin(\pi y/d)H_x^r(x', 0)}{\cos(\pi y/d) - \cosh(\pi(x'-x)/d)}dx' \tag{22a}$$

$$H_y^r(x, y) = \frac{1}{2d}\int_{x'=-\infty}^{\infty} \frac{H_x^r(x', 0)\sinh(\pi(x'-x)/d)}{\cos(\pi y/d) - \cosh(\pi(x'-x)/d)}dx'. \tag{22b}$$

The field expressions in (22) account for the infinite reflections of the magnetic fields between the high permeability head surface and the underlayer [21], and the effect of the gap and the reaction of the underlayer on the surface field are included in the surface field $H_x^r(x, 0)$. For the asymmetrical head considered here, the surface field $H_x^r(x, 0)$ can be derived from the gradient of the potential in (9) [or equally (10)]. Choosing (9) due to the mathematical simplicity of the first linear term in the expression, and evaluating the derivative with respect to x yields the surface field

$$H_x^r(x, 0) = -H_0 - \sum_{m=1}^{\infty} \kappa_m B_m \cos(\kappa_m(x - g/2))(1 - e^{-2\kappa_m d}) \tag{23}$$

where $H_0 = 2U_0/g$, and the coefficients B_m are given explicitly in (10b). It is possible to integrate (22) exactly using the surface field distribution in (23), however, the solution is intractable and in terms of the hypergeometric series function. The magnetic fields in (22) can be numerically evaluated more conveniently and quickly using the inverse fast Fourier transform from (21). Alternatively, in this paper, the fields in (22) were more easily integrated numerically over the gap length using the surface field in (23).

Fig. 9 shows the magnetic fields for the asymmetrical head for different degrees of corner asymmetry with head-to-underlayer separation $d/g = 0.2$, calculated at a head spacing $y/g = 0.1$ using finite elements (straight lines) and the theoretical models in (22) and (23) (dashed lines). The presence of the soft underlayer enhances H_y at the expense of H_x, with H_x confined to the pole corners, as shown in Fig. 9(a). Following a similar pattern to the head fields

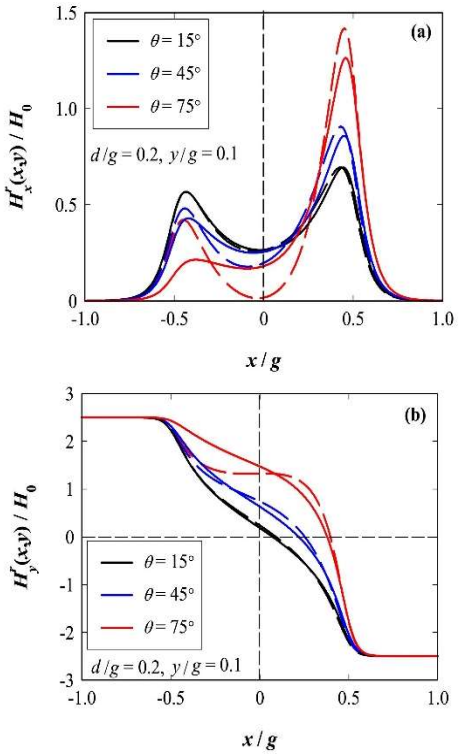

Fig. 9. (a) Normalized x-field component and (b) y-field component for the asymmetrical head in the presence of an SUL for different corner angles θ, calculated for a head-to-underlayer separation $d/g = 0.2$ at distance $y/d = 0.1$ from the head surface. Solid lines are the finite-element calculations, and the dashed lines are from the theoretical model in (22) and using the surface field distribution from (23).

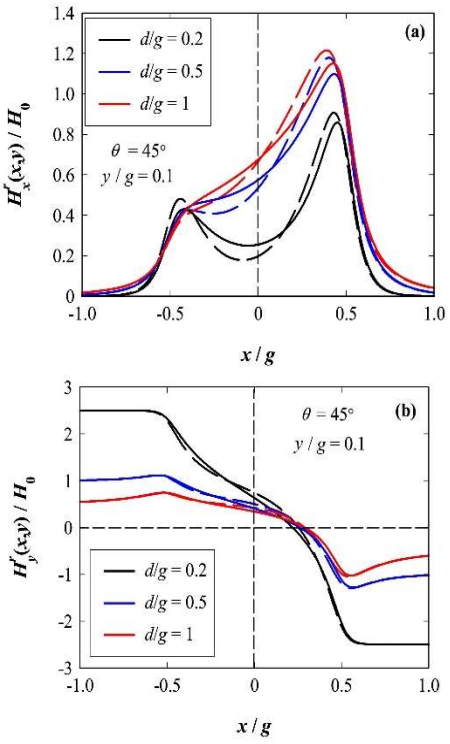

Fig. 10. (a) Normalized x-field component and (b) y-field component for the asymmetrical head in the presence of an SUL, for exterior corner angle $\theta = 45°$. Solid lines are for the finite-element calculations, and the dashed lines are from the theoretical model in (22) and using the surface field from (23).

without an underlayer, the increase in the exterior corner angle θ increases the asymmetry in the magnetic fields in general, and particularly increases the magnitude of H_x near the acute corner (at $x = g/2$). With increases in θ, the zero-crossing in H_y shifts toward the right corner, as shown in Fig. 9(b), following the shift in the surface potential. Beyond the head corners and over the pole regions, H_y tends to a constant magnitude that depends only on the ratio of d/g, as shown in Fig. 9(b). This dependence can be easily derived from (22b) by evaluating the limit $x \to \pm\infty$, thus reducing the convolution integral to $1/2d \int_{x'=-g/2}^{g/2} H_x^r(x', 0)dx'$. Substitution of (23) and integration yields the constant normalized field $H_y^r/H_0 \approx \pm g/2d$ [i.e., H_y over the head poles is determined by the first, long wavelength, term of the surface field in (23)].

The normalized rms deviation between H_x^r calculated using (22a) and the finite-element calculations is small at 2.5% for $\theta = 15°$, and increases to 4.5% for $\theta = 45°$, and reaches 7% for $\theta = 75°$. The approximate H_y^r again exhibits closer agreement with the finite-element calculations, as shown in Fig. 9(b), particularly for small exterior corner angles with normalized rms deviation of 0.7% when $\theta = 15°$. The deviation, however, increases to 1.5% for $\theta = 45°$, and is 4.4% with when $\theta = 75°$. The deviation of the approximate field models from the accurate finite-element calculations in Fig. 9 is mainly confined to the central region of the gap. This is where the surface potential expressions in (4) or (5), derived based on the approximate boundary value problem described in Fig. 6, predict a lower surface potential gradient (see Fig. 5) and, therefore, fields in that region compared with the finite element solution. This is caused by the use of the approximate expression for the normal derivative of the surface potential in (9) for the evaluation of the series coefficients. This deviation can be reduced using a more accurate expression for the normal derivative of the surface potential in evaluating the coefficients in (6) [determined from (19), for example]. However, care must be exercised in this case, since the resulting surface potential will not be consistent with the boundary value problem in Fig. 6, with expected derivations from the correct solution near the gap corner regions.

The dependence of the magnetic fields on the head-to-underlayer separation is shown in Fig. 10 for a fixed corner angle $\theta = 45°$. For small $d/g < 0.5$, H_x^r is confined and have maxima near the head corners, as shown in Fig. 10(a). Increasing the head-to-underlayer separation enhances the magnitude of H_x^r at the acute pole corner, and beyond $d/g > 0.5$ causes only modest changes to the magnetic fields as they become comparable with the fields without an underlayer. The normalized rms derivation between the

approximation in H_x^r and finite-element calculations starts at 5% for $d/g = 0.2$, and reduces to 4% with increased head-to-underlayer spacing at $d/g = 1$. For increasing values of $d/g > 0.5$, H_y^r decreases in amplitude, and the fields beyond the pole corners fall to zero following the behavior of the fields in the absence of the underlayer, as shown in Fig. 10(b). The rms deviation between the approximate and exact H_y^r fields in this case is 1.5% at $d/g = 0.2$ and increases to 2.7% for $d/g = 1$ in line with the previously estimated rms deviation values in the absence of the underlayer.

IV. Fourier Transform of Surface Fields

The magnetic fields everywhere beyond the head surface were determined in Section III from the convolution of the head surface field with Green's function for the 2-D geometry, as shown in Fig. 1. In particular, (15) and (21) show that the wavelength content of the magnetic fields is primarily determined by the Fourier transform of the surface field, before being filtered by spacing losses when moving away from the head surface. Thus, the surface field transform provides details on the wavelength content of the magnetic fields without any spacing losses, and will be determined next for the asymmetrical head in the presence and the absence of an SUL. These surface field transforms are also valuable for the numerical evaluation of the magnetic fields using the inverse Fourier transform.

A. Without Underlayer

The x-component of the magnetic field along the surface of the asymmetrical head is derived from the gradient of the potential in (2) and is given in (17). The surface field in (17) reveals the two connected characteristics of the surface potential and fields for asymmetrical heads, namely, the shift of the zero-crossing of the potential and, therefore, field locations with the change in corner angle θ (through x_0), and the scaling of the x-axis by x_0 which affects the magnitude and the width of the distribution of the fields with the change in θ. Both of these effects contribute to the reduction of effective gap length and narrowing of field distributions toward the acute head corner, as illustrated previously.

Evaluating the Fourier transform [defined in (12a)] of the surface field in (17) yields

$$H_x(k,0) = \frac{-gH_0}{2x_0}\left\{\left[-2x_0\cos\left(\frac{kg}{2}\right)+jg\sin\left(\frac{kg}{2}\right)\right] + j\frac{kg}{2x_0}\left(\frac{g^2}{4}-x_0^2\right)e^{\frac{-jkg^2}{4x_0}}\times\left[\mathrm{Ei}\left(j\frac{kg}{2x_0}\left(\frac{g}{2}-x_0\right)\right) - \mathrm{Ei}\left(j\frac{kg}{2x_0}\left(\frac{g}{2}+x_0\right)\right)\right]\right\} \quad (24)$$

where Ei is the exponential integral function [23]. The Fourier transform in (24) is complex due to the asymmetrical nature of the fields. Fig. 11 shows the calculated magnitude of the Fourier transform in (24) for different exterior corner angles. At $\theta = 0°$, the spectrum is the well-known sinc function describing the Fourier transform of the constant (Karlqvist)

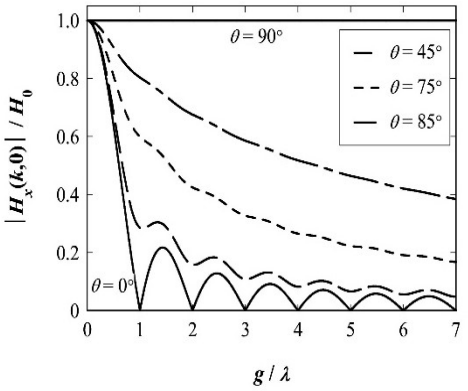

Fig. 11. Normalized head surface field transform for the asymmetrical head (in the absence of an underlayer) as a function of exterior corner angle θ. Solid lines: spectra of symmetrical heads, including the Karlqvist head ($\theta = 0°$) and the narrow-gap head ($\theta = 90°$).

surface field over the gap region, with nulls at exact multiples of the gap length. Increasing the exterior angle θ reduces the effective gap length of the head and narrows the field spatial distribution, therefore, increasing the magnitude of the spectrum at shorter wavelengths (higher k), and diluting the gap nulls. The broadening of the spectrum continues with increasing θ until the narrow-gap (or far field) limit is attained at $\theta = 90°$, corresponding to infinitely small gap length and infinitely narrow surface field distribution, which is represented by the constant spectrum in Fig. 11.

B. With Underlayer

The presence of a soft underlayer causes an enhancement of H_y^r, making it of practical importance for magnetic recording. Nevertheless, the x-component of the surface field $H_x^r(k,0)$ still decides the surface wavelength spectrum of H_y^r, as indicated by (21b). Convolving $H_x^r(k,0)$ with the low-pass filter term $1/\tanh(kd)$ in (21b) further enhances the short wavelengths in the spectrum, therefore, increasing the magnitude of H_y^r over the head poles with reduction in head-to-underlayer separation d, as shown in Fig. 10(b). $H_x^r(k,0)$ can be determined from the gradient of (4) [or equally (5)] at $y = 0$. For mathematical convenience, the surface field in (23) will be used again, with Fourier transform given by

$$H_x^r(k,0) = -gH_0\frac{\sin(kg/2)}{(kg/2)} - 2k\sum_{m=1}^{\infty} j^m\kappa_m B_m(1-e^{-2\kappa_m d}) \times \frac{\sin\left(g/2(k+\kappa_m)\right)}{k^2-\kappa_m^2}. \quad (25)$$

The surface field spectrum in (25) follows the same dependence on exterior corner angle θ, as that indicated in Fig. 11, in the absence of an underlayer, and will not be illustrated here. In particular, the width and, therefore, wavelength content of the spectrum in (25) also increases with increasing θ, due to the reduction in effective gap and narrowing of field distributions. The effect of the head-to-underlayer spacing on head surface transform in (25) is shown in Fig. 12 for $\theta = 45°$. Reducing the head-to-underlayer separation results

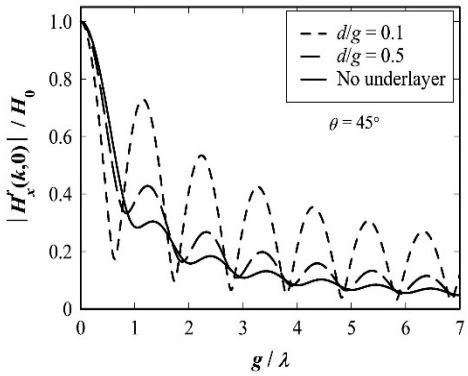

Fig. 12. Normalized head surface field transforms for an asymmetrical head in the presence of an underlayer for $\theta = 45°$ at different head-to-underlayer spacings.

in displacement of the gap nulls toward larger wavelengths (smaller k) and increases in the amplitude of the ripples in the spectrum. This behavior persists for all other corner angles.

V. Conclusion

This paper provided a closed-form approximate model for the surface magnetic potential of the asymmetrical head in two-dimensions, demonstrating a very good agreement with 2-D finite-element calculations, for a wide range of exterior corner angles from 0° (rectangular head) to 90° (narrow-gap head). The theory is 2-D and assumes infinite track-width heads, and based on the static scalar magnetic potential, and therefore, ignores head transients. Moreover, pole corner and SUL saturation effects were neglected in this approximate and analytical treatment.

A general analytical theory was developed to model the reaction of an SUL on the surface potential of any 2-D head structure. This theory was applied to the asymmetrical head and predicted, to a very good agreement with finite-element calculations, the surface potential and fields from asymmetrical heads as functions of head corner angle and head-to-underlayer separation.

The analytical models for the surface potential with and without an underlayer were convolved with the 2-D Green's function for the asymmetrical head to derive relatively simple closed-form expressions for the magnetic fields beyond the surface of asymmetrical heads. The approximate magnetic fields were in a very good agreement with finite-element calculations over a wide range of corner inclination angles and head-to-underlayer separations. The analytical expressions revealed that the magnetic fields from asymmetrical heads may be derived from a weighted sum of the horizontal and vertical field components.

Exact expressions for the Fourier transforms of the asymmetrical head surface fields were also derived, correctly demonstrating the increase in the wavelength content of the field spectrum with increasing exterior corner angle (due to the reduction in effective gap length and narrowing of the field distributions).

The theory presented here can be used to evaluate the magnetic fields of 2-D head structures with multiple asymmetrical gaps, and easily incorporated into numerical studies of magnetic recording with minimum computational effort.

Appendix
Solution of Laplace's Equation Using the Translated Sine Transform

Laplace's equation in two-dimensions for the scalar magnetic potential ϕ for the geometry shown in Fig. 6 in the absence of the underlayer (i.e., $d \to \infty$) is given by

$$\frac{\partial^2 \phi}{\partial x^2} + \frac{\partial^2 \phi}{\partial y^2} = 0.$$

Taking the translated sine integral transform of Laplace's equation, defined for $\phi(x, y)$ as

$$\bar{\phi}(\kappa_n, y) = \int_{x=-g/2}^{g/2} \phi(x, y) \sin(\kappa_n (x - g/2)) dx$$

and applying successive integration by parts, observing the boundary conditions indicated in Fig. 6 with eignvalues $\kappa_n = n\pi/g$, reduces Laplace's equation to the ordinary differential equation

$$\frac{\partial^2 \bar{\phi}}{\partial y^2} - \kappa_n^2 (\bar{\phi} - \bar{v}) = 0 \tag{A.1}$$

where the eignvalues $\kappa_n = n\pi/g$ and eigenfunctions $\sin(\kappa_n(x - g/2))$ satisfy the boundary conditions shown in Fig. 6, and allow asymmetrical description of $\phi(x, 0)$ in the transform. $\bar{v}$ is the integral transform of the linear gap potential at $y = 0$, and is defined by

$$\bar{v}(\kappa_n, 0) = \int_{x=-g/2}^{g/2} \left(\frac{2U_0 x}{g} \right) \sin(\kappa_n (x - g/2)) dx.$$

The general solution to (A.1) is given by

$$\bar{\phi}(\kappa_n, y) = Ce^{\kappa_n y} + De^{-\kappa_n y} + \bar{v} \tag{A.2}$$

where C and D are the constants of the integration. Application of the boundary conditions that $\bar{\phi}$ vanishes as $y \to \infty$, with prescribed surface potential $\bar{\phi}(\kappa_n, 0)$ at $y = 0$ yields the particular solution of (A.2) as

$$\bar{\phi}(\kappa_n, y) = (\bar{\phi}(\kappa_n, 0) - \bar{v}) e^{-\kappa_n y} + \bar{v}. \tag{A.3}$$

The normal derivative of the integral transform of the potential is, therefore, given by

$$\frac{\partial \bar{\phi}(\kappa_n, y)}{\partial y} = -\kappa_n (\bar{\phi}(\kappa_n, 0) - \bar{v}) e^{-\kappa_n y}. \tag{A.4}$$

References

[1] B. K. Middleton, "Recording and reproducing processes," in *Magnetic Recording: Technology*, vol. 1, C. D. Mee and E. D. Daniel, Eds. New York, NY, USA: McGraw-Hill, 1987, ch. 2.

[2] J. D. Jackson, *Classical Electrodynamics*, vol. 11, 3rd ed. New York, NY, USA: Wiley, 1999, ch. 2, sec. 2, p. 75.

[3] C. S. Wang and H. L. Huang, "Characteristics of asymmetric heads," *J. Phys. Colloques*, vol. 49, no. C8, pp. C8-2023–C8-2024, 1988.

[4] C. S. Wang and H. L. Huang, "Gap-null free spectral response of asymmetric ring heads for longitudinal and perpendicular recording," *IEEE Trans. Magn.*, vol. 26, no. 5, pp. 2403–2405, Sep. 1990.

[5] Y. Kanai, R. Matsubara, H. Watanabe, H. Muraoka, and Y. Nakamura, "Recording field analysis of narrow-track SPT head with side shields, tapered main pole, and tapered return path for 1 Tb/in^2," *IEEE Trans. Magn.*, vol. 39, no. 4, pp. 1955–1960, Jul. 2003.

[6] R. H. Victora, S. M. Morgan, K. Momsen, E. Cho, and M. F. Erden, "Two-dimensional magnetic recording at 10 Tbits/in^2," *IEEE Trans. Magn.*, vol. 48, no. 5, pp. 1697–1703, May 2012.
[7] J.-S. Yang and C.-R. Chang, "Exact field calculations for asymmetric ring heads," *IEEE Trans. Magn.*, vol. 28, no. 5, pp. 2072–2076, Sep. 1992.
[8] J.-S. Yang and C.-R. Chang, "Magnetic field of an asymmetric ring head with an underlayer," *IEEE Trans. Magn.*, vol. 29, no. 2, pp. 2069–2072, Mar. 1993.
[9] G. J. Fan, "A study of the playback process of a magnetic ring head," *IBM J. Res. Develop.*, vol. 5, no. 4, pp. 321–325, Oct. 1961.
[10] D. T. Wilton, "An analysis of the magnetic field of a ring head with a highly permeable underlayer," *IEEE Trans. Magn.*, vol. 27, no. 4, pp. 3751–3755, Jul. 1991.
[11] G. J. Y. Fan, "Analysis of a practical perpendicular head for digital purposes," *J. Appl. Phys.*, vol. 31, no. 5, pp. S402–S403, 1960.
[12] H. A. Shute, D. T. Wilton, and D. J. Mapps, "Analytic field components for perpendicular thin-film recording heads," *IEEE Trans. Magn.*, vol. 37, no. 6, pp. 3947–3955, Nov. 2001.
[13] S. J. C. Brown, D. T. Wilton, H. A. Shute, and D. J. Mapps, "Analytic solutions for double-element shielded magnetoresistive heads," *IEEE Trans. Magn.*, vol. 35, no. 5, pp. 4339–4350, Sep. 1999.
[14] D. T. Wilton, B. K. Middleton, and M. M. Aziz, "Exact harmonic coefficients for a magnetic ring head," *IEEE Trans. Magn.*, vol. 35, no. 3, pp. 2043–2046, May 1999.
[15] O. Karlqvist, "Calculation of the magnetic field in the ferromagnetic layer of a magnetic drum," *Trans. Roy. Inst. Technol., Stockholm, Sweden*, vol. 86, pp. 1–27, 1954.
[16] T. J. Szczech and P. R. Iverson, "An approach for deriving field equations for magnetic heads of different geometrical configurations," *IEEE Trans. Magn.*, vol. 22, no. 5, pp. 355–360, Sep. 1986.
[17] *Comsol Multiphysics*. [Online]. Available: http://www.comsol.com/comsol-multiphysics, accessed Nov. 2015.
[18] H. N. Bertram and C. W. Steele, "Pole tip saturation in magnetic recording heads," *IEEE Trans. Magn.*, vol. 12, no. 6, pp. 702–706, Nov. 1976.
[19] H. L. Huang, T. Y. Lee, and Y.-T. Huang, "Saturation effects on read/write characteristics of asymmetric ring head," *IEEE Trans. Magn.*, vol. 28, no. 5, pp. 2650–2652, Sep. 1992.
[20] H. N. Bertram, *Theory of Magnetic Recording*. Cambridge, U.K.: Cambridge Univ. Press, 1994.
[21] D. S. Bloomberg, "Spectral response from perpendicular media with gapped head and underlayer," *IEEE Trans. Magn.*, vol. 19, no. 4, pp. 1493–1502, Jul. 1983.
[22] D. T. Wilton, H. A. Shute, and D. J. Mapps, "Accurate approximation of fields and spectral response functions for perpendicular recording heads," *IEEE Trans. Magn.*, vol. 35, no. 4, pp. 2172–2179, Jul. 1999.
[23] M. Abramowitz and I. A. Stegun, *Handbook of Mathematical Functions: With Formulas, Graphs, and Mathematical Tables*. Washington, DC, USA: United States Government Printing Office, 1972, p. 231.
[24] J. J. M. Ruigrok, *Short-Wavelength Magnetic Recording: New Methods and Analyses*. Oxford, U.K.: Elsevier, 1990.

C. Conference attended

International Conference on Advances in Applied Mathematics and Mathematical Physics: Aug. 2014, in Istanbul, Yildiz Technical University of Istanbul, Turkey to present the poster '**Magnetic Fields from Asymmetrical Magnetic Recording Heads**'.

This poster has been selected as the best poster in the conference.

References

[1] A. S. Hoagland, “Perpendicular Magnetic Recording History of Magnetic Disk Storage Based on Perpendicular Magnetic Recording,” *IEEE Trans. Magn.*, vol. 39, no. 4, pp. 1871–1875, 2003.

[2] A. ALMamun, G. Guo, and Bi. Chao, *Hard Disk Drive, Mechatronics and Control*. Taylor and Francis Group, LLC., 2007.

[3] X. W. Shan and A. M. Taratoin, *Magnetic Information Storage Technology*, ELECTROMAG. California: AP Academic Press, 1999.

[4] E. Grochowski and A. I. David, “Outlook for Maintaining Areal Density Growth in Magnetic Recording,” *IEEE Trans. Magn.*, vol. 30, no. 6, pp. 3797–3800, 1994.

[5] E. Grochowski, “Computer Storage Consultant,” *hard disk drive*, 2013. [Online]. Available: http://edwgrochowski.com/bio.html. [Accessed: 18-Jun-2015].

[6] M. Lucas, “60TB disk drives could be a reality in 2016,” *computer world*, 2012. [Online]. Available: http://www.computerworld.com/article/2504784/data-center/60tb-disk-drives-could-be-a-reality-in-2016.html. [Accessed: 09-Apr-2016].

[7] M. Gubbins, R. Chantrell, and G. Goldbeck, “Integrated Recording Model for Heat Assisted Magnetic Recording (HAMR) ‘EMMC case study: Seagate Technology’’,” 2016.

[8] Mark H. Kryder, “History and Future of Data Storage Technology,” *Illionis Insititute of Technology*, 2015. [Online]. Available: https://iit.edu/news/iittoday/?p=48135. [Accessed: 10-Apr-2016].

[9] E. Grochowski, A. I. David, D. A. Thompson, and A. I. David, “Outlook for Maintaining Areal Density Growth in Magnetic Recording,” *IEEE Trans. Magn.*, vol. 30, no. 6, pp. 3797–3800, 1994.

[10] Z. Z. Bandic and R. H. Victora, “Advances in Magnetic Data Storage Technologies,” *IEEE Trans. Magn.*, vol. 96, no. 11, pp. 1749–1753, 2008.

[11] S. H. Charap and L. Pu-Ling, “Thermal stability of recorded information at high densities,” *Magn. IEEE Trans.*, vol. 33, no. 1, p. 978–983., 1997.

[12] Y. Shiroishi, K. Fukuda, I. Tagawa, H. Iwasaki, S. Takenoiri, H. Tanaka, H. Mutoh, and N. Yoshikawa, “Future Options for HDD Storage,” *IEEE Trans. Magn.*, vol. 45, no. 10, pp. 3816–3822, Oct. 2009.

[13] D. Yan, “Micromagnetic Study Of Perpendicular Magnetic Recording Media’’, PhD thesis,” University Of Minnesota, 2012.

[14] A. Moser, K. Takano, D. T. Margulies, M. Albrecht, Y. Sonobe, Y. Ikeda, S. Sun, and E. E. Fullerton, “Magnetic recording: advancing into the future,” *J. Phys. D. Appl. Phys.*, vol. 35, no. 19, pp. R157–R167, 2002.

[15] H. N. Bertram and M. Williams, “SNR and density limit estimates: a comparison of longitudinal and perpendicular recording,” *IEEE Transl. J. Magn. Japan*, vol. 36, no. 1, 2000.

[16] R. Wood, Y. Hsu, and Marilee Schultz, *Perpendicular Magnetic Recording Technology*. San Jose,USA: Hitachi Global Storage Technologies, 2007.

[17] A. S. . Hoagland, “High-Resolution Magnetic Recording Structures,” *IEEE Trans. Magn.*, vol. 2, no. 2, pp. 90–104, Apr. 1958.

[18] S. N. Piramanayagam, “Perpendicular recording media for hard disk drives,” *J. Appl. Phys.*, vol. 102, pp. 1–22, 2007.

[19] R. Wood, “The feasibility of magnetic recording at 1 Terabit per square inch,” *IEEE Trans. Magn.*, vol. 36, no. 1, pp. 36–42, 2000.

[20] C. Piguet, T. R. Reed, B. Vasic, and E. M. Kurtas, *Coding and Signal Processing for Magnetic Recording Systems*. London: CRC PRESS, 2005.

[21] B. Y. Tanaka, “Technology : From Research to Commercialization,” *IEEE Trans. Magn.*, vol. 96, no. 11, pp. 1754–1760, 2008.

[22] M. L. Plumer, J. van Ek, and W. C. Cain, “New paradigms in magnetic recording,” *Phys. Canada*, vol. 67, no. 2006, p. 25, 2011.

[23] R. Wood, “Shingled Magnetic Recording and Two-Dimensional Magnetic Recording Acknowledgements,” Hitachi GST, San Jose, California, 2010.

[24] K. Sakhrat and L. Dmitri, *Perpendicular Magnetic Recording*, 1st ed. New Yourk: Kluwer Academic Publishers, 2004.

[25] K. Chooruang, “Studies of Signal and Noise Properties of Perpendicular Recording Media’’, PhD thesis,” Exeter University, 2010.

[26] L. Néel, “Théorie du traînage magnétique des ferromagnétiques en grains fins avec applications aux terres cuites,” *Ann. Géophys*, vol. 5, no. 2, pp. 99–136, 1949.

[27] K. Josephat, “Modeling Data Storage In Nano-Island Magnetic Materials,” University of Manchester, 2011.

[28] B. M. H. Kryder, E. C. . Gage, T. W. Mcdaniel, W. A. Challener, R. E. Rottmayer, G. Ju, Y. Hsia, M. F. Erden, and J. Thiele, “Magnetic Recording,” *Proc. IEEE*, vol. 96, no. 11, pp. 1810–1835, 2008.

[29] J. Zhu, X. Zhu, and T. Yuhui, “Microwave Assisted Microwave Recording, (Data Storage Systems Center, Dec.,2007,” *Data Storage Systems Center, Dept. of Electrical and Computer Engineering, Carnegie Mellon University,* 2007. [Online]. Available: http://www.google.co.uk/url?sa=t&rct=j&q=&esrc=s&source=web&cd=2&ved=0CFcQFjAB&url=http://www.idema.org/wp-content/downloads/1856.pdf&ei=YBL2T4ypG5Om8gOArrCzBw&usg=AFQjC

NHWQP4jDicLcMOpLSICa7s0BolrnA. [Accessed: 05-Jul-2012].

[30] R. M. Ikkawi, “Heat Assisted Magnetic Recording for Areal Densities Beyond 1Tbit/in2’’, PhD thesis,” University Of California Riverside, 2008.

[31] G. Winkler, D. Suess, J. Lee, J. Fidler, M. a. Bashir, J. Dean, a. Goncharov, G. Hrkac, S. Bance, and T. Schrefl, “Microwave-assisted three-dimensional multilayer magnetic recording,” *Appl. Phys. Lett.*, vol. 94, no. 23, p. 232501, 2009.

[32] H. Zheng, “Investigation of Bit Patterned Media , Thermal Flying Height Control Sliders and Heat Assisted Magnetic Recording in Hard Disk Drives’’, PhD thesis,” University Of California, San Diego, 2011.

[33] A. Amer, D. D. E. Long, E. L. Miller, J. F. Pâris, and S. J. Thomas Schwarz, “Design issues for a shingled write disk system,” *IEEE Transl. J. Magn.*, vol. 9, no. 10, p. 978, 2010.

[34] S. Greaves, Y. Kanai, and H. Muraoka, “Shingled recording for 2-3 Tbit/in2,” *IEEE Trans. Magn.*, vol. 45, no. 10, pp. 3823–3829, 2009.

[35] Y. Kanai, R. Matsubara, H. Watanabe, O. A. Mohammed, H. Muraoka, and Y. Nakamura, “Recording field analysis of narrow-track SPT head with side-shields,” *Joint NAPMRC 2003. Digest of Technical Papers [Perpendicular Magnetic Recording Conference]*. p. 62, 2003.

[36] R. Wood, M. Williams, A. Kavcic, and J. Miles, “The Feasibility of Magnetic Recording at 10 Terabits Per Square Inch on Conventional Media,” *IEEE Transactions on Magnetics*, vol. 45, no. 2. pp. 917–923, 2009.

[37] R. H. Victora, S. M. Morgan, K. Momsen, E. Cho, and M. F. Erden, “Two-Dimensional Magnetic Recording at 10 Tbits/in2,” *IEEE Trans. Magn.*, vol. 48, no. 5, pp. 1697–1703, 2012.

[38] Y. Kanai, Y. Jinbo, T. Tsukamoto, S. J. Greaves, K. Yoshida, and H. Muraoka, “Finite-Element and Micromagnetic Modeling of Write Heads for Shingled Recording,” *Magnetics, IEEE Transactions on*, vol. 46, no. 3. pp. 715–721, 2010.

[39] C. S. Wang and H. L. Huang, “Characteristics Of Asymmetric Heads,” *J. Phys.*, vol. 49, no. 12, pp. 2023–2024, 1988.

[40] N. H. Yeh, “Review of head-media coupling in magnetic recording,” *Magnetics, IEEE Transactions on*, vol. 21, no. 5. pp. 1338–1343, 1985.

[41] E. Kim, Y. H. Im, Y. Kim, K. J. Lee, K. Lee, and N. Y. Park, “Head design scheme for perpendicular recording with single layered media,” *IEEE Trans. Magn.*, vol. 37, no. 4, pp. 1382–1385, 2001.

[42] S. I. Iwasaki and K. Ouchi, “On design of Co-Cr perpendicular recording media for usage of a ring-type head,” *IEEE Trans. Magn.*, vol. 26, no. 1, pp. 97–99, 1990.

[43] D. T. Wilton, “An analysis of the magnetic field of a ring head with a highly

permeable underlayer," *IEEE Trans. Magn.*, vol. 27, no. 4, pp. 3751–3755, 1991.

[44] D. T. Wilton, D. M. Mckirdy, H. a. Shute, J. J. Miles, and D. J. Mapps, "3-D head field modeling for perpendicular magnetic recording," *Jt. NAPMRC 2003 Dig. Tech. Pap.*, p. 7803, 2003.

[45] S. Iwasaki, "Perpendicular Magnetic Recording," *IEEE Trans. Magn.*, vol. 16, no. 1, pp. 71–76, 1980.

[46] Y. Kanai and K. Yamakawa, "Narrow-track perpendicular write heads," *J. Magn. Magn. Mater.*, vol. 321, no. 6, pp. 518–525, Mar. 2009.

[47] M. Mallary, A. Torabi, and M. Benakli, "One terabit per square inch perpendicular recording conceptual design," *IEEE Trans. Magn.*, vol. 38, no. 4 I, pp. 1719–1724, 2002.

[48] K. Nakamoto, H. Hoshiya, H. Katada, T. Okada, M. Hatatani, K. Hoshino, N. Yoshida, I. Nunokawa, K. Etoh, and K. Watanabe, "CPP-GMR reader and wraparound shield writer for perpendicular recording," *IEEE Trans. Magn.*, vol. 41, no. 10, pp. 2914–2919, 2005.

[49] D. T. Wilton, "Comparison of ring and pole head magnetic fields," *IEEE Trans. Magn.*, vol. 26, no. 3, pp. 1229–1232, May 1990.

[50] M. M. Aziz, "Signal and Noise Properties of Longitudinal Thin-Film Media'', PhD thesis," University of Manchester, 1999.

[51] I. Megory-cohen and T. D. Howell, "Exact Field Calculations for Asymmetric Finite Pole-Tip Ring Heads," *IEEE Trans. Magn.*, vol. 24, no. 3, pp. 2074–2080, 1988.

[52] H. L. Huang, T. Y. Lee, and Yuh-Tyng Huang, "Saturation effects on read/write characteristics of asymmetric ring head," *IEEE Trans. Magn.*, vol. 28, no. 5, pp. 650–651, 1992.

[53] 0. Lopez, W. P. Wood, N. H. Yeh, and M. Jursich, "Interaction of a ring head and double layer media-field calculations," *IEEE Trans. Magn.*, vol. MAG-18, no. 10, pp. 1179–1181, 1982.

[54] D. Bloomberg, "Spectral response from perpendicular media with gapped head and underlayer," *IEEE Trans. Magn.*, vol. 19, no. 4, pp. 1493–1502, 1983.

[55] J. Yang and C. Chang, "Magnetic field of an asymmetric ring head with an underlayer," *IEEE Trans. Magn.*, vol. 29, no. 2, pp. 2069–2072, Mar. 1993.

[56] W. K. Westmijze, "Studies on magnetic recording," *Philips Res. Rep*, vol. 8, pp. 161–183, 1953.

[57] 0. Karlqvist, "Calculation of the magnetic field in the ferromagnetic layer of a magnetic drum," *Trans. Roy. Inst. Technol. Stock. Sweden*, vol. 86, no. 1, pp. 1–27, 1954.

[58] J. D. Jackson, *Classical Electrodynamics Third Edition*, 3rd ed. United State -NY: Library of Congress Cataloging-in-Oublication Data, 1999.

[59] T. SUZUKI and S.-I. IWASAKI, "An Analysis of Magnetic Recording Head fields Using a Vector Potential," *IEEE Trans. Magn.*, no. September, pp. 536–538, 1972.

[60] G. Fan, "Analysis of a practical perpendicular head for digital purposes," *J. Appl. Phys*, vol. 31, no. 5, p. 402, 1960.

[61] D. T. Wilton, B. K. Middleton, and M. M. Aziz, "Exact Harmonic Coefficients for a Magnetic Ring Head," *IEEE Trans. Magn.*, vol. 35, no. 3, pp. 2043–2046, 1999.

[62] N. Curland and J. Judy, "Calculation of exact ring head fields using conformal mapping," *Magnetics, IEEE Transactions on*, vol. 22, no. 6. pp. 1901–1903, 1986.

[63] J. R. Hwu, K. Chen, and S. Ananthan, "Calculation of Exact Ring Head Fields Using Conformal Mapping," *IEEE Trans. Magn.*, vol. M, no. 6, pp. 1425–1426, 1994.

[64] E. O. Brigham, *The Fast Fourier Transform and Its Applications*. Prentice Hall Avantek, Inc., 1988.

[65] H. N. Bertram, *Theory of Magnetic Recording*, 1st ed. New York: Cambridge University Press, 1994.

[66] D. T. Wilton, H. A. Shute, and D. J. Mapps, "Accurate approximation of fields and spectral response functions for perpendicular recording heads," *IEEE Trans. Magn.*, vol. 35, no. 4, pp. 2172–2179, Jul. 1999.

[67] G. Fan, "A study of the playback process of a magnetic ring head," *IBM J. Res. Dev.*, vol. 5, pp. 321–325, 1961.

[68] H. Muraoka and Y. Nakamura, "Quantification of Perpendicular Magnetic Recording with Double Layer Media," *J. Magn. Soc. Japan*, vol. 21, no. S2, pp. 157–162, 1997.

[69] W. A. Baird, "An Evaluation and Approximation of the Fan Equations Describing Magnetic Fields near Recording Heads," *IEEE Trans. Magn.*, vol. 16, no. 5, pp. 1350–1352, Jan. 1980.

[70] L. Huang and H. Y. Deng, "Comparison of ring head and SPT head write fields," *IEEE Trans. Magn.*, vol. 22, no. 5, pp. 1305–1309, Sep. 1986.

[71] L. Lapidus and F. G. Pinder, *Numerical Solution of Partial Differential Equations in Science and Engineering*, vol. 64, no. 4. New York: John Wiley & Sons, INC, 1983.

[72] J. J. M. Ruigrok, *Short-Wavelength Magnetic Recording: New Methods And Analyses*. Oxford, UK: Elsevier Advanced Technology, 1990.

[73] W. H. Press, S. A. Teukolsky, W. T. Vetterling, and B. P. Flannery, *Numerical Recipes in C: The Art of Scientific Computing*, 2nd editio. Cambridge: Cambridge

University Press, 1992.

[74] G. A. Bertero, H. N. Bertram, and D. M. Barnett, “Fields and transforms for thin film heads,” *IEEE Trans. Magn.*, vol. 29, no. 1, pp. 67–76, 1993.

[75] D. Litvinov, R. M. Chomko, L. Abelmann, K. Ramstöck, G. Chen, and S. Khizroev, “Micromagnetics of a Soft Underlayer,” *IEEE Trans. Magn.*, vol. 36, no. 5, pp. 2483–2485, 2001.

[76] T. J. Szczech and P. R. Iverson, “An Approch for Deriving Field Equations for Magnetic Recording Heads of Different Geometrical Configurations,” *IEEE Trans. Magn.*, vol. MAG-22, no. 5, pp. 355–360, 1986.

[77] H. A. Shute, “Mathematical Analysis of Novel Magnetic Recording Heads’’, PhD thesis,” University of Plymouth, 1995.

[78] J. Mallinson and C. Steele, “Theory of linear superposition in tape recording,” *IEEE Trans. Magn.*, vol. 5, no. December, pp. 886–890, 1969.

[79] D. Lindholm, “Reproduce characteristics of rectangular magnetic heads,” *Magn. IEEE Trans.*, vol. 12, no. 6, pp. 710–712, 1976.

[80] D. Tjaden, “Some notes on ‘superposition’ in digital magnetic recording,” *IEEE Trans. Magn.*, vol. 9, no. 3, 1973.

[81] D. A. Lindholm, “Dependence of reproducing gap null on head geometry,” *IEEE Trans. Magn.*, vol. 11, no. 6, pp. 1692–1696, 1975.

[82] D. A. Lindholm, “Magnetic Fields of Finite Track Width Heads,” *IEEE Trans. Magn.*, vol. M, no. 5, pp. 1460–1462, 1977.

[83] K. Okuda, K. Suwka, and K. G. Ashar, “An Analytical Three-Dimensional Field Model Of A Perpendicular Recording Head,” *IEEE Trans. Magn.*, vol. 24, no. 6, pp. 2479–2481, 1988.

[84] D. GAIER, *Konstruktive Methoden der konformen Abbildung*. Berlin: Springer, 1964.

[85] H. Peter, *Applied and Computational Complex Analysis, Discrete Fourier Analysis, Cauchy Integrals, Construction of Conformal Maps, Univalent Functions*. Canada: John Wiley & Sons, Inc., 1993.

[86] T. A. Driscoll and Lloyd N. Trefethen, *Schwarz-Christoffel Mapping*. Oxford, UK: Cambridge University Press, 2002.

[87] R. Wegmann, “Methods for numerical conformal mapping, in Handbook of Complex Analysis, Geometric Function Theory,” *R. Kuhnau, Elsevier*, vol. 2, pp. 351–477, 2005.

[88] S. Ganguli, “Conformal Mapping and its Applications,” *IEEE Trans. Med. Imaging*, vol. 23, no. 8, pp. 1–4, 2004.

[89] J. S. Yang and H. L. Huang, “Calculation of exact head and image fields of recording heads by conformal mapping,” *IEEE Trans. Magn.*, vol. 25, no. 3, pp. 2761–2768, 1989.

[90] A. D. Booth, “On two problems in potential theory and their application to the design of magnetic recording heads for digital computers,” *Br. J. Appl. Phys.*, vol. 3, no. 10, pp. 307–308, Oct. 1952.

[91] I. Elabd, “A study of the field around magnetic heads of finite length,” *IEEE Trans. Audio*, vol. 11, no. 1, pp. 21–27, 1963.

[92] M. Steinback, A. Joel, and T. J. Szczech, “Exact solution for the field of a perpendicular head,” *IEEE Trans. Magn.*, vol. M, no. 6, pp. 3117–3119, 1981.

[93] C. K. Lim, E. S. Kim, S. Y. Yoon, S. H. Kong, H. S. Lee, H. S. Oh, and Y. S. Kim, “Effect of soft underlayer magnetic anisotropy on perpendicular recording process,” *J. Magn. Magn. Mater.*, vol. 310, pp. 2680–2682, 2007.

[94] V. Minuhin, “Comparison of sensitivity functions for ideal probe and ring-type heads,” *IEEE Trans. Magn.*, vol. 20, no. 3, pp. 488–494, 1984.

[95] C. S. Wang and H. L. Huang, “Gap-null free spectral response of asymmetric ring heads for longitudinal and perpendicular recording,” *Magnetics Conference, 1990. Digests of INTERMAG ’90. International*. p. FP-FP, 1990.

[96] J. Yang and C. Chang, “Exact field calculations for asymmetric ring heads,” *Magn. IEEE Trans.*, vol. 28, no. 5, pp. 2072–2076, 1992.

[97] I. Megory-cohen and T. D. Howell, “Exact field calculations for asymmetrical finite-pole-tip ring heads,” *IEEE Trans. Magn.*, vol. 24, no. 3, pp. 2074–2080, 1988.

[98] V. B. Minuhin, “General solution for the field of polygonal electromagnet,” *IEEE Trans. Magn.*, vol. 29, no. 6 pt 3, pp. 4121–4141, 1993.

[99] D. Meeker, “Finite Element Method Magnetics,” *QinetiQ North America*, 2014. [Online]. Available: http://www.femm.info/wiki/HomePage. [Accessed: 01-Jun-2015].

[100] Dassault Systèmes Simulia, “Getting Started With ABAQUS,” *ABAQUS VERSION 6.6*. ABAQUS, Inc., pp. 1–621, 2010.

[101] C. Multiphysics, “COMSOL Multiphysics Modeling Guide.” COMSOL, pp. 1–518, 2008.

[102] T. I. C. Scientific, “Lab - Introduction to Finite Element Methods and COMSOL Multiphysics Using a finite element method to compute the shape of a soap film FEM for PDEs Introduction to COMSOL Multiphysics,” vol. Scientific, no. 5. pp. 1–5, 2013.

[103] CST, “CST- Computer Simulation Technology,” 2016. [Online]. Available:

https://www.cst.com/. [Accessed: 13-Apr-2016].

[104] T. Chai and R. R. Draxler, “Root mean square error (RMSE) or mean absolute error (MAE)? -Arguments against avoiding RMSE in the literature,” *Geosci. Model Dev.*, vol. 7, no. 3, pp. 1247–1250, 2014.

[105] H. M. Sugawara and R. C. MacCallum, “Effect of Estimation Method on Incremental Fit Indexes for Covariance Structure Models,” *Appl. Psychol. Meas.* , vol. 17, no. 4, pp. 365–377, Dec. 1993.

[106] C. D. Mee and E. D. Daniel, *Magnetic Recording; Vol. I: Technology*. New York, NY, USA: McGraw-Hill, Inc., 1986.

[107] K. Z. Gao, O. Heinonen, and Y. Chen, “Read and write processes, and head technology for perpendicular recording,” *J. Magn. Magn. Mater.*, vol. 321, no. 6, pp. 495–507, Mar. 2009.

[108] I. S. Gradshteyn and I. M. Ryzhik, *Table of Integrals, Series, and Products*, Seventh Ed. California: Academic Press is an imprint of Elsevier, 2007.

[109] C. Ferreira and J. L. López, “Asymptotic expansions of the Hurwitz–Lerch zeta function,” *J. Math. Anal. Appl.*, vol. 298, no. 1, pp. 210–224, Oct. 2004.

[110] D. T. Wilton, D. J. Mapps, and H. a. Shute, “Exact field calculations for conventional and graded magnetization thin film recording heads,” *IEEE Trans. Magn.*, vol. 30, no. 2, pp. 253–263, 1994.

[111] T. Szczech and P. Iverson, “An approach for deriving field equations for magnetic heads of different geometrical configurations,” *Magnetics, IEEE Transactions on*, vol. 22, no. 5. pp. 355–360, 1986.

[112] M. Abramowitz and I. Stegun, *Handbook of Mathematical Functions*, Tenth prin. National Bureau of Standards, 1972.

[113] H. N. Bertram and C. W. Steele, “Pole Tip Saturation in Magnetic Recording Heads,” *IEEE Trans. Magn.*, vol. MAG-12, no. 6, pp. 702–706, 1976.

[114] Y. Nakamura, “Conditions For Ultra-High Density Magnetic Recording,” *J. Magn. Soc. Japan*, vol. 13, 1989.